Transpiration Cooling of a Hypersonic Vehicle

Hassan Saad Ifti

Wolfson College

University of Oxford

A thesis submitted for the degree of

Doctor of Philosophy

Michaelmas 2021

Acknowledgements

It is hard to put into words, how thankful I am to the people who helped me come this far and how grateful I am for everything that I have achieved. Nonetheless, it is worth a try, even if I fail. Although as I try, it is proving to be more difficult than I thought. As I sit here in my room at Wolfson College, I'm becoming rather emotional.

Towards the end of my degree in Stuttgart, in a rather difficult phase of my life, I was browsing the website of the *Centre for Hypersonics* at the University of Queensland, looking for a PhD studentship. I came across an interesting thesis of someone by the name of Dr Matthew McGilvray. Upon going through his thesis, I was compelled to send him an email inquiring whether he had an opportunity for a mere being like me. To my surprise, he wrote back saying he'll be in Stuttgart for work and that we should meet face-to-face. So we did. All this time, I was under the impression that this professor is a relatively older fellow. I was surprised to see such a young professor when we eventually met at the *Bar Vicino* for a coffee. Matt showed me the facilities in his newly formed Hypersonics Group, a very young group. This is when I was persuaded to apply to Oxford for a *DPhil* studentship. Otherwise, I would've never thought of applying to a place like Oxford. In the past five years, working closely with Matt, I have realised how incredibly talented he is. I've seen him grow from a young PI to a *Fellow of the Royal Academy of Engineering*. And I've observed our small research group become the only *Centre of Excellence in Hypersonics* in the UK. I'm so proud to have been there as one of the pioneers. Matt, thank you so much for everything that you've done for me. In my first year, you said I should learn to "*take the bull by the horn*." I hope I have. I hope I have attained a fraction of your talent throughout these years. We are very different in nature, often having opposite personalities. But I believe we have achieved something beautiful together. Thank you; thank you for these incredible, life-changing five years.

Next, I must thank Dr Tobias Hermann. Tobi joined our lab as a postdoc just three months after I had started and mentored me regularly. I didn't have any experience in experimentation when I started this DPhil, and I have you to thank, Tobi, for teaching me how to setup up optical diagnostic tools. I still remember the moment when our UHTC sample blew off! We've come a long way. Today, you're a *Future Leaders Fellow*! I'm ever so grateful to have you as my mentor. You're an excellent scientist, and I'm keen to see what you do next. Merci vielmals!

I'd like to extend my gratitude to Dr Jim Merrifield for his constant support for the last couple of years in setting up the numerical simulations. I have always

enjoyed my trips to FGE in Emsworth. Although there is a strong difference in the weather, it reminded me of my time in Tucson, Arizona. I wonder why. Perhaps, it's the numerics! And Craig Parsons, thank you ever so much for helping us with the IT setup.

This acknowledgements section would be incomplete without mentioning the support I received from Professor Luc Vandeperre of Imperial College London and his team. I have immensely enjoyed our collaboration on UHTCs. As an experimentalist in aerothermodynamics, this was an incredible opportunity for me to expand my knowledge of porous media and their application.

This endeavour wouldn't have been possible without the immense support from Dr Luke Doherty, Chris Hambidge, and Dr Laurent Le Page. Luke, thanks for hearing me out last year when I was going through a very stressful time. Your contribution to the group is invaluable and you're a great teacher. Thanks to you, I can perform much better uncertainty analyses and pick any pipe fitting! Chris, formally I should thank you for operating the tunnel for me and advising me during my PDR and CDR. I am of course thankful for that, but I really thank you for all the pub sessions you had with me. It's a shame that we couldn't manage another *crazy night* at *Plush*. Laurent, thank you for being there when I had to talk and cheers for proof reading my work on UHTCs. I still owe you a bottle!

The work presented in this thesis required cumbersome, and often challenging, experimental setups and instrumentation. Gregory King deserves all the praise for the instrumentation involved in this work. Greg, cheers for coming over to the lab during the nationwide lockdown last year just to paint my model – I'll never forget this. And special thanks to William Godfrey, Hal Surtell, and Jason McCluskey for their assistance in building the experimental rigs. And I have been lucky to meet a friend like Dr Ikhyun Kim towards the end of last year. What an absolute *geezer* you are! Maïlys, thanks for operating the tunnel for my last campaign and making the control room a jolly place!

In my early days in the lab, Professor Peter Ireland, Professor David Gillespie, Dr Alex Bucknell, and Dr Pete Forsyth helped me incredibly to get my head around experimental and measurement techniques. I'm ever so grateful for this. I also thank my friend Jack Lavender, who shared his wealth of engineering knowledge from the very first day.

Andy, you've always helped me keep my sanity with the coffee breaks. You're an amazing friend. Marc, throughout these years, you have been a friend, a colleague,

and of course my flat-mate. I have learnt a lot of discipline from you – *not just drinking bottled water!* Imran, cheers for all the help during my campaign last year. Wow – you're married now! I'm so happy for you. William and Philipp, cheers for helping me out whenever I needed a hand. Well, a big THANK YOU to the whole Hypersonics Group for making me feel at home and doing *shots* (tunnel shots – yeah right!) with me. *In life, we celebrate!*

I cannot begin to express my gratitude to Anna and Alex for taking care of all my 'urgent' purchase orders! Also, Dr Alex Murry, Jonnolly, Aravin, and Anton – cheers for everything. And Cristina, I wholeheartedly thank you for saving lunch for me at the cafeteria when I was doing my experimental campaign. You're the sweetest person ever!

Farhaz, Shamir, Amita, MAK, Kristina, Monzy, Helena, Abhishek, Michael, Andrew Bustard, and Rathieshan – I have no words to express my gratitude towards you. You have kept me sane – well, whatever sanity I had to begin with – throughout my DPhil life. It would be a long list if I were to mention all of my dearest friends in Oxford. You know who you are, and I thank all of you for making this magical place a home for me. Marius, Henning, Rouaid, Helge, Thiru, Philipp, and Darbaz, my *Habibis*, I look forward to our next trip to Vegas! Cheers for your support for so many years. Apropos of Vegas, I haven't forgotten you, my dearest *VagabondZ*! I'm immensely proud of all of you.

I'm deeply indebted to my mentors, Dr Markus Kloker and Professor Markus Stroppel of the University of Stuttgart, Christoph Weispfennig and Shirin Gleba of Airbus, Professor Hermann Fasel of the University of Arizona, and Hans-Dieter Bell of Karlsruhe Institute of Technology, for their regular encouragement and guidance. I would also like to take this opportunity to thank my teachers from my high school in Bangladesh, Rofiqul Jewel and Sakhawat Hossain, for preparing me for an academic life at the highest level. We had nothing, just pen and paper. Turns out, there is no need for a *fancy* school. All we need is a symphony of eager minds!

Oh, before I forget, the funding ($$$) for this research by the EPSRC grant 'Transpiration Cooling Systems for Jet Engine Turbines and Hypersonic Flight' (reference: EP/P000878/1) is gratefully acknowledged.

It must be mentioned the last two years of this DPhil project was severely hampered by *Covid-19*. I was faced with funding and visa issues whilst struggling to get my final experimental campaign done. My deepest gratitude is reserved for

Sir Tim Hitchens (President, Wolfson College), Emily Eastham (my Senior Tutor, Wolfson College), Megan Roper (Academic Registrar, Wolfson College), Professor Jonathan Pila (my adviser, Wolfson College), and Anna Hedge (Oxford Student Immigration Team) for their support during this unprecedented time. I'd also like to acknowledge everyone who played a part in making my life easy in the eight months that I spent in Mymensingh during the pandemic. This time was critical for the data analysis for this thesis. Special thanks to Auntie Saleha, Uncle Mahfuz, and Uncle Masum, for their encouragement during this difficult time.

It is during the tenure of my DPhil candidacy that my life's story went viral on *Humans of Oxford University*. Ever since, I have received thousands of loving messages from all over the world. I don't deserve this much love, but it surely did make my childhood memories a little more bearable. THANK YOU! In addition to the scientific contributions made in this thesis, this thesis itself is a testament that someone like me can thrive at the highest echelon of education despite not being able to read or write until the age of thirteen, let alone do mathematics and physics or speak multiple foreign languages.

To my parents, Selina and Lutful, thank you ever so much for giving me a chance when *society* gave up on me. All that I am, and all that I'll ever be, is because of you. I remember, *society* once said that you must have committed some crime or sin in the past for having a *handicapped* child like me. Well, if they were right, those sins were pretty *damn good* if you ask me!

Samara and Sami, we've come a long way. All those years of struggle in Germany, and look where we are today. To us! And Sami, cheers for not only proof reading this thesis but also for being the encouraging big brother I needed. Good luck with your DPhil! You'll ace it. And Ishfaq and Oni, you guys are truly an inspiration! Imran, bruv! I'm so proud of you — not because you're becoming an engineer soon, but because you're chasing your dreams. Keep rocking in Australia! Rishad, you're our youngest brother, but you're the most mature of us all. I'm so proud of the young man you've become. Cheers for making sure I could work on my thesis in Mymensingh! It meant the world to me. And finally, Zorro, my fluffy buddy, you've spent almost the same amount of time as I did analysing data and working on the analytical model sitting on my desk. You've been an amazing assistant. For your contribution, I bestow upon you the degree of *DPaws in Hyper-meow-sonics*.

To all my friends and family, thanks for understanding me. Sorry that I wasn't available, and apologies for forgetting the important dates. I'm sorry. I am, rather, poorly made.

P.S.: Exactly twelve years ago, I left my home in Mymensingh, Bangladesh, and embarked upon a journey as a teenager to achieve the dream of becoming an Aerospace Engineer, a very far-fetched dream at the time. Twelve years later, I have not only attained that goal but also had the opportunity to conduct research in, and contribute to, the field of Aerospace Sciences using world-class facilities to my heart's content. I am ever so thankful to everybody who believed in me on this magical journey. Thank you.

This thesis is dedicated to my late Grandfather,
who defended the eastern border of the British Empire within the *RAF* in *WWII*.

Statement of Originality

I hereby declare that this submission is my own work and to the best of my knowledge, it contains no materials previously published or written by another person, or substantial proportions of material that have been accepted for the award of any other degree at the University of Oxford or any other educational institution, except where due acknowledgement is made in this thesis. Any contribution made to this research by others, with whom I have worked at the University of Oxford or elsewhere, is explicitly acknowledged in the thesis. I also declare that the intellectual content of this thesis is the product of my own work, except to the extent that assistance from others in the project's design and conception or in style, presentation, and linguistic expression is acknowledged.

Signed by: Hassan Saad Ifti

List of Publications

First-authored journal articles included in this thesis:

1. **Ifti, H.S.**, Hermann, T., McGilvray, M., Larrimbe, L., Hedgecock, R. & Vandeperre, L.J. (2022), "Flow Characterisation of Porous Ultra-High-Temperature Ceramics for Transpiration Cooling." *AIAA Journal.*

2. **Ifti, H.S.**, Hermann, T., Ewenz Rocher, M., Doherty, L., Hambidge, C., McGilvray, M. & Vandeperre, L.J. (2022), "Laminar Transpiration Cooling Experiments in Hypersonic Flow." *Experiments in Fluids.*

3. **Ifti, H.S.**, Hermann, T., McGilvray, M., & Merrified, J. (2022), "Numerical Simulation of Transpiration Cooling in a Laminar Hypersonic Boundary Layer." *Journal of Spacecraft and Rockets.*

4. **Ifti, H.S.**, Hermann, T. & McGilvray, M. (2022), "Analytical Model of Transpired-Coolant Concentration at Downstream Wall in High-Speed Laminar Flow." *AIAA Journal.*

First-authored conference papers relevant to this thesis but not included herein:

5. **Ifti, H.S.**, Hermann, T., & McGilvray, M. (2018). "Flow Characterisation of Transpiring Porous Media for Hypersonic Vehicles." *In 22nd AIAA International Space Planes and Hypersonics Systems and Technologies Conference. American Institute of Aeronautics and Astronautics.*
https://doi.org/10.2514/6.2018-5167

6. **Ifti, H.S.**, Hermann, T., & McGilvray, M. (2019),"Transpiration Cooling at Mach 5 Employing Porous UHTC." *International Conference on Flight vehicles, Aerothermodynamics and Re-entry Missions and Engineering, Monopoli, Italy.*

Co-authored journal and conference papers during the tenure of the author's DPhil candidacy (not included herein):

7. Ewenz Rocher, M., Hermann, T., McGilvray, M., **Ifti, H.S.**, Vieira, J., Hambidge, C., Quinn, M.K., Grossman, M., Vandeperre, L.J. (2021), "Pressure-sensitive Paint Diagnostic to Measure Species Concentration on Transpiration-Cooled Walls." *Experiments in Fluids.*
https://doi.org/10.1007/s00348-021-03355-9

8. Cerminara, A., Hermann, T., **Ifti, H.S.**, Deiterding, R., Sandham, N., and McGilvray, M. (2020), "Influence of Instability Modes on Cooling Performance in Hypersonic Boundary Layer with Slot Injection." *Aerospace Science And Technology.*
https://doi.org/10.1016/j.ast.2020.106409

9. Ewenz Rocher, M, T. Hermann, M. McGilvray, **Ifti, H.S.**, and Quinn, M.K. (2019), "Studying the Film Effectiveness of Transpiration Cooled Walls Using Pressure Sensitive Paint." *International Conference on Flight vehicles, Aerothermodynamics and Re-entry Missions and Engineering, Monopoli, Italy.*

10. Hermann, T., McGilvray, M., **Ifti, H.S.**, Hufgard, F., & Löhle, S. (2020). "Thermal Impulse Response in Porous Media for Transpiration-Cooling Systems." *Journal of Thermophysics and Heat Transfer*, 34(2), 447-456.
https://doi.org/10.2514/1.t5841

11. Bucknell, A., McGilvray, M., Gillespie, D., Parker, L., Forsyth, P., **Ifti, H. S.**, Reed, A. (2019). "Experimental Study and Analysis of Ice Crystal Accretion on a Gas Turbine Compressor Stator Vane." *In SAE Technical Paper Series. SAE International.*
https://doi.org/10.4271/2019-01-1927

12. Ewenz Rocher, M., McGilvray, M., Hermann, T. A., **Ifti, H. S.**, Hufgard, F., Eberhart, M. F., Vandeperre, L. J. (2019). "Testing a Transpiration Cooled Zirconium-Di-Boride Sample in the Plasma Tunnel at IRS." *In AIAA Scitech 2019 Forum. American Institute of Aeronautics and Astronautics.*
https://doi.org/10.2514/6.2019-1552

13. Hermann, T. A., McGilvray, M., **Ifti, H. S.**, Hufgard, F., & Loehle, S. (2019). "Fluid-Solid Heat Exchange in Porous Media for Transpiration Cooling Systems." *In AIAA Scitech 2019 Forum. American Institute of Aeronautics and Astronautics.*
https://doi.org/10.2514/6.2019-0537

14. Hermann, T. A., **Ifti, H. S.**, McGilvray, M., Doherty, L. & Geraets, R. P. (2018). "Mixing Characteristics in a Hypersonic Flow around a Transpiration Cooled Flat Plate Model. *In HiSST: International Conference on High-Speed Vehicle Science Technology.*

"People who wish to analyze nature without using mathematics must settle for a reduced understanding."

— *Richard Phillips Feynman*

Abstract

In this thesis, a porous Ultra-High-Temperature Ceramic (UHTC) made of zirconium diboride (ZrB_2) is qualified for the purpose for transpiration cooling for the first time. Subsequently, the mixing mechanism between the coolant and a laminar, hypersonic boundary-layer gas at the wall downstream of a transpiration-cooled injector is investigated. This has led to understanding the mixing process at the wall in a laminar boundary layer.

Porous UHTCs are a candidate group of materials for transpiration cooling of hypersonic vehicles due to their exceptionally high melting point, typically above 3000 K. Their high operating temperature permits a higher amount of radiative cooling than that achievable with conventional materials, which reduces the required coolant mass flow rate to cool the surface. This thesis experimentally examines the internal and external flow behaviour of porous UHTC made of zirconium diboride (ZrB_2) for the purpose of transpiration cooling. A dedicated ISO standard permeability test rig was built. The outflow velocity distribution was acquired employing miniature hot-wire anemometry. The data obtained for the pressure loss across the porous samples agree with the Darcy-Forchheimer model for flow in porous media; respective Darcy and Forchheimer permeability coefficients are calculated and reported. Cleaning the surface of the samples using sandpaper or an ultrasonic bath raised the permeability coefficient by up to 19%. The outflow velocity maps exhibit a good flow uniformity with an average standard deviation of 25.1% with respect to the mean value. Individual jets are absent, and the velocity varies within the same order of magnitude.

The mixing between the coolant and the boundary-layer gas downstream of an injector – for transpiration/film cooling – has been extensively studied for turbulent flows; however, only a handful of studies concerning laminar mixing exist, particularly in hypersonic flows. In this thesis, the concentration of the coolant gas at the wall and the heat flux reduction downstream of a transpiring injector in a hypersonic, laminar flow are experimentally measured and examined. Experiments are performed in the Oxford High Density Tunnel at Mach 7. A flat-plate model is coated with Pressure-sensitive Paint (PSP) to spatially resolve the film and obtain a film effectiveness based on coolant concentration. Thin-film arrays are installed to measure the heat flux reduction. Six different cases are studied featuring Nitrogen and Helium as the coolant gas, where the blowing ratio is varied from 0.0406% to 0.295%. The unit Reynolds number of the flow is 12.9×10^6 m^{-1}. A coolant concentration of up to 95% is achieved immediately downstream of the injector. The film concentration drops in a monotonic fashion farther downstream; however, a constant film coverage of 5 mm to 20 mm immediately downstream of the injector is observed in cases with a higher blowing ratio. A film coverage above 15% over three

injector-lengths is present even for the lowest blowing ratio. Heat flux reduction is achieved in all cases; an onset of boundary-layer transition is not promoted. The concentration effectiveness obtained from PSP is compared with the thermal film effectiveness calculated from the heat flux reduction. The latter is found to be higher than the former for all data points. Subsequently, a collapse of the thermal effectiveness is achieved and a modified analytical correlation is proposed.

A two-dimensional simulation study of transpiration cooling in a laminar, hypersonic boundary layer using the Thermochemical Implicit Non-Equilibrium Algorithm (TINA) – a Navier-Stokes solver was undertaken. Coolant concentration and heat flux results are compared to data obtained from the experiments. TINA successfully predicts the mixing rate at the wall as a function of the stream-wise direction for all blowing ratios. The simulations are more successful in predicting the mixing downstream of the injector compared to the mixing on the injector, especially at low blowing ratios. A collapse of the thermal effectiveness values calculated from simulation data is achieved, which agrees with laminar correlations within an absolute value of $\pm 10\%$. It is shown that, when the concentration effectiveness is close to 1 at the injector, the temperature gradient becomes negative at locations immediately downstream of the injector, resulting in a negative heat flux. The acceleration of the coolant in the stream-wise direction downstream promotes dissipation of energy, which results in a reduction in the temperature of the coolant and thereby induces a negative temperature gradient close to the injector.

Finally, an analytical model based on one-dimensional diffusion is proposed to predict the mixing between the coolant gas and boundary-layer gas at the wall downstream of a transpiring injector in a laminar flow. The model is validated against the experimentally obtained coolant concentration data. It successfully predicts the mixing at the wall downstream within 17% of the experimental data. It is shown that this mixing mechanism at the wall in laminar flows is fully described by the process of diffusion. The coolant coverage at a given downstream location is promoted when the stream-wise velocity decreases, the blowing ratio increases, or the diffusion coefficient drops. Subsequently, a mass budget calculation is performed for a transpiration-cooled hypersonic vehicle employing the analytical model. The model predicts a 3.6 times less coolant mass requirement when Helium is used as the coolant gas as opposed to Nitrogen for the chosen trajectory. However, Helium requires twice the storage volume compared to Nitrogen.

Contents

List of Figures

1 Introduction

1.1 The Pursuit of Hypersonic Flight

Any object that travels at speeds greater than Mach 5, i.e. five times the speed of sound, is typically considered a hypersonic vehicle. Rockets, re-entering capsules, intercontinental ballistic missiles, and future spaceplanes are examples of hypersonic vehicles. In recent times, a revived pursuit of hypersonic flight is taking place. Geopolitical tension between the West and their adversaries Russia and China fuelled the advancement of hypersonic missiles and glide vehicles (Button, 2018). As a result, research budget for hypersonics has seen a steady increase. The Pentagon allocated $2.6 billion, $3.2 billion, and $3.8 billion for 2020, 2021, and 2022, respectively, for hypersonics research (Wasserbly, 2021). Recently, Australia, the United Kingdom, and the United States announced the *AUKUS* partnership, which includes an agreement that will allow the countries to share technical information on long-range hypersonic strike technology (Gill, 2021). On the other hand, envisaged commercial hypersonic passenger planes that could fly from London to New York within two hours seem ever so close with the rise of start-ups such as *Hermeus* in the United States and *Ling Air Skywalk Technology* in China (Stein, 2021). In Australia, *Hypersonix* is developing a re-usable hypersonic launch vehicle for small satellites (Harrison, 2021). And the alluring dream of space travel remains alive with human space flight programmes at SpaceX, Blue Origin, and Boeing. Advancement in computing power, improved ground testing facilities and experimental techniques, use of novel materials, and a better understanding of the flow physics around a hypersonic vehicle through years of research (Leyva, 2017) are gradually making

sustained hypersonic flight a tangible reality. However, the increased funding and renewed interest in hypersonics alone are not enough to make this technology viable as intended, for the revolution of modern flight by hypersonics is not limited by will; it is limited by the unknowns of complex flow physics around such a vehicle, propulsion technology, and material capabilities (Leyva, 2017). Therefore, hypersonic technology – unlike many other emerging technologies – requires broad-range, in-depth basic research for any successful deployment. It is no wonder, therefore, that 120 organisations joined the University Consortium of Applied Hypersonics in the US, whose mission is to enable the innovation to create hypersonic flight vehicles (Stein, 2021). The pursuit of hypersonic flight remains heavily dependent on both fundamental and applied research.

1.2 The Problem of Aerodynamic Heating over Hypersonic Vehicles

The definition of a hypersonic vehicle stated above is imprecise. Unlike in supersonics, where the physical sound barrier has to be overcome at exactly Mach 1, nothing of that sort happens when a vehicle accelerates past Mach 5. Hypersonics is rather better defined by certain flow characteristics that start to manifest themselves at Mach numbers as low as 3. Notable amongst these characteristics are the thin shock layer, viscous interactions, and aerodynamic heating. The latter is in fact one of the key characteristics of hypersonic flows, and its mitigation is the central topic of this thesis.

In the earlier days of high-speed flight and re-entry vehicles, the challenge of aerodynamic heating soon became apparent. Highlighting this aspect of hypersonic flight, von Kármán (1954) ever so elegantly said:

> *"One basic problem has to be mentioned – the problem of safe return to the earth or landing on any celestial body. Any rocket returning from space travel enters the atmosphere with tremendous speed. At such speeds, probably even in the thinnest air, the surface would be heated beyond the temperature endurable by any known material. This problem of the temperature barrier is much more formidable than the problem of the sonic barrier."*

This temperature barrier, or thermal barrier, is what makes hypersonic flight extremely difficult. Even at Mach numbers as low as 3, the aerodynamic heating could pose a challenge for vehicle design. In his paper on aerodynamic heating, van Driest (1956) stated:

> *"The temperature of this layer* [thin layer of air that blankets the body] *increases with the square of the speed* [of the vehicle] *so that, already at a Mach number of 3, the boundary-layer temperature attains a value of about 600 °F* [315 °C]. *Since this temperature is concentrated in the air at the surface of the aircraft, the ease which it flows increasing also with speed. Because of the heat transfer with speed, it appears that a 'thermal barrier' exists much as it appeared in the past that a 'sonic barrier' existed."*

The temperature rises with the square of the speed because the high kinetic energy (proportional to the square of the speed) dissipates into thermal energy and results in convective heating of the vehicle surface. This convective heating dominates up to a speed of approximately 9.1 km/s before the radiative heating from the shocked gas takes over (Anderson, 2006). The total heat flux can be very high, e.g. for the space shuttle, heat fluxes were around 600 kW/m^2, but this can reach as high as 10 MW/m^2 for a smaller nose-radius (Reimer *et al.*, 2012). Furthermore, the high temperature in the boundary layer can cause in a chemically reactive flow resulting in dissociation and ionisation.

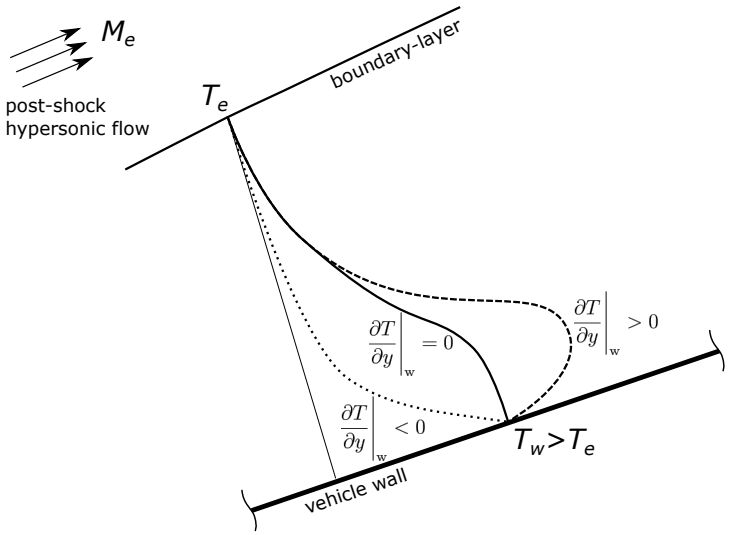

Figure 1.1: Temperature profiles (not to scale). y denotes the wall-normal direction.

The convective heat flux (energy per second per unit area) into the vehicle wall is proportional to the temperature gradient at the wall ($y = 0$), which is given by Fourier's law of heat conduction expressed as

$$\dot{q}_w = k \left. \frac{\partial T}{\partial y} \right|_w . \tag{1.1}$$

Here, k is the thermal conductivity of the gas in wall conditions. When the flow speed increases, the flow becomes compressible and the heat generated by viscous dissipation within the boundary layer is considerably large. As a consequence, the gas temperature close to the wall rises. This temperature is often denoted as the recovery temperature, T_r, in the literature. If the wall temperature, T_w, is matched to the recovery temperature, no temperature gradient will exist at the wall as shown in Fig. 1.1 (solid line, $\left. \frac{\partial T}{\partial y} \right|_w = 0$) and therefore the heat flux is $\dot{q}_w = 0$ according to Eq.(1.1). This wall temperature is defined as the adiabatic wall temperature, $T_{\mathrm{ad}} = T_w = T_r$. The ratio of the adiabatic wall temperature, T_{ad}, and the edge temperature, T_e, is given by

$$\frac{T_{\mathrm{aw}}}{T_e} = 1 + \frac{r(\gamma - 1)}{2} M_e^2, \tag{1.2}$$

where γ is the isentropic exponent, M_e is the edge Mach number, and r is the recovery factor defined as

$$r = \frac{T_{\mathrm{ad}} - T_e}{T_0 - T_e}. \tag{1.3}$$

The recovery factor quantifies the amount of total temperature, T_0, that is recovered close to the wall by viscous dissipation. Typically, approximated values of $r = 0.85$ and $r = 0.89$ are used for laminar and turbulent boundary layers, respectively (van Driest, 1956). As it can be seen from Eq.(1.2), the ratio $\frac{T_{\mathrm{aw}}}{T_e}$ increases with the square of the Mach number. This is illustrated in Fig. 1.2 for air ($\gamma = 1.4$). It can be seen that for a Mach number of $M_e = 5$, $\frac{T_{\mathrm{aw}}}{T_e}$ is approximately 5 and for $M_e = 8$, $\frac{T_{\mathrm{aw}}}{T_e}$ is beyond 10. This demonstrates that even for the lowest edge temperatures, the temperature for an adiabatic (insulated) wall is significantly higher as the Mach number increases and the temperature limit of the wall material will be reached (also

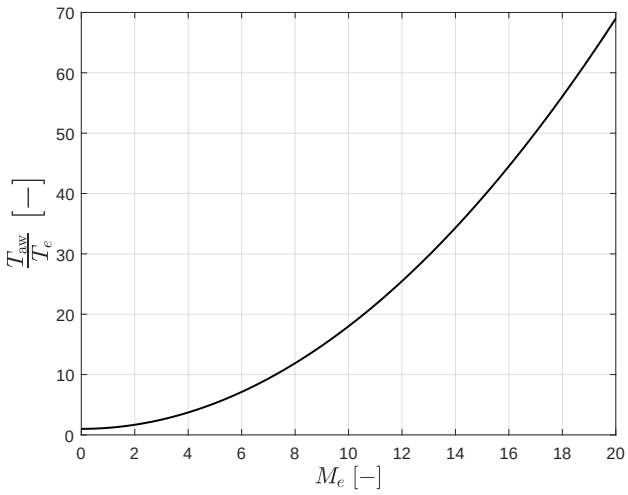

Figure 1.2: Adiabatic wall temperature ratio as a function of Mach number for an adiabatic.

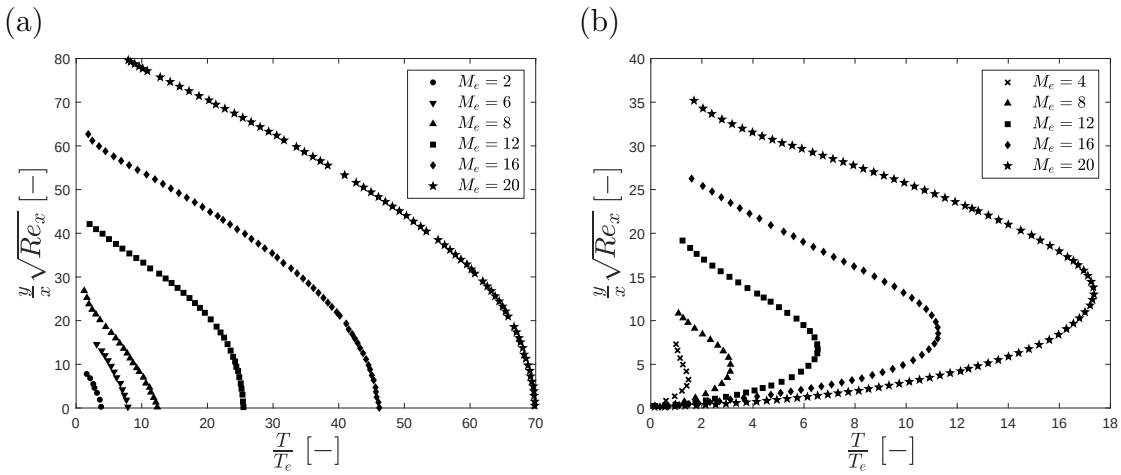

Figure 1.3: Temperature profiles for (a) an adiabatic wall and (b) an isothermal wall in laminar boundary layers. Graphs are recreated from van Driest (1952).

seen in Fig. 1.3a). Instead, if a constant, isothermal wall temperature (below the melting point of the wall material) is maintained, a positive temperature gradient forms at high Mach numbers as shown in Fig. 1.1 (dashed line, $\left.\frac{\partial T}{\partial y}\right|_w > 0$). This leads to a positive heat flux, i.e. $\dot{q}_w > 0$, into the vehicle wall. As shown in Fig. 1.3b, the temperature gradient becomes steeper as the Mach number rises, which results in a higher heat flux, $\dot{q}_w$, at the wall. Unless this heat flux is mitigated, it will eventually increase the wall temperature beyond its melting point.

Vehicles that fly at high Mach numbers are therefore inherently prone to extremely high heat fluxes, and cooling technologies becomes essential for successful

deployment of these vehicles. Over a flight time, t, they endure a total heat load of

$$Q = \int_0^t \dot{q}_w dt. \tag{1.4}$$

Q needs to be minimised to keep the vehicle intact. Broadly, this can be achieved by the following:

i. Minimise the total flight time, t, in high heat flux regions, which can be difficult due to constraints in the mission envelope.

ii. Operate at a higher wall temperature, ideally close to the adiabatic wall temperature, T_{ad}, and minimise wall heat flux, $\dot{q}_w$. This requires use of materials with an extremely high melting point and avoidance of oxidation. The higher temperature would also allow for radiative cooling (Stefan-Boltzmann Law).

iii. Reduce $\dot{q}_w$ by gaseous insulation, especially for peak heating (maximum $\dot{q}_w$).

This mitigation of heat is performed by Thermal Protection Systems (TPS). In the next section, an overview of the different thermal protection systems are presented.

1.3 Thermal Protection Systems

1.3.1 Types of Thermal Protection System

In order to protect hypersonic vehicles from the harsh high-temperature effects, generally the following three types of Thermal Protection System (TPS) concepts (see Fig. 1.4) are present (Kelly & Blosser, 1994; Launius & Jenkins, 2012):

- **Passive:** This concept falls into three general categories: heat sink, hot structure, and insulated structure. The heat sink absorbs almost all of the incident heat and stores it in a large, usually metallic mass. Additional mass may be added to increase the heat storage capability, but in general the concept is limited to short heat pulses. A hot structure allows the temperature to rise until the heat being radiated from the surface is equal to the incident

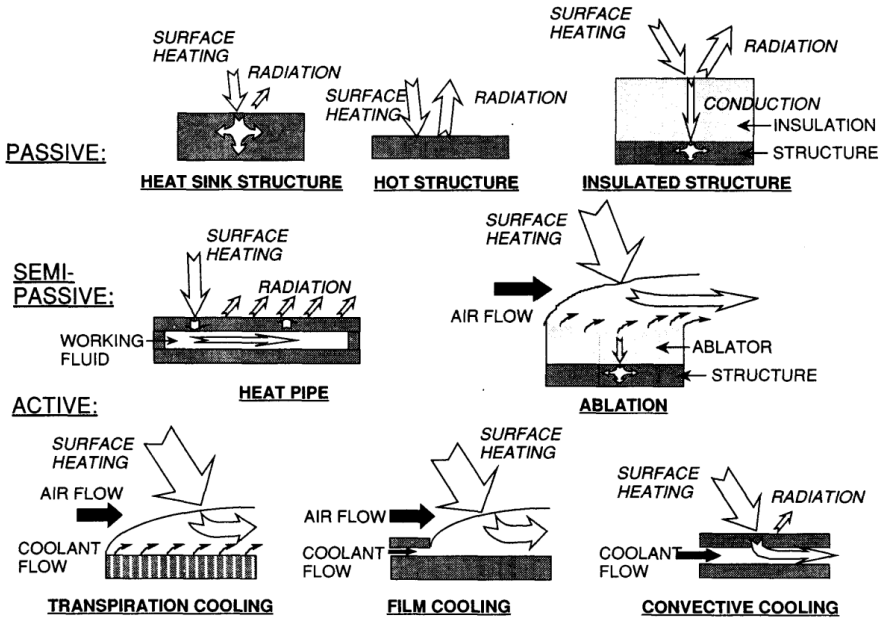

Figure 1.4: Concepts of thermal protection systems (Kelly & Blosser, 1994).

heating. This concept is not limited by the duration of the heat pulse but is restricted to the acceptable surface temperature of the structural material. Insulated structures use an outer shell that radiates most incident heat away from an underlying structure protected by a layer of some insulating material, usually high-temperature ceramic-fibre batt insulation.

- **Semi-passive:** Heat pipes and ablative shields are the main semi-passive methods. The most common semi-passive concept is ablation, however. Ablation is a process in which a material (ablator) sacrifices itself to protect the underlying structure. However, the ablator is consumed in the process, thus limiting the duration of its operation and ruling out re-usability. An example of a modern-day ablator is the Phenolic-Impregnated Carbon Ablator (PICA) is used by SpaceX.

- **Active:** The most widely referred to active cooling methods are film cooling and transpiration cooling. Film cooling uses discrete slots, or rows of discrete holes, to inject a coolant gas into the boundary-layer flow, whereas transpiration cooling ejects the coolant through a porous surface. Although

film cooling is being used widely for gas turbine blades and rocket nozzle walls, none of these active cooling methods has been used for significant hypersonic applications (Esser *et al.*, 2016). However, active cooling is an attractive option as it provides the potential of carrying away large amounts of heat, especially from vehicle parts that are prone to extremely high peak heating.

Regardless of the type, the TPS plays a vital role in the success of the vehicle's mission. Any compromise to the TPS could lead to a catastrophic failure of the vehicle. The choice of the TPS type depends on the mission requirements. Generally, the simplest and lightest option is elected (Kelly & Blosser, 1994). However, more complex options may be required, sometimes even with a mass penalty, to cool vehicle parts that face the highest heat fluxes. The pros and cons of these TPS types are given in Table 1.1. Although passive and semi-passive methods are simpler than active methods, they do not offer the potential of full re-usability that active cooling does. The main added value of active cooling is its re-usability, which could significantly drive down the cost of hypersonic payload transfer. In particular, transpiration cooling a suitable option for hypersonic applications since the injected gas is introduced into the boundary layer through fine pores as opposed to discrete holes in film cooling. Discrete holes could result in individual jets that could trigger transition of the boundary-layer state. In addition, transpiration cooling is more efficient for a given coolant mass flux compared to film cooling with slots (Hermann *et al.*, 2018). As it would be discussed in the following section, transpiration cooling can prevent oxidation of vehicle wall material and thereby enhance the operational temperature of hot structures and aid passive methods to be more efficient. It can also cool and protect parts downstream of the injector, which is particularly useful for parts that cannot be made porous due to the high stress loads on them (e.g. control fin hinges).

Rather than replacing the existing passive and semi-passive methods, transpiration cooling would be best utilised in conjunction with them, enhancing their capability and protecting the parts that endure the highest heat fluxes (e.g. leading edges). This will increase the overall degree of re-usability of a hypersonic vehicle and

TPS Type	Pros	Cons
Passive	• partially re-usable • low complexity • no working fluid • proven technology	• requires materials with high temperature resistance • prone to oxidation
Semi-passive	• mid complexity • no external supply of working fluid required • proven technology • ablators can withstand heat up to 300 MW/m^2 (Uyanna & Najafi, 2020)	• Ablator is not re-usable • adds weight
Active	• regenerative/re-usable • can reduce oxidation of the surface • effective in protecting local regions facing extreme heat flux • protection extends downstream	• high complexity • external supply of working fluid required • could add weight (coolant and pipework) • requires carefully designed injector • could trigger boundary-layer transition • not extensively tested in flight (unproven)

Table 1.1: Pros and cons of TPS types.

allow for cheaper and safer payload transfer and make such flights more accessible. However, this promising technology needs further understanding before it can be deployed successfully. Transpiration cooling is the central topic of the work presented in this thesis and it is discussed in the following section in details.

1.3.2 Transpiration Cooling

Within the category of active cooling, transpiration cooling is a promising technology that could enhance the re-usability of vehicle parts that are subject to high peak heating such as leading edges or control-fin joints. It is a dual-mode protection system that would protect the vehicle parts from both heat and oxidation. This cooling process consists of three different subprocesses (see Fig. 1.5): (a) heat from the wall is convected out by the coolant gas; (b) the coolant gas creates a film (blue) that insulates the wall underneath from the hot cross-flow; and (c) the coolant film protects the wall from free-stream Oxygen and thereby prevents oxidation of the wall, which enables the wall-material to operate at a higher temperature enhancing radiative cooling and reduces recombination heating. The success of the latter two processes depends on the coolant film that is formed on and downstream of the injector. The concentration of this protective film reduces in the stream-wise direction and eventually the film diminishes at a downstream location as it mixes with the incoming hypersonic cross-flow (see the concentration gradient, $C(y)$ in Fig. 1.5).

The mixing mechanism between the boundary-layer gas and the coolant has been a topic of research more than fifty years (Goldstein, 1971; Fujiwara *et al.*, 2017) and several semi-analytical correlation exist, mostly for turbulent flows. However, the exact mixing process and the role of the driving variables are still not understood entirely, and therefore a universal solution is not yet available. Fujiwara *et al.* (2017) highlighted this particular limitation in their recent review paper as follows:

> "Gas properties such as heat capacity, thermal conductivity, and diffusivity are other influential parameters, and correction factors to account for the differences in gas properties have been proposed. However, the existence of multiple factors affecting the flow field makes it impossible to obtain a universal correlation."

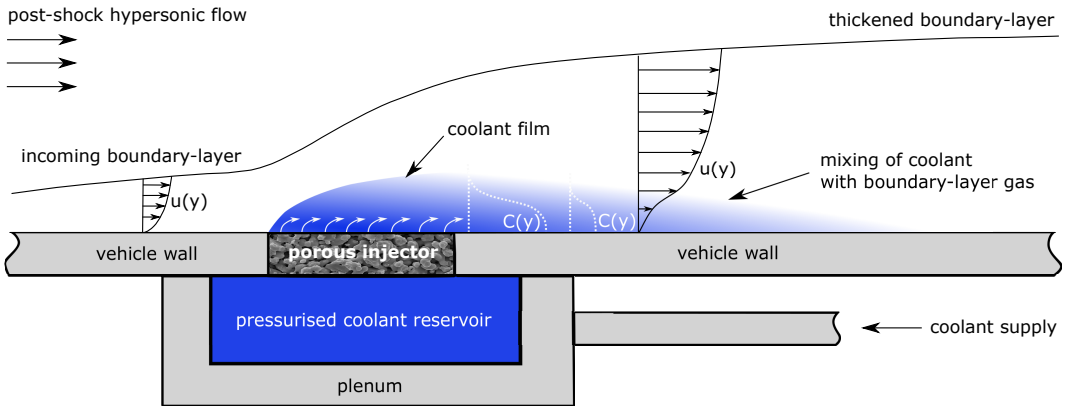

Figure 1.5: Schematic of a flat surface of a hypersonic vehicle with a porous, transpiration cooling injector. Note: not to scale. From Ifti *et al.* (2022*a*).

Moreover, the majority of the studies available in the open literature are concerned with turbulent flows (Goldstein, 1971) because the primary application was for gas turbines blades and rocket nozzles. However, a hypersonic vehicle could fly through all three flow regimes, i.e. laminar, transitional, and turbulent. What is more, these hypersonic vehicles could face the peak heating in the laminar regime (Hermann *et al.*, 2019*b*), where transpiration cooling could be a viable heat mitigation technique. Despite this need, there are only a handful of studies (e.g. Richards & Stollery, 1979; Heufer & Olivier, 2008*b*; Gülhan & Braun, 2010) on film/transpiration cooling in laminar, hypersonic flows and they only involve investigation of the heat flux reduction. However, the Reynolds analogy of heat and mass transfer does not apply in laminar flows (Kays *et al.*, 2005), and therefore the distribution of the coolant's concentration becomes a quantity of major interest.

In addition to the mixing problem, advancement are to be made in the material choice as well. Thus far, porous injectors made of metal (Gascoin, 2011) and carbon-carbon (C/C) type ceramic matrix composites (CMC) have been widely used in recent transpiration cooling studies (Langener *et al.*, 2011; Böhrk, 2014; Löhle *et al.*, 2016; Basore *et al.*, 2016; Dittert *et al.*, 2017). C/C type CMCs are particularly popular due to their manufacturability, low density, high strength (Bacos, 1993), and a high operating temperature of approximately 1800 K (Langener *et al.*, 2011). However, the temperature limit needs to be pushed further in order to enable higher

Mach numbers. Ultra-High-Temperature Ceramics (UHTCs) have an exceptionally high melting point, typically above 3000 K (Wang & Vandeperre, 2014). This high melting point will allow a TPS made of a UHTC lose large amount of heat through radiative cooling according to the Stefan-Boltzmann law. A limitation, however, is the oxidation of UHTCs above 1000 K. As stated earlier, transpiration cooling with an inert gas can mitigate oxidation (Ewenz Rocher *et al.*, 2019). It is therefore not only sensible, but also compelling, to use UHTCs in conjunction with transpiration cooling. In addition, porous UHTCs are made by sintering fine powder grains. This would allow for a more uniform distribution of the outflow compared to the coarse, non-uniform outflow exhibited by C/C CMCs (Dittert *et al.*, 2017). However, no experimental work investigating the suitability of porous UHTCs for application in transpiration cooling is available in the literature.

1.4 Research Aim

The aim of this research is to experimentally qualify porous zirconium diboride (ZrB_2), a UHTC, for the purpose of transpiration cooling and to fully understand the fundamental mixing mechanism between the boundary-layer gas and the coolant at the wall downstream of the injector in a laminar, hypersonic boundary layer. The following contributions are made in this thesis towards achieving this aim:

Evaluation of the internal and external flow characteristics of porous zirconium diboride (ZrB_2) for the purpose of transpiration cooling:

> UHTCs are novel, candidate materials for transpiration cooling, particularly for their exceptionally high melting point (> 3000 K). However, whether they can be utilised for this purpose remains an open question and no experimental work addressing this question is available in the literature.
>
> An ISO 4022 rig was built to determine the permeability behaviour of porous UHTC samples made of sintered zirconium diboride (ZrB_2). The outflow of these samples were characterised with miniature hot-wire anemometry. This

is the first time permeability coefficients and the outflow behaviour of porous UHTCs are reported.

Investigation of the mixing mechanism between the coolant gas and the boundary-layer gas at the wall in terms of coolant concentration and heat flux reduction downstream of a transpiring porous injector in a laminar, hypersonic flow:

Since the Reynolds analogy of heat and mass transfer does not apply to laminar flows, the distribution of the coolant concentration at the wall itself becomes a compelling quantity. However, the handful of studies available in the open literature on laminar, hypersonic film/transpiration cooling only involved heat flux; data on the coolant concentration at the wall downstream of the injector are not available. This leaves a gap in the understanding of the underlying mixing process.

Employing an injector made of porous UHTC, heat flux and concentration data were collected downstream of the injector at Mach 7. Comparison of the numerical and experimental results of the concentration effectiveness show that the mixing rate is successfully captured by a diffusion model, demonstrating that this mixing process in laminar flows is described by the diffusion-advection model.

Development of an analytical model that predicts and describes the mixing process between the boundary-layer gas and the coolant at the wall downstream of the injector in laminar flows:

The downstream mixing of the coolant at the wall is influenced by several variables. Although correlations can help understand the process, they are limited to the flow conditions in which the fitting data were obtained. Ultimately, an analytical model is required to fully understand the mixing mechanism and pinpoint the particular role each variable plays in this mixing process. However, an explanation of the mixing process is not available in the open literature, nor exists an analytical model.

For the first time, an analytical model is proposed to predict the coolant's wall concentration downstream of the injector. The model successfully predicts the experimentally obtained results and a collapse of the data is achieved. The model demonstrated that the mixing mechanism at the wall is described by the process of diffusion. The role of the diffusion coefficient, pressure, temperature, coolant mass flux, and stream-wise velocity in the mixing is discussed based on this model. The model fully describes the downstream mixing mechanism at the wall and can be utilised as a rapid designing tool for downstream transpiration cooling in laminar flows for hypersonic vehicles.

1.5 Thesis Structure

The core work of this thesis is divided in six chapters. This is an integrated thesis, i.e. the chapters representing the results are each a stand-alone journal paper. A preview of the chapters is given below:

- **Chapter 2**: In this chapter, a literature review on the work previously done on film/transpiration cooling by other authors is presented. Relevant physical quantities and results are reported with an emphasis on downstream mixing of the coolant gas. Only a brief review of literature is introduced in this chapter. The reader is referred to the literature review presented in Chapters 3 to 6 for further information.

- **Chapter 3**: The internal and external flow characteristics of porous UHTCs samples made of zirconium diboride (ZrB_2) are presented. The Darcy and Forchheimer permeability coefficients for these samples are reported and the outflow behaviour is discussed. This chapter comprises a journal paper published in the *AIAA Journal* (Ifti *et al.*, 2022*c*).

- **Chapter 4**: Experimental results of transpiration cooling using a porous UHTC injector (characterised in Chapter 2) in a laminar, hypersonic flow are presented and discussed. This chapter comprises a journal paper published in *Experiments in Fluids* (Ifti *et al.*, 2022*a*).

- **Chapter 5**: Results obtained from the numerical simulations are presented with a comparison with experimental data reported in Chapter 4. This chapter comprises a journal paper published in the *Journal of Spacecraft and Rockets* (Ifti *et al.*, 2022*d*).

- **Chapter 6**: An analytical model is constructed based on one-dimensional diffusion. The results obtained from this model are validated against the experimental data reported in Chapter 4. This chapter comprises a journal paper published in the *AIAA Journal* (Ifti *et al.*, 2022*b*).

- **Chapter 7**: A final conclusion of the whole series of work presented in this thesis is drawn, and the added-value of the outcome of this undertaking is discussed.

2 Literature Review

In this chapter, a general overview of past research conducted in film/transpiration cooling that are relevant to the undertaking of this thesis is presented. More specific literature is reviewed in the following four chapters that are each composed of a journal paper.

2.1 Transpiration Cooling

Transpiration cooling could have a wide range of application; from gas turbine blades, rockets nozzles, and scramjets to the exterior of hypersonic vehicles. However, the majority of the studies in the literature are concerned with a common goal of understanding – and in some cases predicting – the mixing between the coolant gas and the external cross-flow in terms of the heat flux reduction. This mixing problem of transpiration cooling can be divided in two regions: (1) on the porous injector and (2) downstream of the injector as illustrated in Fig. 2.1a. In addition, the injection method can be devided in to parts: (1) tangential blowing (Fig. 2.1b) and (2) non-tangential blowing (Fig. 2.1c).

The rate of coolant mass injection is typically quantified by the ratio between the coolant mass flux and the free-stream mass flux, which is known as the blowing ratio. This ratio is defined as

$$F = \frac{\rho_c u_c}{\rho_e u_e}, \tag{2.1}$$

where ρ and u denote the density and velocity, respectively; the subscripts 'e' and 'c' respectively refer to the boundary-layer edge and coolant quantities.

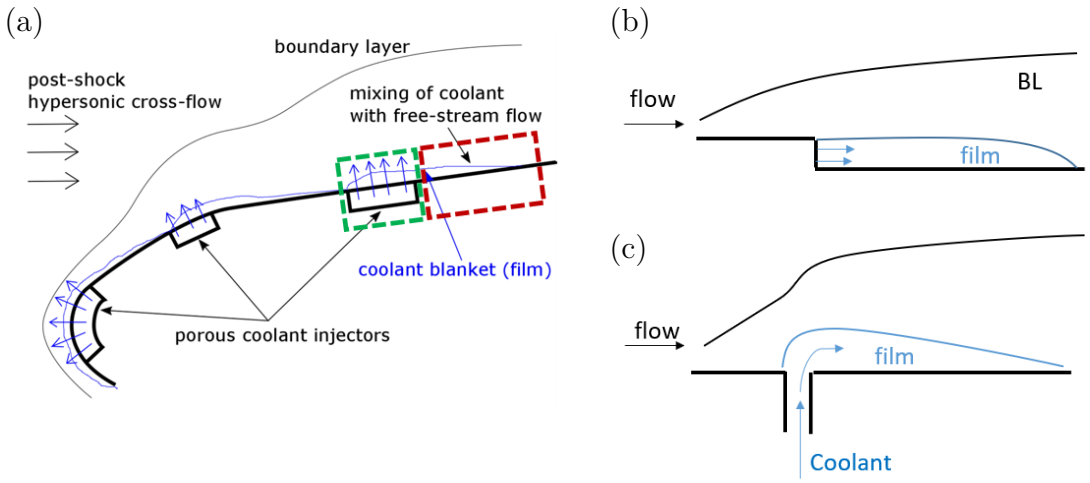

Figure 2.1: (a) schematic of a transpiration cooling leading edge (injector and downstream regions marked in green and red respectively), (b) tangential blowing, and (c) non-tangential blowing. Note: not to scale.

Another common quantity, especially for investigation on the injector, is the the blowing parameter, which is defined as

$$B_h = \frac{F}{St_0}, \tag{2.2}$$

where the subscript '0' denote cases with no blowing, i.e. $F = 0$. Here, St is the Stanton number given by the equation

$$St = \frac{\dot{q}_w}{\rho_e u_e (H_{\text{aw}} - H_w)}, \tag{2.3}$$

where H_w and H_{aw} are the wall and adiabatic wall enthalpies, respectively.

The coverage of the film or the performance of cooling is widely reported in terms of the thermal effectiveness expressed as

$$\eta_{th} = 1 - \frac{St_c}{St_0}. \tag{2.4}$$

An effectiveness of $\eta_{th} = 1$ denotes a full reduction of heat flux, i.e. the heat flux into the surface is $\dot{q}_w = 0$. On the other hand, effectiveness of $\eta_{th} = 0$ refers to a fully diminished film.

Authors have correlated the blowing ratio – or the blowing parameter – of the coolant gas with the cooling effectiveness in various conditions with different gases. In the following sections, the major notable work available in the open literature are briefly discussed.

2.2 Flow Through Porous Media

A fundamental property of transpiration cooling is the use of a porous medium as the injector. This attribute makes it impossible to perform any transpiration cooling study without involving porous media and the flow through them. In Fig. 2.2, a simple, one-dimensional flow through a porous medium is illustrated. Here, the inflow pressure is denoted as $p_{in} = p_1$ and the outflow pressure as $p_{out} = p_2$. The bulk velocity – commonly referred to as the superficial velocity – is denoted with v. The velocity inside the medium is defined as

$$v_m = \frac{v}{\phi}, \tag{2.5}$$

where ϕ is the porosity of the medium. The porosity is defined as

$$\phi = \frac{\text{volume of void}}{\text{total volume}}, \tag{2.6}$$

which is typically given in percentage.

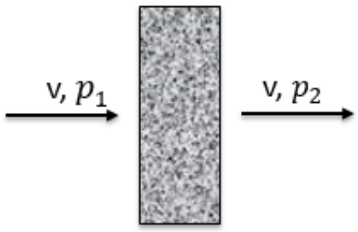

Figure 2.2: One-directional flow through a porous material.

The pressure drop across a porous medium is given by the Darcy-Forchheimer equation (Nield & Bejan, 2013) expressed as

$$-\frac{dp}{dx} = \underbrace{\frac{\mu}{K_D}v}_{\text{viscous term}} + \underbrace{\frac{\rho}{K_F}v^2}_{\text{kinetic term}}, \tag{2.7}$$

or

$$\frac{\Delta p}{L} = \frac{\mu}{K_D}v + \frac{\rho}{K_F}v^2 \tag{2.8}$$

if the pressure gradient is assumed linear. Here ρ and μ are the fluid's density and viscosity, respectively. L is the thickness of the medium. K_D and K_F are

the permeability coefficients, respectively called the Darcy coefficient and the Forchheimer coefficient. The first term of the right-hand-side is the viscous term and accounts for viscous changes, whereas the second term is the inertial term. Hence, the second term becomes prominent only when the Reynolds number based on the pore-diameter is relatively high, i.e when the flow is high in inertial forces. However, the flow through the pores does not necessarily have to be turbulent to achieve this effect. K_D and K_F are material intrinsic properties and are of immense importance for the flow characterisation. A detailed description of the the flow through porous media can be found in Nield & Bejan (2013).

An integrated form of Eq.(2.7) is derived and discussed in Chapter 3 for a constant temperature within the porous medium. Langener *et al.* (2011) derived an integrated form of Eq.(2.7) assuming a linear temperature profile in the porous medium and validated it against experimental data, shown in Fig. 2.3. It can be seen that the normalised differential pressure, $\Delta p/L$, increases as the superficial velocity rises. In other worlds, the required differential pressure increases with the requirement of higher velocities, i.e. mass flow rates or blowing ratios. This is a fundamental feature of flow through a porous media. Any porous medium would have a maximum differential pressure after which it will fail depending on its flexural strength. Furthermore, as the differential pressure is increased, the flow eventually becomes dominated by the Forchheimer regime and the non-linearity of the curve becomes more prominent. Figure 2.3 further illustrates that, for a given velocity, the required differential pressure rises as the gas temperature is increased. This effect is visibly larger in lower velocities because the differential pressure is proportional to the viscosity in the Darcy regime (viscous terms, Eq.(2.7)) and the gas's viscosity μ increases with rising temperature (e.g. Sutherland, 1853). This temperature effect is another aspect of transpiration cooling that constrains the mass flow rate of the coolant since the gas temperature could become significantly high if the porous wall becomes hot due to extreme aerodynamic heating. It is therefore paramount to calculate the required pressure differential for the specific coolant mass flow rate that is needed for a certain flight condition, which makes the

determination of the Darcy and Forchheimer coefficients of the employed injector an indispensable step in designing a transpiration cooling system.

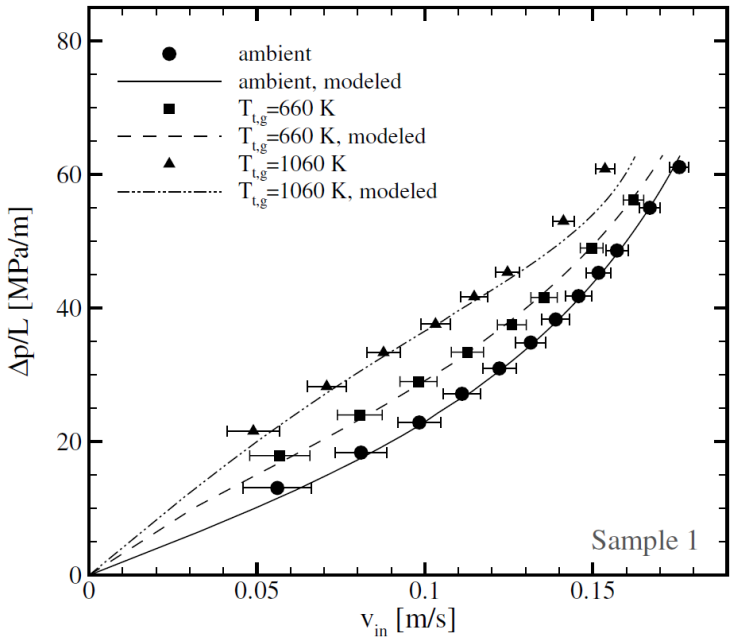

Figure 2.3: Normalised differential pressure versus superficial velocity (sample: C/C). Figure from Langener *et al.* (2011).

For porous materials with regular, spherical particles, Ergun (1952) proposed correlations for K_D and K_F (further details given in Chapter 3). Several other correlations were reported in the literature for spherical or cylindrical particle-based porous materials, and Erdim *et al.* (2015) reviewed 38 of them in their review paper. However, for irregular pore structures, as is the case with most materials suitable for transpiration cooling, the permeability coefficients must be determined experimentally. The measurement of the Darcy and Forchheimer coefficients is a standardised process and exists as a standard (BS EN ISO 4022 2006). A detailed description of a rig built in accordance to this standard is given in Chapter 3.

As mentioned in the preceding chapter, the most widely used materials for transpiration cooling are metals and carbon/carbon (C/C) type CMCs (see Fig. 2.4). In Table 2.1, the permeability coefficients and the porosity are given for selected materials as a reference. These values could vary depending on the porous topology even if the material is the same (e.g. perpendicular vs parallel C/C).

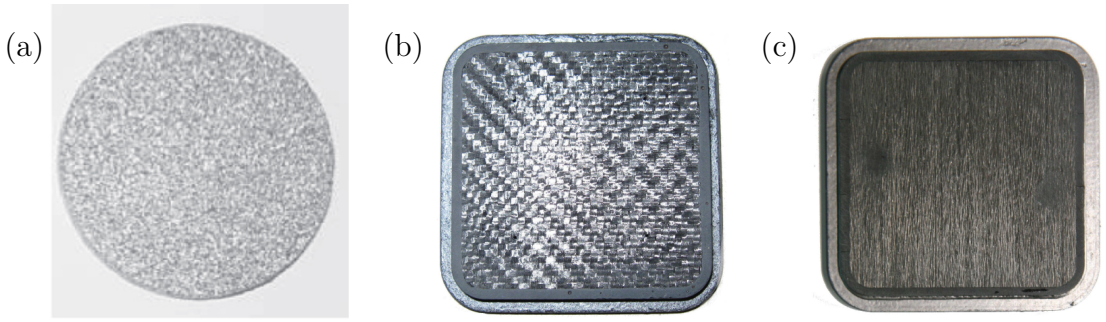

Figure 2.4: Porous samples: (a) Stainless Steel (Gascoin, 2011), (b) C/C (perpendicular), and C/C (parallel) (Schweikert *et al.*, 2013*a*).

Material	K_D [10^{-13} m^2]	K_F [10^{-8} m]	ϕ [%]
Stainless Steel (class 40)	91.9	1630	39.7
C/C (perpendicular)	1.448	1.074	12.4
C/C (parallel)	3.571	5.165	11.1

Table 2.1: Permeability coefficients of Stainless Steel (Gascoin, 2011), C/C (perpendicular), and C/C (parallel) (Schweikert *et al.*, 2013*a*).

Earlier in Chapter 1, it was stated that the first process of transpiration cooling starts in the porous injector. As the coolant seeps in, it carries away heat from the porous wall. This process is dependent on the volumetric heat transfer coefficient, h_v, which is a function of the material's permeability. The Nusselt number, Nu, is given as a function of the volumetric heat transfer coefficient and Darcy coefficient by the following equation:

$$Nu = \frac{h_v K_D}{k_f}, \tag{2.9}$$

where k_f is the thermal conductivity of the fluid (Florio *et al.*, 2016). Since $h_v \propto 1/K_D$, the volumetric heat transfer coefficient drops at larger K_D values. Therefore, if the injector is made relatively permeable, i.e. K_D is increased by larger pore sizes, in order to allow more coolant mass through the injector per unit time, the required differential pressure would be low (reducing stress on the material), but it will decrease the volumetric heat transfer coefficient. This will diminish the intended effect of internal cooling. Hence, the interplay amongst these

quantities must be delicately dealt with for a successful design and the material intrinsic permeability coefficients cannot be ignored.

In Chapter 1, it was mentioned that C/C has been widely used in recent transpiration cooling studies due to its favourable properties. Since one of the objectives of this thesis is to qualify porous UHTCs for transpiration cooling, it is sensible to compare it to the most widely used material, i.e. C/C. A selection of properties are comparing the two is given in Table 2.2 (C/C data from Schweikert *et al.* (2013*a*) and UHTC data from Wang & Vandeperre (2014) and personal communication with Vandeperre). First of all, ZrB_2 has a significantly higher melting point compared to C/C. If oxidation can be mitigated, ZrB_2 can offer multiple times higher radiative cooling (details are discussed in Chapter 3). Further, ZrB_2 has a higher thermal conductivity, k, which helps to spread the heat load across the material. However, ZrB_2 and UHTCs in general are brittle and have a low flexural strength, typically below $\sigma_f = 200$ MPa. In comparison, C/C is ductile and has a tensile strength of over $\sigma_t = 1100$ MPa. In addition, C/C has a lower density than UHTCs. Therefore, C/C features a much higher strength-to-density ratio. Despite this limitation of strength, the use of UHTCs in heat shield applications is compelling due to their thermal properties. With fibre reinforcement or a substructure, UHTCs would be able to endure higher stresses. For this study, however, only sintered UHTCs made of ZrB_2 will be examined (in Chapter 3).

Material	$\rho_{\phi=100\%}$ [kg/m^3]	σ_t or σ_f [MPa]	k [W/mK]	Melting point [K]
C/C	> 1400	< 1100	~ 13.5	~ 1800
UHTC (ZrB_2)	6080	< 200	56	3505

Table 2.2: Comparison of selected properties between C/C and UHTC.

2.3 Mixing on a Porous Injector

Kays *et al.* (2005) and Meinert *et al.* (2001) proposed analytical models for predicting the cooling efficiency over a transpiration cooled wall in a turbulent boundary layer. Eckert *et al.* (1958), on the other hand, proposed one for laminar boundary layers.

Strauss *et al.* (2017) compared six correlations for a transpiring wall in a turbulent boundary layer, including that of Kays *et al.* (2005) and Meinert *et al.* (2001), with experimentally obtained data employing porous walls made of sintered stainless steel. The authors used K-type thermocouples to measure the transpiring wall temperature in a supersonic flow with blowing ratios up to approximately 8%. It was shown that all of the correlations overestimated the cooling efficiency by up to 25% (see Fig. 2.5).

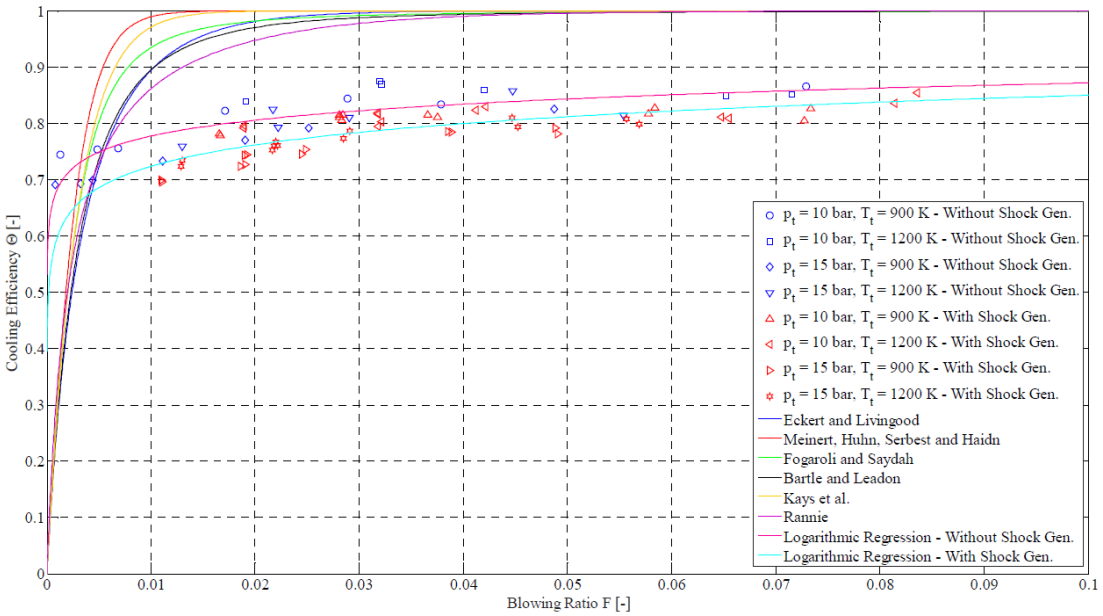

Figure 2.5: Cooling efficiency on the porous injector versus blowing ratio (experimental data vs models). Figure from Strauss *et al.* (2017).

Langener *et al.* (2011) reported a better agreement between those correlations and experimentally obtained data using a porous carbon/carbon (C/C) injector at lower blowing ratios, i.e. only up to 0.1%, and employing air, Argon, and Helium as the coolant (see Fig. 2.6). Schweikert *et al.* (2013*b*) experimentally examined the velocity and temperature profiles over a transpiring C/C segment in a subsonic, turbulent flow with bowing ratios up to 0.7%. Kuhn & Hald (2008) and Esser & Gülhan (2008) performed experiments in hypersonic flows and demonstrated successful cooling over the porous injector. Since the mixing on the injector is not part of the aim of this thesis, further details are omitted.

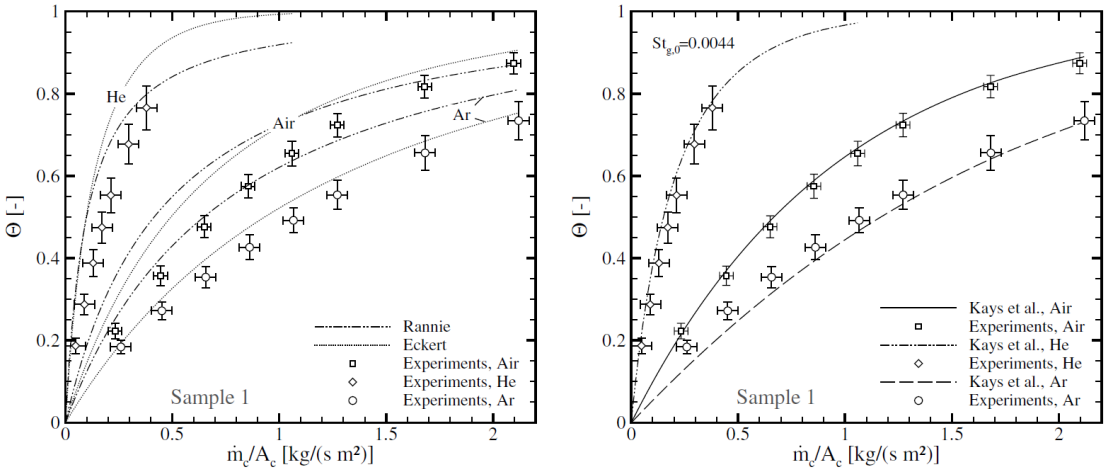

Figure 2.6: Cooling efficiency on the porous injector versus blowing ratio (experimental data vs models). Figure from Langener *et al.* (2011).

2.4 Mixing Downstream of the Injector

Downstream of the injector, the mixing problem becomes similar to that of film cooling, which has been extensively studied for more than 50 years. Authors have proposed correlations for film cooling effectiveness downstream of the injector, generally based on the energy equation and a turbulent velocity profile. Goldstein (1971) reviewed an array of these correlations, including those that varied in slot or hole geometry and injection type, i.e. tangential and non-tangential injection. Although the majority of the studies were concerned with slot or hole injectors in subsonic flow, some were conducted in supersonic flows featuring a porous injector (Goldstein *et al.*, 1968; Goldstein & Jabbari, 1970). These correlations are all based on an energy balance model (Goldstein, 1971) as shown in Fig. 2.7. It is assumed that mass is entrained from the external boundary layer at a rate of $\dot{m}'_e(x')$ and mixes with the coolant mass injected at $\dot{m}_c$. It is further assumed that the entrained mass grows similarly as a boundary layer starting from and as a function of x' (coordinate defined in Fig. 2.7). Continuity yields the total mass flow rate,

$$\dot{m}_{\text{tot}} = \dot{m}_c + \dot{m}'_e(x'), \tag{2.10}$$

and the following is obtained from the energy balance:

$$\dot{m}_{\text{tot}} \bar{c}_p \overline{T} = \dot{m}_c c_{p,c} T_c + \dot{m}'_e(x') c_{p,e} T_e. \tag{2.11}$$

Here, the average heat capacity for constant property gas is given by

$$\bar{c_p} = \frac{\dot{m}_c c_{p,c} + \dot{m}'_e(x') c_{p,e}}{\dot{m}_c + \dot{m}'_e(x')} \tag{2.12}$$

and the average temperature of the mixture is obtained by substituting Eq.(2.10) and Eq.(2.12) in Eq.(2.11) as follows:

$$\overline{T} = \frac{\dot{m}_c c_{p,c} T_c + \dot{m}'_e(x') c_{p,e} T_e}{\dot{m}_c c_{p,c} + \dot{m}'_e(x') c_{p,e}}. \tag{2.13}$$

The thermal film effectiveness is alternatively defined as

$$\eta_{th}(x') = \frac{T_e - \overline{T}(x')}{T_e - T_c}. \tag{2.14}$$

Substituting Eq.(2.13) in Eq.(2.14) yields

$$\eta_{th}(x') = \frac{1}{1 + \dfrac{\dot{m}'_e(x') c_{p,e}}{\dot{m}_c c_{p,c}}}. \tag{2.15}$$

The coolant mass flow rate is obtained from

$$\dot{m}_c = \rho_c u_c s, \tag{2.16}$$

where s is the length of the injector. The entrained mass flow rate is determined by

$$\dot{m}'_e(x') = \int_0^{\delta(x')} \rho_e u(y) dy, \tag{2.17}$$

where a suitable velocity profile, $u(y) = u_e f\left(\dfrac{y}{\delta(x')}\right)$, and the boundary-layer thickness starting from x', $\delta(x')$, are selected for laminar or turbulent flows. Subsequently by substituting Eq.(2.16) and Eq.(2.17) in Eq.(2.15) yields

$$\begin{aligned}
\eta_{th}(x') &= \frac{1}{1 + \dfrac{c_{p,e}}{c_{p,c}} \dfrac{\rho_e u_e \int_0^{\delta(x')} u(y/\delta(x'))dy}{\rho_c u_c s}} \\
&= \frac{1}{1 + \dfrac{c_{p,e}}{c_{p,c}} \dfrac{1}{Fs} \int_0^{\delta(x')} u(y/\delta(x'))dy} \quad \ldots \left[\because F = \frac{\rho_c u_c}{\rho_e u_e}\right] \\
&= \frac{1}{1 + \dfrac{c_{p,e}}{c_{p,c}} \xi} \quad \ldots \left[\text{with } \xi = \frac{1}{Fs} \int_0^{\delta(x')} u(y/\delta(x'))dy\right].
\end{aligned} \tag{2.18}$$

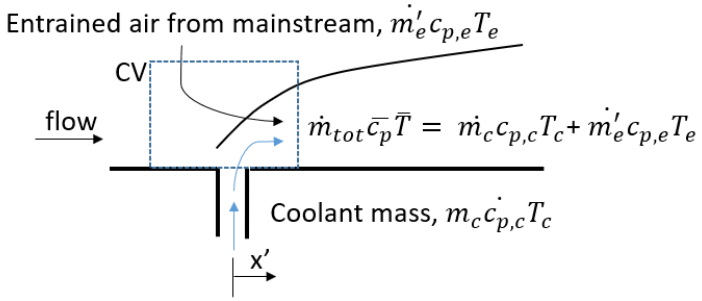

Figure 2.7: Control volume around the region of injection (not to scale).

A correlation factor ξ is defined that is widely used in downstream mixing studies. The effectiveness, η_{th}, is generally plotted over ξ and a model is created by regression of experimental data. The model typically has a form of

$$\eta_{th}(x') = \frac{a_1}{1 + a_2 \frac{c_{p,e}}{c_{p,c}} \xi^{a_3}}, \tag{2.19}$$

where a_1, a_2, and a_3 are coefficients determined by the regression. Authors in the past have used different velocity profiles and experimental data obtained at different flow conditions and proposed many correlation. The compressibility effect is mostly taken into account by multiplying the correlation factor by the square-root of the Chapman-Rubesin factor, $C^* = (\rho^* \mu^*)^{0.5} (\rho_e \mu_e)^{-0.5}$, evaluated at Eckert's reference temperature (Eckert, 1956). A collection of the correlations can be found in Goldstein (1971).

Despite the success of these correlations, limitations still exits on their universal use. A recent review on high-speed film cooling by Fujiwara *et al.* (2017) highlighted this aspect of the problem, mainly due to the large number of variables involved. As mentioned in the previous chapter, most of the emphasis for such mixing correlations has been on turbulent boundary layers since the application is intended for cooling of gas turbine blades or rocket nozzles, and only a handful of studies on film cooling or transpiration cooling in a laminar boundary layer are available in the literature, experimental and numerical studies combined. Heufer & Olivier (2008*a*) proposed a correlation factor based on the energy equation similar to Goldstein (1971) but with a laminar velocity profile. The authors validated the correlation numerically and experimentally using a slot injector on a flat plate in laminar, supersonic

flows, and demonstrated a collapse of the data as shown in Fig. 2.8. Different slot geometries and coolant gases were used in the experiments by Hombsch & Olivier (2013) in supersonic flows, where the authors demonstrated that film cooling was much more effective in laminar flows than turbulent ones. Further, a correlation for laminar mixing was proposed (shown in Fig. 2.9; correlation given in Chapter 4). Keller *et al.* (2015) performed direct numerical simulations to investigate the influence of different coolant gases in a Mach 2.6, laminar flow over a flat plate and compared the simulation to the data from Hombsch & Olivier (2013). The authors highlighted the difficulty in expanding the existing correlations due to the large number of variables that influence the mixing.

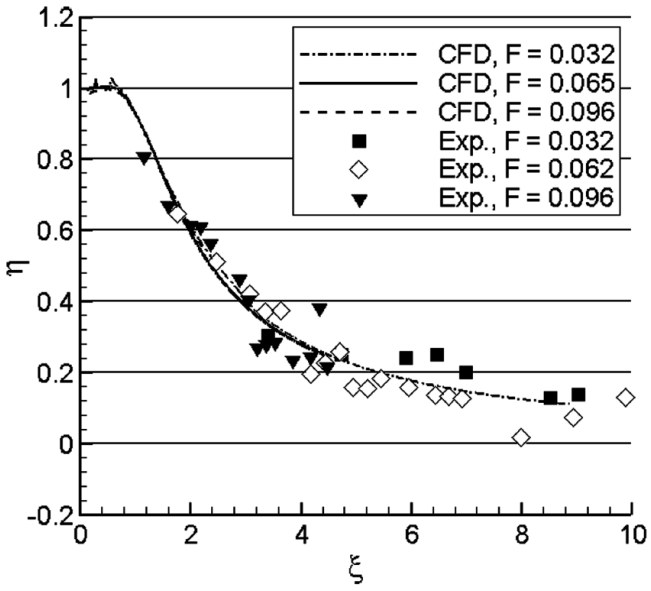

Figure 2.8: Film effectiveness over correlation factor in logarithmic scale. Figure from Heufer & Olivier (2008*a*).

The success of film cooling in laminar, hypersonic flows were demonstrated by Heufer & Olivier (2008*b*) where a flat-plate model was used featuring a slot injector. Gülhan & Braun (2010) further demonstrated the high efficiency of transpiration cooling downstream of a porous injector made of metal in laminar, hypersonic flows over a flat plate. The authors employed infrared thermography to spatially resolve the thermal trace of the film downstream. One of the earlier experimental studies,

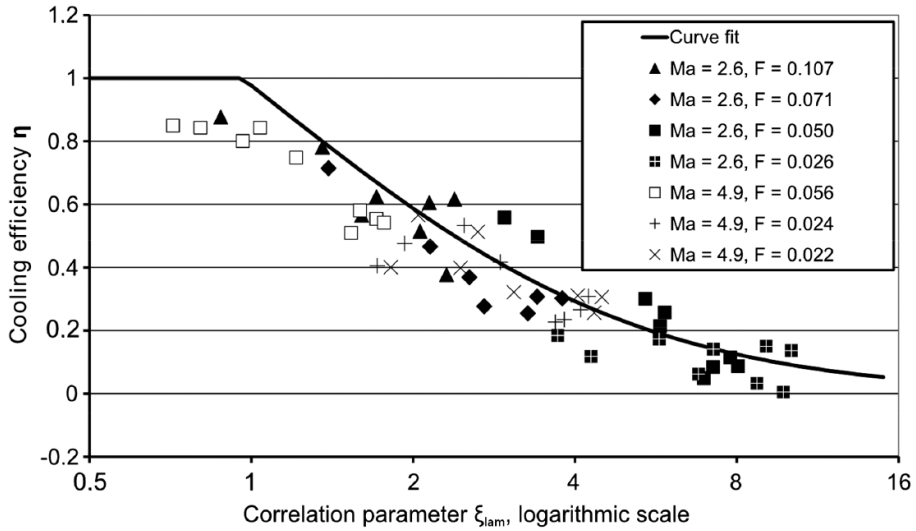

Figure 2.9: Film effectiveness over correlation factor in logarithmic scale (solid line denotes the correlation). Figure from Hombsch & Olivier (2013).

however, was conducted by Richards & Stollery (1979), where tangential injection was employed to cool a flat plate at Mach 10 in a hypersonic boundary layer. The authors proposed a discrete-layer theory based on conduction.

A general concern of transpiration or film cooling in a laminar boundary layer is triggering the onset of transition by blowing too much coolant (Schneider, 2012). This has been experimentally shown by Tanno *et al.* (2016), where higher blowing ratios lead to early transition of the boundary layer and transpiration heating occurred in return.

A large number of these studies – concerning both laminar and turbulent flows – looked into the effect of different gases as the coolant. A consensus amongst the authors is that lighter gases, such as Hydrogen and Helium, perform better in cooling due to their high specific heat capacity.

In terms of methods, thermocouples, thin-film gauges, or Infrared Thermography have been used to measure the temperature or heat flux reduction. In relatively recent years, Zhang & Jaiswal (2001), Charbonnier *et al.* (2009), and Narzary *et al.* (2012) – amongst others – have successfully utilised Pressure-sensitive Paint (PSP) to measure the film concentration and used the heat and mass transfer analogy in turbulent flows to construct the film effectiveness.

This measure is given by the film effectiveness expressed as

$$\begin{aligned}\eta_c &= \frac{C_w - C_e}{C_c - C_e} \\ &= 1 - \frac{1}{\left(\dfrac{p_{O_2,\,\text{air}}}{p_{O_2,\,\text{foreign gas}}} - 1\right)\dfrac{W_{\text{foreign gas}}}{W_{\text{air}}} + 1},\end{aligned} \tag{2.20}$$

where C is the concentration and subscript 'w' stands for concentration at the wall; $p_{O_2,\,\text{air}}$ and $p_{O_2,\,\text{foreign gas}}$ are Oxygen partial pressures with air and foreign gas injections, respectively, at the same blowing ratio. W_{air} and $W_{\text{foreign gas}}$ denote the respective molar masses (Charbonnier *et al.*, 2009; Bashir *et al.*, 2017). A film effectiveness of $\eta_c = 1$ corresponds to a full displacement of the air by the foreign gas, whereas $\eta_c = 0$ indicates that no displacement of air is achieved and the film is fully diminished. Essentially, this film effectiveness based on coolant concentration quantifies the physical presence of the film in terms of its concentration. For sufficiently turbulent flows, it can be assumed that $\eta_c \approx \eta_{th}$. Rallabandi *et al.* (2011) compared PSP results to data in the literature to confirm that the thermal effectiveness can be determined by Eq.(2.20) in fully turbulent flows (see Fig. 2.10).

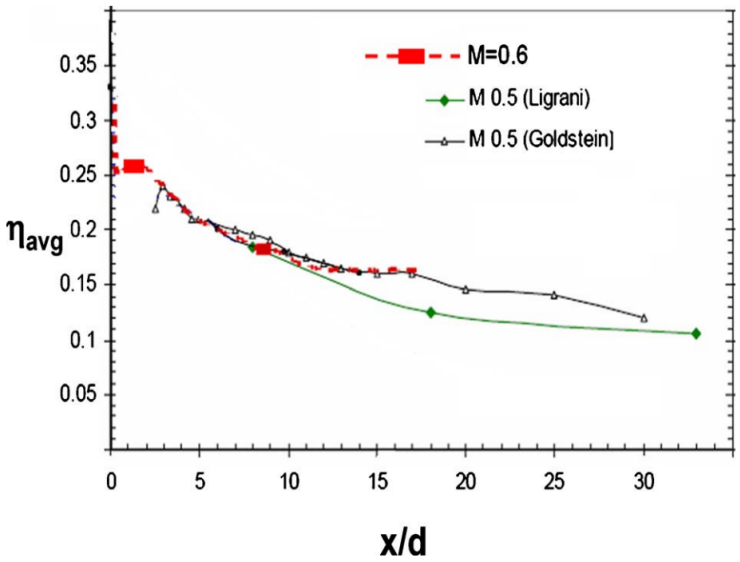

Figure 2.10: Span-wise averaged film effectiveness versus normalised stream-wise direction. Figure from Rallabandi *et al.* (2011). Here, M denotes the blowing ratio, F, and the red curve represents the PSP data from Rallabandi *et al.* (2011). The green and black curves respectively denote the results from Ligrani *et al.* (1994) and Goldstein & Jin (2000).

The assumption of $\eta_c \approx \eta_{th}$ is only valid when the ratio of the Schmidt number and the Prandtl number is at unity, i.e. when the Lewis number is 1, which is the case for a fully turbulent flow (Kays *et al.*, 2005; Goldstein, 1971). Since this does not apply to laminar flows, the PSP technique can only provide information on the concentration of the film, not the heat flux reduction.

2.5 Effect of Injector Type on Downstream Film

The type of the injector has an effect on the downstream film, which has been demonstrated by several authors.

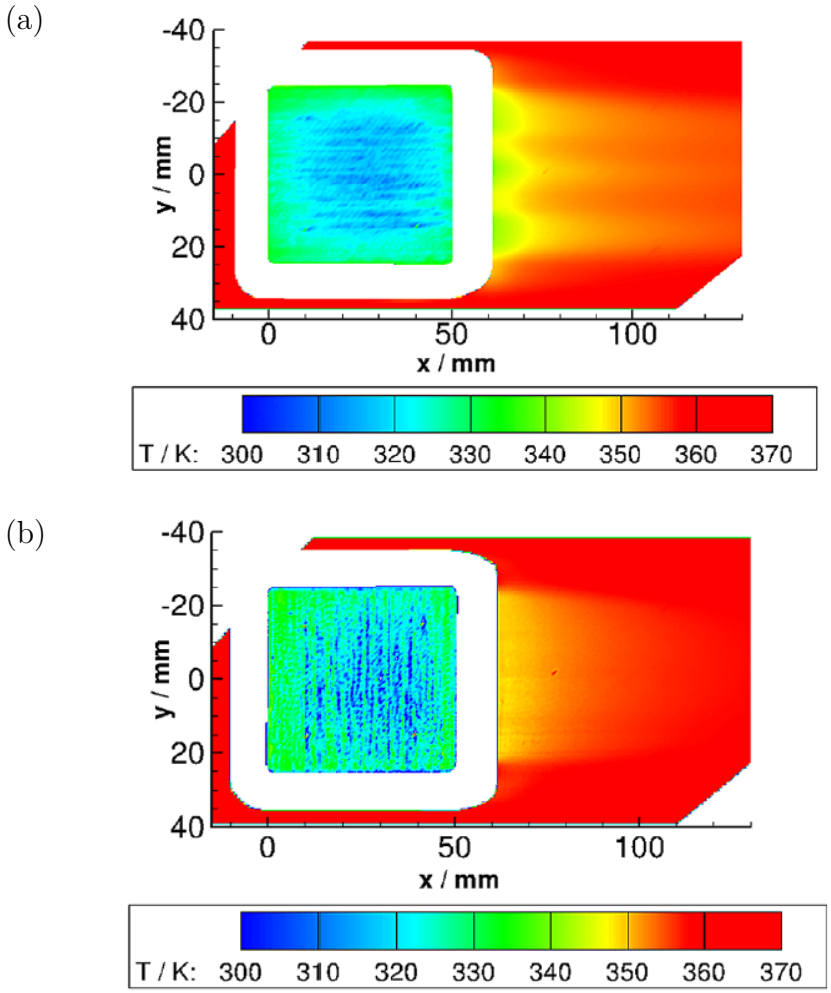

Figure 2.11: Experimentally obtained wall temperature (IR thermography): (a) C/C plies parallel to flow and (b) C/C plies perpendicular to flow. Blowing ratio both cases: $F = 1\%$. Figure from König *et al.* (2019).

Basore *et al.* (2016) showed that a C/C type CMC injector performed better in reducing the heat flux downstream compared to an Oxygen compatible CMC injector or a Multi-Port Injector Array (MPIA) in both laminar and transitional hypersonic flows; C/C type CMC also achieved the longest coverage of the film downstream.

In Hermann *et al.* (2018), it was shown that transpiration cooling requires approximately two orders of magnitude lower blowing ratios to obtain a similar film effectiveness using a porous UHTC injector compared to a slot injector. In a separate work (Ifti *et al.*, 2019), the authors showed that a non-uniform injector could lead to non-uniformities in the downstream film, emphasising the need of a uniform outflow of the injector. Similar observations were made by König *et al.* (2019) using C/C injectors. The authors demonstrated that the downstream film is significantly different for a C/C injector when the orientation of the plies are varied (see Fig. 2.11). The results were replicated by numerical simulations using the outflow characterisation as a boundary condition. This shows that the choice of the injector is a non-trivial aspect of efficiency in transpiration cooling, and it underpins the importance of outflow characterisation of the injector used.

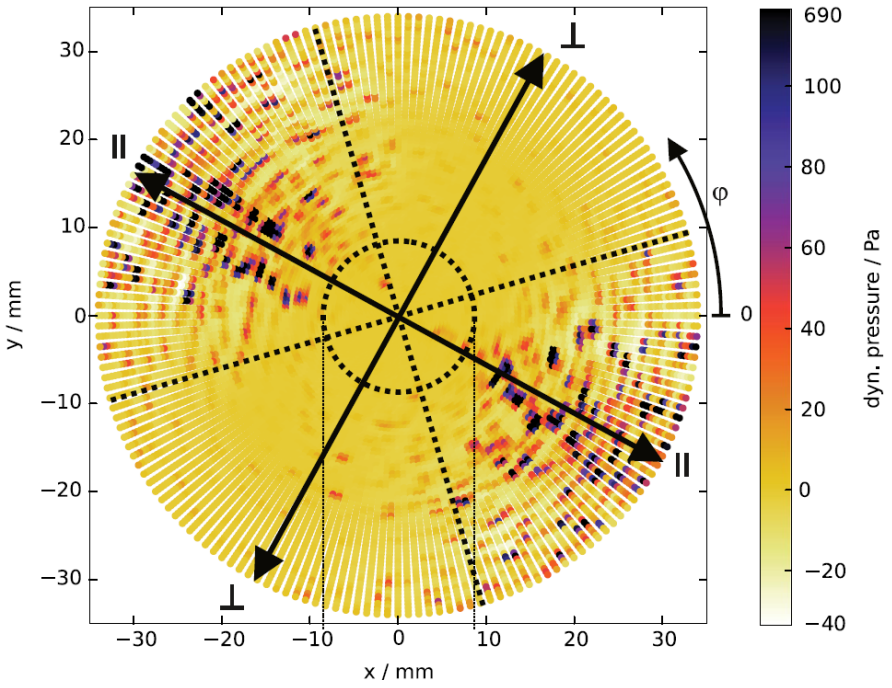

Figure 2.12: Dynamic pressure distribution over a transpiring cone made of C/C. Figure from Dittert *et al.* (2017).

Dittert *et al.* (2017) performed a pitot-survey over a transpiring cone made of C/C and showed that significant non-uniformity is present in the outflow of such materials. As shown in Fig. 2.12, the outflow features discrete jets that are up to two orders of magnitude higher than the average. This could not only result in a non-uniform film, but also trip the boundary layer from laminar to turbulent. It is therefore paramount that these injectors are characterised for their outflow prior to employing them in any transpiration cooling applications, from tunnel testing to real vehicles.

3

Flow Characterisation of Porous Ultra-High-Temperature Ceramics for Transpiration Cooling

Preamble

The first segment of the research aim of this thesis is to qualify porous Ultra-High-Temperature Ceramics (UHTC) for the purpose of transpiration cooling. In this chapter, the internal and external flow characteristics of a UHTC made of zirconium diboride (ZrB_2) are experimentally examined and its suitability for transpiration cooling application is analysed and discussed. This chapter is composed of a journal paper published in the *AIAA Journal* (Ifti *et al.*, 2022*c*). The content and structure of this chapter represent 100% of the main body of the original paper.

Authors of the original paper: **Ifti, H.S.**, Hermann, T., McGilvray, M., Larrimbe, L., Hedgecock, R. & Vandeperre, L.J.

Author contribution:

Ifti, H.S.: Lead author, conceptualisation, data curation, formal analysis, and writing.

Hermann, T.: Supervision as postdoctoral assistant in the project.

McGilvray, M.: Supervision as principal investigator and funding acquisition.

Larrimbe, L., Hedgecock, R. & Vandeperre, L.J.: Manufacturing of the UHTC samples.

Associated Appendices: Appendix A.

3.1 Introduction

A hypersonic vehicle experiences extreme heat fluxes due to aerodynamic heating (van Driest, 1956), which becomes detrimental for the vehicle at very high Mach numbers, especially during the re-entry into Earth's atmosphere or a planetary entry, e.g. into Mars. At re-entry speeds (approximately Mach 25), it becomes extremely challenging for an entry body to safely return back to Earth due to the high heat flux on the vehicle's surface (Anderson, 2006). Several types of Thermal Protection Systems (TPS) are therefore in use today that protect the payload from overheating.

In addition to the TPS needs of hypersonic spacecraft in operation today – such as the carbon-phenolic ablative heat shields on returning capsules – envisaged re-usable hypersonic passenger vehicles, e.g. the Skylon (Varvill & Bond, 2008), will require protection from high heat loads (Esser *et al.*, 2016). The recent unveiling of Boeing's hypersonic passenger jet and Lockheed Martin's SR-72 highlights the interest in sustained, atmospheric hypersonic flight, where high heat fluxes will occur on the leading edges. Although the state-of-the-art heat mitigation techniques – e.g. passive methods such as heat sinks and semi-passive methods such as ablation (Launius & Jenkins, 2012) – are successful for vehicles in operation at present, these conventional thermal protection systems have a low degree of re-usability. This limitation results in a higher cost of payload transfer. A re-usable, high-performing thermal protection system could therefore drive this cost down, making space and hypersonic flight more accessible. The pursuit of a novel, re-usable TPS is critical to both present and future hypersonic flight. Amongst the possible re-usable TPS candidates, transpiration cooling has shown promise (Tanno *et al.*, 2016; Böhrk, 2014). Although it comes with added complexity – and could add weight to the vehicle – transpiration cooling has the potential to minimise or remove the use of ablative material and increase re-usability of spacecraft or hypersonic cruise vehicles. The cooling process by transpiration generally takes place by three different effects. A schematic of the process is shown in Fig. 3.1. The pressurised coolant gas in the reservoir seeps through the porous material and thereby absorbs the heat from it by convection. This keeps cooling the material as long as there is a temperature

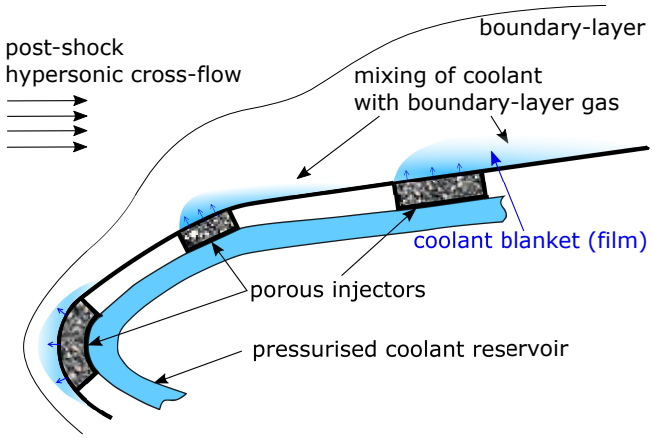

Figure 3.1: A leading edge of a hypersonic vehicle with porous, transpiration cooling injectors (not to scale).

gradient between the material and the coolant gas, which accounts for the first effect. The second effect comes into play when the injected coolant gas leaves the porous material and convects downstream (see Fig. 3.1). This forms a thin blanket or film of coolant gas, which acts as an insulation between the wall and the incoming hot gas flow and thus prevents the wall from overheating. In addition, if the material can be raised to a higher temperature, the rate of heat radiated back into space can be increased. This however requires the avoidance of oxidation of the material in use, which can be the third effect of transpiration cooling if an inert gas is used as the coolant (Ewenz Rocher *et al.*, 2019). This effect can additionally decrease the rate of plasma recombination and thereby further reduce heating.

The amount of coolant can be actively varied by modifying the injection rates, although this is limited due to the potential lift-off of the jets that could lead to early transition of the boundary layer (Schneider, 2012). The boundary layer thickens due to the blanket (film) of coolant gas as shown in Fig. 3.1. The coolant gas eventually starts mixing with the boundary-layer gas; consequently, the insulating blanket diminishes at some downstream location depending on the strength of mixing. This length of the effective insulating blanket (i.e. effectiveness), the mixing, and the injection are of importance. However, to fully comprehend these complex phenomena, it is sensible to first understand the behaviour of the outflow through porous media without the complications introduced by the hypersonic cross-flow. In

a separate work (Ifti *et al.*, 2019), the authors showed that a non-uniform injector leads to a non-uniform film downstream. It is therefore important to analyse the outflow characteristics of a particular sample in order to interpret the respective influence of coolant injection into a cross-flow.

Various materials from metals to ceramic matrix composites (CMC) have been investigated as potential porous media for hypersonic application. Carbon-carbon (C/C) type CMC has been used extensively for transpiration cooling experiments by DLR (Böhrk, 2014; Dittert *et al.*, 2017; Böhrk & Beyermann, 2010), ITLR (Langener *et al.*, 2011; Schweikert *et al.*, 2013*a*), and IRS (Löhle *et al.*, 2016). The reason for this choice lies in its high operational temperature of approximately 1800 K (Langener *et al.*, 2011), producibility, low density, and, foremost, high specific strength and modulus (Bacos, 1993). Gascoin (2011), Gascoin *et al.* (2012), and Najmi *et al.* (2016) performed permeability tests on stainless steel, bronze, and CMCs and reported their permeability coefficients. Further, Dittert *et al.* (2017) showed that the outflow of porous CMC exhibits significant local non-uniformities, which could potentially lead to film separation or early transition of the boundary layer.

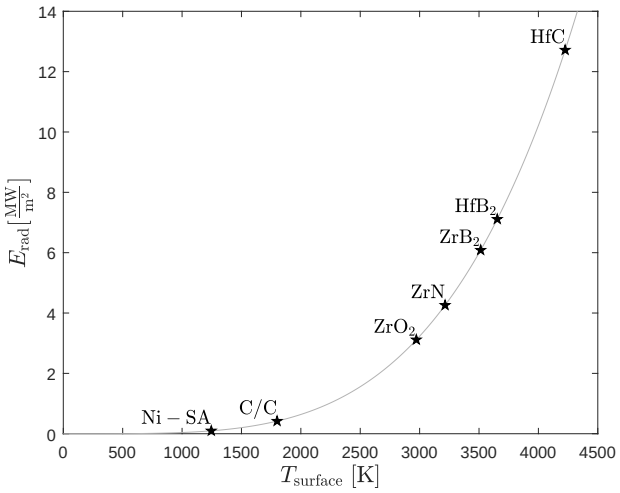

Figure 3.2: Cooling capability by radiation versus melting point of Ni-SA, C/C, and a number of UHTCs assuming an emissivity of 0.7 (the grey, solid line denotes the Stefan-Boltzmann law).

UHTCs have an exceptionally high melting point, generally above 3000 K (Wang & Vandeperre, 2014). This property enables them to have higher surface

temperatures that result in a higher amount of cooling by radiation (heat radiated back to space) compared to conventional materials as shown in Fig. 3.2. Radiative cooling of UHTCs (ZrO_2 to HfC) is multiple times higher than that of carbon-carbon (C/C) type CMC or Nickel Super Alloys (Ni-SA). A higher amount of radiative cooling allows for a lower coolant mass injection rate required to cool the surface. This reduces the required coolant mass that needs to be carried in the vehicle and thereby increases its payload capacity. Although UHTCs (ZrN to HfC in Fig. 3.2) oxidise at higher temperature, transpiration cooling with an inert gas as the coolant can mitigate oxidation (Ewenz Rocher *et al.*, 2019) and thereby enable an operating temperature that is close to their respective melting point. Thus, transpiration cooling employing UHTCs as the porous injector becomes a compelling technology for thermal management of a hypersonic vehicle, which makes UHTCs an exceptionally promising candidate group of materials for transpiration cooling. However, data on flow characteristics of transpiring porous UHTCs are not available in the literature.

In this paper, porous samples made of zirconium diboride (ZrB_2), a UHTC, are experimentally studied for their permeability and outflow characteristics. This is the first time a porous UHTC's flow characteristics are examined for the purpose of transpiration cooling. The Darcy and Forchheimer coefficients are determined for samples of different porous structures and porosities using a dedicated ISO standard test rig (BS EN ISO 4022:2006, 2006). The uniformity and jet behaviour of the outflow are measured and observed using miniature hot-wire anemometry. In contrast to conventional pitot probes, miniature hot-wire probes feature a smaller sensor (wire dimensions: 5 μm in diameter, 1.25 mm in length) that allows for a finer spatial resolution when traversing over an area.

3.2 UHTC Samples

The porous UHTC samples used for this paper are made of zirconium diboride (ZrB_2), which has a density of $\rho_{\phi=100\%} = 6080$ kg/m^3 in a 100% densified state. The melting point and thermal conductivity of ZrB_2 are 3505 K (Wang & Vandeperre, 2014) and 56 W/mK (Lee *et al.*, 2014), respectively. The different porosities and

Sample ID	Porosity, ϕ [%]	D [mm]	L [mm]	Type	Treatments	Batch number
UHTC-2	42	70	5	partially sintered	abrasion	1
UHTC-3	41	70	5	partially sintered	abrasion	1
UHTC-4	41	70	5	partially sintered	abrasion	1
UHTC-5	41	80	5	partially sintered	ultrasonic bath	2
UHTC-6	41.1	80	5	partially sintered	ultrasonic bath, abrasion	2
UHTC-7	41.6	80	5	partially sintered	ultrasonic bath	2
UHTC-8	40.9	80	5	partially sintered	ultrasonic bath	2
UHTC-9	32.5	80	5	partially sintered	ultrasonic bath	3
UHTC-10	31.6	80	5	partially sintered	ultrasonic bath	3
UHTC-11	32.6	80	5	partially sintered	ultrasonic bath	4
UHTC-12	39.5	80	5	partially sintered	ultrasonic bath	4
UHTC-13	34.6	80	5	partially sintered	ultrasonic bath	4

Table 3.1: UHTC sample overview.

porous structures in these samples are achieved by partial sintering (see Fig. 3.3). Partial sintering is the most conventional technique for making porous ceramics. The pores are produced by incomplete fusion of the particles. As it can be seen in Fig. 3.3b, pores with a refined size remain among the grains after the sintering in this method. Commercial ZrB_2 powder (grade B, H.C. Starck, Germany) was used as the starting material. The powder was loaded into a 70 mm, or 80 mm, diameter graphite die. To minimise reaction between the graphite die and precursor powder, the inner walls of the dies were lined with thin graphite paper before the powder was loaded. Hot pressing was completed in a graphite resistance-heated vacuum hot press furnace. During exploration, the final hot pressing temperatures were varied between 1273 K and 2273 K, but the samples used here were all produced by hot pressing at 1973 K with a dwell time of 60 minutes to yield a porosity of approximately 40%. The applied pressure was gradually increased to 12 MPa and maintained for 15 minutes at each sintering temperature. After cooling, the graphite paper was removed by grinding.

An overview of the tested samples is given in Table 3.1. In total, twelve samples were tested. A layer of residue – formed by locally densified powder particles – could be observed on the surfaces of some of the partially sintered samples, and therefore it was decided to abrade the surfaces with sandpaper by hand. Subsequently, samples UHTC-2, UHTC-3, and UHTC-4 were tested for their permeability characteristics

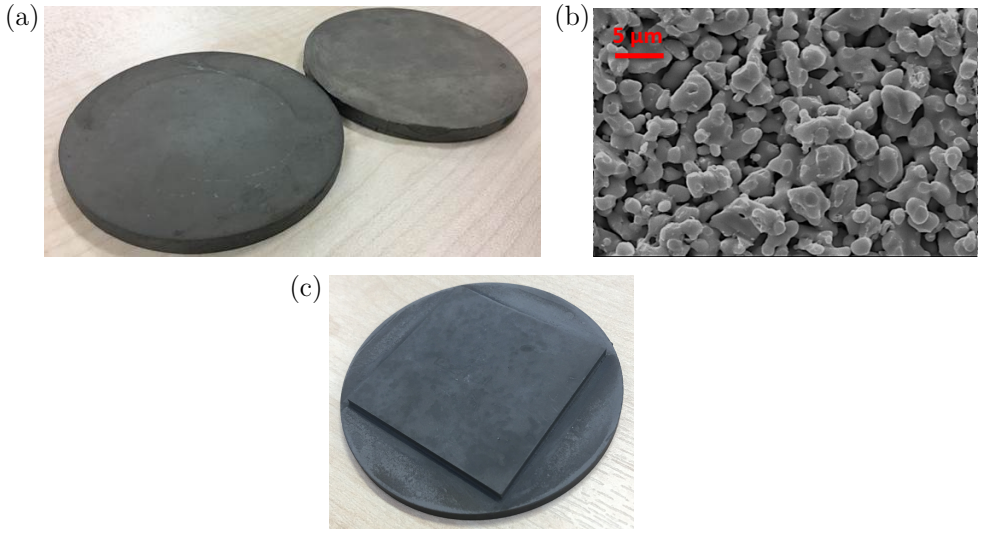

Figure 3.3: ZrB_2 porous sample: (a) 70 mm diameter samples with 5 mm thickness, (b) a scanning electron microscopy (SEM) micrograph of the microstructure of a sample, and (c) a sample machined with EDM.

before and after sanding the surface with sandpaper. The next batches of samples, i.e. UHTC-5 to UHTC-13, were treated in an ultrasonic bath to get rid of the residue, and to verify the effectiveness of the ultrasonic bath, permeability tests were performed on UHTC-6 before and after sanding. After completing the permeability tests, all samples were machined with Electrical Discharge Machining (EDM) into a disc form of ⌀60 mm × 3 mm with an extrude of 39.5 mm × 39.5 mm × 2 mm (see Fig. 3.3c) for the outflow experiments.

3.3 Darcy-Forchheimer Permeability Test

The pressure drop across a porous medium is governed by the Darcy-Forchheimer equation (Nield & Bejan, 2013), expressed in differential form as

$$-\frac{dp}{dx} = \underbrace{\frac{\mu}{K_D}v}_{\text{viscous term}} + \underbrace{\frac{\rho}{K_F}v^2}_{\text{kinetic term}} . \tag{3.1}$$

Here, K_D and K_F are material intrinsic permeability coefficients respectively known as the Darcy coefficient and the Forchheimer coefficient; v is the superficial velocity of the flowing medium (also known as the bulk velocity). The left-hand-side of Eq.(3.1) stands for the pressure gradient across the porous medium, whereas the two

terms on the right-hand-side denote the viscous and kinetic losses, respectively. At very low velocities, the kinetic term is negligible and the flow is in the Darcy regime. In this case, the kinetic term of Eq.(1) is left out and the equation becomes the Darcy equation. However, at higher velocities, the kinetic term dominates and the flow enters the Forchheimer regime, requiring the full Darcy-Forchheimer equation.

Equation 3.1 is integrated by separation of variables over the thickness, L, and from p_{in} to p_{out} as

$$-\int_{p_{in}}^{p_{out}} pdp = \int_0^L \left(\frac{\mu \dot{m} RT}{K_D A} + \frac{\dot{m}^2 RT}{K_F A^2}\right) dx \; ... \left[\because v = \frac{\dot{m} RT}{pA} \text{ (continuity)}\right],$$

where $\dot{m}$ is the mass flow rate through area A and R is the specific gas constant. With a constant temperature assumption, $T = T_{in}$, in the whole porous domain, the integration yields the following equation:

$$\frac{p_{in}^2 - p_{out}^2}{2} = \frac{\mu(T_{in}) \dot{m} R T_{in}}{K_D A} L + \frac{\dot{m}^2 R T_{in}}{K_F A^2} L$$

Finally, substitution by $v_{in} = \dfrac{\dot{m} R T_{in}}{pA}$ and $\rho_{in} = \dfrac{p_{in}}{R T_{in}}$ yields the Darcy-Forchheimer equation in its integrated form:

$$\frac{p_{in}^2 - p_{out}^2}{2 p_{in} L} = \frac{\mu(T_{in})}{K_D} v_{in} + \frac{\rho_{in}(p_{in},\, T_{in})}{K_F} v_{in}^2. \tag{3.2}$$

Here, the subscripts '*in*' and '*out*' respectively denote input and output quantities. The normalised differential pressure, $\dfrac{p_{in}^2 - p_{out}^2}{2 p_{in} L}$, is henceforth expressed as $\dfrac{\Delta p}{L}$. Since the dynamic viscosity – calculated from Sutherland's law (Sutherland, 1853) – and the density – obtained from the ideal gas law – of the fluid are functions of temperature, a modified version of Eq.(3.2) proposed by Langener *et al.* (2011) can be used in the case of a thermal gradient in the material. However, Eq.(3.2) is sufficient for the purpose of this paper as the temperature non-uniformity is negligible for the conducted experiments.

3.3.1 Permeability Test Rig

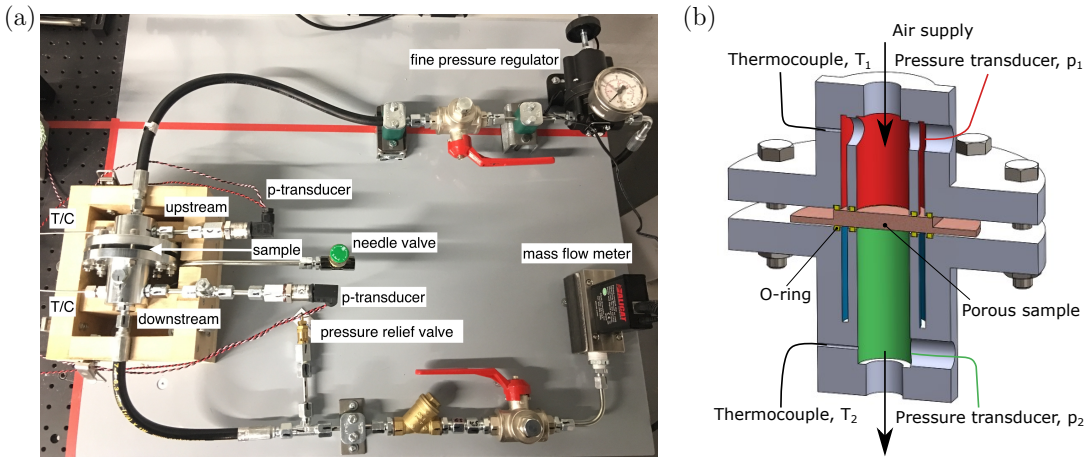

Figure 3.4: (a) Darcy-Forchheimer ISO 4022 Permeability Test Rig and (b) a cutaway of the clamping body including its instrumentation.

In order to determine the permeability coefficients, a test rig has been designed and built in accordance with the ISO 4022 standard (BS EN ISO 4022 2006). The porous sample is clamped between the upstream and downstream parts as shown in Fig. 3.4a. A K-type thermocouple (T/C) and a pressure transducer (Gems 3100 Series) are fitted to either part; these record the values of $T_1 = T_{in}$, $T_2 = T_{out}$, $p_1 = p_{in}$, and $p_2 = p_{out}$ (see Fig. 3.4b). During a test, the input pressure is increased in steps using a fine-adjustment pressure regulator (Fairchild 10292H). Adhering to the ISO 4022 standard, the mass flow rate is measured at a downstream location (Alicat M Series mass flow meter). The through-flow area for this rig is $A = 1.911 \times 10^{-4}$ m^2 (through-flow diameter of 15.6 mm).

A gradient-free optimisation method proposed by Nelder & Mead (1965) is employed to obtain the permeability coefficients, K_D and K_F. The minimisation criterion for this simplex search solution is given by

$$f(\vec{K}) = \frac{\left\| \left.\frac{\Delta p}{L}\right|_{\mathrm{DF}} - \left.\frac{\Delta p}{L}\right|_{\mathrm{exp}} \right\|}{\left\| \left.\frac{\Delta p}{L}\right|_{\mathrm{exp}} \right\|}, \tag{3.3}$$

where $\vec{K} = [K_D\ K_F]^T$. Here, $\left.\frac{\Delta p}{L}\right|_{\text{exp}}$ is obtained from the experimental data points, $\left.\frac{\Delta p}{L}\right|_{\text{DF}}$ is given by the right-hand-side of Eq.(3.2), and the symbol $\|.\|$ denotes the euclidean norm. For a two-dimensional space, the Nelder-Mead algorithm employs three points and – for each iteration – picks the best point that satisfies $f = f_{min}$. Per iteration, j, the three points are updated by reflection, outside/inside contraction, and shrinking until the conditions $|f^{(j+1)} - f^{(j)}| \leq \epsilon$ and $|\vec{K}^{(j+1)} - \vec{K}^{(j)}| \leq \epsilon$ both are fulfilled. A termination tolerance of $\epsilon = 1 \times 10^{-10}$ is selected here.

3.3.2 Validation

In order to validate the results obtained from the permeability test rig, a porous disc of sintered bronze (SIKA-B 8: 89% Cu + 11% Sn) (see Fig. 3.5a) provided by GKN Sinter Metals Filters GmbH was tested. The experimentally obtained permeability coefficients along with the permeability coefficients stated on the manufacturer's data sheet (Filter-Elements, 2003) for SIKA-B 8 are given in Table 3.2. The corresponding test results are illustrated in Fig. 3.5d.

Whilst the Darcy coefficient obtained from the experiment is in close agreement with that from the data sheet, the Forchheimer coefficient is lower by a factor of approx. 5. In Fig. 3.5d, it can be seen that the normalised differential pressure (blue dot-dashed line) obtained from Eq.(3.2) using the coefficients from the data sheet under-predicts the pressure loss across the medium in comparison to the experimental data as the superficial input velocity increases. This is due to the fact that the manufacturer performed the permeability tests at very low differential pressures (Filter-Elements, 2003) where the flow was dominated by the Darcy component, and thus the test did not capture a representative Forchheimer coefficient. Hence, despite matching the Darcy coefficient with a discrepancy of only 7.5%, a different approach to validating the rig was required to account for the flow in the Forchheimer regime.

Several correlations exist for predicting the pressure loss across a porous material that is composed of a packed bed. Erdim *et al.* (2015) reviewed and evaluated 38 correlations from the literature. The most widely used correlation for a packed

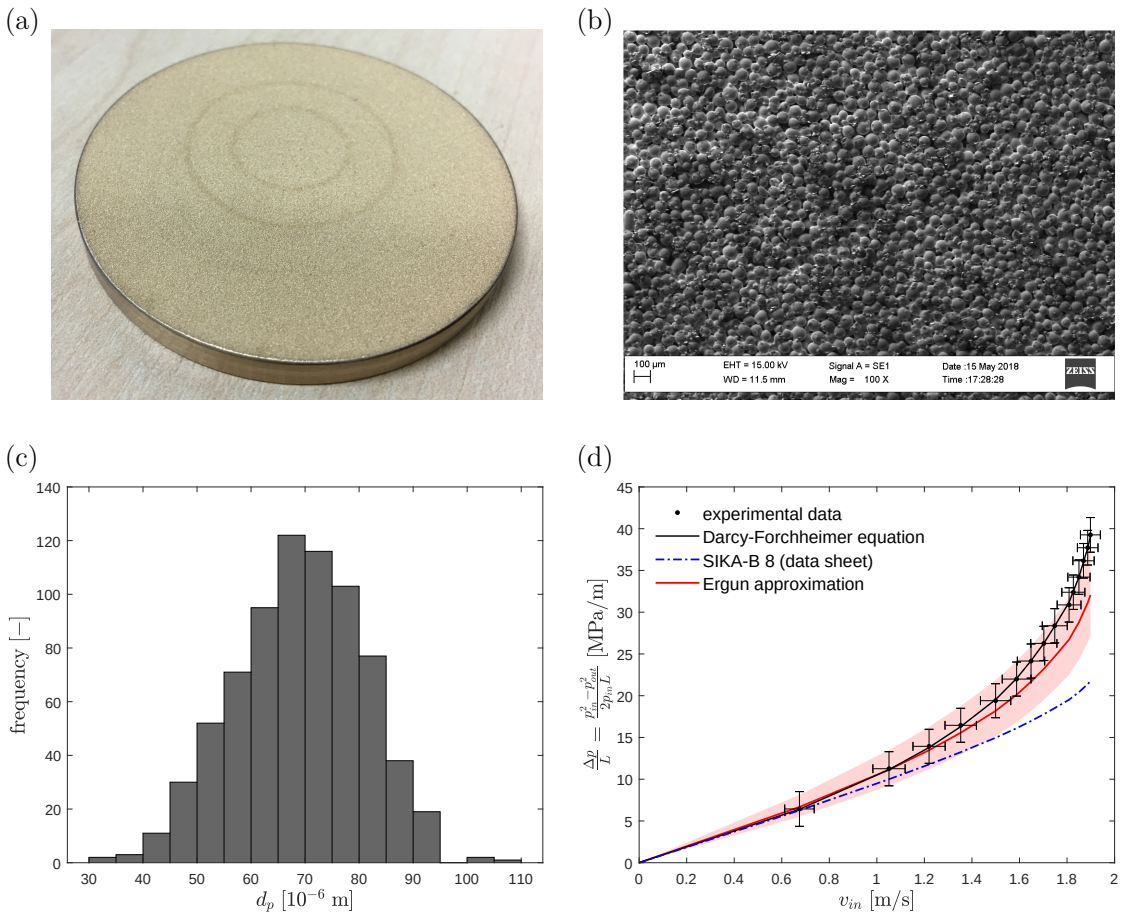

Figure 3.5: (a) SIKA-B 8 (⌀60 mm × 5 mm), (b) SEM image of SIKA-B 8 at ×100 magnification (courtesy: Dr Elsiddig Elmukashfi), (c) histogram of the diameter of 742 particles of SIKA-B 8, and (d) normalised differential pressure versus superficial input velocity of SIKA-B 8 (the light-red band represents the uncertainty in Ergun approximation, i.e. in Eq.(3.4) and Eq.(3.5).

Source	K_D [10^{-12} m^2]	K_F [10^{-6} m]
ISO 4022 experiment	2.162	1.023
SIKA-B data sheet (Filter-Elements, 2003)	2	5.2
Ergun approximation	1.971	1.623

Table 3.2: Permeability coefficients of SIKA-B 8.

bed of spherical, mono-sized particles was proposed by Ergun (1952), where the Darcy and Forchheimer coefficients were respectively proposed as

$$K_{D,\,\mathrm{Ergun}} = \frac{\phi^3 d_p^2}{150(1-\phi)^2} \tag{3.4}$$

and

$$K_{F,\,\mathrm{Ergun}} = \frac{\phi^3 d_p}{1.75(1-\phi)}. \tag{3.5}$$

Here, d_p is the diameter of the particles in the packed bed and ϕ is the porosity of the material. Since the SIKA-B 8 sample is made of regular spherical particles (Filter-Elements, 2003), these correlations are appropriate for modelling the flow through it. SEM images (see Fig. 3.5b) of either surface of a single SIKA-B 8 disc were taken to measure the particle diameter, where the scale on the SEM images was taken as the reference. The measured diameter, d_p, of $n_p = 742$ particles yielded a distribution shown in Fig. 3.5c with a mean of $\bar{d}_p = 68.9 \times 10^{-6}$ m and a standard deviation of $\sigma_{d_p} = 11.8 \times 10^{-6}$ m. Furthermore, a density based measurement – comparing the weight of this sample to the theoretical weight of a fully dense one of identical volume – determined a porosity of $\phi = 30.1\%$.

Since the diameter is a distribution, rather than a single value, the normalised differential pressure was evaluated at the Sauter mean diameter (Sauter, 1926), $d_p = d_{32}$, to approximate the Ergun correlation (henceforth annotated as 'Ergun approximation', e.g. in Fig. 3.5d). The Sauter mean diameter is defined as

$$d_{32} = \frac{\sum \overline{d_{p,i}}^3 f_i}{\sum \overline{d_{p,i}}^2 f_i}, \tag{3.6}$$

where $\overline{d_{p,i}}$ denotes the average diameter within the i-th bin in the histogram and f_i refers to the corresponding frequency or count. The Sauter mean diameter represents the equivalent spherical diameter that has the same effective surface of that in the entire distribution. The calculated permeability coefficients from Eq.(3.4) and Eq.(3.5) using the Sauter diameter, $d_p = d_{32}$, are given in Table 3.2 (Ergun approximation). The pressure loss obtained from the Ergun approximation (solid, red line) is plotted in Fig. 3.5d. The light-red band represents the uncertainty in the Ergun approximation, i.e. in Eq.(3.4) and Eq.(3.5), which was obtained by employing

Moffat's error propagation method described in Appendix 3.6. The individual error in the diameter, δd_p, was estimated as a systematic bias uncertainty (Coleman & Steele Jr., 2009) in measuring the diameter of the spheres from SEM images. This was estimated to be equivalent to two pixels and equal for all measurements. The relative uncertainty in the porosity, $\frac{\delta\phi}{\phi}$, was estimated to be ±3%.

Fig. 3.5d demonstrates a good agreement between the experimentally measured pressure drop and the Ergun approximation. At higher velocities, however, there is a slight divergence. This is reflected in the permeability coefficients as well (Table 3.2). The experimentally obtained value for K_D matches the one calculated from the Ergun approximation within 9.7%, whereas the K_F value differs by 37%. For reference, the uncertainty in the experimentally measured value is 12% for K_D as well as for K_F. The discrepancy in K_F can be attributed to the wide particle size distribution in SIKA-B 8. Keyser *et al.* (2006) and Koekemoer & Luckos (2015) showed in separate studies that the Ergun correlation evaluated at the Sauter mean diameter under-predicts the pressure loss when the particle size distribution is wide. This trend is evident in the present case. However, the Ergun approximation under-predicts the experimentally measured pressure drop by only up to 18% within the tested velocity range. This difference is within the ±50% prediction accuracy reported by Macdonald *et al.* (1979) for such correlations.

Overall, the experimental data and the Ergun approximation, along with their respective uncertainties, are in good agreement. The measured values of the permeability coefficients, K_D and K_F, are close to that obtained by the Ergun approximation, and the associated discrepancies are within the range reported in the literature. The validation is thereby concluded.

3.3.3 Results and Discussion

The permeability coefficients for all twelve UHTC samples yielded from the Nelder-Mead simplex search solution are given in Table 3.3 along with their respective uncertainties. A *Monte Carlo* simulation was performed to determine the uncertainties (see Appendix 3.6 for details). For the tested samples, the order of the Darcy

Sample ID	K_D [10^{-14} m^2]	δK_D [10^{-14} m^2]	$\frac{\delta K_D}{K_D}$ [%]	K_F [10^{-7} m]	δK_F [10^{-7} m]	$\frac{\delta K_F}{K_F}$ [%]
UHTC-2	2.998	±0.055	±1.8	1.59	±0.43	±27
UHTC-3 (prs)	3.107	±0.061	±2.0	1.31	±0.31	±23
UHTC-3 (pos)	3.297	±0.063	±1.9	1.26	±0.25	±20
UHTC-4 (prs)	0.596	±0.047	±7.9	0.023	−0.008, +0.015*	−36, +63*
UHTC-4 (pos)	0.912	±0.048	±5.3	0.075	−0.024, +0.045*	−32, +60*
UHTC-5	2.956	±0.064	±2.2	1.11	±0.29	±26
UHTC-6 (prs)	3.754	±0.069	±1.8	1.70	±0.36	±21
UHTC-6 (pos)	3.731	±0.073	±2.0	1.54	±0.33	±22
UHTC-7	3.726	±0.061	±1.6	1.97	±0.37	±19
UHTC-8	3.775	±0.067	±1.8	1.74	±0.35	±20
UHTC-9	0.340	±0.027	±7.9	0.014	−0.006, +0.008*	−39, +58*
UHTC-10	0.280	±0.024	±8.5	0.020	−0.012, +0.038*	−58, +193*
UHTC-11	0.392	±0.027	±7.0	0.072	−0.051, +0.361*	−71, +506*
UHTC-12	1.045	±0.037	±3.5	0.252	−0.095, +0.20*	−38, +78*
UHTC-13	0.747	±0.026	±3.7	0.41	−0.26, +2.2*	−64, +527*

* The large uncertainties in K_F result in an asymmetric distribution.

Table 3.3: Permeability coefficients and their corresponding uncertainties. Note: 'prs' and 'pos' stand for pre-sand and post-sand, respectively.

coefficient ranges from 10^{-15} m^2 to 10^{-14} m^2 and the Forchheimer coefficient from 10^{-9} m to 10^{-7} m. The through-flow results are showcased in Fig. 3.6 for UHTC-3 (post-sand). The normalised differential pressure is plotted against the superficial input velocity including the uncertainties of the experimental data in form of error bars. The solid line, which represents the Darcy-Forchheimer equation, is obtained by using the K_D and K_F values in Eq.(3.2). In Fig. 3.6, it can be observed that the experimental data follow the Darcy-Forchheimer equation, which is within the uncertainties. At lower velocities, the curve is fairly linear; however, as the velocity rises, the non-linearity of the curve becomes prominent. Furthermore, it can be seen (Fig. 3.6) that the flow enters the Forchheimer regime at higher velocities and deviates from the projected Darcy equation significantly as the superficial input velocity rises. At $v_{in} = 0.35$ m/s, this discrepancy reaches up to approx. 12%, demonstrating the importance of using the Darcy-Forchheimer equation instead of the Darcy equation for this type of materials at higher through-flow velocities.

The effect of sanding on the overall permeability behaviour is presented in Fig. 3.7. Upon sanding, the samples demonstrated a clear improvement in their permeability,

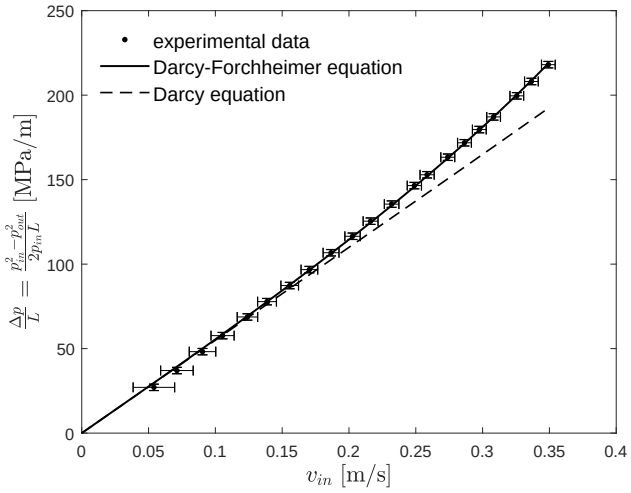

Figure 3.6: Results for UHTC-3 (post-sand): normalised differential pressure versus superficial input velocity.

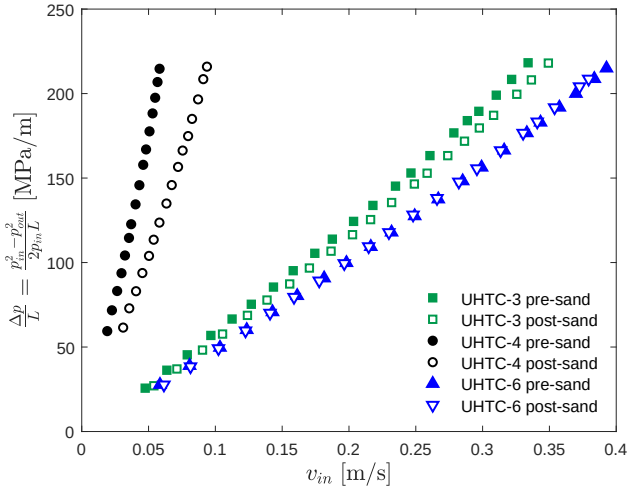

Figure 3.7: Sanding effect on the permeability characteristics of (a) samples (UHTC-3 and UHTC-4) not treated in an ultrasonic bath (black and green) and a sample (UHTC-6) treated in an ultrasonic bath (blue).

which is shown in Fig. 3.7 (UHTC-3 and UHTC-4). The Darcy coefficient increased by 6.1% for UHTC-3 and 19% for UHTC-4 (values obtained from Table 3.3), which are outside the uncertainty bounds of 2.0% and 7.9%, respectively. For a given differential pressure, this translates into a rise in velocity by up to approx. 5% and 60% respectively for UHTC-3 and UHTC-4. Although the overall permeability is increased by sanding off the surface, there is a possibility that the residual grains from the process block the pores to some extent. This effect however was not possible to account for with the current experimental setup and processes;

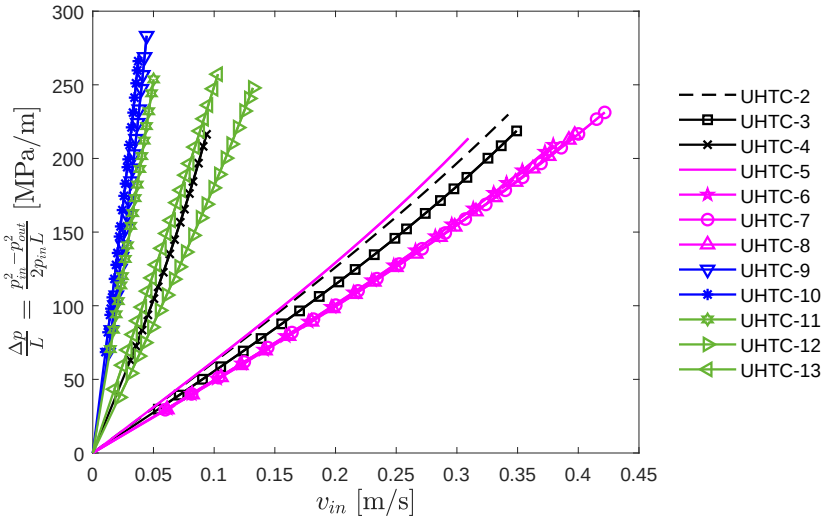

Figure 3.8: Comparison amongst all samples: normalised differential pressure versus superficial input velocity. Note: only post-sand data are presented, where applicable. Each batch is represented with a single colour; black: batch 1, magenta: batch 2, blue: batch 3, and green: batch 4.

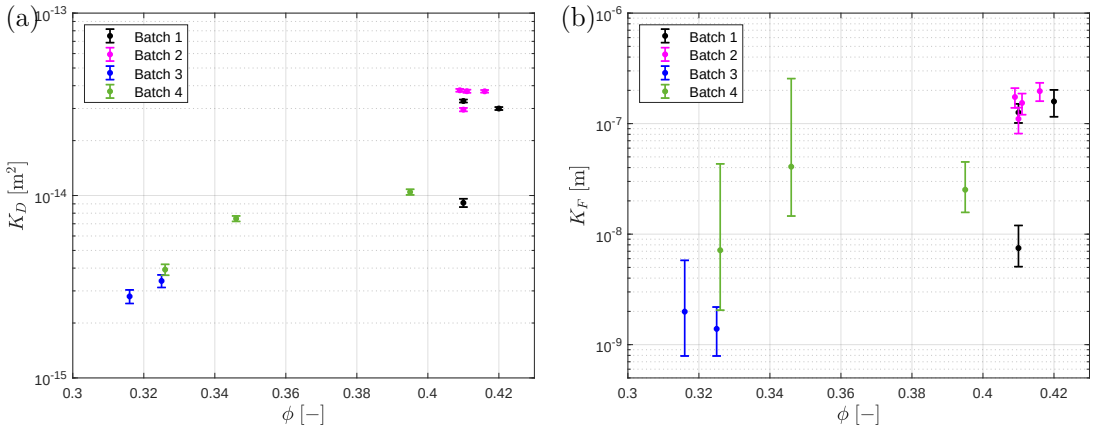

Figure 3.9: Permeability coefficients versus porosity: (a) Darcy coefficient and (b) Forchheimer coefficient. Note: only post-sand data are presented, where applicable. Each batch is represented with a single colour.

instead, the next batches of samples, i.e. UHTC-5 to UHTC-13, were treated in an ultrasonic bath. The effectiveness of the ultrasonic bath is demonstrated in Fig. 3.7 (UHTC-6), where the permeability test was performed before and after sanding. Overall, the data sets taken before and after sanding fall atop each other. The change in the Darcy coefficient here is 0.6%, which is within its uncertainty of 1.8% (see Table 3.3). This proves the ultrasonic bath to be effective, and therefore the sanding process is not necessary.

A comparison amongst all the twelve UHTC samples in terms of their permeability characteristics is illustrated in Fig. 3.8. Here, it can be observed that, for a given differential pressure, the permitted flow through can vary by an order of magnitude across the different batches (Table 3.1), e.g. for a given normalised differential pressure, $\frac{\Delta p}{L} = 200$ MPa/m, the through-flow velocity ranges between $v_{in} = 0.025$ m/s and $v_{in} = 0.4$ m/s. This is because the permeability coefficients vary by an order of magnitude in comparison (Table 3.3). The variation in these coefficients can be attributed to the corresponding porosities (Table 3.1). This relationship between the porosity and permeability coefficients is visualised in Fig. 3.9. Although some outliers exist (UHTC-4 in batch 1 and UHTC-11 in batch 4), the general trend shows that an increase in porosity from $\phi \approx 32\%$ to $\phi \approx 42\%$ results in an order of magnitude rise in the Darcy coefficient, K_D (Fig. 3.9a), and in contrast, two orders of magnitude in the Forchheimer coefficient, K_F (Fig. 3.9b).

Furthermore, it can be seen that within the first batch of samples (batch 1), i.e. UHTC-2 to UHTC-4, that were not treated in an ultrasonic bath but were sanded, UHTC-4 is an outlier and the rest are fairly similar in terms of their superficial velocity (see Fig. 3.8) and permeability coefficients (see Table 3.3). Analogous to batch 1, there is an outlier, i.e. UHTC-5, in batch 2, where the rest of the samples demonstrate a similar behaviour in terms of permeability. The deviation, however, is less compared to the first batch, and the data obtained from samples UHTC-6, UHTC-7, and UHTC-8 overlap fairly well. Moreover, the slight deviation in their permeability coefficients falls within the respective uncertainties – indicating the effectiveness of the ultrasonic bath and the uniformity amongst these UHTCs. In contrast, the outliers, UHTC-4 and UHTC-5, suggest that there are occasional non-uniformities within these samples, and emphasise the need for running the permeability test for each individual sample even if they are manufactured with the same conditions. Batch 4 also demonstrates irregularities. These non-uniformities could occur from locally closed pores, i.e. increased amount of closed porosity, or local patches of more densified material. In addition, it is worth noting that the through-flow took place covering an area of $A = 1.911 \times 10^{-4}$ m^2, which is

approx. 4–5% of the total surface area of the entire sample, depending on the sample's diameter. This means that not all local non-uniformities are captured within this permeability test.

3.4 Outflow Experiments

As discussed in the previous section, the UHTC samples can feature irregularities even within a single batch. This indicates that the outflow of these samples could behave in an irregular fashion as well. Therefore, it is necessary to measure the outflow velocity distribution of each sample manufactured in the current process, particularly before employing it in wind tunnel experiments. In order to examine the specially-resolved outflow characteristics of transpiring UHTCs, a bench-top rig has been designed, where the outflow velocity can be mapped and visualised using hot-wire anemometry. In this paper, the outflow behaviour of UHTC-7 and UHTC-8 are characterised.

3.4.1 Setup

A machined UHTC sample (see Fig. 3.3c) is glued and sealed onto a cover-plate by silicon, and subsequently the cover-plate is attached to a plenum that is fitted with a pressure transducer (Gems 3100 Series) and a gas inlet as shown in Fig. 3.10a. A K-type thermocouple is fed through the gas inlet. The plenum is located atop a set of motorised traverses (Thorlabs MTS50/M-Z8) that move in orthogonal directions with respect to each other. This allows for the sample to be traversed in a two-dimensional plane, $x - y$.

Due to the fine porous structures of the UHTCs, a miniature hot-wire probe is employed (Dantec Dynamics P14; wire dimensions: 5 μm in diameter, 1.25 mm in length). The hot-wire anemometry is run in CTA (Constant Temperature Anemometry) mode (Jørgensen, 2005; Bruun, 2002). During operation, the hot-wire probe is attached to a stationary support and the plenum is traversed at a pre-defined step-size on either direction (see Fig. 3.10b). The height of the probe from the sample's surface, z, is adjusted by a fine translation stage (Thorlabs DTS50/M).

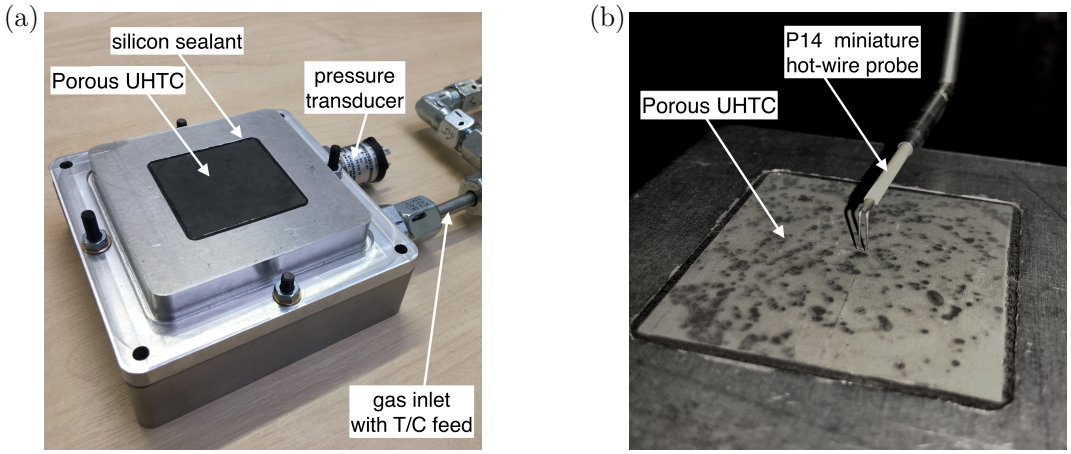

Figure 3.10: (a) A UHTC sample attached to the plenum and (b) a miniature hot-wire probe, P14, in operation.

The choice of the calibrator is of particular importance as the velocities involved in this experiment are low. The probe is calibrated with Dantec's *StreamLine Pro Automatic Calibrator*, which is capable of a wide velocity range, i.e. 0.02 m/s to $>$ 300 m/s, that includes a sufficiently low velocity regime. The collected calibration data are fitted with King's law (Jørgensen, 2005; Bruun, 2002), which is expressed as

$$E^2 = A + Bv^n, \; 0.4 \leq n \leq 1.0. \tag{3.7}$$

Here, E and v are the voltage acquired from the CTA and the corresponding velocity is set on the calibrator. The regression coefficients are $A = 1.688$, $B = 0.6203$, and $n = 0.8708$. The exponent's value of $n = 0.8708$ is within the range for low-velocity calibrations reported by Aydin & Leutheusser (1980) and Tsanis (1987), i.e. $n \approx 0.6 - 1.0$. The calibration curve is plotted in Fig. 3.11 along with the prediction interval of this fit.

Since ZrB_2 is thermally conductive, the near-wall effect of hot-wires (Bhatia *et al.*, 2006) needs to be taken into account. Measurements taken below the height of $z = 3$ mm experience this effect as shown in Fig. 3.12, where the flow velocity is zero. A correction to account for this is performed as $E^2_{\text{corr}} = E(z)^2 - E_0^2$, where $E(z)$ is the voltage at a given probe height z and E_0 is the nominal voltage away from the wall, which is constructed by taking the average of the values lying on the asymptote (dashed line in Fig. 3.12).

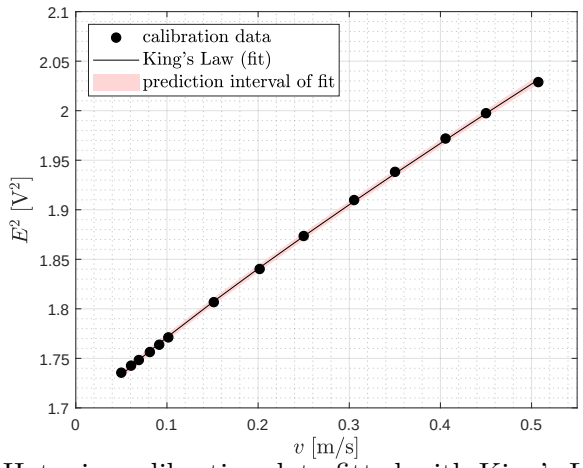

Figure 3.11: Hot-wire calibration data fitted with King's Law ($R^2 = 0.99$).

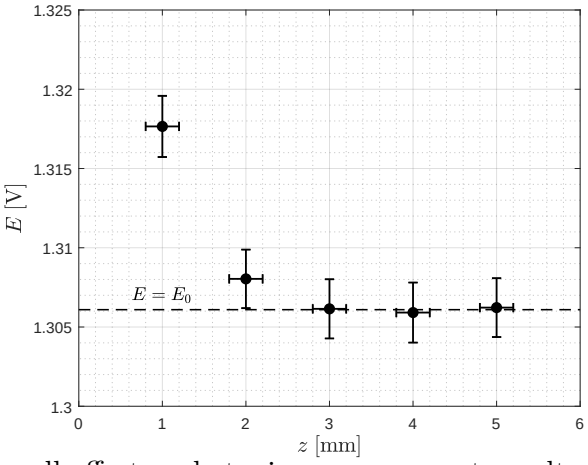

Figure 3.12: Near-wall effect on hot-wire measurements: voltage versus wall-normal distance. Note: the error bar for voltage is obtained from the standard deviation and an estimated uncertainty of $\Delta z = \pm 0.2$ mm is plotted for distance.

For each run, an area of 43 mm × 43 mm is covered with a step-size of 1 mm × 1 mm. This covers the through-flow area of 39.5 mm × 39.5 mm. The plenum pressure, p_{plenum}, plenum temperature, T_{plenum}, and hot-wire data are acquired for each step. The overall process takes about 3.5 hours to complete and the plenum pressure fluctuates slightly over time, which leads to minor discrepancies in the velocity across the sample. Hence, the measured velocity from the hot-wire, v_{hw}, at each cell is normalised as

$$\bar{v}_{out} = \frac{v_{hw}}{v_{out}}, \tag{3.8}$$

where v_{out} is the superficial output velocity obtained from the Darcy-Forchheimer

equation

$$\frac{p_{in}^2 - p_{out}^2}{2p_{out}L} = \frac{\mu(T_{out})}{K_D} v_{out} + \frac{\rho_{out}(p_{out},\ T_{out})}{K_F} v_{out}^2, \tag{3.9}$$

expressed in terms of output quantities. Here, the input and output conditions correspond to the plenum and atmospheric conditions, respectively, for each measurement location. The non-dimensional output velocity, $\bar{v}_{out}$, therefore incorporates the fluctuations in the plenum pressure and also shows how close the obtained velocity is compared to the theoretical Darcy-Forchheimer velocity, e.g. it would be equal at unity, i.e. $\bar{v}_{out} = 1$. This also serves as a baseline quantity to compare the uniformity of a particular measurement location with its neighbouring ones.

3.4.2 Results and Discussion

The outflow results obtained from the hot-wire anemometry are presented in Fig. 3.13. Figures 3.13c and 3.13d show the outflow maps in terms of the non-dimensional output velocity, $\bar{v}_{out}$, for UHTC-7 and UHTC-8, respectively. The corresponding histograms are shown in Figs. 3.13e and 3.13f. Reference images of UHTC-7 and UHTC-8 are respectively embedded in Figs. 3.13a and 3.13b. The plenum pressure was set at $p_{\text{plenum}} = 4$ bar (g) with air as the injected gas. The hot-wire probe was set at a height of $z = 2$ mm. In Table 3.4, the mean velocity measured by the hot-wire probe, $\overline{v}_{hw}$, is compared against the velocity obtained from the mass flow meter, $v_{\dot{m}}$, for both samples. The mean velocity form hot-wire anemometry is in close agreement with the mass flow meter's velocity for both UHTC-7 and UHTC-8. The discrepancy between the two measurement sources is 7.6% for UHTC-7 and 5.9% for UHTC-8, which are within the uncertainty in $v_{\dot{m}}$ (Table 3.4). This verifies

Sample ID	$\overline{v}_{hw} \pm \delta\overline{v}_{hw}$ [m/s]	$\frac{\delta\overline{v}_{hw}}{\overline{v}_{hw}}$ [%]	$v_{\dot{m}} \pm \delta v_{\dot{m}}$ [m/s]	$\frac{\delta v_{\dot{m}}}{v_{\dot{m}}}$ [%]
UHTC-7	0.481 ± 0.012	2.50	0.447 ± 0.046	10.2
UHTC-8	0.433 ± 0.012	2.77	0.409 ± 0.042	10.3

Table 3.4: Comparison between velocities obtained from hot-wire anemometry and mass flow meter.

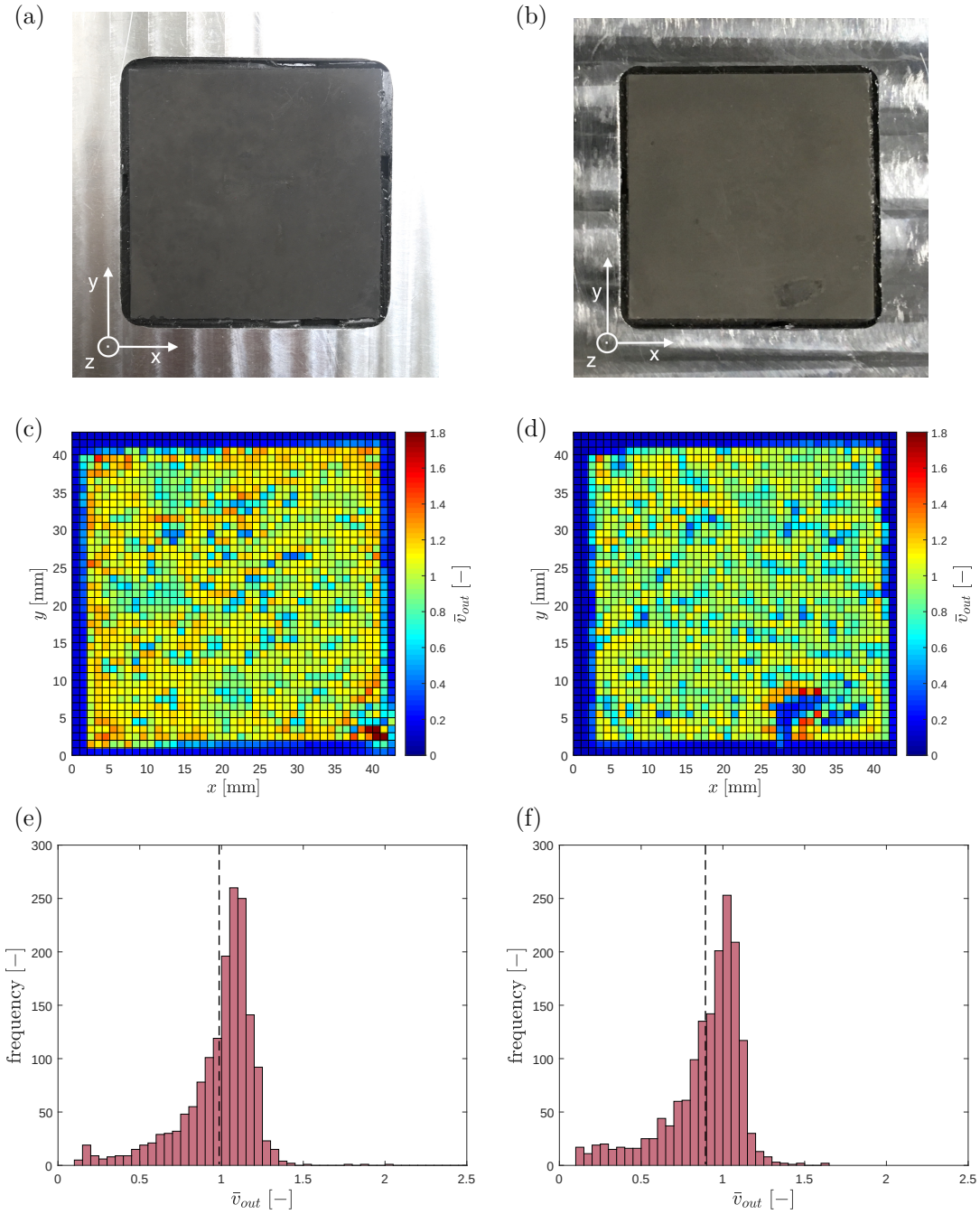

Figure 3.13: Reference frame for traversing: (a) UHTC-7 and (b) UHTC-8; outflow map in terms of the non-dimensional output velocity, $\bar{v}_{out}$: (c) UHTC-7 and (d) UHTC-8; and histogram of $\bar{v}_{out}$: (e) UHTC-7 and (f) UHTC-8 (the dashed line represents the mean value). The injected gas is air at $p_{\text{plenum}} = 4$ bar (g). Height of the probe is at $z = 2$ mm.

the overall hot-wire velocity measurement, especially the performed calibration at these low speeds and the wall correction.

Figures 3.13c and 3.13d demonstrate a fairly uniform velocity distribution across the samples. The contour level in terms of the non-dimensional output velocity, $\bar{v}_{out}$, is close to 1 over the majority of the outflow region. This is further evident in the corresponding histograms in Figs. 3.13e and 3.13f. The mean value, represented by the dashed line, is close to 1 for both samples, which demonstrates that the obtained spatial measurements largely adhere to the theoretical value calculated by the Darcy-Forchheimer equation. The standard deviations are 0.24 (UHTC-7) and 0.23 (UHTC-8), which respectively correspond to 24.4% and 25.8% on the mean value (average of the two: 25.1%). Most importantly, the velocity varies within the same order of magnitude, which suggests that unwanted jets are absent. There is a small region of approximately twice the mean velocity on the bottom-right corner of UHTC-7 (Fig. 3.13c). This could be due to a small leakage or a more permeable zone locally. On UHTC-8, there is a small area where no outflow is present (from $x = 27$ mm to $x = 39$ mm and $y = 2$ mm to $y = 9$ mm, 3.13d). This is a densified region that can be seen on the sample itself in Fig. 3.13b. Apart from these outlying regions, both samples show a regular flow-field with practically no blockage.

Overall, the outflow of these UHTCs exhibits a good uniformity. As there is no individual jet or large blockages, the coolant mass can be injected in a fairly uniform fashion into the boundary layer for the purpose of transpiration cooling. However, the outflow characteristics of two different samples are not identical, and large variations could exist in the current manufacturing process. It is therefore necessary to characterise the outflow of each sample before use. These velocity maps could be used as a boundary condition in numerical modelling and as a reference to interpret the mass flow distribution in wind tunnel experiments.

3.5 Conclusion

The permeability and outflow behaviour of porous Ultra-High-Temperature Ceramics (UHTC) made of ZrB_2 were experimentally examined to assess their suitability

for transpiration cooling, a thermal protection system that could enhance the re-usability of hypersonic vehicles such as rockets and spaceplanes. It is shown that the flow through these UHTCs can be successfully modelled by the Darcy-Forchheimer equation even at higher through-flow velocities, and the corresponding permeability coefficients are measured in an ISO 4022 rig featuring a through-flow diameter of 15.6 mm and reported along with their respective uncertainties. A change in porosity, from $\phi \approx 32\%$ to $\phi \approx 42\%$, results in an order of magnitude jump in the Darcy coefficient, whereas the Forchheimer coefficient increases by two orders of magnitude, approximately. Cleaning the surface of the porous samples – in form of sanding or ultrasonic bath – increased the Darcy coefficient by up to 19%. Velocity maps obtained from hot-wire anemometry demonstrate good outflow characteristics that behave in a uniform fashion. The standard deviation of the velocity distribution is 25.1% with respect to the mean value. No individual jets are present. The results published here can be used in numerical modelling and experimental design of wind tunnel testing, where porous injectors made of UHTC are involved. Furthermore, the permeability coefficients could help designers predict the coolant mass budget for vehicles that will feature transpiration cooling. Whilst the brittleness of porous UHTC restricts its ease of application – in terms of the flow characteristics – it is demonstrably a befitting candidate for transpiration cooling.

Appendix

3.6 Uncertainty Analysis

The uncertainties in the variables $\frac{\Delta p}{L}$, μv_{in}, and $\rho_{in} v_{in}^2$ were calculated using Moffat's error propagation method (Moffat, 1988) defined as

$$\delta X = \sqrt{\sum_{i=1}^{N} \left(\frac{\partial X}{\partial Y_i} \delta Y_i \right)^2}, \tag{3.10}$$

where each variable is given as $X = X(Y_1, Y_2, ..., Y_N)$. Here, X is the variable which is calculated from measurements, Y_i, using data from the experiment. The uncertainties in Y_i, denoted by δY_i, are determined from the uncertainty given by

Gauge	Variable	Absolute error [%]	F.S.O. error [%]	F.S.O.	Reading error [%]
Pressure transducer, Gems 3100	p_{in}	n/a	0.25	40 bar (g)	n/a
Pressure transducer, Gems 3100	p_{out}	n/a	0.25	25 bar (g)	n/a
Thermocouple, K-type	T_{in}, T_{out}	0.5 K	n/a	n/a	n/a
Mass flow meter, Alicat M Series	$\dot{m}$	n/a	0.2	250 slpm	0.8

Table 3.5: Apparatus uncertainties. F.S.O. = full scale output.

the manufacturer of the employed equipment (see Table 3.5). In order to find the uncertainties in the permeability coefficients, a Monte Carlo simulation (Coleman & Steele Jr., 2009) was performed for 1×10^6 events. For this purpose, 1×10^6 random events were created for the aforementioned variables around each experimental data point which followed a Gaussian distribution. The Gaussian distribution was defined by an expected value of $E = X$ and a standard deviation of $\sigma = \frac{\delta X}{2}$. Hence, the uncertainty δX was given by a confidence interval of 95% for each variable, and thus the process 'simulated' 1×10^6 events of the same experiment within the given bounds of uncertainty. Subsequently, the Nelder-Mead simplex search optimisation process was carried out for each event, hence 1×10^6 times, which yielded Gaussian distributions for K_D and K_F. The uncertainties for the permeability coefficients were determined as $\delta K_D = \pm 2\sigma$ and $\delta K_F = \pm 2\sigma$ – and therefore within a confidence interval of 95% – from their respective distributions.

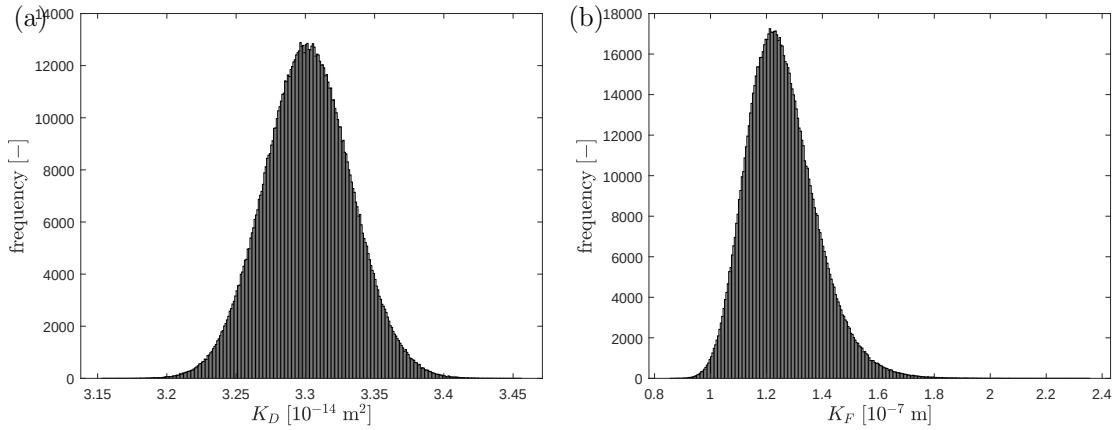

Figure 3.14: Histogram of (a) K_D and (b) K_F for 1×10^6 events obtained from the Monte Carlo Simulation. Sample: UHTC-3 (pos).

The histograms of K_D and K_F for UHTC-3 (pos) generated from the Monte Carlo simulation are respectively illustrated in Fig. 3.14a and Fig. 3.14b, and

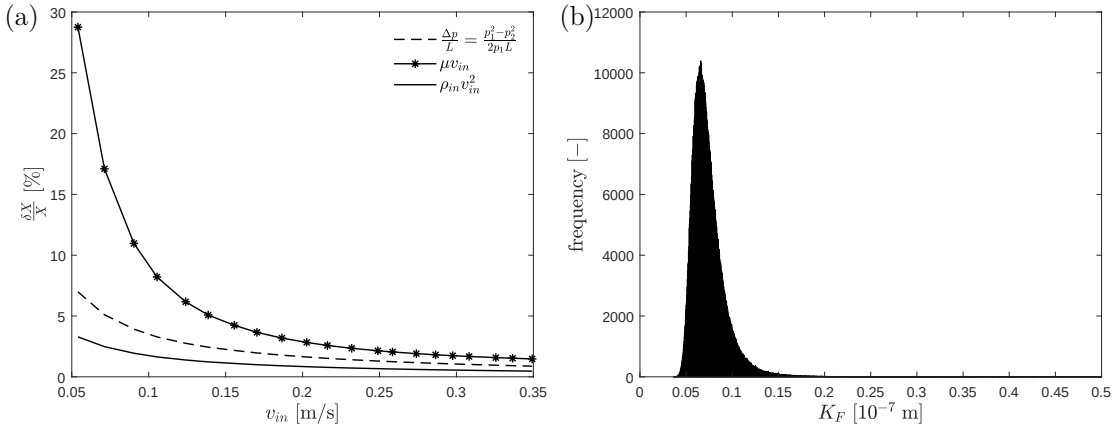

Figure 3.15: (a) Uncertainties of different variables for each data point with respect to their corresponding superficial input velocity and (b) asymmetric histogram of K_F obtained from the Monte Carlo Simulation; sample: UHTC-4 (pos).

the corresponding uncertainties in variables $\frac{\Delta p}{L}$, μv_{in}, and $\rho_{in} v_{in}^2$ are shown in Fig. 3.15a. For cases where the uncertainties in the permeability coefficients are high, the Monte Carlo simulation yields an asymmetric distribution. The uncertainties for the coefficients within a confidence interval of 95% is calculated from a probabilistically symmetric distribution according to Coleman & Steele Jr. (2009) after filtering out any value that is equal or larger than unity. A histogram of such a case (UHTC-4) is presented in Fig. 3.15b.

4

Laminar Transpiration Cooling Experiments in Hypersonic Flow

Preamble

The second segment of the research aim of this thesis is to investigate the mixing mechanism between the coolant and a laminar, hypersonic boundary-layer gas at the wall downstream of a transpiring injector. In this chapter, results of laminar transpiration cooling experiments conducted at Mach 7 employing a flat-plate model are presented. The coolant's wall concentration and heat flux data were collected downstream of the injector. A porous UHTC, characterised in the preceding chapter, was used as the injector. This chapter is composed of a journal paper published in *Experiments in Fluids* (Ifti *et al.*, 2022*a*). The content and structure of this chapter represent 100% of the main body of the original paper.

Authors of the original paper: **Ifti, H.S.**, Hermann, T., McGilvray, M., Ewenz Rocher, M., Doherty, L., Hambidge, C. & Vandeperre, L.J.

Author contribution:

Ifti, H.S.: Lead author, conceptualisation, data curation, formal analysis, and writing.

Hermann, T.: Supervision as postdoctoral assistant in the project.

McGilvray, M.: Supervision as principal investigator and funding acquisition.

Ewenz Rocher, M., Doherty, L., & Hambidge, C.: Assistance in experimental setup.

Vandeperre, L.J.: Manufacturing of the UHTC samples.

Associated Appendices: Appendices B, C, D, and E.

4.1 Introduction

Hypersonic vehicles are subject to extremely high heat fluxes due to aerodynamic heating (van Driest, 1956), which becomes detrimental for the vehicle at very high Mach numbers. Different types of Thermal Protection Systems (TPS) are therefore in use today that protect the vehicles from overheating. Although these state-of-the-art heat mitigation techniques – such as heat sinks (passive) and ablation (semi-passive) – are successful for vehicles operated at present, these conventional thermal protection systems often have a low degree of re-usability, especially when the vehicle experiences high peak heating. This constraint results in a higher cost of payload transfer. A re-usable, high-performing thermal protection system could therefore drive this cost down, making space and hypersonic flight more accessible. The pursuit of a novel, re-usable TPS is critical to both present and future hypersonic flight. Transpiration cooling is a promising, candidate technology that could enable a re-usable TPS for hypersonic vehicles such as rockets or spaceplanes. In particular, it could be employed in conjunction with conventional thermal protection systems for vehicle parts that experience high peak heating such as leading edges or control-fin joints (e.g. fin hinges of SpaceX Starship). Transpiration cooling is an active cooling method where a coolant gas is injected through a porous material into the boundary layer. The cooling process comprises three different effects (see Fig. 4.1): (a) heat from the wall is convected out by the fluid; (b) the coolant gas

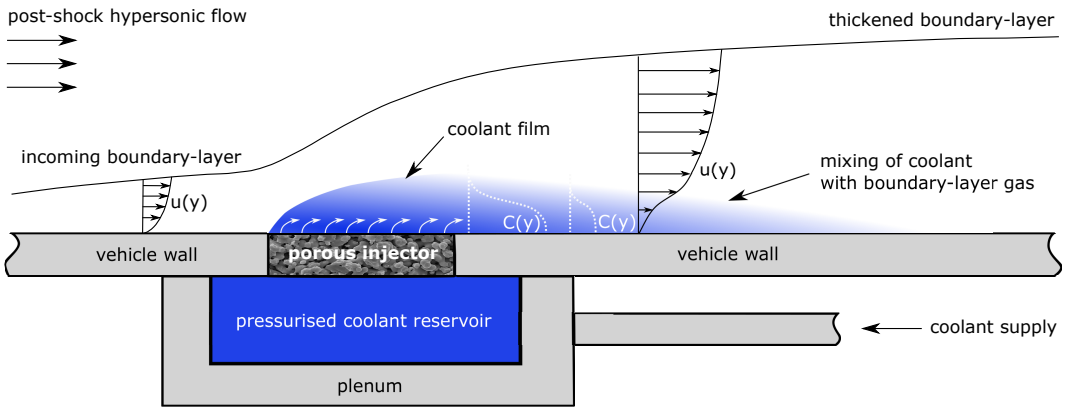

Figure 4.1: Schematic of a flat surface of a hypersonic vehicle with a porous, transpiration cooling injector. Note: not to scale.

creates a film (blue) that insulates the wall underneath from the hot cross-flow; and (c) the coolant film protects the wall from free-stream Oxygen and thereby prevents oxidation of the wall, which enables the wall-material to operate at a higher temperature enhancing radiative cooling and reduces recombination heating. The success of the latter two processes depends on the coolant film that is formed on and downstream of the injector. This protective film loses its concentration in the stream-wise direction and eventually diminishes at a downstream location as it mixes with the incoming hypersonic cross-flow (see the concentration gradient, $C(y)$ in Fig. 4.1). In practice, transpiration cooling would act as a dual-mode protection system that would protect the vehicle from both heat and oxidation.

The majority of the studies are concerned with a common goal of understanding – and in some cases predicting – the mixing between the coolant gas and the external cross-flow. This mixing problem of transpiration cooling can be divided in two regions: (1) on the porous injector and (2) downstream of the injector. Authors have correlated the blowing ratio of the coolant gas, i.e. the ratio between the coolant mass flux and the free-stream mass flux (Eq.(4.1)), with the cooling effectiveness in various conditions with different gases. There is a vast amount of work in the literature on this topic spanning more than 50 years (Goldstein, 1971; Fujiwara *et al.*, 2017). However, most studies are concerned with turbulent flows only.

A hypersonic vehicle may fly through all three flow regimes, i.e. laminar, transitional, and turbulent, and therefore cooling in each flow regime could become important for such a vehicle. What is more, a hypersonic vehicle could experience its highest peak heating in the laminar regime (Hermann *et al.*, 2019*b*). Despite this need, only a handful of studies on film cooling or transpiration cooling in a laminar boundary layer are available in the literature, experimental and numerical studies combined. Heufer & Olivier (2008*a*) proposed a correlation factor based on the energy equation similar to Goldstein (1971) but with a laminar velocity profile. The authors validated the correlation factor numerically and experimentally using a slot injector on a flat plate in laminar, supersonic flows and achieved a collapse of the data. Different slot geometries and coolant gases were used in the

experiments by Hombsch & Olivier (2013) in supersonic flows, where the authors demonstrated that film cooling was much more effective in laminar flows than turbulent ones, and a correlation was proposed. Keller *et al.* (2015) performed direct numerical simulations to investigate the influence of different coolant gases in a Mach 2.6, laminar flow over a flat plate and compared the simulation to the data from Hombsch & Olivier (2013) and demonstrated a collapse of the data for different gases by multiplying the correlation factor by the ratio of specific heat capacities raised to the exponent of 0.33. The success of film cooling in laminar, hypersonic flows was demonstrated by Heufer & Olivier (2008*b*) where a flat-plate model was used featuring a slot injector. Gülhan & Braun (2010) further demonstrated the high efficiency of transpiration cooling downstream of a porous injector in laminar, hypersonic flows over a flat plate. One of the earlier experimental studies was conducted by Richards & Stollery (1979), where tangential injection was employed to cool a flat plate at Mach 10 in a hypersonic boundary layer. The authors proposed a discrete-layer theory based on heat conduction. All of these studies, however, concern heat flux reduction only, not the concentration of the coolant gas at the wall. Since the heat and mass transfer analogy does not apply to laminar flows (Kays *et al.*, 2005), the coolant gas's concentration distribution on the wall becomes a compelling quantity in order to understand the mixing process in laminar boundary layers. However, experimental data on the concentration distribution, particularly in laminar, hypersonic flows, are not available in the literature.

In this paper, the concentration of the transpiring coolant gas at the wall downstream of the injector – along with the corresponding heat flux reduction – is experimentally measured and examined in a laminar, hypersonic boundary layer. This is the first time the distribution of the coolant's concentration at the wall downstream of a transpiring injector in a laminar, hypersonic flow is reported. A flat-plate model is used in the Oxford High Density Tunnel (HDT) at Mach 7. This model allows to investigate the mixing problem without any geometric complexity and contribute to the existing, large body of work in the literature based on flat-plate geometries (e.g., Heufer & Olivier, 2008*a*; Hombsch & Olivier,

2013; Hermann *et al.*, 2019*b*; Gülhan & Braun, 2010). A porous injector made of partially sintered zirconium diboride (ZrB_2) is used (diameter of its pores is below 10 μm). The coolant film concentration at the wall downstream of the injector is spatially resolved using Pressure-sensitive Paint (PSP). The corresponding heat flux reduction is measured with thin-film gauges.

4.2 Methodology

The experiments were conducted in the Oxford High Density Tunnel (HDT) that was operated in Ludwieg tube mode (McGilvray *et al.*, 2015; Wylie & McGilvray, 2019; Wylie, 2020) at Mach 7. Data were acquired on an NI PXIe-8135 controller with NI PXIe-6368 acquisition cards at 2 MS/s/channel. A flat-plate model was employed that was mounted at an angle of attack of AoA = 0°. For reference, the core flow diameter ranges from 280 mm to 320 mm at the nozzle exit and from 200 mm to 240 mm at an axial location 418 mm downstream thereof (Wylie, 2020). The experimental model and diagnostic methods are discussed in the following sections.

4.2.1 Flat-Plate Model

A flat-plate model with a top surface area of 577 mm × 125 mm was employed (see Fig. 4.2a). The top plates were made of C250 tooling plates (roughness Ra of 0.4 microns). The joints between the plates were made flush by centring dowel pins and any gap between the joints was filled with cement to ensure a smooth finish. A porous injector (made of ZrB_2) of 39.5 mm × 39.5 mm was placed on the symmetry line of the plate at $x = 160$ mm from the leading edge (see Fig. 4.2b for microstructure). A plenum was attached underneath the porous injector and pipework was in place to feed in the injection gas. The plenum was fitted with a thin (⌀0.0762 mm), fast-response K-type thermocouple (in-house, response time < 1 ms) and a Kulite pressure transducer (HEL-375-35BARA) in order to measure the temperature and pressure of the coolant gas, respectively. The model featured a coat of the Porous, Fast-Response Pressure-sensitive Paint (PSP) (Sellers *et al.*, 2016) from Innovative Scientific Solutions, Inc. (ISSI) on the surface downstream

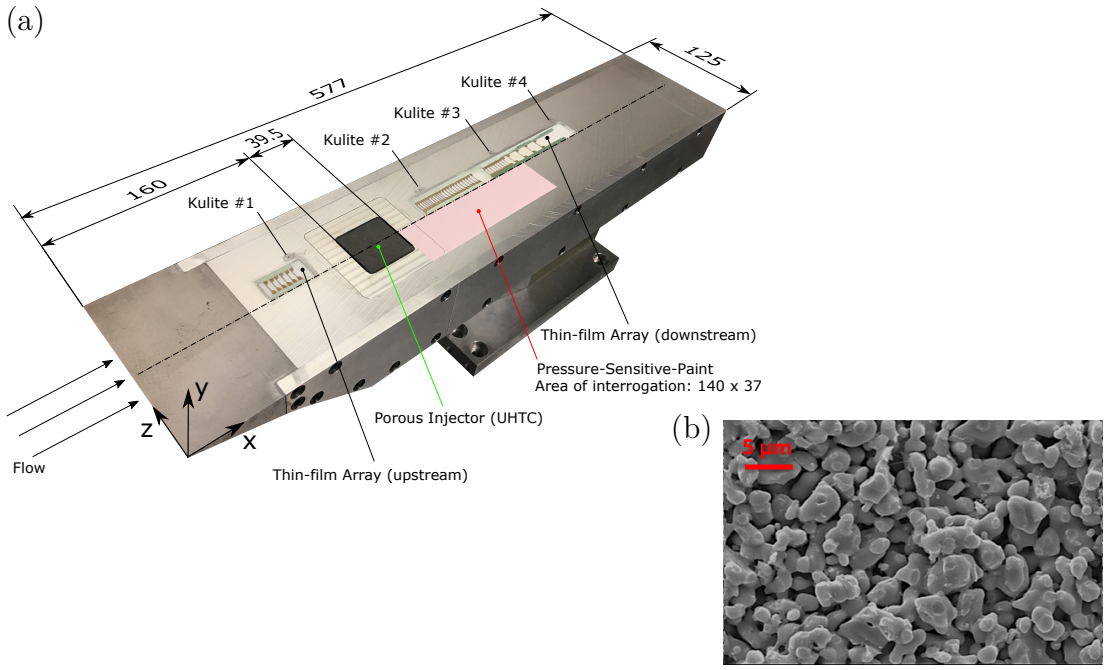

Figure 4.2: (a) Flat-plate model instrumented with Kulite pressure transducers, thin-film arrays, and a porous injector (UHTC). A PSP layer is painted downstream of the injector. Note: all dimensions are in millimetres. (b) A scanning electron microscopy (SEM) micrograph of the microstructure of the UHTC injector (Ifti *et al.*, 2022*c*).

of the porous injector – starting at $x = 200$ mm from the leading edge – on one side of the symmetry line. This is a three-component, single-luminophore PSP that has a response time under 100 μs, a pressure sensitivity of 0.6% per kPa, and a range of $0 - 200$ kPa. The PSP coat had an area of interrogation of 140 mm $\times$ 37 mm. On the other side of the symmetry line, Macor-based Platimun thin-film arrays were instrumented upstream ($x = 96$ mm to 116 mm) and downstream ($x =$ 230 mm to 358 mm) of the injector. The plate was further instrumented with four flush-mounted Kulite pressure transducers (XCS-093-5A). The coat of PSP was used for measuring the concentration of the injected coolant gas downstream and the thin-film arrays measured the resulting heat flux reduction. In addition to measuring heat flux, the thin-film arrays were employed to determine the boundary-layer state, i.e. laminar, transitional, or turbulent, with no injection.

4.2.2 Flow Condition and Blowing Ratios

The blowing ratio, i.e. the ratio of the injected coolant mass flux to the boundary-layer edge mass flux, is defined as

$$F = \frac{\rho_c u_c}{\rho_e u_e}, \tag{4.1}$$

where the subscripts 'c' and 'e' respectively denote coolant quantities at the surface and the edge quantities. ρ and u are density and velocity, respectively. The blowing parameter, on the other hand, is given by the equation

$$B_h = \frac{F}{St_0}, \tag{4.2}$$

where St_0 is the Stanton number on the injector at $F = 0$. In Table 4.1, the six blowing ratios used in this study are presented along with their respective blowing parameters. Nitrogen was used as the coolant gas for Cases 1 to 4 and Helium for Cases 5 to 6. The Mach number, unit Reynolds number, total pressure, and total temperature were respectively $M = 7$, $Re_u = 12.9 \times 10^6$ m^{-1}, $p_0 = 1.738$ MPa, and $T_0 = 470.1$ K. Further details on the calculation of flow quantities are presented in Appendix B and an uncertainty analysis for relevant quantities are given in Appendix D.

Case	F [%]	B_h [−]	Coolant gas
1	0.0406	1.49	N_2
2	0.0818	2.99	N_2
3	0.153	5.59	N_2
4	0.295	10.8	N_2
5	0.0416	1.52	He
6	0.08	2.93	He

Table 4.1: Overview of blowing cases. Flow condition: $Re_u = 12.9 \times 10^6$ m^{-1}, $p_0 = 1.738$ MPa, and $T_0 = 470.1$ K. Uncertainties in F and B_h are respectively ±11.0% and ±29.5%.

The outflow distribution of the employed porous injector was characterised by hot-wire anemometry with air injection. Details of the process can be found in Ifti *et al.* (2022*c*). The obtained velocity map is illustrated in Fig. 4.3.

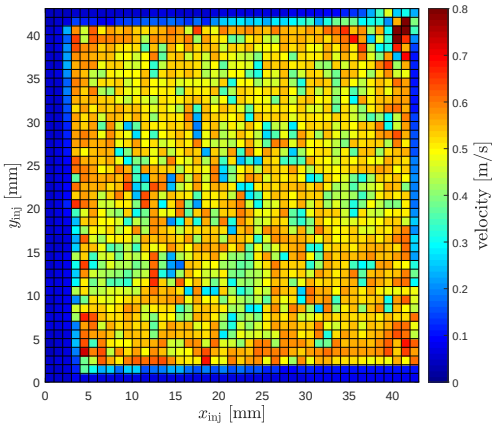

Figure 4.3: Velocity map of the porous ZrB_2 injector. Injected gas: air. Gas temperature: 24 °C. Differential pressure: 4 bar. Thickness of injector: 5 mm.

4.2.3 Measurement of Wall Coolant Concentration

The relative coolant concentration on the wall was measured by Pressure-sensitive-Paint (PSP). A Luminus PT-120-TE UV high power LED was positioned above the model. The LED was turned on for approximately 5 s before each shot. The LED temperature rises when it is operated, which was measured by its built-in thermistor. The LED intensity is a linear function of its temperature, and therefore the recorded intensity was scaled by the measured LED temperature rise to allow for repeatable illumination between shots. The emitted radiation passed through a UV bandpass filter with a central wavelength of 390 nm and a full width at half maximum of 125 nm. The luminophore in the Porous, Fast-Response Pressure-Sensitive Paint is excited by the UV radiation and achieves a higher state of energy that results in an emission in the red wavelength spectrum as it returns to its ground state. The emitted radiation from the PSP reflected off a flat mirror and was captured by a high-speed camera (Photron FASTCAM Mini AX200 type 900K) that was fitted with a red filter (550 nm) and placed outside the test section (Hermann *et al.*, 2018). The images were captured at a frame rate of 6400 fps, shutter speed of 156.25 μs, a bit depth of 12, and a resolution of 1024×512. The acquisition of images was started before the flow arrival and continued for the whole duration of the test. The images were spatially transformed to a rectangle that represents the physical

geometry of the flat-plate model and passed through an image stabilisation algorithm prior to post-processing. A schematic of the PSP setup is illustrated in Fig. 4.4.

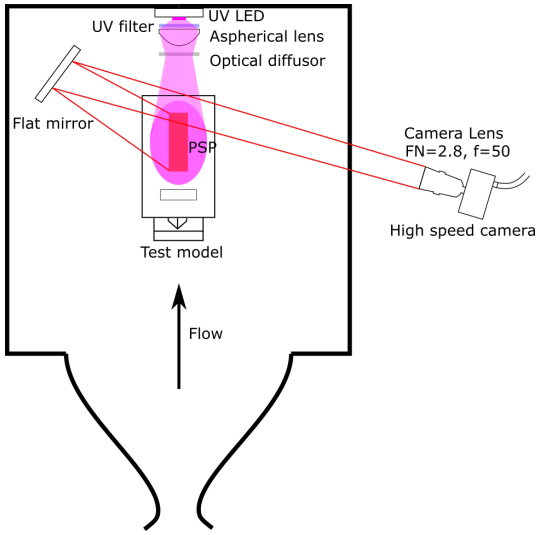

Figure 4.4: Schematic of the PSP setup (not to scale). Figure from Hermann *et al.* (2018).

The excitation of PSP luminophores is quenched by Oxygen, and therefore an increase in Oxygen partial pressure, p_{O_2}, results in a lower intensity, I, of the emitted radiation, and vice-versa. This characteristic can be expressed in the power law form of the Stern-Volmer equation (Quinn *et al.*, 2011) as

$$\frac{I_{\text{ref}}}{I} = c_1 p_{O_2}^n + c_2, \; 0 < n \leq 1.0. \tag{4.3}$$

Here, I_{ref} refers to the intensity reference value taken before the flow arrival. The coefficients, c_1, c_2, and n were determined by a regression analysis from calibration data. For the current experiments, the reference value were taken prior to the flow arrival when the test section was near vacuum (approximately 80 Pa). A pixel-by-pixel calibration was performed by collecting data from a shot without injecting any coolant gas. The pressure values were obtained from the average pressure measured by the surface-mounted Kulites. Five data points are obtained from five different flow conditions for pressure, p_{O_2}, and intensity ratio, I_{ref}/I, and an additional data point is obtained from the data acquired prior to the flow arrival. Calibration data were collected on a daily basis to reduce the effect of

PSP degradation. The R-squared value (coefficient of determination) for each pixel was calculated to quantify the quality of regression. The spatially averaged (across all pixels) R-squared value for these calibrations is $R^2 \geq 0.99$. Since the same calibration is applied to all the other shots with gas injection, a trace of the film can be identified as the quenching is influenced by the film. Injected Nitrogen or Helium gas hinders the quenching by displacing air in the boundary layer. Comparing a case with air injection and one with a foreign gas injection at the same blowing ratio, in this case Nitrogen or Helium, gives a measure of how much air is displaced by the foreign gas, i.e. to what extent the foreign gas is forming a film. A concentration film effectiveness is defined as

$$\begin{aligned} \eta_c &= \frac{C_w - C_e}{C_c - C_e} \\ &= 1 - \frac{p_{O_2,\,\text{foreign gas}}}{p_{O_2,\,\text{air}}}, \end{aligned} \tag{4.4}$$

where C is the concentration and subscript 'w' stands for concentration at the wall; $p_{O_2,\,\text{air}}$ and $p_{O_2,\,\text{foreign gas}}$ are Oxygen partial pressures with air and foreign gas injections, respectively, at the same blowing ratio. A concentration film effectiveness of $\eta_c = 1$ corresponds to a full displacement of the air by the foreign gas, whereas $\eta_c = 0$ indicates that no displacement of air is achieved and the film is fully diminished. Since η_c is calculated for every pixel, it yields a spatial map of the whole film downstream of the porous injector. Essentially, this film effectiveness based on coolant concentration quantifies the physical presence of the film in terms of its concentration. Unlike in the case of turbulent flow, this effectiveness is not equivalent to the thermal effectiveness as the heat and mass transfer analogy cannot be assumed in laminar flows. Eq.(4.4) is strictly a measure of relative concentration.

4.2.4 Heat Flux Measurement and Determination of Boundary Layer State

The thin-film arrays measure the heat flux along the stream-wise direction. As the flow convects over the plate, the temperature of the Macor rises. This recorded temperature rise, ΔT, is used to compute the wall heat flux, $\dot{q}_w$, by applying the

impulse response convolution approach of Oldfield (2008). The thermal product of Macor is $\sqrt{\rho c_p k} = 1705$ Jm^{-2}K^{-1}s$^{-0.5}$ (Macor data sheet). The impulse response is calculated with an assumption of heat conduction into a one-dimensional semi-infinite slab. According to Schultz & Jones (1973), this assumption is valid as long as the thermal penetration depth during the test is shorter than the thickness of the material. For Macor, this minimum depth is 2.65 mm over a time period of 600 ms. The Macor arrays installed in the flat plate had a minimum depth of 7 mm.

The heat flux measurement had two purposes: (a) to quantify the heat flux reduction by transpiration cooling and (b) to determine the boundary-layer state. The latter was achieved by measuring the heat flux without coolant injection and comparing it to Eckert's heat flux correlations for laminar and turbulent boundary layers over a flat plate (Eckert, 1956) respectively expressed as

$$St^*_{\text{lam}} = \frac{0.332}{\sqrt{Re^*_x}}(Pr^*)^{-2/3} \tag{4.5}$$

and

$$St^*_{\text{turb}} = \frac{0.0296}{(Re^*_x)^{0.2}}(Pr^*)^{-2/3}. \tag{4.6}$$

Here, St is the Stanton number. The superscript '$*$' here denotes quantities that are evaluated at Eckert's reference temperature.

In Fig. 4.5, the experimentally obtained heat flux data for five different flow conditions – from a shot without coolant injection – are plotted versus Re^*_x. The Eckert reference curves for laminar and turbulent boundary layers, i.e. Eq.(4.5) and Eq.(4.6), are illustrated alongside. The experimental data points lie atop Eckert's laminar curve upstream (all 6 active gauges shown) of the injector as well as immediately downstream (all active gauges up to 272.5 mm shown). The onset of natural transition (no blowing) took place approximately at $x = 310$ mm (not shown in Fig. 4.5).

The heat flux reduction by transpiration cooling is formulated as the isothermal cooling effectiveness

$$\eta_{th} = 1 - \frac{St_c}{St_0}, \tag{4.7}$$

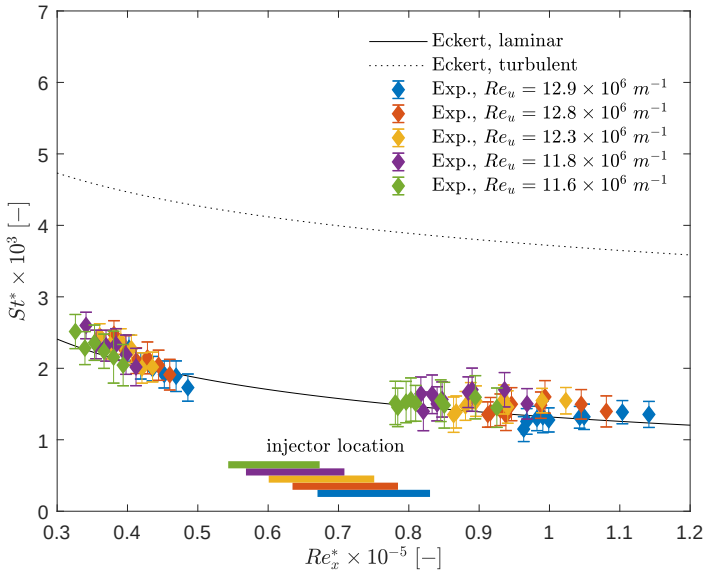

Figure 4.5: Comparison with Eckert correlation: St^* versus Re_x^* at $F = 0$.

where the subscripts 'c'and '0' respectively denote cooled and uncooled cases. A case of 100% cooling, i.e. zero heat flux to the wall, would result in an effectiveness of 1. Eq.(4.7) is only valid for small blowing ratios and cases where the coolant gas is similar to the free-stream gas (Heufer & Olivier, 2008*a*). It is also invalid for downstream locations that are close to the injector. The obtained values of η_{th} can be correlated by a factor defined by Heufer & Olivier (2008*a*) as

$$\xi = \frac{1}{Fs}\sqrt{\frac{x - x_s}{x_s^{1.16}}\frac{C^* x}{Re_u}}, \tag{4.8}$$

where x_s is the slot location from the leading edge, s is the slot length, and C^* is the Chapman-Rubesin factor evaluated at Eckert's reference temperature. The effect of different coolant gases can be taken into account by multiplying the correlation factor, ξ, by the ratio of the specific heat capacities of the free-stream gas and the coolant gas, $c_{p,e}/c_{p,c}$, with an appropriate exponent, which has been demonstrated by Keller *et al.* (2015). Hombsch & Olivier (2013) proposed the correlation obtained from experimental data for blowing ratios ranging from 2.2% to 10.7% expressed as

$$\eta_{th} = \begin{cases} 1 & \text{for } \xi \leq 0.96, \\ [1 + 0.38(\xi - 0.96)]^{-1.6} & \text{for } \xi > 0.96. \end{cases} \tag{4.9}$$

4.3 Results and Discussion

Contour plots of Oxygen partial pressure, p_{O_2}, are presented in Figs. 4.6a-f for all blowing cases (see Table 4.1). The corresponding concentration effectiveness, η_c, (obtained from Eq.(4.4)) are respectively illustrated in Figs. 4.6g-l. The origin of the x and y axes is shown in Fig. 4.2. These contour plots show the physical trace of the film that is spatially resolved. As blowing ratio, F, increases for a given coolant gas, the Oxygen partial pressure decreases (Cases 1 to 4 for Nitrogen and Cases 5 to 6 for Helium). This is expected as the injected gas forms a film downstream and displaces the air in the boundary layer, and this process is more successful with higher mass flux of the coolant gas. The plots of concentration effectiveness on the other hand visualises the film in terms of the relative concentration of the coolant gas. As expected, the coolant concentration is higher immediately downstream of the injector and gradually reduces downstream with higher values of x. The cases with the highest blowing ratio for Nitrogen and Helium, i.e. Case 4 and Case 6 respectively, exhibit a concentration effectiveness of approximately 1 ($\eta_c \approx 0.95$) immediately downstream of the injector ($x = 200$ mm to $x = 240$ mm). This indicates that the air is almost fully displaced here and a coolant coverage close to 100% is achieved at this location. With rising blowing ratio, the 'V' shape of the film becomes more prominent, which is consistent with the results shown in Hermann *et al.* (2018). This is due to the Mach angle effect emanating from the two corners of the model as shown in Fig. E.1 (see Appendix E). A two-dimensional (2D) flow can only be assumed within this 'V' shaped zone due to the aspect ratio of the model. In contrast to the non-uniform film coverage discussed in Ifti *et al.* (2019), the film trace in the current results does not demonstrate noticeable non-uniformities. This is expected because the injector (UHTC-7, see Fig. 4.3) employed in the current experiments has a significantly more uniform outflow than the one used in Ifti *et al.* (2019).

The difference between Nitrogen and Helium injection can be seen by comparing Cases 1 and 2 (Figs. 4.6g and 4.6h) to Cases 5 and 6 (Figs. 4.6k and 4.6l), respectively. The blowing ratios are matched approximately between Cases 1 and 5 as well as Cases 2 and 6. A clear difference between the two gases are observed. For approximately

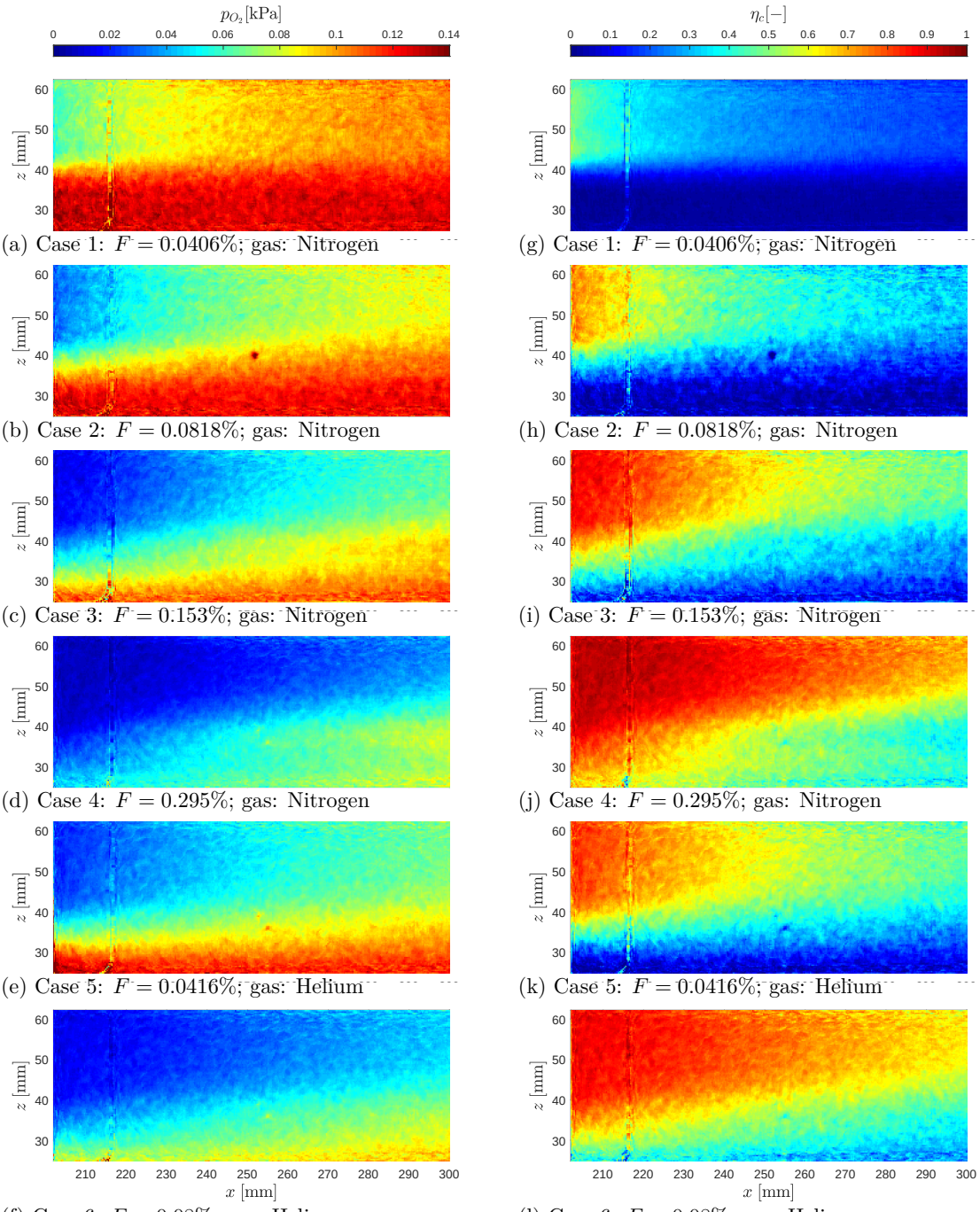

(a) Case 1: $F = 0.0406\%$; gas: Nitrogen

(g) Case 1: $F = 0.0406\%$; gas: Nitrogen

(b) Case 2: $F = 0.0818\%$; gas: Nitrogen

(h) Case 2: $F = 0.0818\%$; gas: Nitrogen

(c) Case 3: $F = 0.153\%$; gas: Nitrogen

(i) Case 3: $F = 0.153\%$; gas: Nitrogen

(d) Case 4: $F = 0.295\%$; gas: Nitrogen

(j) Case 4: $F = 0.295\%$; gas: Nitrogen

(e) Case 5: $F = 0.0416\%$; gas: Helium

(k) Case 5: $F = 0.0416\%$; gas: Helium

(f) Case 6: $F = 0.08\%$; gas: Helium

(l) Case 6: $F = 0.08\%$; gas: Helium

Figure 4.6: PSP results for Cases 1 to 6 (top to bottom) at $Re_u = 12.9 \times 10^6$ m^{-1}: Contours of downstream Oxygen partial pressure, p_{O_2}, from (a) to (f) and film effectiveness, η_c, from (g) to (l). Refer to Fig. 4.2a for axis origin.

the same blowing ratio, the cases with Helium injection forms a much stronger film downstream of the injector. This is consistent with the findings reported in the literature, e.g. Richards & Stollery (1979), where Helium was shown to be more effective in terms of the heat flux reduction versus Nitrogen. However, the results in this paper demonstrate that this is not only due to the gas's thermal properties but also the physical trace of the film itself. This effect can be attributed to the higher plenum pressure, p_{inj}, required for Helium injection compared to Nitrogen for the same blowing ratio. Since Helium's molecular weight is lower than that of Nitrogen, a higher plenum pressure is required to achieve the same mass flux through the injector. This leads to two differences at the exit: Helium exits at a higher velocity due to its lower density at a given edge pressure, p_e, and Helium contains more gas particles than Nitrogen since a higher plenum pressure results in a higher mole number; in other words, the higher mole number would lead to a larger volume for Helium at the exit. Combined, these two effects result in a seven times higher volumetric flow rate, $\dot{Q}$, of Helium when its mass flow rate, $\dot{m}$, is matched with Nitrogen. This higher volumetric flow rate of Helium compared to Nitrogen accounts for the better film coverage of Helium, which has been noted by Gülhan & Braun (2010) and Hombsch & Olivier (2013) as well. In the case with the highest blowing ratio for either gas, i.e. Case 4 and Case 6, the coolant diffuses laterally and therefore the film is wider than the span of the injector (injector edge is at $z = 40$ mm). This effect could also be due to the detachment of the boundary layer over the injector at these high blowing ratios (Murray *et al.*, 2017) and the resulting kidney vortices at the span-wise edges of the injector (Haven & Kurosaka, 1997).

The span-wise averaged values of the concentration effectiveness are plotted versus the stream-wise direction, x, in Fig. 4.7 (solid lines). The average is taken between $z = 50$ mm and $z = 60$ mm (2.5 mm short of the centreline) assuming a two-dimensional film. As seen in Fig. 4.6, this assumption is valid all the way up to $x = 300$ mm. The blowing ratio is increased by a factor of 2 (approximately) between the cases for a particular gas (see Table 4.1). In addition to the absolute values of the concentration effectiveness, a clear discrepancy is noticeable in the

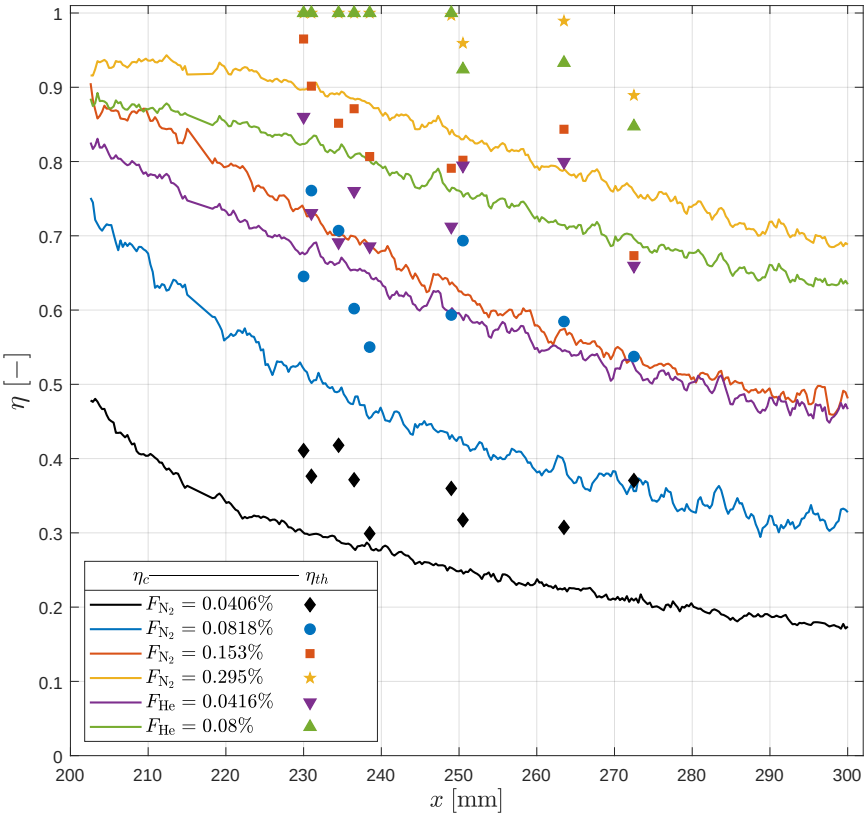

Figure 4.7: Span-wise averaged concentration effectiveness, η_c (solid line), and thermal effectiveness, η_{th} (marker), versus stream-wise direction, x.

shape of the η_c profile. Cases 1 and 2 exhibit a traditional, concave downward, monotonic fall with larger x values, whereas the curves in Cases 3 and 4 start as a plateau downstream of the injector at $x = 200$ mm, drop 10 mm to 20 mm downstream, and follow a concave downward trend after an inflection. The plateaus in Cases 3 and 4 are close to $\eta_c = 0.9$, i.e. almost a full coverage of the coolant gas exists immediately downstream of the injector for these relatively higher blowing ratios. The plateau itself indicates a discrete region, where the coolant gas and the boundary-layer gas are still separate. The curves follow a downward trend as the two gas layers start to mix with each other. In contrast, Cases 1 and 2 – the cases with the lowest blowing ratios – do not exhibit this discrete region and the start is at $\eta_c \approx 0.5$ and $\eta_c \approx 0.75$ downstream of the injector, which indicates that the mixing already started upstream on the injector. Essentially, with increasing blowing ratio, i.e. coolant mass flux, the film coverage improves on the injector as

well as downstream thereof (Cases 1 to 4). With enough coolant mass flux (Cases 3 and 4), a discrete layer is achieved. The coverage of this discrete layer is also dependant on the blowing ratio (Case 3 versus Case 4). As already shown in the contour plots in Fig. 4.6, the cases with Helium injection (Cases 5 and 6) feature a better film coverage than their Nitrogen counterparts (Cases 1 and 2), which is visible in Figs. 4.7 as well. The trend of the curves for Cases 5 and 6 are slightly dissimilar to those of Cases 1 and 2 due to the higher volume and the different form factor of the Helium film. The discrete region is not present in Cases 5 and 6; however, Case 6 features a slope immediately downstream of the injector that is close to a plateau. This trend indicates that a discrete region can be formed similar to the Nitrogen cases, i.e. Cases 3 and 4, with Helium too if the blowing ratio is higher. Overall, a remarkable film coverage above 15% can be achieved up to three injector-lengths (3×39.5 mm) downstream of the injector with these relatively low blowing ratios. For reference, a shot-to-shot repeatability of the concentration effectiveness is given in Appendix C (see Fig. C.1).

Fig. 4.7 also shows the thermal effectiveness, η_{th}, for all cases. For the cases with the highest blowing ratio for either gas, i.e. Case 4 and Case 6, the thermal effectiveness is above one at locations nearer to the injector. This is due to negative heat flux at those locations for these cases. The thermal effectiveness is the isothermal cooling effectiveness according to Eq.(4.7), and therefore a negative Stanton number with injection, i.e. $St_c < 0$, would lead to an effectiveness value of $\eta_{th} > 1$. Essentially, Eq.(4.7) is not valid at these particular locations and blowing ratios. This effect of over-cooling close to the injector can be observed in the work by Keller *et al.* (2015), Heufer & Olivier (2008*a*,*b*), and Hombsch & Olivier (2013) – all in supersonic or hypersonic flows. The experimentally obtained isothermal cooling effectiveness reported by Heufer & Olivier (2008*a*,*b*) and Hombsch & Olivier (2013) are higher than unity immediately downstream of the slot injector. Simulations performed by Keller *et al.* (2015) yielded an isothermal cooling effectiveness greater than 1.2 within one slot-length downstream of the slot injector when Helium was employed as the coolant gas. In this work, values

of η_{th} that are greater than one are assigned a value of unity (see Cases 4 and 6 in Fig. 4.7). The results for thermal effectiveness show that cooling is achieved for all cases and the blowing ratios used in the current tests did not promote a boundary-layer transition and thereby transpiration heating as reported by Tanno *et al.* (2016), where higher blowing ratios were used.

It can be further observed in Fig. 4.7 that the thermal effectiveness, η_{th}, is generally higher than the concentration effectiveness, η_c, and can be larger by up to 0.3. A noticeable scatter is present in the data for the thermal effectiveness; however, the trend of $\eta_{th} > \eta_c$ is consistent for the majority of the data points. This is expected since the flow is laminar and the mixing process is not expedited by turbulent mixing and the heat and mass transfer analogy does not apply. In absence of turbulent mixing, the coolant film is diffused into the boundary-layer gas, which is a slower process than turbulent mixing. Hence, a better thermal effectiveness is achieved.

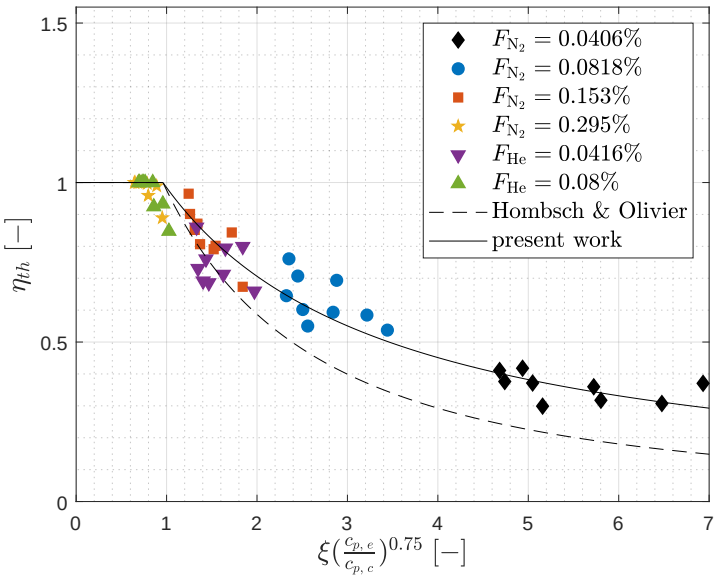

Figure 4.8: Thermal effectiveness, η_{th}, versus correlation factor, ξ, at $Re_u = 12.9 \times 10^6$ m^{-1}. Present work represents Eq.(4.10).

In Fig. 4.8, the thermal effectiveness, η_{th}, is plotted versus the correlation factor, ξ. A scaling factor of $(c_{p,e}/c_{p,c})^{0.75}$ is used to account for the Helium cases. For the current dataset, an exponent of 0.75 was more successful in collapsing the data than the exponent of 0.33 used by Keller *et al.* (2015). It can be seen that the data points

from Cases 5 and 6 that were assigned a value of 1 fall below $\xi(c_{p,e}/c_{p,c})^{0.75} = 0.96$, where the theoretical value is 1. This demonstrates again that Eq.(4.7) would not apply to these locations. For the remaining cases, a satisfactory collapse of the data is achieved. However, the trend deviates from the correlation by Hombsch & Olivier (2013), i.e. Eq.(4.9). This is not surprising as the blowing ratios and flow conditions in Hombsch & Olivier (2013) were different (higher blowing ratios, lower Mach numbers). A modified correlation for the data in this work is proposed as follows:

$$\eta_{th} = \begin{cases} 1 & \text{for } \xi \leq 0.96, \\ [1 + 0.4(\xi - 0.96)]^{-1} & \text{for } \xi > 0.96. \end{cases} \tag{4.10}$$

The current set of data further demonstrates the difficulty in achieving a general correlation for this mixing problem in laminar flows as opposed to turbulent flows. Since turbulent mixing does not occur in laminar flows, the mixing process is dominated by diffusion and shear-layer effects.

4.4 Conclusion

The mixing process between the coolant gas and the external flow downstream of film cooling holes or a transpiration cooling injector has been a subject of numerical and experimental investigation for more than fifty years. However, the majority of these studies are concerned with turbulent flows. Only few of the studies address laminar mixing. In particular, experimental data of downstream mixing in laminar, hypersonic flows have been reported by only a handful of authors. These studies, however, only investigated the heat flux reduction. Experimental data on the coolant's concentration at the wall are not available. In this study, transpiration cooling experiments were performed in a laminar, hypersonic flow in the Oxford High Density Tunnel (HDT) to measure the coolant's concentration distribution at the wall downstream of the injector along with the resulting heat flux reduction. A flat-plate model featuring a porous injector made of zirconium diboride was employed. The model was instrumented with thin-film arrays to measure the heat flux over the plate. A coat of Pressure-sensitive Paint (PSP) was placed downstream

of the injector to measure the concentration of the coolant gas at the wall and spatially resolve the film downstream of the injector. Six different cases were tested. Nitrogen and Helium were used as the coolant gas. The blowing ratio ranged from 0.0406% to 0.295%. The PSP results show an excellent film coverage for these low blowing ratios reaching up to 95% of coolant concentration immediately downstream of the injector. Even 100 mm downstream of the injector, the coolant concentration was found to be approximately 20% for the lowest blowing ratio of 0.0406% with Nitrogen injection and approximately 50% for the lowest blowing ratio of 0.0416% with Helium injection. For the highest blowing ratio for Nitrogen and Helium, i.e. 0.295% and 0.08% respectively, the coolant concentration was respectively 70% and 65%, approximately, 100 mm downstream of the injector. For the same blowing ratio, Helium forms a more formidable film compared to Nitrogen due to its seven times higher volumetric flow rate. For both gases, the film monotonically decays with downstream distance; however, in cases with relatively higher blowing ratios, the film concentration remains constant immediately downstream of the injector, indicating formation of a discrete layer of binary gas. The film eventually starts to decay monotonically farther downstream. In all six cases, a heat flux reduction is achieved downstream of the injector. The onset of transition was not triggered by injection and the boundary layer remained laminar in all cases. For the cases with the highest blowing ratio, both with Nitrogen and Helium, a negative heat flux was recorded immediately downstream of the injector. The effectiveness based on coolant concentration obtained from PSP and the thermal effectiveness acquired from the thin-film arrays are compared. It is shown that the latter is generally higher than the former. Finally, a collapse of the thermal effectiveness is achieved and a modified correlation is proposed. The results published here add to the insight of how downstream mixing occurs in a laminar, hypersonic boundary layer. Further, these results could aid the validation process of numerical tools that aim to model various phenomena involving laminar mixing in high-speed flows.

5

Numerical Simulation of Transpiration Cooling in a Laminar Hypersonic Boundary Layer

Preamble

In this chapter, a numerical simulation study of laminar transpiration cooling is performed using the Thermochemical Implicit Non-Equilibrium Algorithm (TINA) – a Navier-Stokes solver. The results are compared to experimental data reported in the preceding chapter. This chapter is composed of a journal paper published in the *Journal of Spacecraft and Rockets* (Ifti *et al.*, 2022*d*). The content and structure of this chapter represent 100% of the main body of the original paper.

Authors of the original paper: **Ifti, H.S.**, Hermann, T., McGilvray, M., & Merrified, J.

Author contribution:

Ifti, H.S.: Lead author in conceptualisation, data curation, formal analysis, and writing.

Hermann, T.: Supervision as postdoctoral assistant in the project.

McGilvray, M.: Supervision as principal investigator and funding acquisition.

Merrified, J.: Assistance in numerical setup.

Associated Appendices: N/A.

5.1 Introduction

Hypersonic vehicles, such as rockets or spaceplanes, are subject to extreme heat fluxes as a result of aerodynamic heating (van Driest, 1956). A thermal protection system (TPS) is therefore required to protect the vehicle from overheating. Transpiration cooling is a promising technology that could enable a re-usable TPS for hypersonic vehicles. It is an active cooling method where a coolant gas is injected through a porous material into the boundary layer. The cooling process comprises three different effects (see Fig. 5.1): (a) heat from the wall is convected out by the coolant fluid; (b) the coolant gas creates a film (blue) that insulates the wall underneath from the hot cross-flow; and (c) the coolant film protects the wall from free-stream Oxygen and thereby prevents oxidation of the wall, which enables the wall-material to operate at a higher temperature enhancing radiative cooling. The success of the latter two processes depends on the coolant film that is formed on and downstream of the injector. This protective film loses its concentration in the stream-wise direction and eventually diminishes at a downstream location as it mixes with the incoming hypersonic cross-flow (see the concentration gradient, $C(y)$ in Fig. 5.1).

There is a vast amount of work on the downstream mixing in turbulent boundary layers (Goldstein, 1971). However, only a handful of studies (Richards & Stollery, 1979; Heufer & Olivier, 2008*a*; Hombsch & Olivier, 2013; Keller *et al.*, 2015; Brune *et al.*, 2014) are concerned with the downstream mixing in a laminar boundary layer. This is a limitation since hypersonic vehicles could face peak heating in the laminar regime (Hermann *et al.*, 2019*b*). The existing studies that compare numerical results to experiments are concerned with the heat flux reduction only. However, the coolant's concentration itself becomes an important quantity to understand the mixing process between the coolant gas and the boundary-layer gas since a direct relation between heat and mass transfer coefficient cannot be assumed in laminar flows unlike in turbulent cases.

In this paper, numerical simulations of transpiration cooling in a laminar, hypersonic flow are performed. The coolant concentration and heat flux reduction results are compared to laminar transpiration cooling experiments conducted at

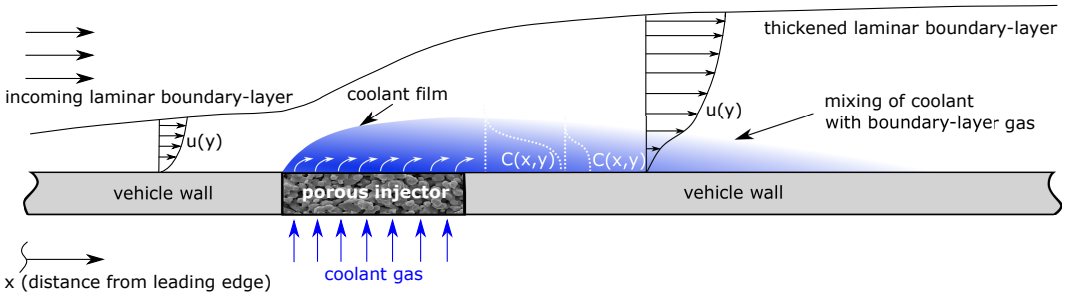

Figure 5.1: Schematic of a flat surface with a porous, transpiration cooling injector (not to scale).

Mach 7 in the Oxford High Density Tunnel (HDT), where Pressure-sensitive Paint (PSP) and thin-film gauges were respectively used to measure the wall concentration and heat flux reduction downstream of the injector on a flat plate (Ifti *et al.*, 2022*a*).

5.2 Methodology

5.2.1 Experiments

Transpiration cooling experiments in a laminar boundary layer employing a flat-plate model (see Fig. 5.2) were conducted in the Oxford High Density Tunnel (HDT) at Mach 7 (see Ifti *et al.*, 2022*a*, for details). The flat-plate model was at an angle of attack of AoA = 0°. A porous injector (39.5 mm × 39.5 mm) made of sintered zirconium diboride (ZrB_2) was situated 160 mm downstream of the leading edge. The boundary-layer static pressure, temperature and wall temperature were respectively p_e = 542.04 Pa, T_e = 43.53 K, and T_w = 293 K. The total pressure

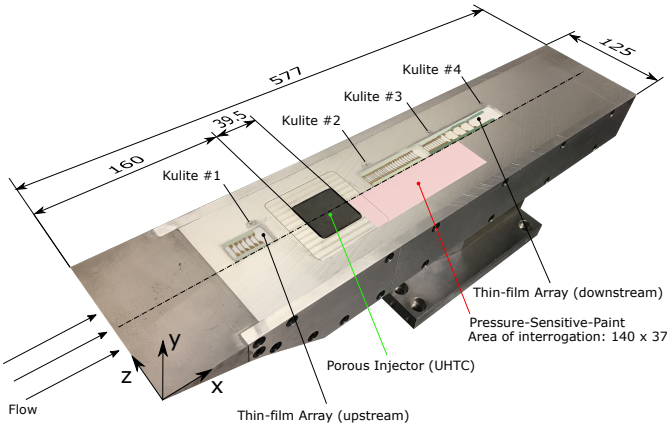

Figure 5.2: Flat-plate model with PSP coat downstream of the porous injector (Ifti *et al.*, 2022*a*).

and total temperature were $p_0 = 1.738$ MPa and $T_0 = 470.1$ K, respectively. The boundary-layer edge velocity was $u_e = 925.9$ ms^{-1}. The blowing ratios (Cases 1 to 6) are given in Table 5.1. For reference, the blowing ratio is defined as

$$F = \frac{\rho_c u_c}{\rho_e u_e} \tag{5.1}$$

and the blowing parameter as

$$B_h = \frac{F}{St_0}, \tag{5.2}$$

where ρ denotes the density and St_0 is the Stanton number at the injector location without blowing.

Pressure sensitive-paint (PSP) with an area of interrogation of 140 mm × 37 mm was applied immediately downstream of the injector to measure the relative concentration of the injected coolant gas at the wall. The PSP was excited by an LED of 390 nm (centre wavelength) and the emitted, higher wavelength radiation was captured by a camera fitted with a red filter (lower wavelength cut-off: 550 nm). This excitation is quenched by Oxygen in the air, and therefore the illumination can be calibrated by collecting illumination data for different flow static pressures (measured by surface mounted Kulite pressure transducers) without coolant injection. By applying the same calibration to cases with coolant (foreign gas) injection, a trace of the film can be identified as the quenching is influenced by the film. Injected coolant gas (Nitrogen or Helium) hinders the quenching by displacing air in the boundary layer. Comparing a case with air injection and one with a foreign gas injection at the same blowing ratio, gives a measure of how much air is displaced by the foreign gas, i.e. to what extent the coolant is forming a film. The concentration film effectiveness is defined as

$$\eta_c = 1 - \frac{p_{O_2,\,\text{foreign gas}}}{p_{O_2,\,\text{air}}}, \tag{5.3}$$

where $p_{O_2,\,\text{air}}$ and $p_{O_2,\,\text{foreign gas}}$ are Oxygen partial pressures with air and foreign gas injections, respectively, at the same blowing ratio. A span-wise average of 10 mm

close to the centreline – where the film is two dimensional – is taken to reduce the data for η_c to one dimension, which varies only in the stream-wise direction, x.

Thin-film gauges installed upstream and downstream of the injector measured the heat fluxes, which were compared to Eckert's correlation (Eckert, 1956) for laminar boundary layers to ensure that the boundary layer was laminar during the experiments. The heat flux reduction by transpiration cooling is formulated as the isothermal cooling effectiveness

$$\eta_{th} = 1 - \frac{St_c}{St_0}, \tag{5.4}$$

where St is the Stanton number and the subscripts 'c' and '0' respectively denote cooled and uncooled cases. A case of 100% cooling, i.e. zero heat flux to the wall, would result in an effectiveness of 1. Eq.(5.4) is only valid for small blowing ratios and cases where the coolant gas is similar to the free-stream gas (Heufer & Olivier, 2008*a*). It is also invalid for locations that are in close proximity to the injector. The obtained values of η_{th} can be correlated by a factor defined by Heufer & Olivier (2008*a*) as

$$\xi = \frac{1}{Fs}\sqrt{\frac{x - x_s}{x_s^{1.16}}\frac{C^* x}{Re_u}}, \tag{5.5}$$

where x_s is the slot location from the leading edge, s is the slot length, and $C^* = (\rho^*\mu^*)^{0.5}(\rho_e\mu_e)^{-0.5}$ is the Chapman-Rubesin factor evaluated at Eckert's reference temperature (Eckert, 1956). Re_u is the unit Reynolds number and μ the viscosity. The effect of different coolant gases can be taken into account by multiplying the correlation factor, ξ, by the ratio of the specific heat capacities of the free-stream gas and the coolant gas, $c_{p,e}/c_{p,c}$, with an appropriate exponent, which has been demonstrated by Keller *et al.* (2015). Hombsch & Olivier (2013) proposed a correlation obtained from experimental data expressed as

$$\eta_{th} = \begin{cases} 1 & \text{for } \xi \leq 0.96, \\ [1 + 0.38(\xi - 0.96)]^{-1.6} & \text{for } \xi > 0.96. \end{cases} \tag{5.6}$$

A modified correlation was proposed in Ifti *et al.* (2022*a*) given as

$$\eta_{th} = \begin{cases} 1 & \text{for } \xi \leq 0.96, \\ [1 + 0.4(\xi - 0.96)]^{-1} & \text{for } \xi > 0.96. \end{cases} \tag{5.7}$$

Case	1	2	3	4	5	6
F [%]	0.0406	0.0818	0.153	0.295	0.0416	0.08
B_h [−]	1.49	2.99	5.59	10.8	1.52	2.93
Coolant gas	N_2	N_2	N_2	N_2	He	He

Table 5.1: Overview of blowing cases.

5.2.2 Numerical Approach

Two-dimensional simulations were performed employing the Thermochemical Implicit Non-Equilibrium Algorithm (TINA) – a Navier-Stokes solver developed by Fluid Gravity Engineering Ltd. for supersonic and hypersonic flows. TINA is a point or line implicit time marching solver with spatial gradient calculated to second-order accuracy. It employs an approximate Riemann solver in conjunction with flux limiters for the inviscid fluxes. A Total Variation-Diminishing (TVD) shock capturing algorithm is used which ensures non-oscillatory behaviour near shock waves at essentially any free stream Mach number. Air was used as the main flow, which was simulated as a perfect gas matching the flow conditions in the experiments stated in Section 5.2.1. Futher details can be found in Netterfield (1991, 1992).

A flow over the flat-plate geometry described above was simulated. A computational domain of 340 mm × 58 mm was employed with a total of 50511 grid points. The grid is equidistant in the stream-wise direction ($\Delta x = 1 \times 10^3$ m) and stretched in the wall-normal direction with a first cell height of $\Delta y = 2.5 \times 10^{-6}$ m (elected based on a grid convergence study). This yielded a wall cell Reynolds number of $Re_{\text{cell}} < 1$, which ensures that the high gradients close to the wall are sufficiently resolved.

At the wall, the nodes between 160 mm and 200 mm were set to a permeable boundary condition, which prescribes the mass flux of the injected coolant gas. Simulations were run for all cases presented in Table 5.1.

The wall condition was set as isothermal at $T_w = 293$ K. The variation of species viscosity with temperature for Oxygen, Nitrogen, and Helium was modelled using Blottner curve fits (Blottner *et al.*, 1971). Species thermal conductivity is derived from species viscosity using the formula of Eucken (1913). The mixture

viscosity and thermal conductivity are calculated using the mixing rule of Wilke (2004). The diffusion velocity of each species is assumed to be proportional to the gradient in the species mole fraction only with species diffusion coefficient taken from the work of Lee (1984). Here, a baseline diffusion coefficient, D, is first derived from the mixture viscosity using a constant Schmidt number of $Sc = 0.5$. The mole fraction based species diffusion coefficient is then defined as

$$D_i = \frac{\frac{M_i}{M}(1 - W_i)D}{1 - X_i}, \tag{5.8}$$

where the molecular weight of the species is given as

$$M = \left[\sum_{j=1}^{N_s} \frac{W_j}{M_j}\right]^{-1}. \tag{5.9}$$

Here, W and X respectively stand for the mass and mole fractions of the species; the indices i and j denote a species within a total of N_s species. Zero net mass diffusion is then ensured using the Ramshaw correction (Ramshaw, 1990). The mixing rule used in this transport model provides more reliable results when used with species of similar molecular weights. As such, it is expected to provide more accurate results for simulations with Nitrogen coolant when compared with those with Helium coolant. The physical models in TINA were not modified to match the experimental data for this work.

The mole fraction of the coolant gas (Nitrogen or Helium), X_c, in the flow field was extracted from the simulation results. A non-dimensional coolant concentration is defined as follows:

$$C(x, y) = \frac{X_c(x, y) - X_{c,e}}{1 - X_{c,e}}. \tag{5.10}$$

A concentration of $C = 1$ would be possible at locations where the coolant gas's mole fraction is exactly at unity, i.e. $X_c = 1$.

In order to remain consistent with the experimental concentration effectiveness, simulations with air at corresponding blowing ratios were performed and the concentration effectiveness was calculated as

$$\eta_c = 1 - \frac{X_{\text{coolant gas},w} p_{O_2,\text{ coolant gas},w}}{X_{\text{air},w} p_{O_2,\text{ air},w}}. \tag{5.11}$$

5.3 Results and Discussion

5.3.1 Coolant Concentration Distribution and Concentration Effectiveness

The coolant concentration profiles for all cases are plotted in Fig. 5.3. The wall-normal axis is normalised by the corresponding boundary-layer thickness, $\delta = y(0.99u_e)$, for each case (δ values are shown in Fig. 5.4). On the injector at $x = 165$ mm, $x = 180$ mm, $x = 198$ mm, $x = 200$ mm (blue), the concentration curves monotonically increase towards the wall. All cases apart form Case 4 feature a negative concentration gradient at the wall, i.e. $\left.\frac{\partial C}{\partial y}\right|_w < 0$. The concentration at the wall, C_w, is not at unity for these cases. The value of C_w at the injector increases with rising blowing ratio. In Case 4 (Fig. 5.3d), the concentration at the wall reaches $C_w = 1$ and the wall concentration gradient approaches $\left.\frac{\partial C}{\partial y}\right|_w = 0$ since the higher blowing ratio forms a discrete layer of coolant gas.

Downstream of the injector (red), the concentration curves remain monotonic but have a zero concentration gradient at the wall, i.e. $\left.\frac{\partial C}{\partial y}\right|_w = 0$, due to the impermeable wall. At larger values of x, the concentration drops in all cases (red) as the coolant mixes through diffusion with the external boundary-layer gas. The curves become shallower with rising x and the peak of the curves – the wall concentration, C_w – decreases. At the end of the injector ($x = 200$ mm), C_w is lower than the value of C_w at $x = 198$ mm for the lower blowing ratio cases. i.e. Cases 1, 2, and 5, due to the mixing with the external gas. The concentration gradient at the wall also becomes shallower at $x = 200$ mm compared to $x = 198$ mm as the permeable boundary condition changes to an impermeable one.

The difference between Nitrogen and Helium injection at the same blowing ratio can be observed by comparing Figs. 5.3a and 5.3b to Figs. 5.3e and 5.3f, respectively. For a given F, Helium injection results in a higher coolant coverage both at the injector and downstream thereof. This difference is due to Helium's seven times higher volumetric flow rate than Nitrogen's at the same mass flux, and it is consistent with the experimental finding reported in Ifti *et al.* (2022*a*) and Langener *et al.* (2011).

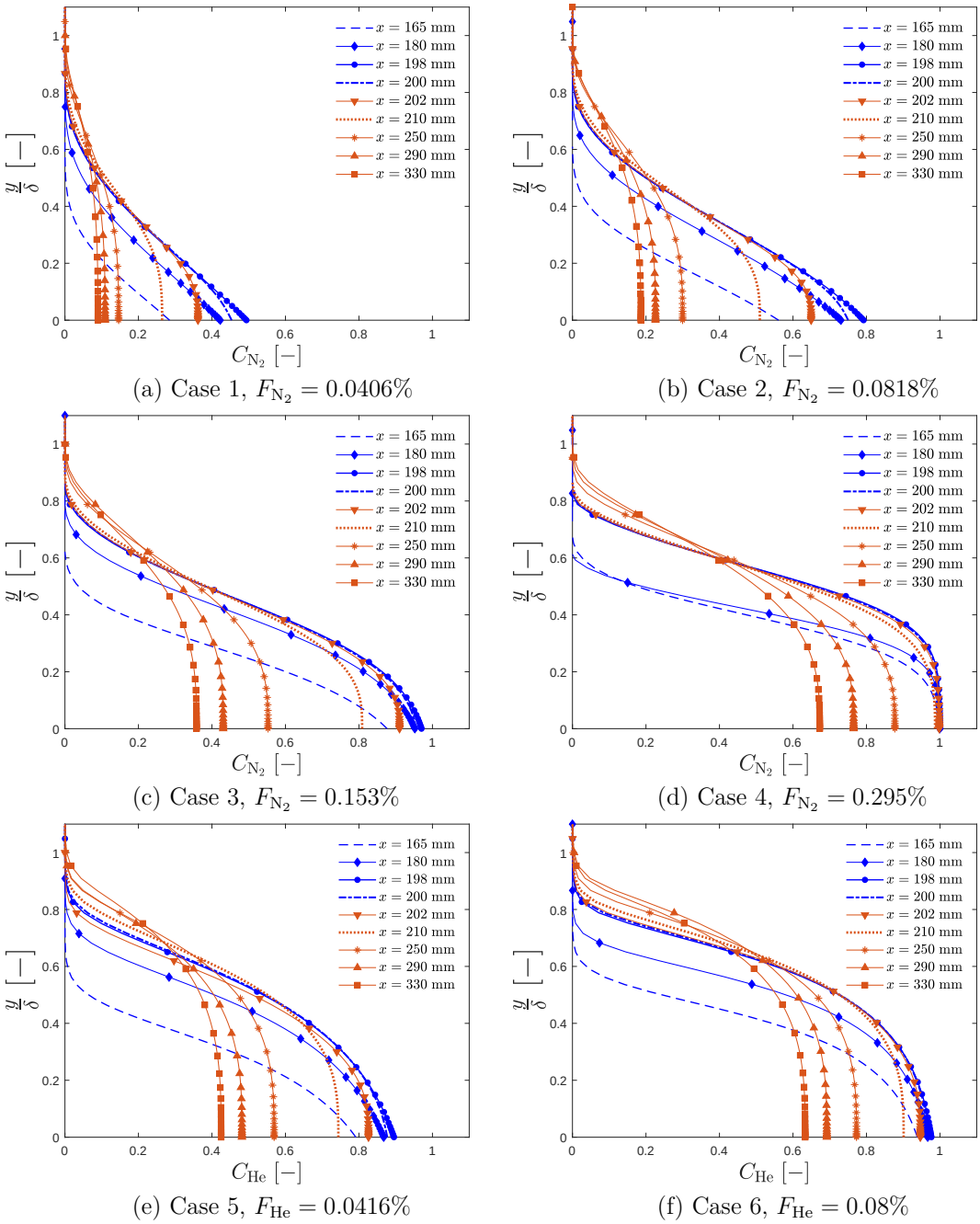

(a) Case 1, $F_{N_2} = 0.0406\%$

(b) Case 2, $F_{N_2} = 0.0818\%$

(c) Case 3, $F_{N_2} = 0.153\%$

(d) Case 4, $F_{N_2} = 0.295\%$

(e) Case 5, $F_{He} = 0.0416\%$

(f) Case 6, $F_{He} = 0.08\%$

Figure 5.3: Coolant concentration profiles from numerical simulation (TINA).

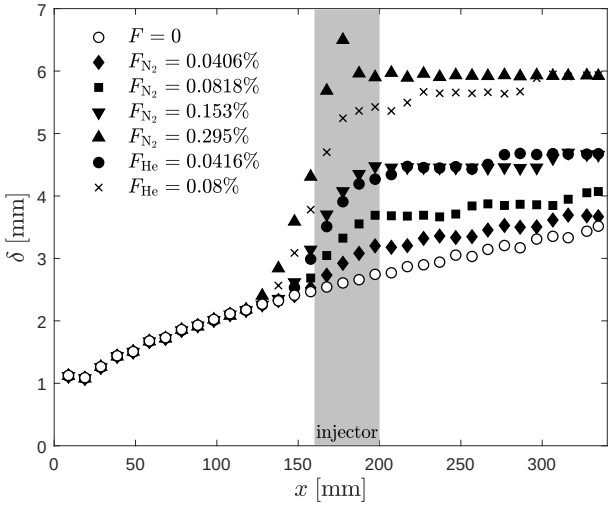

Figure 5.4: Boundary-layer thickness, δ, versus stream-wise direction, x.

In Fig. 5.5, the concentration effectiveness, η_c, obtained from both simulations and experiments, is illustrated as a function of the stream-wise direction, x, for all cases. At the higher blowing ratio cases for each gas, i.e. Cases 3, 4, and 6, the simulation results match the experimental results within $\Delta\eta_c = \pm 0.1$. For the lower blowing ratio cases, the results differ by up to $\Delta\eta_c = \pm 0.2$. The reason for this large deviation can be attributed to the initial value of η_c immediately downstream of the injector ($x = 200$ mm). This observation indicated that the mixing process on the injector is not fully captured with the current simulation at the lower blowing ratios. The mixing on the injector is a function of the type of porous material used. It is not only dependent on the pore size and structure, but could also be influenced by the physical and aerodynamic roughness of the porous injector, especially at lower blowing ratios where only a thin layer of coolant gas is formed. As F is increased, the mixing on the injector is captured more successfully, which is evident from the initial concentration effectiveness in Fig. 5.5. In all cases, however, a remarkable match between the simulation results and experimental results is seen for the slope of the η_c curves, which demonstrates that the mixing rate as a function of x downstream of the injector is fully captured by the current simulations.

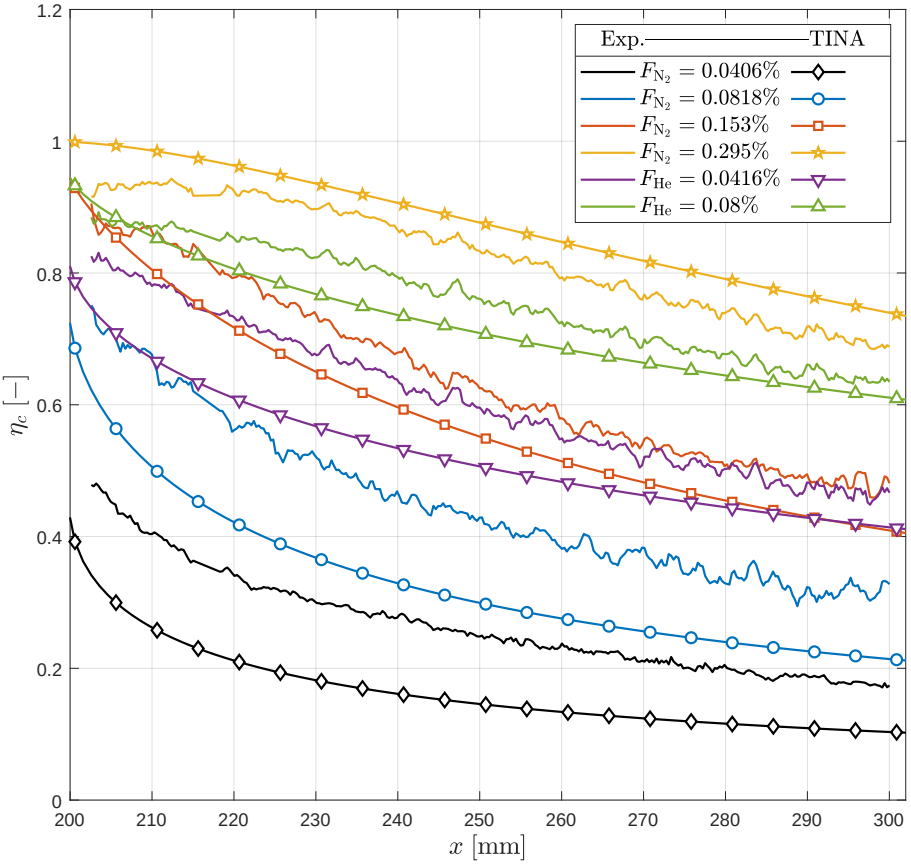

Figure 5.5: Concentration effectiveness, η_c, versus stream-wise direction, x.

5.3.2 Thermal Effectiveness

The thermal effectiveness, η_{th}, is plotted versus the correlation factor (Eq. (5.5)), ξ, in Fig. 5.6. The values of η_{th} at $\xi < 1$ are set to unity if they are great than 1 (see Section 5.3.3 for explanation). A successful collapse of the simulation data is achieved for cases with Nitrogen injection. Similar to the observation made by Keller *et al.* (2015), a perfect collapse of the data was not possible for the Helium cases. However, an exponent of 0.75 (Ifti *et al.*, 2022*a*) yielded a better collapse than 0.33 (Keller *et al.*, 2015).

For the Nitrogen cases, it can be observed that the simulation results for the higher blowing cases, i.e. Case 3 and Case 4, are close to the experimental data and the correlation proposed in Ifti *et al.* (2022*a*). Curves for the smaller blowing ratio cases, on the other hand, are lower than the experimental data and the correlation

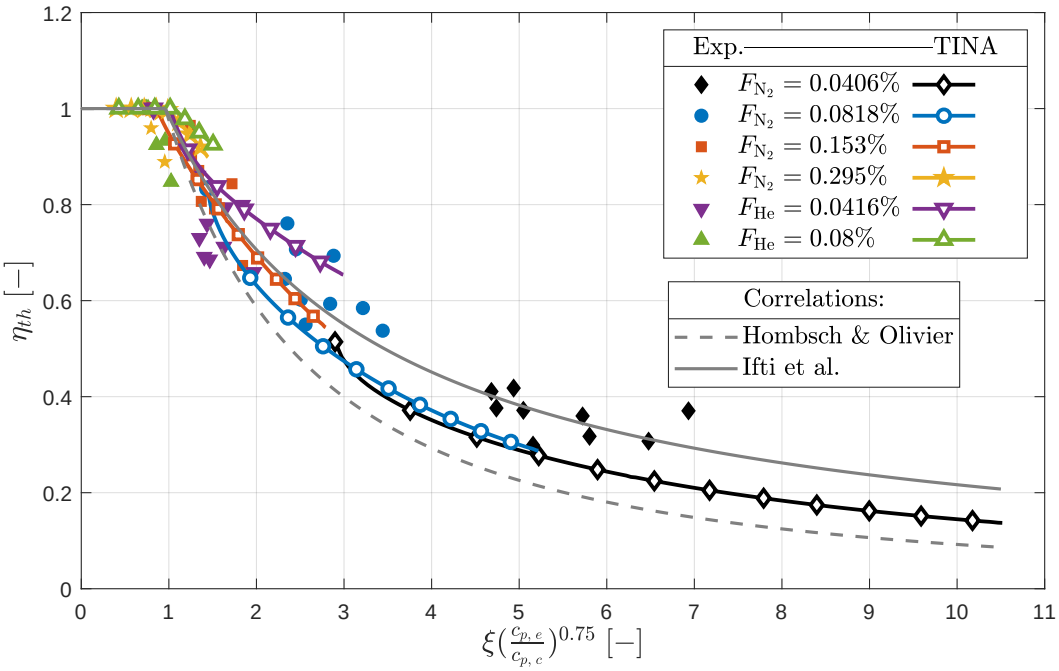

Figure 5.6: Thermal effectiveness, η_{th}, versus correlation factor, ξ. Correlations from Hombsch & Olivier (2013) and Ifti *et al.* (2022*a*).

curve (Ifti et al.), i.e. cooling is under-predicted by TINA. This is not surprising because the concentration effectiveness obtained from simulated data for these cases (Case 1 and Case 2) is lower than those measured in the experiments as shown in Fig. 5.5 and discussed in the previous section. Overall, the thermal effectiveness, η_{th}, yielded by the current simulations is within $\Delta\eta_{th} = \pm 0.1$ of the correlations for laminar flows (Hombsch & Olivier and Ifti et al.).

5.3.3 Boundary-Layer Profiles

As mentioned in Section 5.3.2, the thermal effectiveness can be $\eta_{th} > 1$ at $\xi < 1$. This is because Eq.(5.4) is only valid for low blowing ratios and farther downstream of the injector. At higher blowing ratios and in close proximity to the injector, ξ is below 1. Theoretically, η_{th} in this region is defined as 1, but the actual value can be greater than unity due to a different flow field close to the injector at high blowing ratios. In order to gain an insight into what happens in this region, boundary-layer profiles are examined in this Section.

The normalised stream-wise velocity profiles, u/u_e, and temperature profiles,

T/T_e, obtained from the simulations are illustrated in Fig. 5.7 and Fig. 5.8, respectively, for all blowing cases. The wall-normal axis is normalised by the boundary-layer thickness, δ. A close-up view of the wall-near region is placed as an inset in every sub-figure. Profiles are picked at $x = 100$ mm (upstream of the injector, black), $x = 180$ mm (middle of the injector, blue), $x = 200$ mm (end of the injector, blue), $x = 210$ mm (10 mm downstream of the injector, red), and $x = 330$ mm (130 mm downstream of the injector, red).

In Fig. 5.7, it can be seen that the velocity profile (black) represents a Blasius profile (Blasius, 1908) for laminar boundary layers at zero pressure gradient upstream of the injector. On the injector, the profiles (blue) inflect due to the low stream-wise velocity from blowing (injected coolant gas only has a wall-normal velocity at the wall). As expected, the higher blowing ratio cases cause a stronger inflection. However, no separation of the boundary layer is observed for the simulated cases.

In the Nitrogen cases (Fig. 5.7a-d), the velocity profiles downstream of the injector become fuller as the coolant gas is accelerated in the stream-wise direction by shear stress from the external boundary-layer flow. At larger x values, the profiles approaches the Blasius profile (trend seen in profiles at $x = 210$ mm and $x = 330$ mm). In contrast, the velocity profiles immediately downstream of the injector become fuller than the Blasius profile in the Helium cases (see profile at $x = 210$ mm in Figs. 5.7e and 5.7f). This is due to the difference in density between Helium and Nitrogen. This behaviour is also visible for profiles at the end of the injector, i.e. at $x = 200$ mm.

The temperature profiles upstream of the injector (black) exhibit a typical non-monotonic trend with a positive gradient at the wall, i.e. $\left.\frac{\partial T}{\partial y}\right|_w > 0$, resulting in heating of the wall. This non-monotonic trend is present on the injector (blue) for Cases 1, 2, and 5. At higher blowing ratios, however, the trend changes as the gradient at the wall approaches $\left.\frac{\partial T}{\partial y}\right|_w = 0$ (see inset, Fig. 5.8c, 5.8d, and 5.8f). As the coolant is injected at the wall temperature, T_w, the injection builds up a layer of gas at wall temperature.

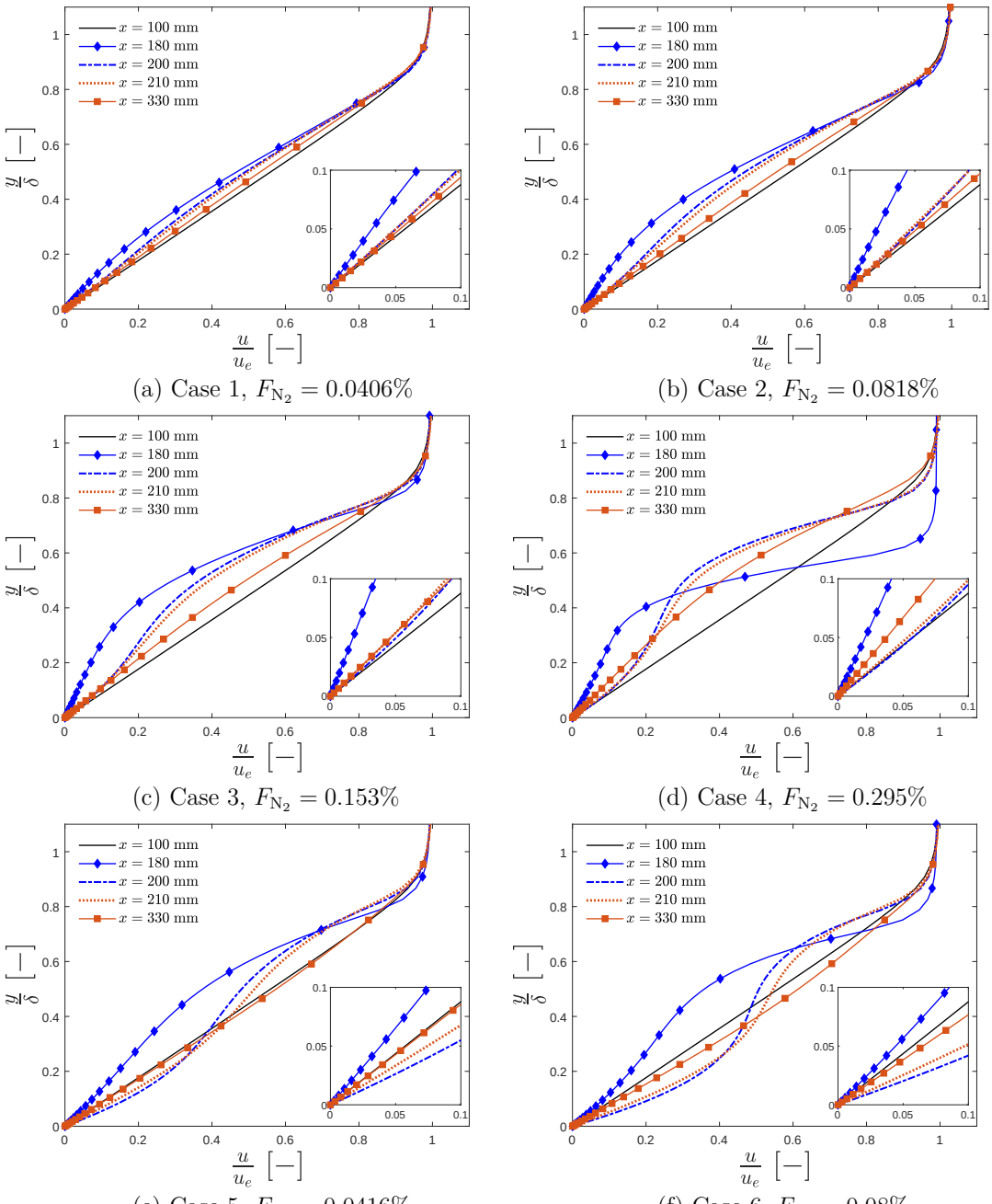

(a) Case 1, $F_{N_2} = 0.0406\%$

(b) Case 2, $F_{N_2} = 0.0818\%$

(c) Case 3, $F_{N_2} = 0.153\%$

(d) Case 4, $F_{N_2} = 0.295\%$

(e) Case 5, $F_{He} = 0.0416\%$

(f) Case 6, $F_{He} = 0.08\%$

Figure 5.7: Normalised stream-wise velocity profiles from numerical simulations (TINA).

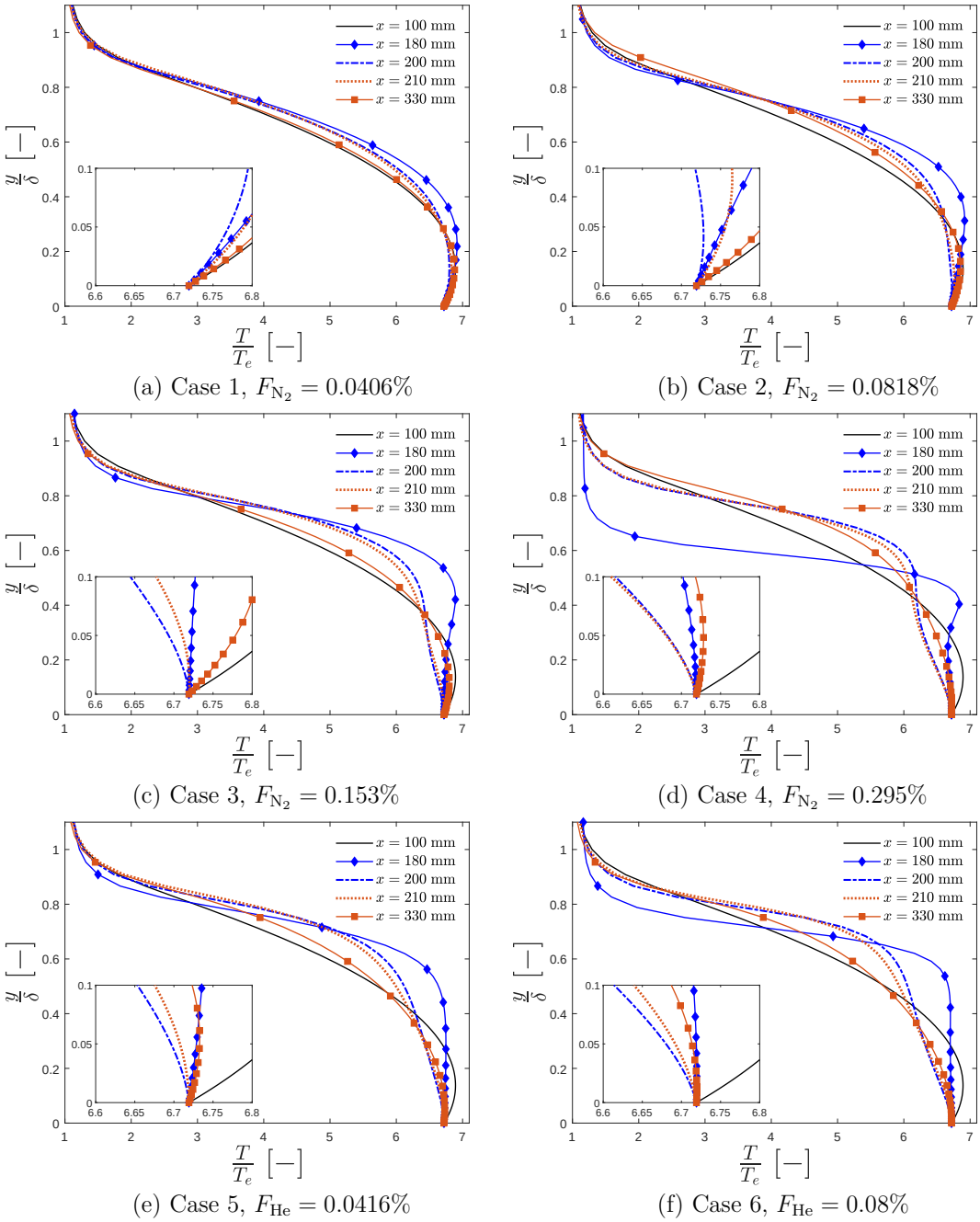

(a) Case 1, $F_{N_2} = 0.0406\%$

(b) Case 2, $F_{N_2} = 0.0818\%$

(c) Case 3, $F_{N_2} = 0.153\%$

(d) Case 4, $F_{N_2} = 0.295\%$

(e) Case 5, $F_{He} = 0.0416\%$

(f) Case 6, $F_{He} = 0.08\%$

Figure 5.8: Normalised temperature profiles from numerical simulations (TINA).

At $x = 200$ mm (end of the injector) and $x = 210$ mm (10 mm downstream of the injector), the profiles drop below the wall temperature in Cases 3 to 6 (see inset, Fig. 5.8c-f). In Cases 4 (Fig. 5.8d) and 6 (Fig. 5.8f), the temperature drops so much so that the gradient at the wall becomes negative, i.e. $\left.\frac{\partial T}{\partial y}\right|_w < 0$, resulting in a negative heat flux. This phenomenon is captured in heat flux data obtained from the current simulations as well as the experiments as presented in Fig. 5.9. This phenomenon is also present close to the injector in the work by Keller *et al.* (2015), Heufer & Olivier (2008*b*,*a*), and Hombsch & Olivier (2013), where the coolant temperature was close to the wall temperature. These authors reported a thermal effectiveness greater than 1, i.e. $\eta_{th} > 1$ very close to the injector and at $\xi < 1$, which indicates a negative heat flux occurred at those locations. ξ reduces for higher F values and lower x values, and therefore the phenomenon of negative heat flux appears close to the injector at higher blowing ratios as seen in Case 4 and Case 6. This phenomenon is discussed in the following paragraph.

When the coolant is injected at a higher blowing ratio, it forms an almost complete layer of coolant gas on the porous injector, and immediately downstream of it. This gas is initially close to zero stream-wise velocity when it is injected (see Figs. 5.7d and 5.7f). The temperature of the injected gas is approximately the wall temperature T_w (see Figs. 5.8d and 5.8f). On the porous injector and immediately downstream of it, this creates a boundary-layer profile of almost stagnant gas at wall temperature, i.e. a constant profile of T_w from the wall to the coolant layer height.

Upon getting into contact with the external cross flow the coolant gas layer is accelerated due to the shear stress of the external flow (see profile at $x = 210$ mm in Figs. 5.7d and 5.7f). This leads to the coolant gas establishing a velocity profile which leads to dissipation of thermal energy (the term $\mu(\partial u/\partial y)^2$ in energy equation). Classically this effect is expressed as a recovery factor $T_r = rT_0$, i.e. the driving temperature of the heat transfer is lower than the total temperature T_0. In this case, the total temperature of the coolant layer is close to the the wall temperature, as the injected gas started at near zero stream-wise velocity at T_w. Therefore, the driving temperature of the wall heat transfer can only be lower than

the wall temperature (as shown in Figs. 5.8d and 5.8f) and a negative heat flux is experienced. This effect only applies if the film is almost entirely comprised of coolant gas, i.e. η_c of close to 1. Fig. 5.9 shows that only cases with high η_c promote a Stanton numbers below zero (Cases 4 and 6). In cases where η_c is significantly below 1, hot external gas has already mixed with the coolant layer which drives the effective recovery temperature up and therefore increases heat transfer. In Fig. 5.10, the temperature profiles at $x = 210$ mm and $x = 330$ mm for all cases are plotted. It can be observed that close to the injector (see Fig. 5.10a), the temperature gradient change from positive to negative as the blowing ratio is increased. The temperature gradient becomes negative for Cases 4 and 6, which results in a negative heat flux (see Fig. 5.9). Farther downstream (see Fig. 5.10b), no negative temperature gradient exists regardless of the blowing ratio.

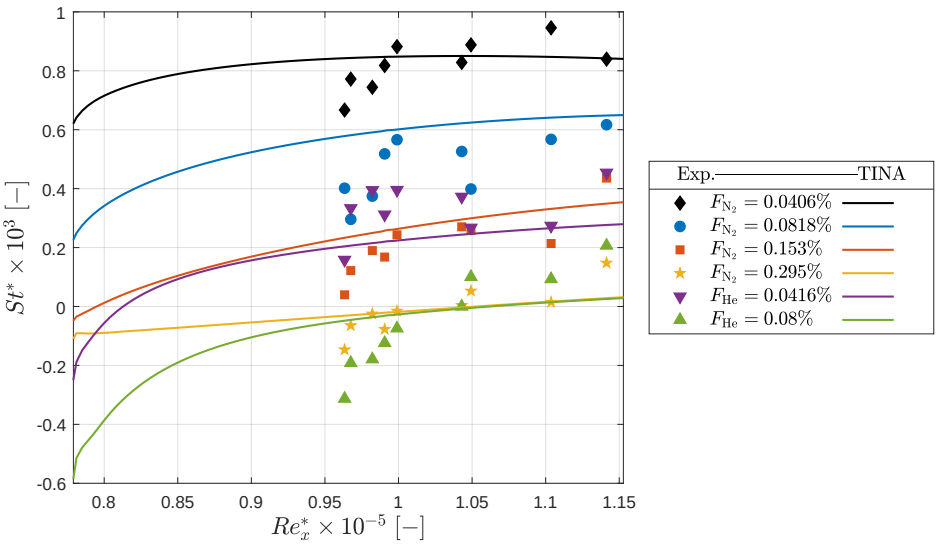

Figure 5.9: Stanton number, St^*, versus Reynolds number based on stream-wise direction starting from the leading edge, Re_x^*. The plot shows values starting from immediately downstream of the injector. St^* and Re_x^* are evaluated at Eckert's reference temperature (Eckert, 1956).

This effect is stronger for Helium because it is a lighter gas. It is accelerated more than the heavier Nitrogen and an established velocity profile is reached earlier downstream of the injector (Fig. 5.7f, $x = 210$ mm). This leads to a higher shear stress in the boundary layer, which promotes larger energy dissipation. Therefore, the driving temperature in the Helium cases is lower and the negative heat flux

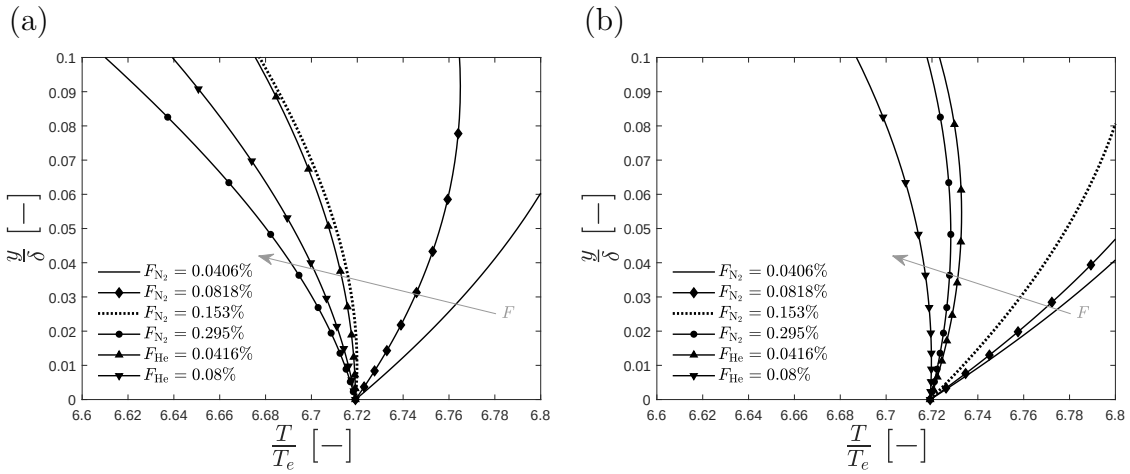

Figure 5.10: Normalised temperature profiles at (a) $x = 210$ mm and (b) $x = 330$ mm for all cases (TINA).

is more pronounced (Fig. 5.9). This trend is even stronger at the end of the injector, i.e. at $x = 200$ mm.

Counteracting effects are mixing, i.e. diffusive mass transfer of hot gas into the coolant layer for laminar flows, and heat conduction from the outside flow. These two effects thus diminish the negative heat flux by effectively increasing the driving temperature of the surface heat transfer. For high η_c, the dissipative effect dominates, whilst mixing and heat conduction dominate for cases with low η_c (visible in Fig. 5.9).

5.4 Conclusion

In this work, two-dimensional simulations of transpiration cooling in a laminar, hypersonic boundary layer were performed employing the Thermochemical Implicit Non-Equilibrium Algorithm (TINA) – a Navier-Stokes solver developed by Fluid Gravity Engineering Ltd. Coolant concentration and heat flux results are compared to data obtained from laminar transpiration cooling experiments conducted in the Oxford High Density Tunnel (HDT) employing a flat-plate geometry at Mach 7. Simulations for six different blowing ratios are performed using Nitrogen and Helium as the coolant gas. The concentration effectiveness matches the experimental data within ± 0.1 for higher blowing ratios and ± 0.2 for lower blowing ratios. The

simulation results successfully predict the mixing rate at the wall as a function of the stream-wise direction for all blowing ratios. This shows that the simulations are not as successful in predicting the mixing on the injector at low blowing ratios as they are downstream of the injector. The simulations further demonstrate that the mixing process at the wall can be predicted by an advection-diffusion model. A collapse of thermal effectiveness calculated from simulation data is achieved using a laminar film cooling correlation factor, which lies within ± 0.1 of the correlations for laminar flows in the literature. Wall-normal profiles of coolant concentration, stream-wise velocity, and temperature are examined upstream, at the middle, and downstream of the injector. It is shown that, when the concentration effectiveness is close to 1 at the injector, the temperature gradient becomes negative at locations immediately downstream of the injector, resulting in a negative heat flux. This phenomenon of negative heat flux is captured both in the experiments and the current simulations. It is evident from the velocity profiles that the coolant is accelerated in the stream-wise direction downstream, which promotes dissipation of energy. This results in a reduction in the temperature of the coolant that is injected at the wall temperature and thereby induces a negative temperature gradient that leads to negative heat flux in close proximity to the injector.

6

Analytical Model of Transpired-Coolant Concentration at Downstream Wall in High-Speed Laminar Flow

Preamble

In Chapters 4 and 5, it was concluded that the downstream mixing at the wall can be modelled by advection-diffusion in laminar flows where turbulent mixing is absent. As the keystone contribution towards the research aim of this thesis, an analytical model based on one-dimensional diffusion is developed in this chapter. The model is subsequently validated against the experimental data presented in Chapter 4. This chapter is composed of a journal paper published in the *AIAA Journal* (Ifti *et al.*, 2022*b*). The content and structure of this chapter represent 100% of the main body of the originally submitted paper.

Authors of the original paper: **Ifti, H.S.**, Hermann, T., & McGilvray, M.

Author contribution:

Ifti, H.S.: Lead author, conceptualisation, analytical model development, formal analysis, and writing.

Hermann, T.: Supervision as postdoctoral assistant in the project.

McGilvray, M.: Supervision as principal investigator and funding acquisition.

Associated Appendices: N/A.

6.1 Introduction

High-speed vehicles are prone to high heat fluxes due to aerodynamic heating (van Driest, 1956). Passive, semi-passive, and active cooling methods are available options to mitigate this heating. Amongst the active cooling methods, transpiration cooling is a promising technology that could enhance the re-usability of vehicle parts that are subject to high peak heating such as leading edges or control-fin joints. It is a dual-mode protection system that would protect the vehicle parts from both heat and oxidation. This cooling process consists of three different subprocesses (see Fig. 6.1): (a) heat from the wall is convected out by the coolant gas; (b) the coolant gas creates a film (blue) that insulates the wall underneath from the hot cross-flow; and (c) the coolant film protects the wall from free-stream Oxygen and thereby prevents oxidation of the wall, which enables the wall material to operate at a higher temperature enhancing radiative cooling and reduces recombination heating. The success of the latter two processes depends on the coolant film that is formed on and downstream of the injector. The concentration of this protective film reduces in the stream-wise direction and eventually the film diminishes at a downstream location as it mixes with the incoming cross-flow (see the concentration gradient, $C(x, y)$ in Fig. 6.1).

The majority of the studies available in the literature are concerned with a common goal of understanding – and in some cases predicting – the mixing between the coolant gas and the external cross-flow, both on and downstream of the injector. The downstream mixing is of particular interest because the coolant gas injected through the injector can be further utilised to cool the downstream parts and protect them from oxidation. This reduces the required mass of coolant that needs to be carried in the vehicle. In addition, it can be used to cool parts that cannot be made porous due to their complexity or the high stresses they endure (e.g. a fin hinge). Furthermore, this technique can be employed to cool or protect optical windows on hypersonic vehicles by placing the injector upstream of the window (Tropf *et al.*, 1987; Giles, 1988).

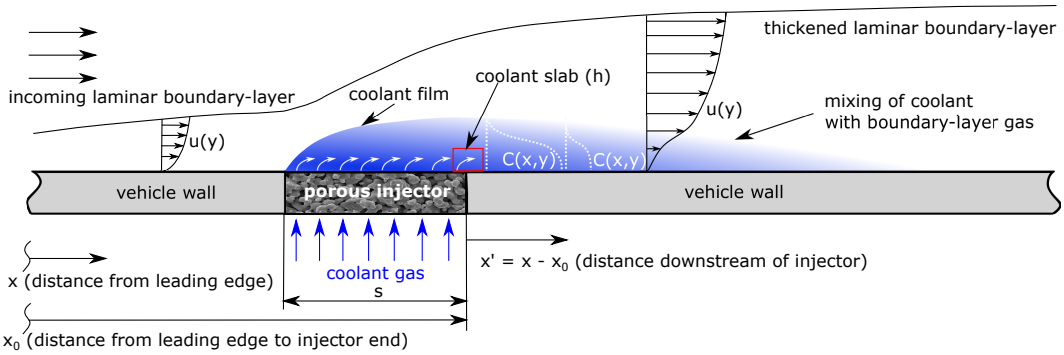

Figure 6.1: Schematic of a flat surface with a porous, transpiration cooling injector (not to scale).

A vast amount of work on downstream mixing spanning more than 50 years is available in the literature (Goldstein, 1971). These studies range from mixing at the wall to the aerodynamic effects (Fitt *et al.*, 1985; Yavuzkurt *et al.*, 1980*a*,*b*). However, most studies are concerned with turbulent flows only, mostly for film cooling applications in turbine blades and rocket nozzle walls. A high-speed vehicle, particularly a hypersonic vehicle, may fly through all three flow regimes, i.e. laminar, transitional, and turbulent, and therefore cooling in each flow regime could become important for such a vehicle. Furthermore, a hypersonic vehicle could experience its highest peak heating in the laminar regime (Hermann *et al.*, 2019*b*). In spite of this need, only a handful of studies on film cooling or transpiration cooling in a laminar boundary layer are available in the literature.

One of the first experimental studies was conducted by Richards & Stollery (1979), where tangential injection was employed in a hypersonic boundary layer to cool a flat plate at Mach 10. The authors proposed a discrete-layer theory based on heat conduction. Heufer & Olivier (2008*a*) proposed a correlation factor based on the energy equation similar to Goldstein (1971) but with a laminar velocity profile. The authors validated the correlation numerically and experimentally using a slot injector on a flat plate in laminar, supersonic flows. Different slot geometries and coolant gases were used in the experiments by Hombsch & Olivier (2013) in supersonic flows, where the authors demonstrated that film cooling was much more effective in laminar flows than turbulent ones, and a correlation was proposed.

However, these studies focus on heat flux reduction only, not the concentration of the coolant gas at the wall.

In a recent study, Ifti *et al.* (2022*a*) proposed a new correlation for laminar mixing based on experimental heat flux data obtained at flow conditions and coolant mass injection rates different from those in the study by Hombsch & Olivier (2013). The authors demonstrated that a universal correlation for laminar mixing – independent of flow conditions, the coolant gas, and injection rates – was not possible in the traditional approach used in film cooling theory due to the fundamental difference in the mixing mechanism in laminar boundary layers in absence of turbulent mixing. The Reynolds analogy between heat and mass transfer (Kays *et al.*, 2005) does not apply to laminar flows (the ratio of Schmidt number and Prandtl number is not equal to unity). Therefore, the concentration distribution of the coolant gas at the wall becomes a compelling quantity for understanding the mixing process in laminar boundary layers.

Furthermore, Ifti *et al.* (2022*a*) – by experimentally obtaining spatially-resolved concentration data – demonstrated that the cooling effectiveness is not only affected by the thermal properties of the coolant gas but also by its physical form and trace, i.e. concentration. For instance, it is widely known that Helium is a better coolant than Nitrogen because of Helium's higher heat capacity; however, at a given coolant mass flux, Helium also forms a more formidable film due to its seven times higher volumetric flow rate compared to that of Nitrogen. This phenomenon has been discussed by Gülhan & Braun (2010), Keller *et al.* (2015), and Hombsch & Olivier (2013) as well. It is therefore necessary to understand the formation and mixing of the physical film, predict the coolant concentration, and identify the variables that drive the mixing with respect to the coolant's concentration.

The coolant's concentration is a key parameter for designing an oxidation protection system. Oxidation protection or reduction can allow certain materials, such as ultra-high-temperature ceramics (UHTCs), to operate at temperatures above 3000 K without failing as experimentally shown by Ewenz Rocher *et al.* (2019). A high operational temperature would enable a higher amount of passive radiative

cooling (Ifti *et al.*, 2022*c*). In addition, predicting the ratio of the coolant gas and the boundary-layer gas can help improve the current film cooling correlations for laminar flows. Most correlations or correlation factors for laminar film cooling in the literature are based on the assumption of a fully mixed gas mixture (e.g., Heufer & Olivier, 2008*a*), which is not the case in a laminar boundary layer. The correct prediction of the ratio of gases becomes particularly important in cases where the coolant gas properties are significantly different from those of the boundary-layer gas, e.g. Helium injection in air. To the authors' knowledge, no model exists in the open literature to date that describes the mixing process at the wall in a laminar boundary layer.

In this article, an analytical model based on one-dimensional diffusion is proposed to describe this mixing process and predict the coolant concentration at the wall downstream of the injector. The model is validated against experimentally obtained coolant concentration data at the wall downstream of a porous injector on a flat plate at zero pressure gradient in a laminar, Mach 7 flow (reported in Ifti *et al.*, 2022*a*). This is the first time an analytical model is reported to describe the mixing mechanism between the coolant and the boundary-layer gas at the wall in a laminar flow.

6.2 Methodology

6.2.1 Analytical Model

The fluid downstream of the injector is modelled as a moving slab (annotated in red in Fig. 6.1) of a binary gas composition that advects downstream at the boundary-layer edge velocity, $u_e = x'/t$, where t is time. It is assumed that the coolant gas diffuses in the wall-normal direction, y, as the slab advects downstream. A solution for the coolant concentration at the wall, i.e. at $y = 0$, is sought as a function of the downstream distance, $x' = x - x_0$.

The one-dimensional, unsteady diffusion equation is given as

$$\frac{\partial C}{\partial t} = D\frac{\partial^2 C}{\partial y^2}, \tag{6.1}$$

where C is the non-dimensional concentration of the coolant gas ($C \in [0,1]$) and D is the diffusion coefficient (Crank, 1979). The coordinate y denotes the wall-normal direction. With time, $t = x'/u_e$, a solution to Eq.(6.1) is an error function according to Crank (1979) expressed as

$$\frac{C(x',y)}{C_0} = \frac{1}{2}\left[\mathrm{erf}\left(\frac{h-y}{\sqrt{4Dx'/u_e}}\right) + \mathrm{erf}\left(\frac{h+y}{\sqrt{4Dx'/u_e}}\right)\right] \ldots [y \geq 0]. \tag{6.2}$$

Here, x' is the downstream distance (see Fig. 6.1), u_e is the stream-wise, boundary-layer edge velocity, and C_0 and h respectively denote the initial coolant concentration (maximum value 1 or 100%) and initial height of the coolant slab at $x' = 0$, i.e. immediately downstream of the injector. The downstream distance can be expressed in terms of the distance from the leading edge, x, as $x' = x - x_0$, where x_0 is the length from the leading edge to the injector end. At the wall, i.e. at $y = 0$, Eq.(6.2) reduces to

$$\eta_c = C(x,0) = C_0\mathrm{erf}\left(\sqrt{\frac{u_e h^2}{4D(x-x_0)}}\right) = C_0\mathrm{erf}(\zeta) \ldots [x - x_0 > 0]. \tag{6.3}$$

Equation (6.3) is the concentration effectiveness at the wall. A value of $\eta_c = 1$ denotes a full coolant film coverage, whereas a value of $\eta_c = 0$ refers to a fully diminished coolant film. A driving parameter is defined as ζ. The diffusion coefficient, D, is calculated for a binary gas mixture (boundary-layer gas, 1, to coolant gas, 2) defined as

$$D = D_{12} = 0.0018583 \times T^{3/2}\sqrt{\frac{1}{M_1} + \frac{1}{M_2}}\frac{101325 \times 10^{-4}}{r_{12}^2 \sigma_{12} p}, \tag{6.4}$$

where M, r, and σ are respectively the molar mass, binary collision diameter, and temperature dependent collision integral (Bird *et al.*, 2007). D is evaluated at the boundary-layer edge static pressure, $p = p_e$, and the wall temperature, $T = T_w$.

The initial concentration does not necessarily start at 1 immediately downstream of the injector, i.e. at $x' = 0$; it is a function of the injected coolant mass flux, injector type, and mixing between the coolant gas and boundary-layer gas on top of the injector. For this study, the value of C_0 is experimentally determined (see

Section 6.2.3); however, it could be determined by numerical simulations or future analytical models. The remaining quantity that is required is the initial slab height, h. A separate model is proposed to find h in the following section.

6.2.2 Model for Initial Slab Height

Model Description

A schematic of the coolant slab height is illustrated in Fig. 6.2. At $x' = 0$, the slab height has the highest concentration. As the slab travels downstream, the concentration distribution becomes wider with its peak dropping (see profiles at $x' = x_1$ and $x' = x_2$).

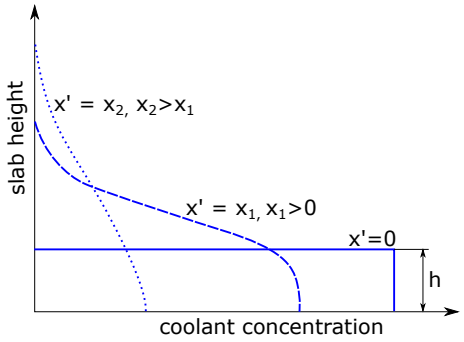

Figure 6.2: Schematic of slab height distribution.

A simple model is constructed to obtain the slab initial height, h. This height is defined as

$$h = h' + \delta_{\text{ent}}. \tag{6.5}$$

h' is obtained from the continuity equation across the control volume presented in Fig. 6.3 (blue, dashed line). The continuity equation yields

$$\begin{aligned} \rho_c u_c s &= \rho_c u_e h' \\ \Rightarrow \qquad h' &= \frac{u_c}{u_e} s, \end{aligned} \tag{6.6}$$

where s is the injector's stream-wise length and the subscripts 'e' and 'c' respectively denote boundary-layer edge and coolant quantities. It is assumed that the coolant reaches the edge velocity, u_e, after becoming tangential to the wall (shown in blue in Fig. 6.3) and obtains a height of h' at the end of the injector.

By substituting the blowing ratio, $F = (\rho_c u_c)/(\rho_e u_e)$, in Eq.(6.6), the following expression for h' is obtained:

$$h' = \frac{\rho_e}{\rho_c} F s \; ... \left[\because \frac{u_c}{u_e} = \frac{\rho_e}{\rho_c} F \right]. \tag{6.7}$$

At the exit of the porous injector, the coolant is at the boundary-layer edge pressure, p_e, and wall temperature, T_w. According to the ideal gas law, the coolant and boundary-layer edge densities are respectively $\rho_c = \dfrac{M_c p_e}{R_G T_w}$ (assuming temperature equilibrium in the porous injector) and $\rho_e = \dfrac{M_{\text{air}} p_e}{R_G T_e}$, where R_G is the universal gas constant, M_c is the molar mass of the coolant gas, and M_{air} is the molar mass of the boundary-layer gas (in this instance, air). Substituting these two equations for ρ_c and ρ_e in Eq.(6.7) yields

$$h' = \frac{M_{\text{air}} T_w}{M_c T_e} F s. \tag{6.8}$$

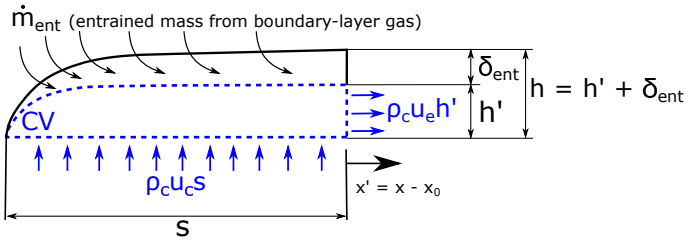

Figure 6.3: Control volume around the injected gas and mass entrainment into the coolant gas over the injector.

The coolant gas mixes with the incoming boundary-layer gas over the injector and some boundary-layer gas is entrained into the coolant slab as shown in Fig. 6.3 (in black). The total slab height, h, is increased by the entrained mass, $\dot{m}_{\text{ent}}$, from the boundary layer. Similar to the entrained mass modelled in film cooling theory (Goldstein, 1971), it is assumed that this entrained mass grows as a boundary layer starting from the injector's starting point. Immediately downstream of the injector, this height becomes equivalent to the laminar boundary-layer thickness given as

$$\delta_{\text{ent}} = \frac{5s}{\sqrt{Re_s}} = 5\sqrt{\frac{\mu_e s}{\rho_e u_e}}, \tag{6.9}$$

according to the Blasius solution (Blasius, 1908), where, μ_e is the viscosity at the boundary-layer edge. Substituting Eq.(6.8) and Eq.(6.9) in Eq.(6.5) yields the final equation for the slab height expressed as

$$h = \frac{M_{\text{air}} T_w}{M_c T_e} F s + 5\sqrt{\frac{\mu_e s}{\rho_e u_e}}. \tag{6.10}$$

Numerical Validation

In order to validate Eq.(6.10), two-dimensional simulations were performed employing the Thermochemical Implicit Non-Equilibrium Algorithm (TINA) – a Navier-Stokes solver developed by Fluid Gravity Engineering Ltd. TINA is a second-order accurate, point and line implicit, time marching algorithm. It employs the approximate Riemann solver in conjunction with flux limiters for the inviscid fluxes. A Total Variation-Diminishing (TVD) shock capturing algorithm was used, which ensures non-oscillatory behaviour near shock waves at essentially any free stream Mach number. Further details can be found in Netterfield (1992, 1991).

A flow over the flat-plate geometry described in Section 6.2.3 was simulated (Ifti *et al.*, 2022*d*). A computational domain of 340 mm × 58 mm was used with a total of 50511 grid points. The grid was equidistant in the stream-wise direction with step size of $\Delta x = 1 \times 10^{-3}$ m and stretched in the wall-normal direction with a first cell height of $\Delta y = 2.5 \times 10^{-6}$ m. This resulted in a wall cell Reynolds number of $Re_{\text{cell}} < 1$, which ensured that the high gradients close to the wall were sufficiently resolved. A perfect gas model was selected. Air was chosen as the main flow gas. The flow conditions were matched with the conditions of the experiments stated in Section 6.2.3.

At the wall, the nodes between 160 mm and 200 mm featured a permeable boundary condition, which was set as the mass flux of the coolant gas. Simulations for four cases of Nitrogen injection with blowing ratios of $F = 0.0406\%$, $F = 0.0818\%$, $F = 0.153\%$, and $F = 0.295\%$, were performed. The mole fraction of Nitrogen, X_{N_2}, in the flow field was extracted from the simulation results. A non-dimensional

concentration quantity is defined as follows:

$$C(x,y) = \frac{X_{\mathrm{N}_2}(x,y) - X_{\mathrm{N}_2,e}}{1 - X_{\mathrm{N}_2,e}}. \tag{6.11}$$

At locations where the mole fraction of Nitrogen is identical to the value at the boundary-layer edge, i.e. $X_{\mathrm{N}_2} = X_{\mathrm{N}_2,e}$, the concentration is $C = 0$. On the other hand, a concentration of $C = 1$ would be possible at locations where the Nitrogen mole fraction is exactly at unity, i.e. $X_{\mathrm{N}_2} = 1$.

In order to determine the effective initial slab height, concentration profiles are extracted immediately downstream of the injector (after $x = 200$ mm), where the impermeable wall boundary condition, $\left.\frac{\partial C}{\partial y}\right|_{y=0} = 0$, is satisfied. The profiles are plotted in Fig. 6.4a. Since these profiles are continuous and monotonic, it is difficult to pinpoint an exact slab height. The slab height is a height up to which the concentration remains close to the wall concentration, C_w, i.e. the concentration at $y = 0$. When compared with the analytical model (Eq.(6.10)), satisfactory results were found (as shown in Fig. 6.4b) with the following criteria for h:

$$h = \begin{cases} y(C = 0.95C_w) & \text{for } C_w < 1, \\ y(C = 0.99C_w) & \text{for } C_w = 1. \end{cases} \tag{6.12}$$

The y locations for the slab height obtained from Eq.(6.12) are shown in Fig. 6.4a (diamond markers). It is not surprising that the criterion for h is different between cases that feature a full film coverage at the wall ($C_w = 1$) and those that do not ($C_w < 1$). As shown in Fig. 6.4a, the profile close to the wall is different for the highest blowing ratio case that has a wall coolant concentration of $C_w = 1$ compared to the lower blowing ratio cases. A wall coolant concentration of $C_w = 1$ represents an intact coolant film at the wall where no mixing has occurred. Thus, the effective initial slab height would be a height where the coolant concentration is approximately the same as the wall coolant concentration ($C(h) = 0.99C_w$). Figure 6.4b illustrates the match between the analytical model for the h presented in Eq.(6.10) and the simulation results for four different blowing ratios. This simple analytical model yields values for h within 10% of the values obtained by the simulation.

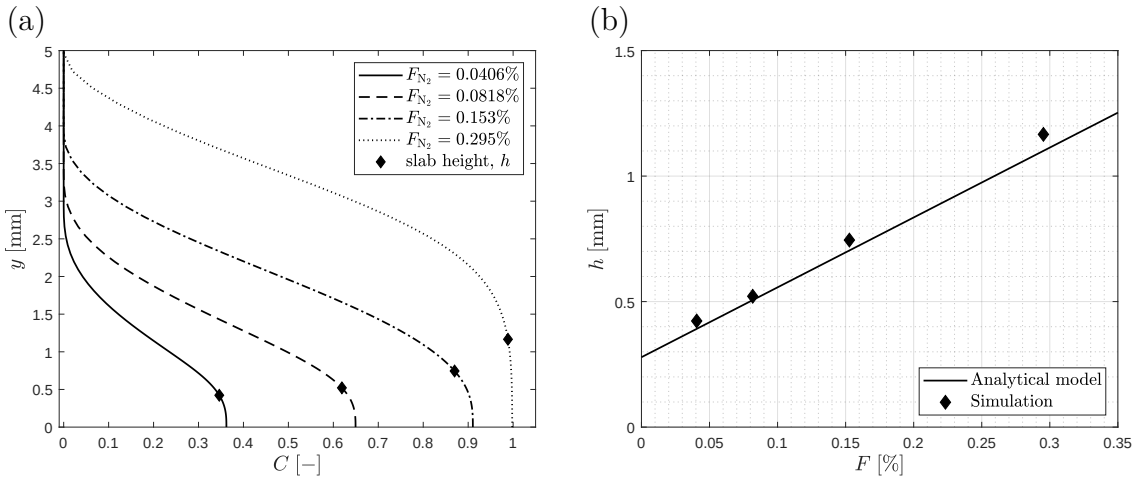

Figure 6.4: (a) Coolant (Nitrogen) concentration profiles obtained from simulation immediately downstream of injector (including slab height locations) and (b) slab height, h, as a function of F (analytical model, Eq. 6.10) versus simulation.

6.2.3 Experiments

Transpiration cooling experiments in a laminar boundary layer employing a flat-plate model (see Fig. 6.5a) were conducted at Mach 7 in the Oxford High Density Tunnel (HDT) (see Ifti *et al.*, 2022*a*, for details). The flat-plate model was at an angle of attack of AoA = 0°. A porous injector (39.5 mm × 39.5 mm) made of sintered zirconium diboride (ZrB_2) was situated 160 mm downstream of the leading edge. Thin-film gauges installed upstream and downstream of the injector measured the heat fluxes, which were compared to the correlation by Eckert (1956) for laminar boundary layers to ensure that the boundary layer was laminar during the experiments. Pressure sensitive-paint (PSP) with an area of interrogation of 140 mm × 37 mm was applied immediately downstream of the injector to measure the relative concentration of the injected coolant gas at the wall. The boundary-layer static pressure, temperature, and wall temperature were respectively $p_e = 542.04$ Pa, $T_e = 43.53$ K, and $T_w = 293$ K. The total pressure, total temperature, and unit Reynolds number were $p_0 = 1.738$ MPa, $T_0 = 470.1$ K, and $Re_u = 12.9 \times 10^6$ m^{-1}. The boundary-layer edge velocity was $u_e = 925.9$ ms^{-1}. The blowing ratios (Cases 1 to 6) are given in Table 6.1.

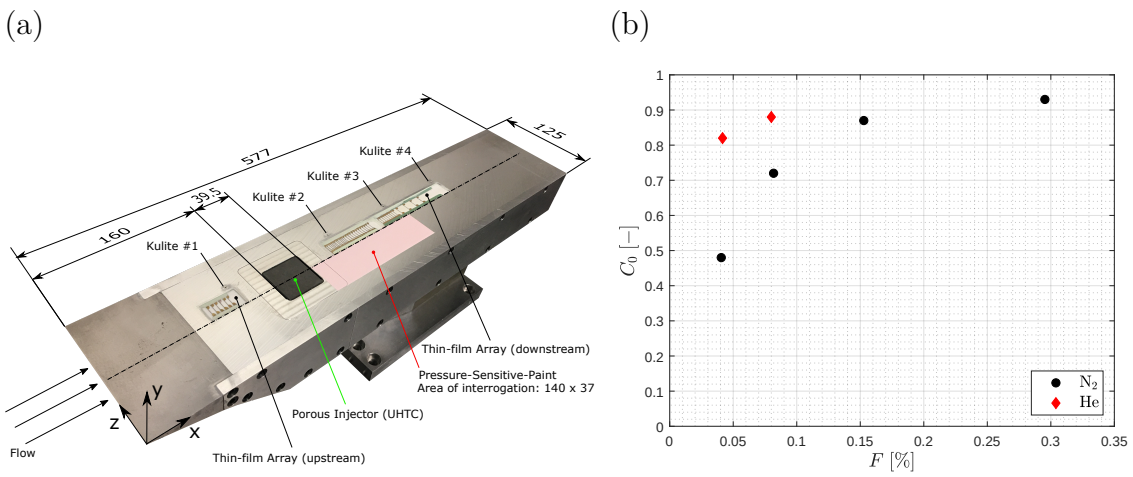

Figure 6.5: (a) Flat-plate model with PSP coat downstream of the porous injector (Ifti *et al.*, 2022*a*) and (b) experimentally obtained C_0 values as a function of F.

The PSP was excited by an LED of 390 nm and the emitted, higher wavelength radiation was captured by a camera fitted with a red filter (550 nm). This excitation is quenched by Oxygen in the air, and therefore the illumination can be calibrated by collecting illumination data for different flow static pressures (measured by surface mounted Kulite pressure transducers) without coolant injection. By applying the same calibration to cases with a foreign gas (coolant), a trace of the film can be identified as the quenching is influenced by the film. Injected coolant gas (Nitrogen or Helium) hinders the quenching by displacing air in the boundary layer. Comparing a case with air injection and one with a foreign gas injection at the same blowing ratio, gives a measure of how much air is displaced by the foreign gas, i.e. to what extent the foreign gas is forming a film. The concentration film effectiveness is defined as

$$\eta_c = 1 - \frac{p_{O_2,\,\text{foreign gas}}}{p_{O_2,\,\text{air}}}, \tag{6.13}$$

where $p_{O_2,\,\text{air}}$ and $p_{O_2,\,\text{foreign gas}}$ are Oxygen partial pressures with air and foreign gas injections, respectively, at the same blowing ratio.

A span-wise average of 10 mm close to the centreline – where the film is two dimensional and uninfluenced by the Mach angle – is taken to reduce the data for η_c to one dimension, which varies only in the stream-wise direction, x. The value of η_c immediately downstream of the injector is taken as the initial concentration,

C_0, for this study, i.e. $C_0 = \eta_c(x' = 0)$. In Fig. 6.5b, the experimentally obtained C_0 values for all cases are plotted as a function of the blowing ratio, F.

Case	1	2	3	4	5	6
F [%]	0.0406	0.0818	0.153	0.295	0.0416	0.08
Coolant gas	N_2	N_2	N_2	N_2	He	He

Table 6.1: Overview of blowing cases.

6.3 Results and Discussion

The results obtained from the analytical solution, i.e. Eq.(6.3), for Cases 1 to 6 are presented in Fig. 6.6a (dashed lines) along with the experimental data (solid lines). For all cases, the match between the analytical solution and the experimental data is encouragingly close, particularly considering the simplicity of the physical assumptions. At larger x values, a discrepancy can be noticed for Cases 3, 4, and 5. This deviation is attributed to the simplistic model (see Eq.(6.10)) employed in this study for the slab height, h. However, this discrepancy is overall within 17% at the farthest downstream location, demonstrating the success of this simple model for h – even for Helium injection. The results not only capture the correct, monotonic trend farther downstream but also the plateau immediately downstream of the injector for cases with a higher blowing ratio, i.e. Cases 3, 4, and 6.

In Fig. 6.6b, a collapse of the experimental data for all cases is showcased with η_c/C_0 as a function of the driving parameter, $\zeta = \sqrt{\frac{u_e h^2}{4D(x-x_0)}}$. These collapsed data further demonstrate that the mixing mechanism at the wall can be described by Eq.(6.3). Figure 6.6b visualises the effect of change in the variables that are involved. As $\zeta \to \infty$, $\eta_c/C_0 \to 1$, and therefore film coverage of 1 can be achieved for higher ζ values (e.g. $\zeta > 2$). Since $\zeta \propto h \propto F$, a higher blowing ratio would result in a higher ζ value, i.e. a better film coverage, which is expected as long as a boundary-layer transition is not triggered. On the other hand, a higher diffusion coefficient, D, or larger x values would result in a lower ζ value, which would in return reduce the film coverage. According to Eq.(6.4), the diffusion coefficient is a function of

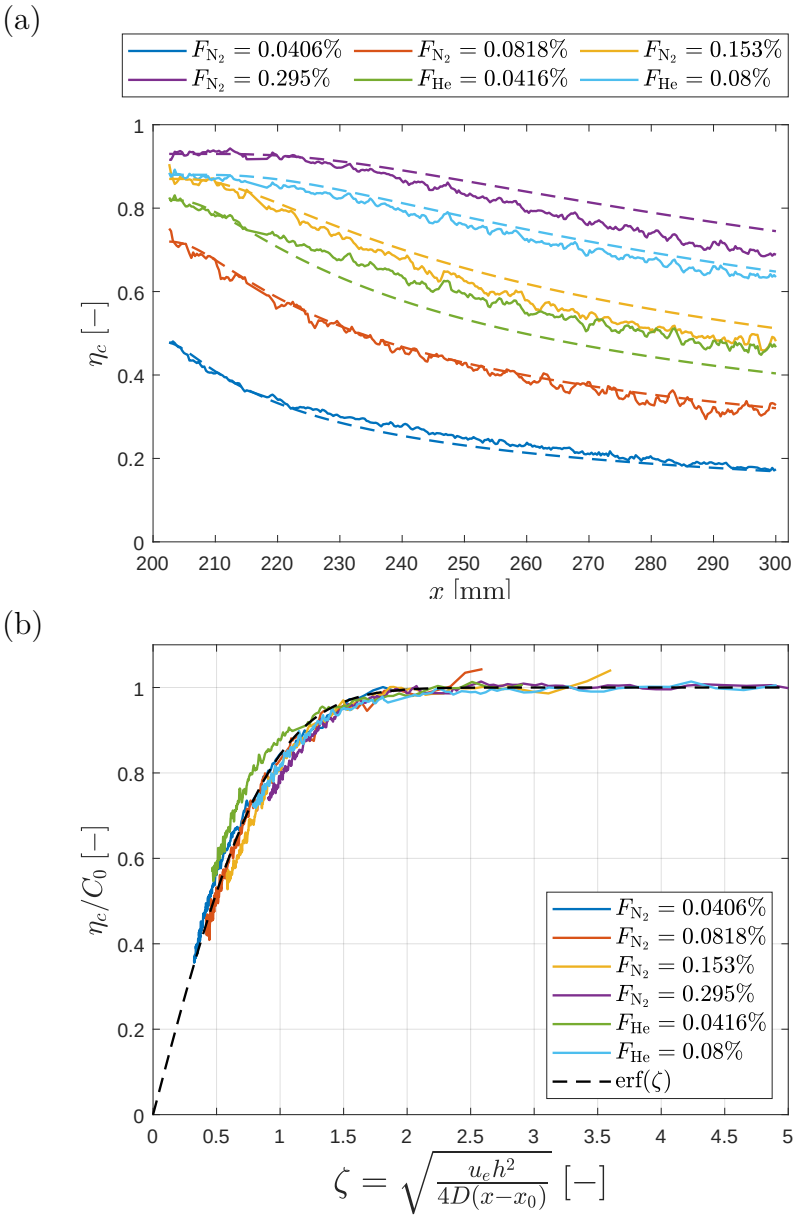

Figure 6.6: Cases 1 to 6: (a) Concentration effectiveness, η_c, versus stream-wise direction, x (solid line: experimental data; dashed line: analytical model, Eq.(6.3) and (b) scaled concentration effectiveness, η_c/C_0, versus driving parameter, ζ.

temperature and pressure ($D \propto T^{3/2}$ and $D \propto 1/p$), and therefore flight conditions at high temperatures and low pressures would increase the diffusion coefficient.

According to Eq.(6.10), the first term in h is proportional to $1/u_e$ (since $F = (\rho_c u_c)/(\rho_e u_e)$) and the second to $1/\sqrt{u_e}$. In the numerator of ζ, the slab height, h, is multiplied by $\sqrt{u_e}$, and therefore the final relationship between the driving parameter and the stream-wise velocity becomes $\zeta \propto 1/\sqrt{u_e}$. If the air density

remains constant and the vehicle accelerates, the edge mass flux, $\rho_e u_e$, would increase, resulting in a lower F and thus h. A higher stream-wise velocity would decrease ζ and thereby the film concentration, η_c.

The collapse of data presented in Fig. 6.6b further demonstrates that this analytical model correctly captures the effect of different coolant gases, in this case Nitrogen and Helium. In Ifti *et al.* (2022*a*) it was experimentally shown that Helium forms a much more formidable film than Nitrogen at the same blowing ratio due to Helium's seven times larger volumetric flow compared to that of Nitrogen. Keller *et al.* (2015) reported this effect in their numerical investigation. This difference in volumetric flow rate for different gases at a given blowing ratio is taken into account in the first term of the right-hand side of Eq.(6.10).

The proposed model is only valid at the wall. The diffusion coefficient, D, is evaluated at the wall temperature, T_w. In the wall-normal direction, D would change due to the temperature gradient in the boundary layer. The assumption of a constant D made in Eq.(6.1) would not hold for the entire fluid in the wall-normal direction. In addition, the model assumes that the coolant is injected at the wall temperature, consistent with the experiments. This model is further limited to cases where the slab height, h, is close to or larger than the incoming boundary-layer thickness in order to assume that the slab reaches the edge velocity, u_e.

Overall, the results demonstrate that the mechanism of downstream mixing at the wall in a laminar boundary layer, where turbulent mixing is absent, is primarily driven by diffusion. The proposed model (Eq. 6.3) can be used to determine the amount of coolant needed to protect a surface from oxidation in laminar conditions. This model provides the exact ratio of the coolant and the boundary-layer gas as a function of downstream distance, which can be implemented in current film cooling models.

6.4 Application

In a transpiration cooling system that is designed for application on a hypersonic vehicle, the coolant gas has to be carried inside the vehicle for a given mission, which

would add to the total weight and volume of the vehicle. In addition, the reservoir and pipework required to store the coolant gas would increase the weight of the vehicle's structure. The combined weight of the required coolant gas on board and its necessary storage structure may result in a high penalty in the payload capacity of a vehicle that utilises transpiration cooling as opposed to conventional thermal protection systems, e.g. ablative heat shields. To investigate the application of transpiration cooling on such vehicles, a thorough coolant mass budget calculation is necessary for the intended mission, which would also allow the determination of structural requirements to store the required amount of coolant gas.

Designing a transpiration cooling system to protect a hypersonic vehicle from heat or oxidation is a multi-variable problem and requires several thousands of iterations before an optimised design can be obtained. In particular, the ever-changing external flow conditions (e.g., pressure, temperature, velocity, etc.) on a hypersonic trajectory demand a point-by-point calculation over the flight duration during which the transpiration cooling system would be active. This makes such design processes prohibitively expensive and lengthy to complete with conventional boundary-layer solvers, even on high performance computers. Engineering correlations or analytical models provide a rapid and inexpensive method to perform these calculations, particularly for first approximation designs. The proposed analytical model is the first of its kind that can be used as a rapid design tool to predict the required coolant mass for a given trajectory and a film coverage requirement in terms of wall coolant concentration in laminar flows. It can also be used on board the vehicle for its systems to self-control the required coolant that needs to be injected at any point in its trajectory. To demonstrate the capability of the model, a mass budget calculation is performed for a generic hypersonic vehicle that requires up to 85% of coolant coverage to protect the wall surface against oxidation over a target distance downstream of a porous injector.

The analytical model is employed to calculate the required coolant mass and the associated storage volume for a transpiration-cooled hypersonic vehicle (see Fig. 6.7a). The total length of the vehicle is 16 m with a leading edge span of $b = 5$ m.

A porous injector of length s and an area of $A = sb$ is situated downstream of the leading edge. The area up to a length of x' downstream of the porous injector is to be protected by a coolant film with a concentration effectiveness of at least 85%, i.e. $\eta_c(x') \geq 0.85$. A generic trajectory with a flight duration of $t_{\text{flight}} = 1333$ s is selected (see Fig. 6.7b). The US Standard Atmosphere Model (1976) is employed to calculated the static pressure and static temperature, both functions of altitude. For simplicity, it is assumed that the static and edge quantities are equal and the boundary layer around the vehicle is strictly laminar throughout the flight.

The static temperature, static pressure, and velocity of the vehicle are substituted as T_e, p_e, and u_e, respectively, in Eq.(6.3) with the condition $\eta_c(x') \stackrel{!}{=} 0.85$. It is assumed that full coverage of the coolant exists on the porous injector, i.e. $C_0 = 1$. An isothermal wall temperature of $T_w = 2000$ K is assumed. The coolant is stored inside the vehicle at a pressure of $p_{\text{storage}} = 300$ bar and a temperature of $T_{\text{storage}} = 300$ K. Configurations with five different s values are calculated with a fixed value of $x' = 10$ m and another set of calculations are performed for five x' values with $s = 0.2$ m set as the injector length. For each configuration, the coolant gas is varied between Nitrogen and Helium. Equation 6.3 is subsequently solved for the blowing ratio, F, at each point on the trajectory. The coolant mass flow rate is obtained from the definition of blowing ratio and the continuity equation as follows:

$$\dot{m}_c = F \rho_e u_e A \; ... \; \big[\text{where } A = sb\big]. \tag{6.14}$$

The total coolant mass is determined by integrating Eq.(6.14) with resect to time, τ, expressed as a function of the flight duration, t_{flight}:

$$m_c(t_{\text{flight}}) = \int_0^{t_{\text{flight}}} \dot{m}_c d\tau. \tag{6.15}$$

Finally, the required volume for storing the coolant gas inside the vehicle is obtained from the equation

$$Q_{c,\text{storage}} = \frac{m_{c,t} R_G T_{\text{storage}}}{M_c p_{\text{storage}}}, \tag{6.16}$$

where $m_{c,t}$ is the total coolant mass required over the total flight duration of $t_{\text{flight}} = 1333$ s, i.e. $m_{c,t} = m_c(t_{\text{flight}} = 1333 \text{ s})$.

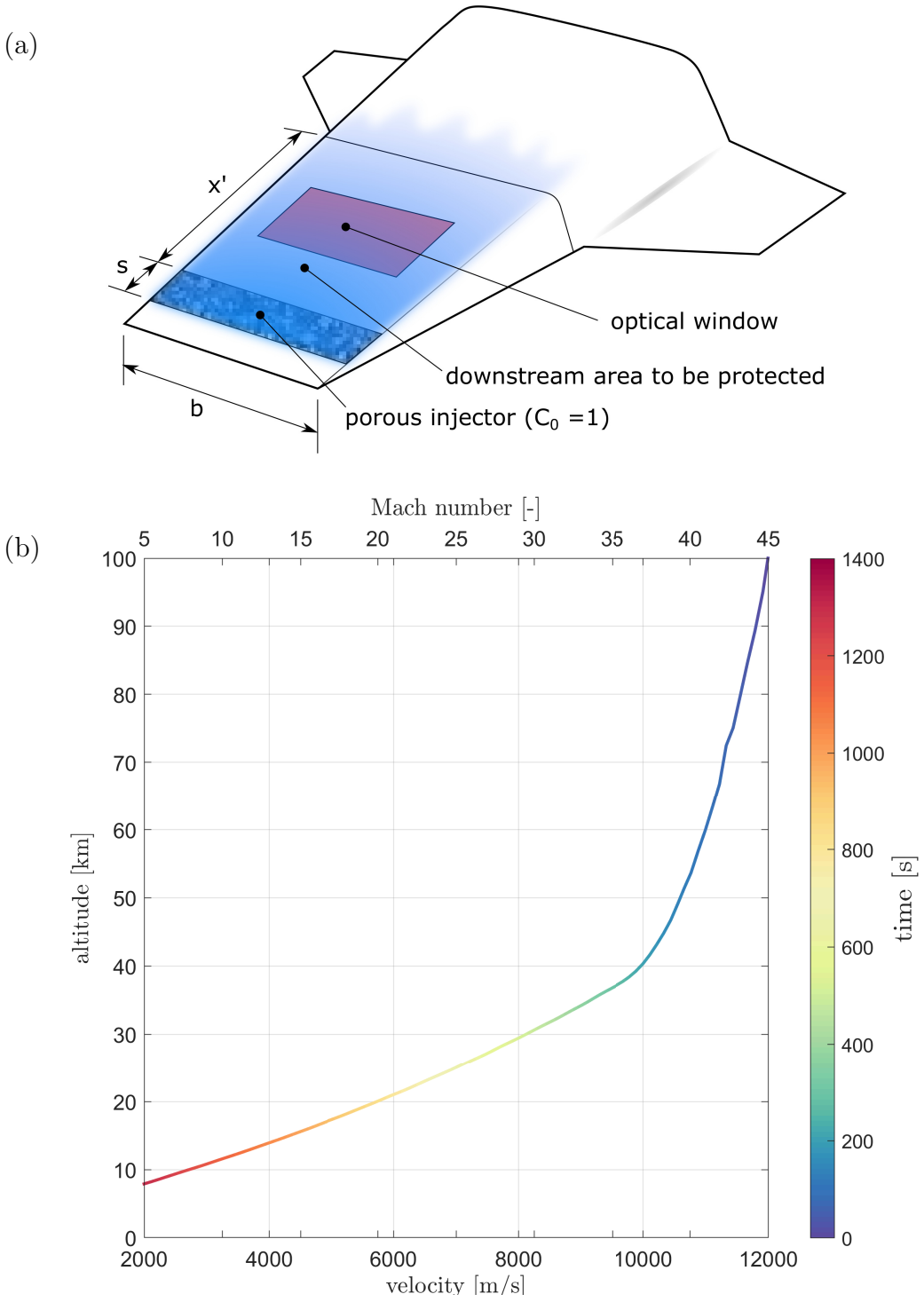

Figure 6.7: (a) Schematic of a transpiration-cooled hypersonic vehicle (not to scale; coolant shown in blue) and (b) a generic trajectory of hypersonic flight.

Results of the coolant mass budget calculation are presented in Fig. 6.8 and Table 6.2. When s is increased, the required blowing ratio, F, drops (see Fig. 6.8a), whereas larger values of x' result in higher F values (see Fig. 6.8b). The corresponding required coolant mass, m_c, is plotted in Figs. 6.8c and 6.8d, respectively for variations in s and x'. Analogous to the blowing ratio, F, the required coolant mass, m_c, decreases with higher s values (Fig. 6.8c) and the opposite trend can be noticed when x' is increased (Fig. 6.8d). According to Eq.(6.10), the coolant's initial slab height, h, thickens when s is increased, and this results in a higher value of the driving parameter, ζ, and therefore η_c, as discussed in Section 6.3. Thus, the required coolant concentration of at least $\eta_c = 85\%$ is achieved with a lower F as s is increased. On the other hand, as x' increases, ζ and η_c drop (note: $x' = x - x_0$), and a higher F is required to maintain the criterion of $\eta_c \geq 85\%$. For a given point in time (t_{flight}), the required coolant mass (Eq. 6.15) follows the same trend as F for variations in both s and x' (compare Figs. 6.8c and 6.8d to Figs. 6.8a and 6.8b) since $m_c \propto F$ when the product $\rho_e u_e A$ is constant according to Eq.(6.14).

For a given set of s and x', the blowing ratio decreases as the flight progresses up until $t_{\text{flight}} \approx 1150$ s (see Figs. 6.8a and 6.8b). After this point in time, the required blowing ratio increases. This is due to the different pressure and temperature distributions in the troposphere starting at an altitude of 11 km (see Fig. 6.7b). This demonstrates the proposed model's ability to easily take these drastic, non-monotonic changes in the flow conditions into account. It can be further seen in Figs. 6.8a and 6.8b that the blowing ratios range from 1% to 35% within the first 400 s of flight (see inset). However, the required total coolant mass is significantly smaller (see Figs. 6.8c and 6.8d) – compared to the mass required over the flight duration that follows – despite the high blowing ratios during this time period. This is because the edge mass flux, $\rho_e u_e$, at these altitudes is relatively low due to the low density in the atmosphere. In other words, the Oxygen partial pressure is significantly lower at these altitudes, and therefore only a small amount of coolant gas is required to protect the vehicle's surface from oxidation. As the vehicle descends, the density of the atmosphere rises and the required F value

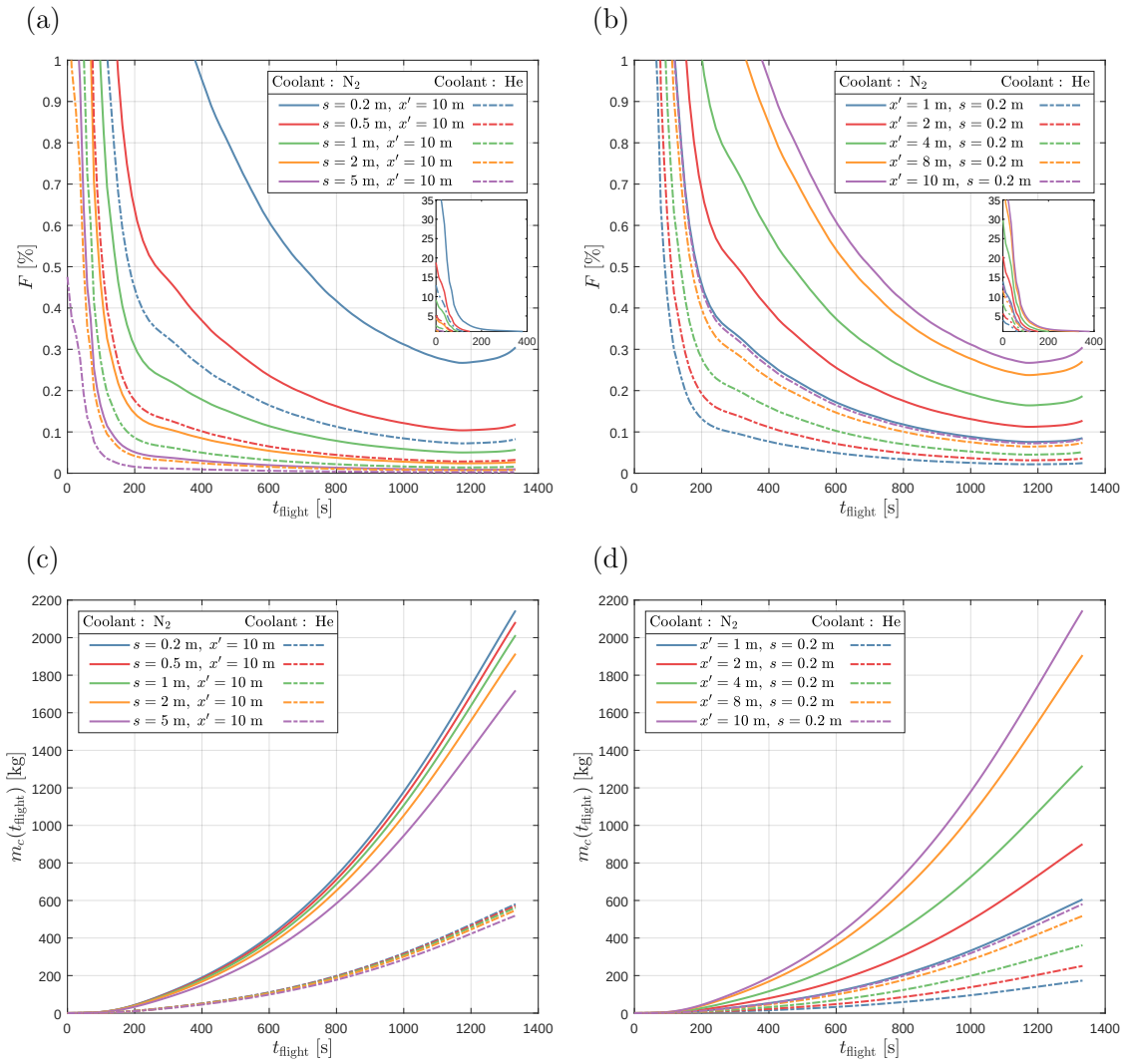

Figure 6.8: Results of coolant mass budget calculation as a function of flight duration, t_{flight}. Required blowing ratio, F: variation in (a) s and (b) x'; required coolant mass, m_c: variation in (c) s and (d) x'. F for flight duration up to $t_{\text{flight}} = 400$ s is plotted in the inset of subplots (a) and (b).

drops. According to Eq.(6.14), however, a higher coolant mass flow rate is needed as the air density, ρ_e, rises drastically.

Fig. 6.8 further illustrates the efficiency of Helium as a protective film. For every variation – as expected – Helium forms a better film coverage for significantly lower total mass compared to Nitrogen as the coolant gas (see Figs. 6.8c and 6.8d). The required total coolant mass for the full flight duration of $t_{\text{flight}} = 1333$ s, denoted as $m_{c,t}$, is given in Table 6.2 for all variations in s and x'. On an average, 3.6 times less coolant mass is needed when Helium is used instead of Nitrogen ($m_{c,t,\text{N}_2}/m_{c,t,\text{He}} = 3.6$). Note that this effect is not identical to the commonly reported

Varied parameter	s [m]					x' [m]				
Input value	0.2	0.5	1	2	5	1	2	4	8	10
N_2, $m_{c,t}$ [kg]	2144.5	2082.7	2013.0	1914.5	1719.0	605.4	900.3	1317.2	1906.9	2144.5
He, $m_{c,t}$ [kg]	580.4	571.6	561.6	547.5	519.6	173.2	251.2	361.5	517.5	580.4
Ratio [-]	3.7	3.6	3.6	3.5	3.3	3.5	3.6	3.6	3.7	3.7
N_2, $Q_{c,\text{storage}}$ [m^3]	6.4	6.2	6.0	5.7	5.1	1.8	2.7	3.9	5.7	6.4
He, $Q_{c,\text{storage}}$ [m^3]	12.1	11.9	11.7	11.4	10.8	3.6	5.2	7.5	10.8	12.1
Ratio [-]	0.53	0.52	0.51	0.50	0.47	0.50	0.51	0.52	0.53	0.53

Table 6.2: Required total coolant mass and volume for flight duration of 1333 s. Note: $x' = 10$ m when s is varied and $s = 0.2$ m when x' is varied.

higher thermal film effectiveness of Helium. A higher thermal film effectiveness stems from the large heat capacity of Helium, which has been reported in numerous studies (e.g., Richards & Stollery, 1979; Meinert *et al.*, 2001; Langener *et al.*, 2011). In the current analysis, it is shown that a similar effect is achieved by strictly considering the coolant's concentration effectiveness at the wall. The thermal and concentration-based effects are connected through the molar mass of the coolant (Meinert *et al.*, 2001), and the proposed model is able to delineate the role of the coolant's molar mass in forming the physical film with respect to its concentration and, consequently, in its final cooling performance.

The required coolant storage volume, $Q_{c,\,\text{storage}}$, over the full flight duration of $t_{\text{flight}} = 1333$ s is given in Table 6.2. For the required coolant mass, the coolant storage volume needed for Nitrogen is, on average, half of that needed for Helium ($Q_{c,\text{storage},N_2}/Q_{c,\text{storage,He}} = 0.51$). Evaluating Eq.(6.16) for Nitrogen and Helium and subsequently constructing the ratio thereof yields

$$\frac{Q_{c,\text{storage},N_2}}{Q_{c,\text{storage,He}}} = \frac{m_{c,t,N_2}}{m_{c,t,\text{He}}} \frac{M_{\text{He}}}{M_{N_2}}. \tag{6.17}$$

With the ratios $m_{c,t,N_2}/m_{c,t,\text{He}} = 3.6$ (from Table 6.2) and $M_{N_2}/M_{\text{He}} = 7$, the ratio $Q_{c,\text{storage},N_2}/Q_{c,\text{storage,He}} = 0.51$ is obtained. For the same mass as Nitrogen, i.e. $m_{c,t,N_2}/m_{c,t,\text{He}} = 1$, Helium would occupy seven times more volume than Nitrogen since $Q_{c,\text{storage,He}} = 7Q_{c,\text{storage},N_2}$ according to Eq.(6.17). Similarly, Helium forms a more formidable film once injected due to its seven times higher volumetric flow rate at a given mass flow rate as discussed by Ifti *et al.* (2022*a*), Gülhan & Braun (2010), Keller *et al.* (2015), and Hombsch & Olivier (2013).

The required coolant storage volume, $Q_{c,\text{storage}}$, is a significant design parameter for the coolant's storage structure and the vehicle's overall volume. In practice, the coolant would be contained at a constant temperature (T_{storage}) inside the vehicle in a pressure vessel that would be limited by a maximum pressure (p_{storage}). This means a lighter gas, i.e. a gas with lower molar mass, M_c, would result in a higher total coolant volume, $Q_{c,\text{storage}}$, for a given $m_{c,t}$ (see Eq. 6.16). The mixing – as predicted by the proposed model – would dictate how large $m_{c,t}$ has to be for a given coolant gas and a target concentration effectiveness, η_c. Although T_{storage} and p_{storage} can be varied theoretically, in practice the variation would be possible only within a narrow range. T_{storage} has to be close to the vehicle's internal temperature, and increasing p_{storage} to reduce the storage volume would require strengthening of the structure, which would add to the total weight of the vehicle.

For the calculated configurations (Table 6.2), the storage volume required for Helium is approximately twice the storage volume needed for Nitrogen. Helium's higher volumetric flow rate – an advantageous property that helps form a better film with a lower mass requirement – becomes a disadvantage for the vehicle's overall volume. It is, therefore, necessary to determine both the required total coolant mass and total coolant storage volume to design a vehicle that utilises transpiration cooling. Both of these critical design parameters can be obtained by using the proposed model.

The analytical model presented in this article can be employed to rapidly perform these coolant mass budget calculations without the need of any significant computational power by simply using the trajectory data, and critical design parameters such as s and x' can be easily varied as demonstrated here. Thousands of iterations of these inexpensive calculations can be performed rapidly to find the optimal design parameters for a given mission.

6.5 Conclusion

Although numerous prediction models exist for predicting the mixing between the coolant film and the boundary-layer gas in turbulent flows, such models are not

widely available for laminar flows. In particular, no model exists that describes the mixing process in terms of the coolant concentration, which is important for laminar flows where the heat and mass transfer analogy does not apply. The coolant concentration is the core parameter for successfully designing an oxidation protection system. In this study, an analytical model based on one-dimensional diffusion is proposed to predict laminar mixing of the coolant at the wall downstream of the injector in terms of concentration. The model is validated against experimental data obtained at Mach 7 employing Nitrogen and Helium as the coolant gas over a flat plate. The analytical results match the experimental data within 17% and correctly predict the slope of the monotonic decay of the coolant concentration. The model further describes the role of variables such as stream-wise velocity, diffusion coefficient, and blowing ratio in the mixing process. A coolant mass budget calculation performed for a transpiration-cooled hypersonic vehicle descending on a generic trajectory shows that using Helium as the coolant gas requires 3.6 times less mass when compared to configurations where Nitrogen is employed as the coolant, demonstrating the efficiency of Helium in forming a protective film downstream of the injector. However, Helium requires twice the storage volume when compared to Nitrogen, a factor that has to be accounted for – if the efficiency of Helium is to be exploited – when designing a vehicle. Lowering the required coolant mass by using a lighter gas such as Helium could come at a cost of a higher overall volume requirement. The proposed analytical model is a useful tool for rapidly performing mass budget calculations to design transpiration cooling systems on supersonic and hypersonic vehicles. The model could also be implemented on board a vehicle to enable a self-controlling system. In particular, the model's prediction of coolant concentration can be directly used to design an oxidation protection system. The concentration distribution obtained from this model could be further employed to improve existing film cooling correlations for laminar flows. Foremost, however, this model explains the mixing mechanism between the coolant film and the boundary-layer gas at the wall in a laminar flow; it is demonstrated that this mixing mechanism at the wall is driven by diffusion.

7 Conclusion

The aim of this endeavour was to (a) qualify porous Ultra-High-Temperature Ceramics for the purpose of transpiration cooling and (b) understand the mixing mechanism at the wall between the coolant gas and the boundary-layer gas downstream of a transpiring injector in a laminar, hypersonic flow. In this chapter, a summary of the contributions made in this thesis towards fulfilling this aim is presented along with a brief outlook to the future.

The first segment of the aim is accomplished in Chapter 3. The permeability and outflow behaviour of porous UHTC made of ZrB_2 were experimentally examined to assess their suitability for transpiration cooling, a thermal protection system that could enhance the re-usability of hypersonic vehicles such as rockets and spaceplanes. It is shown that the flow through these UHTCs can be successfully modelled by the Darcy-Forchheimer equation even at higher through-flow velocities, and the corresponding permeability coefficients are measured in an ISO 4022 rig featuring a through-flow diameter of 15.6 mm and reported along with their respective uncertainties. A change in porosity, from $\phi \approx 32\%$ to $\phi \approx 42\%$, results in an order of magnitude jump in the Darcy coefficient, whereas the Forchheimer coefficient increases by two orders of magnitude, approximately. Cleaning the surface of the porous samples – in form of sanding or ultrasonic bath – increased the Darcy coefficient by up to 19%. Velocity maps obtained from hot-wire anemometry demonstrate good outflow characteristics that behave in a uniform fashion. The standard deviation of the velocity distribution is 25.1% with respect to the mean value. No individual jets are present. The results published here can be used in numerical modelling and experimental design of wind tunnel testing, where porous

injectors made of UHTC are involved. Furthermore, the permeability coefficients could help designers predict the coolant mass budget for vehicles that will feature transpiration cooling. Whilst the brittleness of porous UHTC restricts its ease of application – in terms of the flow characteristics – it is demonstrably a befitting candidate for transpiration cooling.

The latter segment of the aim is attained in three parts in Chapter 4, Chapter 5, and Chapter 6. The mixing process between the coolant gas and the external flow downstream of film cooling holes or a transpiration cooling injector has been a subject of numerical and experimental investigation for more than fifty years. However, the majority of these studies are concerned with turbulent flows. Only few of the studies address laminar mixing. In particular, experimental data of downstream mixing in laminar, hypersonic flows have been reported by only a handful of authors. These studies, however, only investigated the heat flux reduction. Experimental data on the coolant's concentration at the wall are not available. In Chapter 4, transpiration cooling experiments were performed in a laminar, hypersonic flow in the Oxford High Density Tunnel (HDT) to measure the coolant's concentration distribution at the wall downstream of the injector along with the resulting heat flux reduction. A flat-plate model featuring a porous injector made of zirconium diboride was employed. The model was instrumented with thin-film arrays to measure the heat flux over the plate. A coat of Pressure-sensitive Paint (PSP) was placed downstream of the injector to measure the concentration of the coolant gas at the wall and spatially resolve the film downstream of the injector. Six different cases were tested. Nitrogen and Helium were used as the coolant gas. The blowing ratio ranged from 0.0406% to 0.295%. The PSP results show an excellent film coverage for these low blowing ratios reaching up to 95% of coolant concentration immediately downstream of the injector. Even 100 mm downstream of the injector, the coolant concentration was found to be approximately 20% for the lowest blowing ratio of 0.0406% with Nitrogen injection and approximately 50% for the lowest blowing ratio of 0.0416% with Helium injection. For the highest blowing ratio for Nitrogen and Helium, i.e. 0.295% and 0.08% respectively, the coolant concentration was respectively 70% and

65%, approximately, 100 mm downstream of the injector. For the same blowing ratio, Helium forms a more formidable film compared to Nitrogen due to its seven times higher volumetric flow rate. For both gases, the film monotonically decays with downstream distance; however, in cases with relatively higher blowing ratios, the film concentration remains constant immediately downstream of the injector, indicating formation of a discrete layer of binary gas. The film eventually starts to decay monotonically farther downstream. In all six cases, a heat flux reduction is achieved downstream of the injector. The onset of transition was not triggered by injection and the boundary layer remained laminar in all cases. For the cases with the highest blowing ratio, both with Nitrogen and Helium, a negative heat flux was recorded immediately downstream of the injector. The effectiveness based on coolant concentration obtained from PSP and the thermal effectiveness acquired from the thin-film arrays are compared. It is shown that the latter is generally higher than the former. Finally, a collapse of the thermal effectiveness is achieved and a modified correlation is proposed. The results published here add to the insight of how downstream mixing occurs in a laminar, hypersonic boundary layer. Further, these results could aid the validation process of numerical tools that aim to model various phenomena involving laminar mixing in high-speed flows.

In Chapter 5, two-dimensional simulations of transpiration cooling in a laminar, hypersonic boundary layer were performed employing the Thermochemical Implicit Non-Equilibrium Algorithm (TINA) – a Navier-Stokes solver developed by Fluid Gravity Engineering Ltd. Coolant concentration and heat flux results are compared to experimental data reported in Chapter 4. The concentration effectiveness matches the experimental data within ± 0.1 for higher blowing ratios and ± 0.2 for lower blowing ratios. The simulation results successfully predict the mixing rate at the wall as a function of the stream-wise direction for all blowing ratios. This shows that the simulations are not as successful in predicting the mixing on the injector at low blowing ratios as they are downstream of the injector. The simulations further demonstrate that the mixing process at the wall can be predicted by an advection-diffusion model. A collapse of thermal effectiveness calculated from simulation data

is achieved using a laminar film cooling correlation factor, which lies within ±0.1 of the correlations for laminar flows in the literature. Wall-normal profiles of coolant concentration, stream-wise velocity, and temperature are examined upstream, at the middle, and downstream of the injector. It is shown that, when the concentration effectiveness is close to 1 at the injector, the temperature gradient becomes negative at locations immediately downstream of the injector, resulting in a negative heat flux. This phenomenon of negative heat flux is captured both in the experiments and the current simulations. It is evident from the velocity profiles that the coolant is accelerated in the stream-wise direction downstream, which promotes dissipation of energy. This results in a reduction in the temperature of the coolant that is injected at the wall temperature and thereby induces a negative temperature gradient that leads to negative heat flux in close proximity to the injector.

Although numerous prediction models exist for predicting the mixing between the coolant film and the boundary-layer gas in turbulent flows, such models are not widely available for laminar flows. In particular, no model exists that describes the mixing process in terms of the coolant concentration, which is important for laminar flows where the heat and mass transfer analogy does not apply. Ultimately, a full understanding of the mixing mechanism cannot be attained without an analytical model that captures the underlying physics. The *keystone* contribution towards the endeavour of this thesis is presented in Chapter 6 to address this problem. An analytical model based on one-dimensional diffusion is proposed to predict laminar mixing of the coolant at the wall downstream of the injector in terms of concentration. The model is validated against experimental data presented in Chapter 4. The analytical results match the experimental data within 17% and correctly predict the slope of the monotonic decay of the coolant concentration. The model further describes the role of variables such as stream-wise velocity, diffusion coefficient, and blowing ratio in the mixing process. A coolant mass budget calculation performed for a transpiration-cooled hypersonic vehicle descending on a generic trajectory shows that using Helium as the coolant gas requires 3.6 times less mass when compared to configurations where Nitrogen is employed as the coolant,

demonstrating the efficiency of Helium in forming a protective film downstream of the injector. However, Helium requires twice the storage volume when compared to Nitrogen, a factor that has to be accounted for – if the efficiency of Helium is to be exploited – when designing a vehicle. Lowering the required coolant mass by using a lighter gas such as Helium could come at a cost of a higher overall volume requirement. The proposed analytical model is a useful tool for rapidly performing mass budget calculations to design transpiration cooling systems on supersonic and hypersonic vehicles. The model could also be implemented on board a vehicle to enable a self-controlling system. In particular, the model's prediction of coolant concentration can be directly used to design an oxidation protection system. The concentration distribution obtained from this model could be further employed to improve existing film cooling correlations for laminar flows. Foremost, however, this model explains the mixing mechanism between the coolant film and the boundary-layer gas at the wall in a laminar flow; it is demonstrated that this mixing mechanism at the wall is driven by diffusion.

In the future, porous UHTCs should be reinforced for more strength as they are relatively brittle for direct use, especially for cases in which higher differential pressures are required to drive the coolant mass flow. This could be done by fibre reinforcement or attaching a substructure underneath the UHTC layer. As for the mixing, it should be endeavoured to develop an analytical model to describe the mixing mechanism on the porous segment, i.e. where a permeable boundary condition applies. Furthermore, the analytical model presented in this thesis should be challenged by comparing it to experimental data obtained in chemically reacting flows and at non-zero pressure gradients. This could lead to an extension of the current analytical model. Last but not least, the mixing mechanism in the transitional regime (between laminar and turbulent) should be investigated since this has not been widely explored.

In conclusion, the work presented in this thesis has, for the first time, provided a full understanding of the mixing mechanism between the coolant and the external boundary-layer gas at the wall downstream of a transpiration-cooled injector in a

laminar, hypersonic boundary layer. It further qualified a novel, candidate material, i.e. UHTC, for the application of transpiration cooling. It can be said that the overall contribution made in this thesis brings humanity one step closer, however small of a step, towards making sustainable hypersonic flight a tangible reality.

Appendices

A

The Forchheimer Velocity Threshold

In Fig. 3.5d, it can be noticed that the input velocity, v_{in}, tends to an asymptotic limit as the input pressure, p_{in}, increases. This is due to the flow becoming Forchheimer-dominant, i.e. the inertial losses become significantly high. The asymptotic limit of the velocity can be calculated from Eq.(3.2). Substituting $\rho_{in} = \frac{p_{in}}{RT_{in}}$ in Eq.(3.2) and rearranging yields

$$\frac{1}{2L} - \frac{p_{out}^2}{2p_{in}^2 L} = \frac{\mu(T_{in})}{K_D p_{in}} v_{in} + \frac{1}{RT_{in}K_F} v_{in}^2. \tag{A.1}$$

Here, L, $\mu(T_{in})$, K_D, and K_F are constants. As $p_{in} \to \infty$,

$$\begin{aligned} &\lim_{p_{in}\to\infty} \left[\frac{1}{2L} - \frac{p_{out}^2}{2p_{in}^2 L} \right] \\ &= \lim_{p_{in}\to\infty} \left[\underbrace{\frac{\mu(T_{in})}{K_D p_{in}}}_{=0} v_{in} + \frac{1}{RT_{in}K_F} v_{in}^2 \right]. \end{aligned} \tag{A.2}$$

Isolating the input velocity yields an equation for the Forchheimer velocity limit as

$$v_{in,\,F} = \sqrt{RT_{in}K_F \frac{1 - \left(\frac{p_{out}}{p_{in}}\right)^2}{2L}}. \tag{A.3}$$

In a permeability rig built similarly as the presented one here, the output pressure rises due to the impedance caused by the downstream components, such as the mass flow meter, as the input pressure increases. Hence, the pressure ratio, $\frac{p_{out}}{p_{in}}$, is less than unity but not necessarily nought. However, for a constant or relatively low output pressure, this pressure ratio approaches nought as $p_{out} << p_{in}$, and consequently Eq.(A.3) simplifies to

$$v_{in,\,F} = \sqrt{\frac{RT_{in}K_F}{2L}}. \tag{A.4}$$

Porous materials that feature a Forchheimer-dominant flow and are relatively permeable may pose a problem whilst testing them in an ISO 4022 rig as the threshold velocity may be reached before collecting enough data points. This will require setting up the rig with low range pressure transducers and collect data at much lower velocities. The *Forchheimer Threshold*, however, does not affect the mass flow rate as the input density increases continuously with rising input pressure, and hence there is no ramification thereof in the context of transpiration cooling. The *Forchheimer Threshold* can be exploited to determine the Forchheimer coefficient from Eq.(A.4).

B

Measurement of Flow Quantities

In the Ludwieg tube mode, pre-heated, pressurised air is released into an evacuated test section by opening a plug valve. The air flows through a plenum and then is accelerated by a Laval nozzle before reaching the test section, where the flat-plate model is mounted. For the current experiments, a fill pressure of $p_{\text{fill}} = 2000$ kPa and a fill temperature of $T_{\text{fill}} = 500$ K are selected. The pressure in the plenum upstream of the Laval nozzle is measured and approximated as the total pressure, p_0. The total temperature, T_0, is measured in the test section using differentially heated aspirated thermocouples as described in a previous work by Hermann *et al.* (2019*a*). When a shot is fired, the sudden opening of the plug valve releases expansion waves that travel upstream and reflect back downstream. Each of these reflected expansion waves causes a drop in p_0 and T_0, resulting in a change of the flow condition as shown in Fig. B.1 and B.2. This feature of the tunnel enables testing at multiple quasi-steady conditions – each lasting for approximately 30 ms – from one single shot. These quasi-steady conditions are henceforth referred to as Conditions 1, 2, 3, 4, and 5 (annotated in Fig. B.1 and B.2). The Condition 0 is not considered as it is relatively unsteady.

Since AoA = 0°, the edge Mach number, M_e, is equal to the free-stream Mach number, $M_\infty = 7$. The static edge pressure, p_e, is measured by the pressure transducers instrumented on the flat-plate. The edge velocity is calculated by the equation

$$u_e = M_e \sqrt{\gamma R T_e}, \tag{B.1}$$

where γ and R are respectively the isentropic exponent and specific gas constant of air. The edge unit Reynolds number is obtained from the equation

$$Re_u = \frac{\rho_e u_e}{\mu(T_e)}, \tag{B.2}$$

where $\mu(T_e)$ is the dynamic viscosity of the flow. Since $T_e < 89$ K, Keyes' viscosity model (Keyes, 1952), given as

$$\mu(T_e) = \frac{1.488 \times 10^{-6}\sqrt{T_e}}{1 + \frac{122.1}{T_e} \times 10^{-\frac{5}{T_e}}}, \tag{B.3}$$

is employed. The obtained transient unit Reynolds number is plotted in Fig. B.2.

The blowing ratio, i.e. the ratio of the injected coolant mass flux to the boundary-layer edge mass flux, is defined as

$$F = \frac{\rho_c u_c}{\rho_e u_e}, \tag{B.4}$$

where the subscript 'c' denotes coolant quantities at the surface. Due to continuity, the mass flux in the plenum and the mass flux injected into the boundary layer are equal, hence

$$\rho_c u_c = \rho_{\text{inj}} u_{\text{inj}}, \tag{B.5}$$

where the subscript 'inj' stands for quantities inside the plenum. The density of the coolant can be obtained from the ideal gas law,

$$\rho_{\text{inj}} = \frac{p_{\text{inj}}}{R_c T_{\text{inj}}}, \tag{B.6}$$

where R_c is the specific gas constant of the coolant gas. Substituting Eq.(B.2), Eq.(B.4), Eq.(B.5), Eq.(B.6), and $p_{out} = p_e$ in the integrated version of the Darcy-Forchheimer equation (Ifti *et al.*, 2022*c*) yields a form of the Darcy-Forchheimer equation that is directly dependent on the blowing ratio and unit Reynolds number given as follows:

$$\frac{p_{\text{inj}}^2 - p_e^2}{2LR_cT_{\text{inj}}} = \frac{Re_u\mu(T_e)\mu_c(T_{\text{inj}})}{K_D}F + \frac{(Re_u\mu(T_e))^2}{K_F}F^2. \tag{B.7}$$

The values of permeability coefficients, K_D and K_F, are given in Chapter 3.

With a known unit Reynolds number, Re_u, and a plenum pressure, p_{inj}, the positive solution to Eq.(B.7) with respect to 'F' directly yields the blowing ratio. Note that the gas temperature, T_{inj}, measured by the thermocouple in the plenum is close to room temperature, and therefore the coolant gas viscosity, $\mu_c(T_{\text{inj}})$, is calculated using Sutherland's model (Sutherland, 1853) with appropriate constants for the coolant gas in use. When HDT is fired, a constant gas pressure is set in the plenum by the gas injection system in the HDT. This plenum pressure, p_{inj}, is measured during each test by the pressure transducer fitted in the plenum. In Fig. B.2, the transient blowing ratios obtain from Eq.(B.7) are illustrated for six different plenum pressures. Nitrogen was injected for the first four cases and Helium for the last two. These cases are henceforth defined as Cases 1 to 6. Since the unit Reynolds number drops over time during the whole test period, the blowing ratio increases over time. Similar to the unit Reynolds number, the blowing ratio remains almost constant over each condition, from Condition 1 to Condition 5. As a result, five different blowing ratios are achieved from one single shot. The conditions and cases is given in Tables B.1 to B.4. Time-averaged values are given for the unit Reynolds number, Re_u, and blowing ratio, F. The blowing ratios of Cases 5 and 6 (Helium injection) are respectively matched with Cases 1 and 2 (Nitrogen injection). For a given gas, the factor of increment in the blowing ratio between two consecutive cases is approximately 2.

Case	F [%]	B_h [−]	Coolant gas
1	0.0429	1.57	N_2
2	0.0861	3.15	N_2
3	0.161	5.90	N_2
4	0.313	11.5	N_2
5	0.0434	1.59	He
6	0.0834	3.06	He

Table B.1: Overview of blowing cases. Flow condition: $Re_u = 12.8 \times 10^6$ m^{-1}, $p_0 = 1.619$ MPa, and $T_0 = 455.4$ K.

Case	F [%]	B_h [−]	Coolant gas
1	0.0458	1.68	N_2
2	0.0911	3.34	N_2
3	0.171	6.25	N_2
4	0.333	12.2	N_2
5	0.0456	1.67	He
6	0.0877	3.21	He

Table B.2: Overview of blowing cases. Flow condition: $Re_u = 12.3 \times 10^6$ m^{-1}, $p_0 = 1.506$ MPa, and $T_0 = 449.3$ K.

Case	F [%]	B_h [−]	Coolant gas
1	0.0489	1.79	N_2
2	0.0971	3.55	N_2
3	0.181	6.62	N_2
4	0.355	13.0	N_2
5	0.048	1.76	He
6	0.0922	3.38	He

Table B.3: Overview of blowing cases. Flow condition: $Re_u = 11.8 \times 10^6$ m^{-1}, $p_0 = 1.404$ MPa, and $T_0 = 445.0$ K.

Case	F [%]	B_h [−]	Coolant gas
1	0.0515	1.89	N_2
2	0.102	3.72	N_2
3	0.189	6.93	N_2
4	0.372	13.6	N_2
5	0.0498	1.83	He
6	0.0957	3.51	He

Table B.4: Overview of blowing cases. Flow condition: $Re_u = 11.6 \times 10^6$ m^{-1}, $p_0 = 1.306$ MPa, and $T_0 = 437.8$ K.

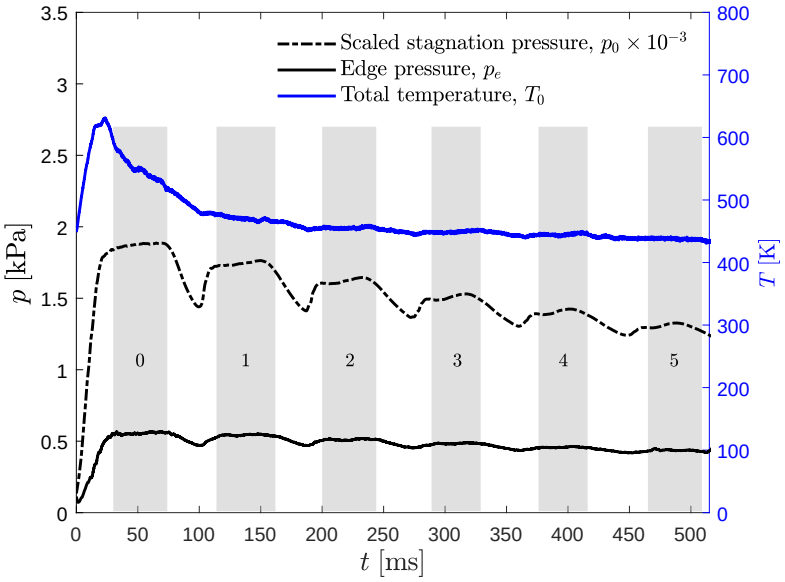

Figure B.1: Measured stagnation pressure, p_0, edge pressure, p_e, and total temperature, T_0, versus test time, t, from one single shot.

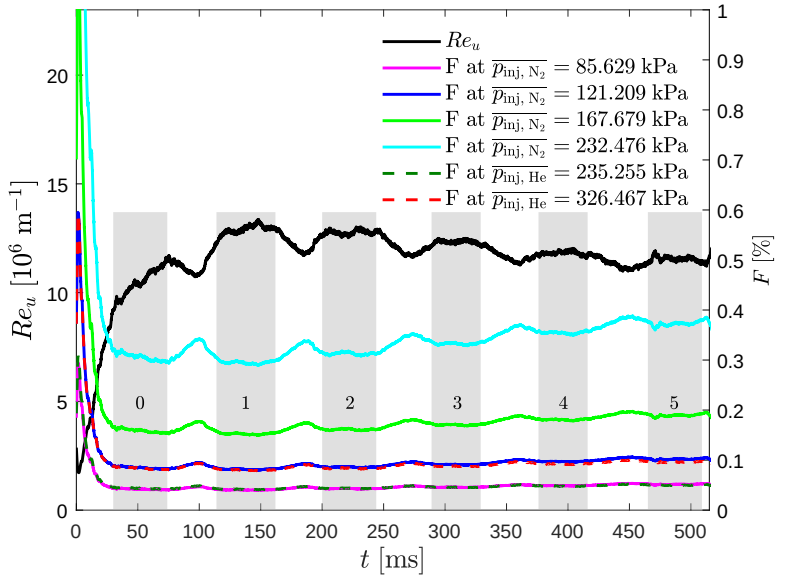

Figure B.2: Unit Reynolds number, Re_u, and blowing ratio, F, versus test time, t. The values of plenum pressure, p_{inj}, are averaged over the test time.

C
Supplementary Results

Shot-to-shot repeatability in the final span-wise averaged concentration effectiveness is demonstrated in Fig. C.1. Here results from two shots, 1190 and 1199, independently calibrated by shots, 1191 and 1198, respectively, are plotted. The results are within $\eta_c = \pm 0.05$.

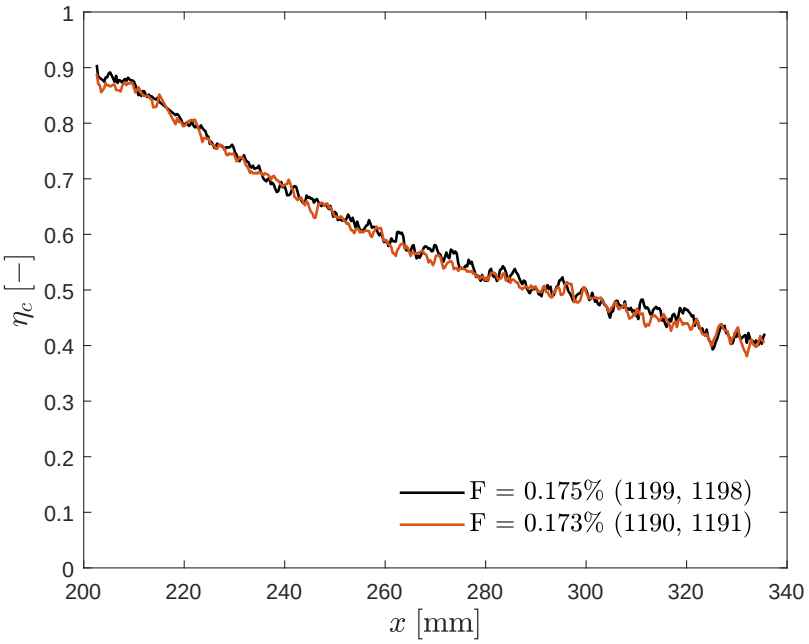

Figure C.1: Repeatability of Case 3: span-wise averaged concentration-based effectiveness, η_c, versus stream-wise direction, x, for shot 1199 calibrated with shot 1198 (black) and shot 1190 calibrated with shot 1191 (red).

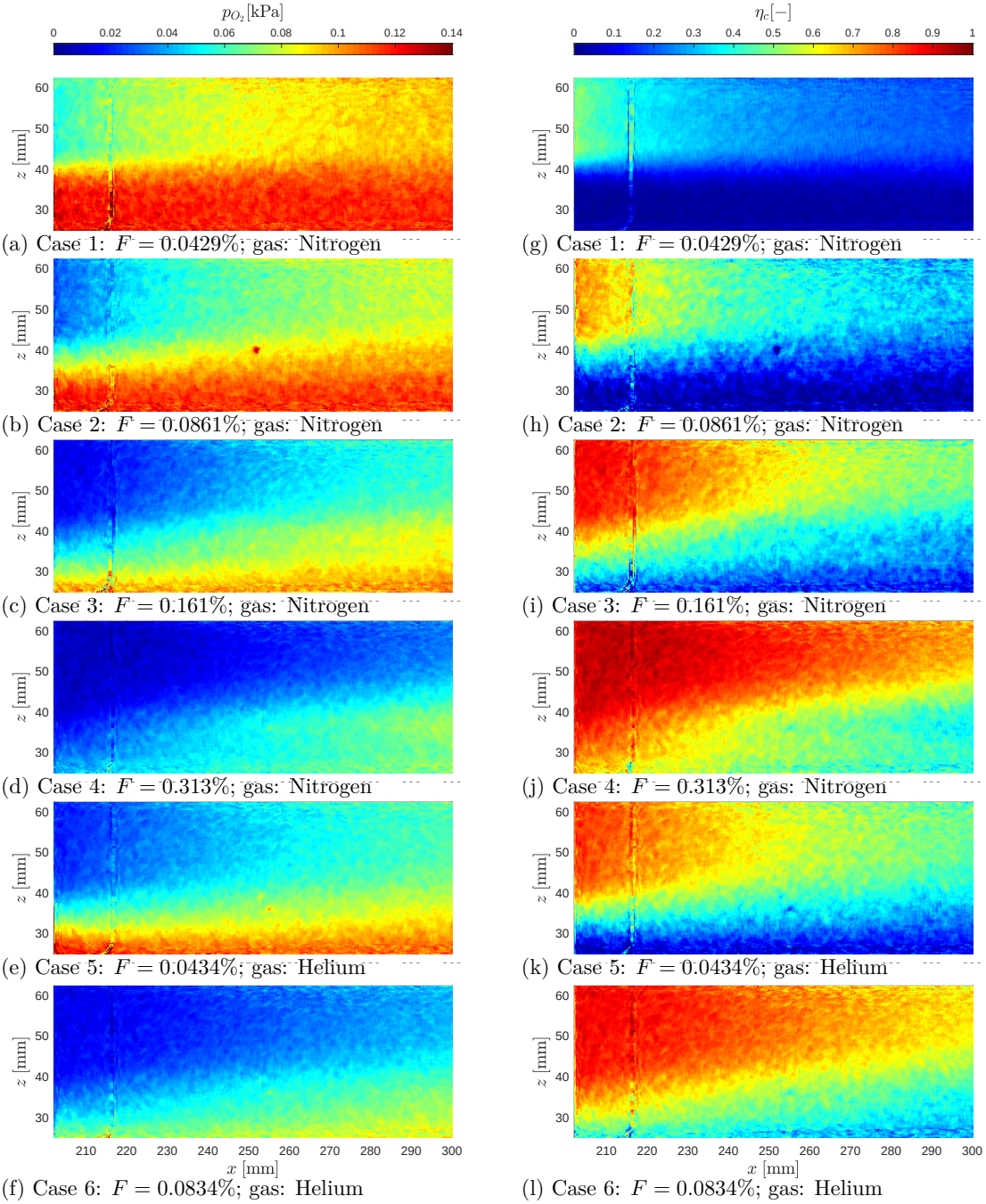

(a) Case 1: $F = 0.0429\%$; gas: Nitrogen (g) Case 1: $F = 0.0429\%$; gas: Nitrogen

(b) Case 2: $F = 0.0861\%$; gas: Nitrogen (h) Case 2: $F = 0.0861\%$; gas: Nitrogen

(c) Case 3: $F = 0.161\%$; gas: Nitrogen (i) Case 3: $F = 0.161\%$; gas: Nitrogen

(d) Case 4: $F = 0.313\%$; gas: Nitrogen (j) Case 4: $F = 0.313\%$; gas: Nitrogen

(e) Case 5: $F = 0.0434\%$; gas: Helium (k) Case 5: $F = 0.0434\%$; gas: Helium

(f) Case 6: $F = 0.0834\%$; gas: Helium (l) Case 6: $F = 0.0834\%$; gas: Helium

Figure C.2: PSP results for Cases 1 to 6 (top to bottom) at $Re_u = 12.8 \times 10^6$ m^{-1}: Contours of downstream Oxygen partial pressure, p_{O_2}, from (a) to (f) and film effectiveness, η_c, from (g) to (l). Refer to Fig. 4.2a for axis origin.

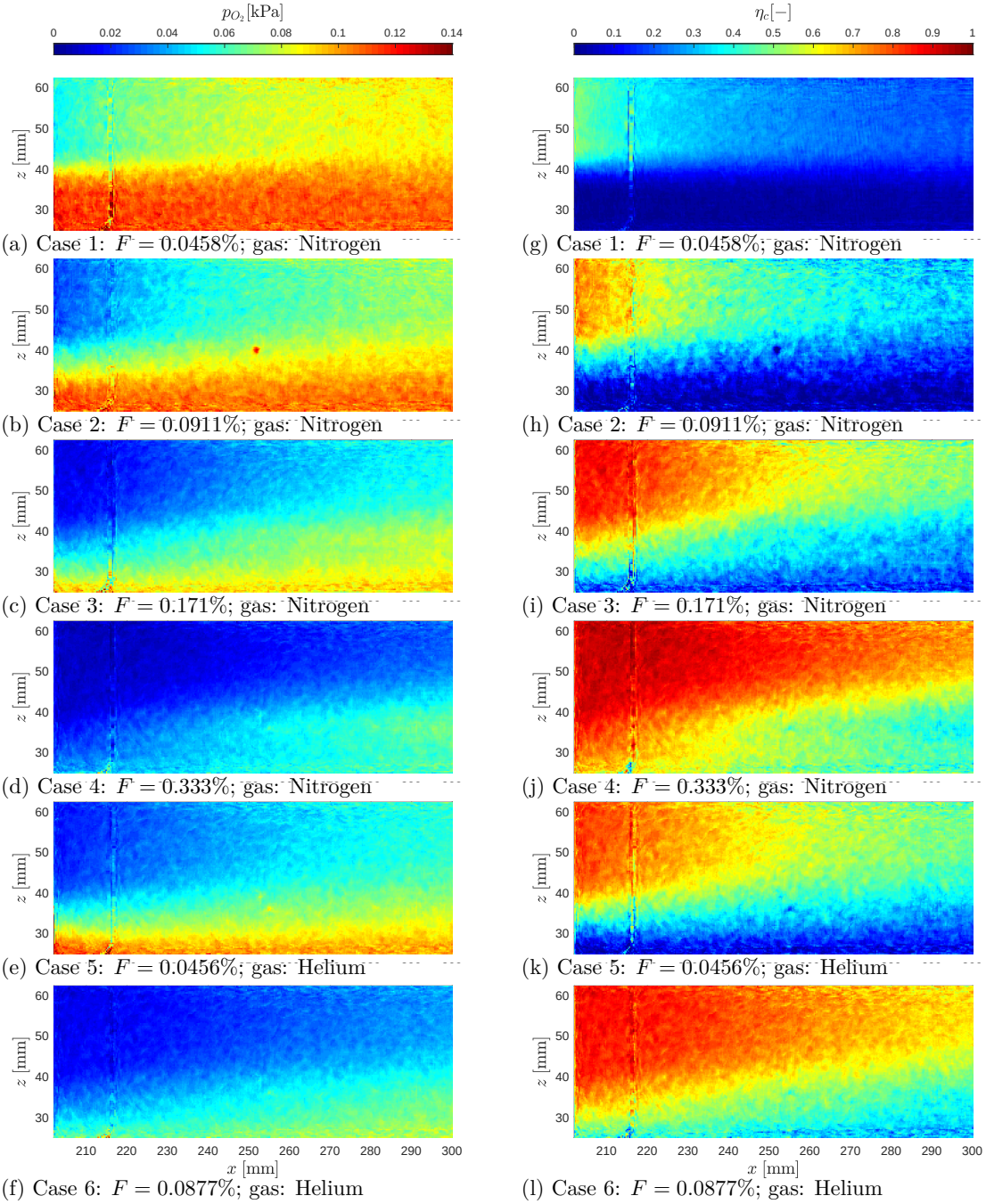

(a) Case 1: $F = 0.0458\%$; gas: Nitrogen (g) Case 1: $F = 0.0458\%$; gas: Nitrogen

(b) Case 2: $F = 0.0911\%$; gas: Nitrogen (h) Case 2: $F = 0.0911\%$; gas: Nitrogen

(c) Case 3: $F = 0.171\%$; gas: Nitrogen (i) Case 3: $F = 0.171\%$; gas: Nitrogen

(d) Case 4: $F = 0.333\%$; gas: Nitrogen (j) Case 4: $F = 0.333\%$; gas: Nitrogen

(e) Case 5: $F = 0.0456\%$; gas: Helium (k) Case 5: $F = 0.0456\%$; gas: Helium

(f) Case 6: $F = 0.0877\%$; gas: Helium (l) Case 6: $F = 0.0877\%$; gas: Helium

Figure C.3: PSP results for Cases 1 to 6 (top to bottom) at $Re_u = 12.3 \times 10^6$ m^{-1}: Contours of downstream Oxygen partial pressure, p_{O_2}, from (a) to (f) and film effectiveness, η_c, from (g) to (l). Refer to Fig. 4.2a for axis origin.

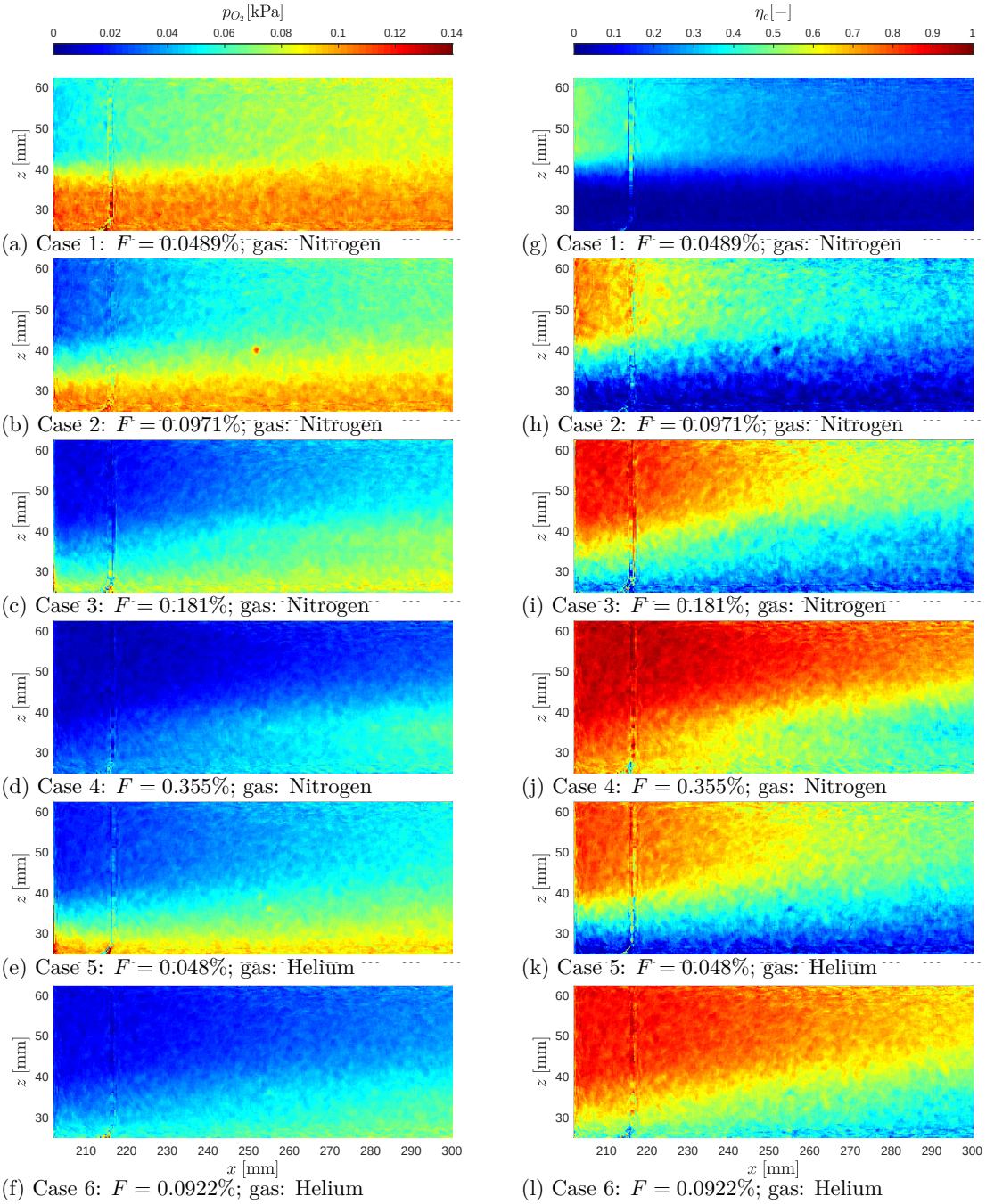

(a) Case 1: $F = 0.0489\%$; gas: Nitrogen (g) Case 1: $F = 0.0489\%$; gas: Nitrogen

(b) Case 2: $F = 0.0971\%$; gas: Nitrogen (h) Case 2: $F = 0.0971\%$; gas: Nitrogen

(c) Case 3: $F = 0.181\%$; gas: Nitrogen (i) Case 3: $F = 0.181\%$; gas: Nitrogen

(d) Case 4: $F = 0.355\%$; gas: Nitrogen (j) Case 4: $F = 0.355\%$; gas: Nitrogen

(e) Case 5: $F = 0.048\%$; gas: Helium (k) Case 5: $F = 0.048\%$; gas: Helium

(f) Case 6: $F = 0.0922\%$; gas: Helium (l) Case 6: $F = 0.0922\%$; gas: Helium

Figure C.4: PSP results for Cases 1 to 6 (top to bottom) at $Re_u = 11.8 \times 10^6$ m^{-1}: Contours of downstream Oxygen partial pressure, p_{O_2}, from (a) to (f) and film effectiveness, η_c, from (g) to (l). Refer to Fig. 4.2a for axis origin.

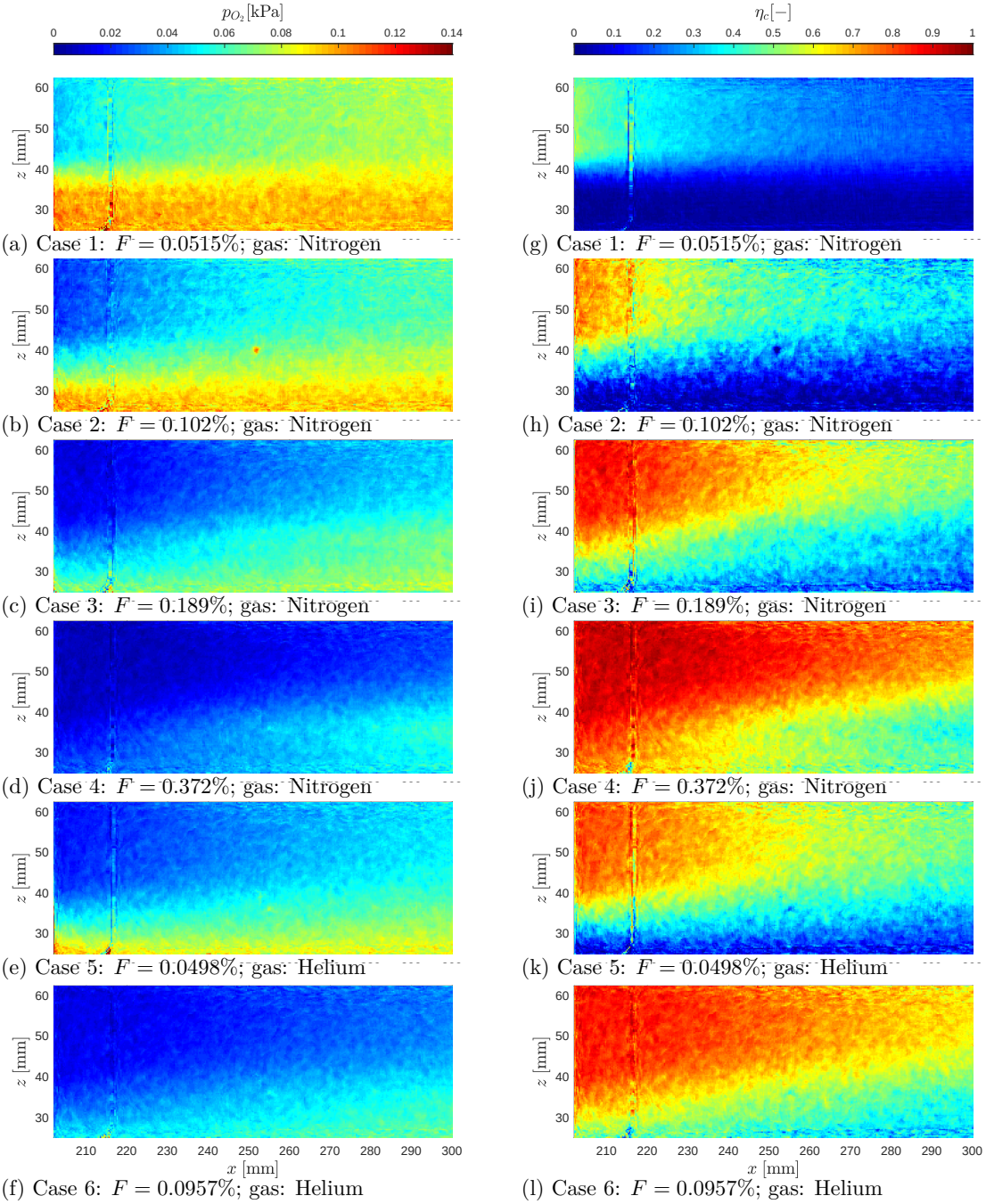

(a) Case 1: $F = 0.0515\%$; gas: Nitrogen (g) Case 1: $F = 0.0515\%$; gas: Nitrogen

(b) Case 2: $F = 0.102\%$; gas: Nitrogen (h) Case 2: $F = 0.102\%$; gas: Nitrogen

(c) Case 3: $F = 0.189\%$; gas: Nitrogen (i) Case 3: $F = 0.189\%$; gas: Nitrogen

(d) Case 4: $F = 0.372\%$; gas: Nitrogen (j) Case 4: $F = 0.372\%$; gas: Nitrogen

(e) Case 5: $F = 0.0498\%$; gas: Helium (k) Case 5: $F = 0.0498\%$; gas: Helium

(f) Case 6: $F = 0.0957\%$; gas: Helium (l) Case 6: $F = 0.0957\%$; gas: Helium

Figure C.5: PSP results for Cases 1 to 6 (top to bottom) at $Re_u = 11.6 \times 10^6$ m^{-1}: Contours of downstream Oxygen partial pressure, p_{O_2}, from (a) to (f) and film effectiveness, η_c, from (g) to (l). Refer to Fig. 4.2a for axis origin.

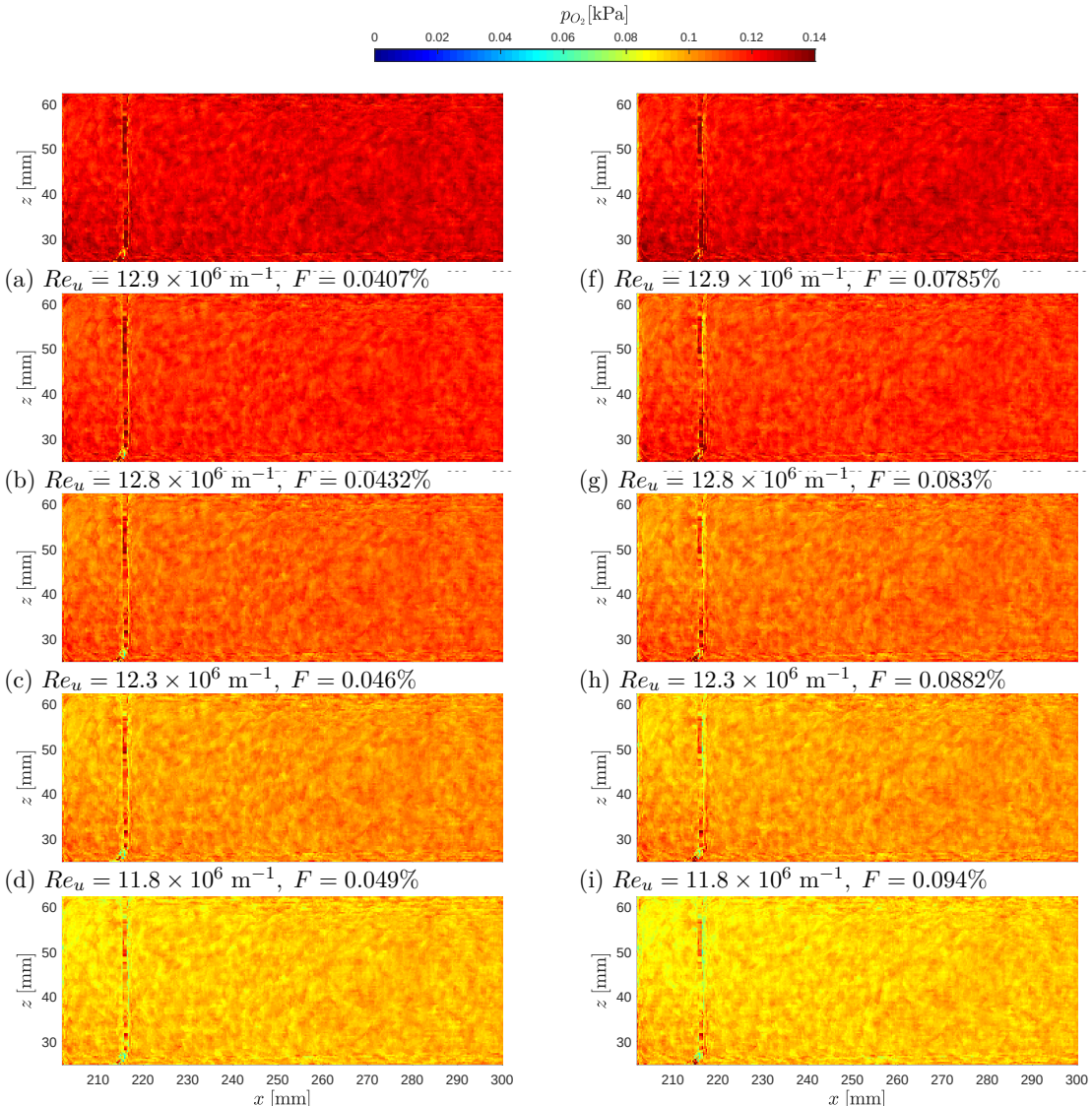

(a) $Re_u = 12.9 \times 10^6$ m^{-1}, $F = 0.0407\%$

(b) $Re_u = 12.8 \times 10^6$ m^{-1}, $F = 0.0432\%$

(c) $Re_u = 12.3 \times 10^6$ m^{-1}, $F = 0.046\%$

(d) $Re_u = 11.8 \times 10^6$ m^{-1}, $F = 0.049\%$

(e) $Re_u = 11.6 \times 10^6$ m^{-1}, $F = 0.0515\%$

(f) $Re_u = 12.9 \times 10^6$ m^{-1}, $F = 0.0785\%$

(g) $Re_u = 12.8 \times 10^6$ m^{-1}, $F = 0.083\%$

(h) $Re_u = 12.3 \times 10^6$ m^{-1}, $F = 0.0882\%$

(i) $Re_u = 11.8 \times 10^6$ m^{-1}, $F = 0.094\%$

(j) $Re_u = 11.6 \times 10^6$ m^{-1}, $F = 0.0992\%$

Figure C.6: Contours of downstream oxygen partial pressure, p_{O_2}, with air injection obtained from PSP data.

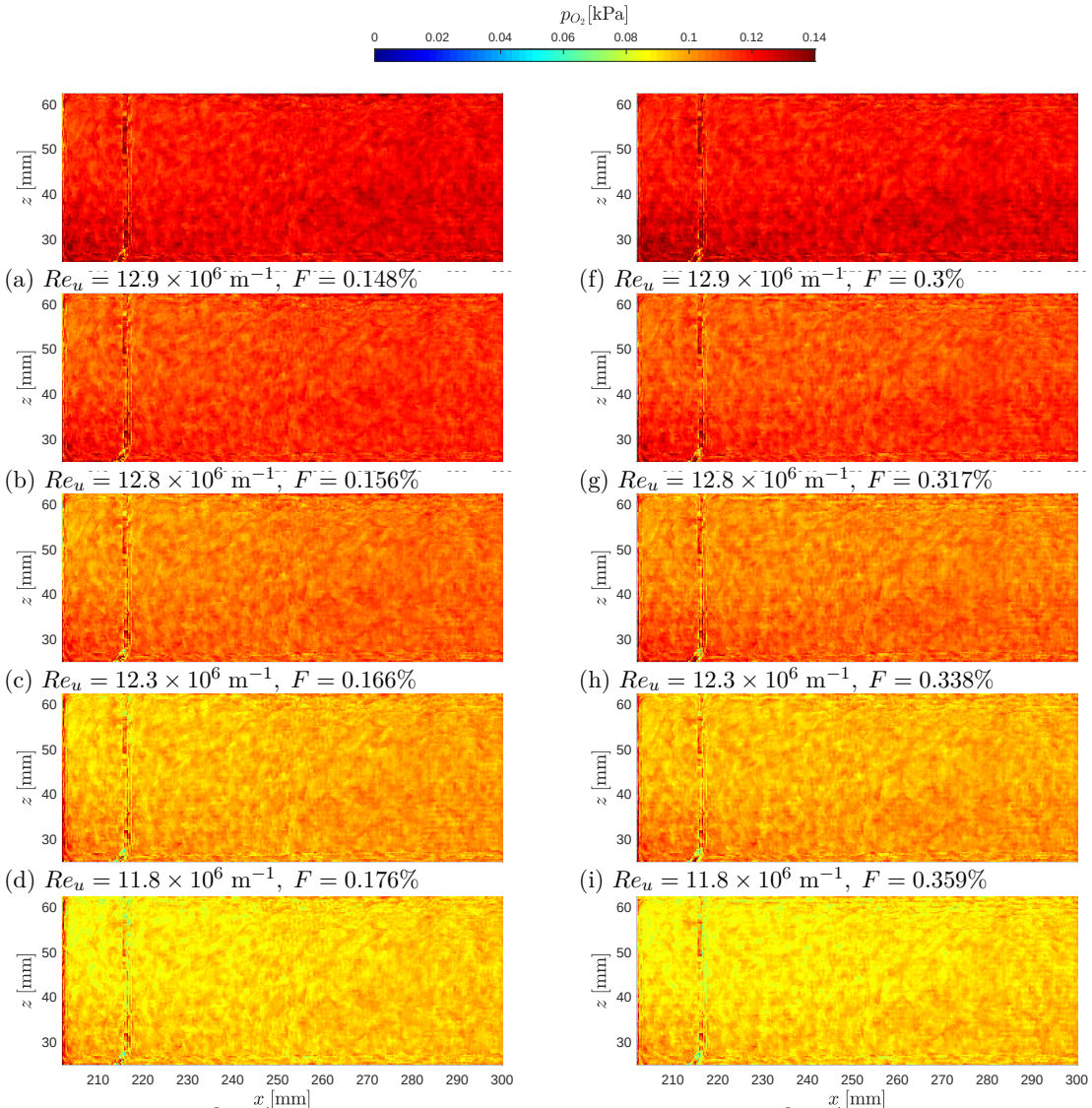

(a) $Re_u = 12.9 \times 10^6$ m^{-1}, $F = 0.148\%$
(b) $Re_u = 12.8 \times 10^6$ m^{-1}, $F = 0.156\%$
(c) $Re_u = 12.3 \times 10^6$ m^{-1}, $F = 0.166\%$
(d) $Re_u = 11.8 \times 10^6$ m^{-1}, $F = 0.176\%$
(e) $Re_u = 11.6 \times 10^6$ m^{-1}, $F = 0.185\%$
(f) $Re_u = 12.9 \times 10^6$ m^{-1}, $F = 0.3\%$
(g) $Re_u = 12.8 \times 10^6$ m^{-1}, $F = 0.317\%$
(h) $Re_u = 12.3 \times 10^6$ m^{-1}, $F = 0.338\%$
(i) $Re_u = 11.8 \times 10^6$ m^{-1}, $F = 0.359\%$
(j) $Re_u = 11.6 \times 10^6$ m^{-1}, $F = 0.377\%$

Figure C.7: Contours of downstream oxygen partial pressure, p_{O_2}, with air injection obtained from PSP data.

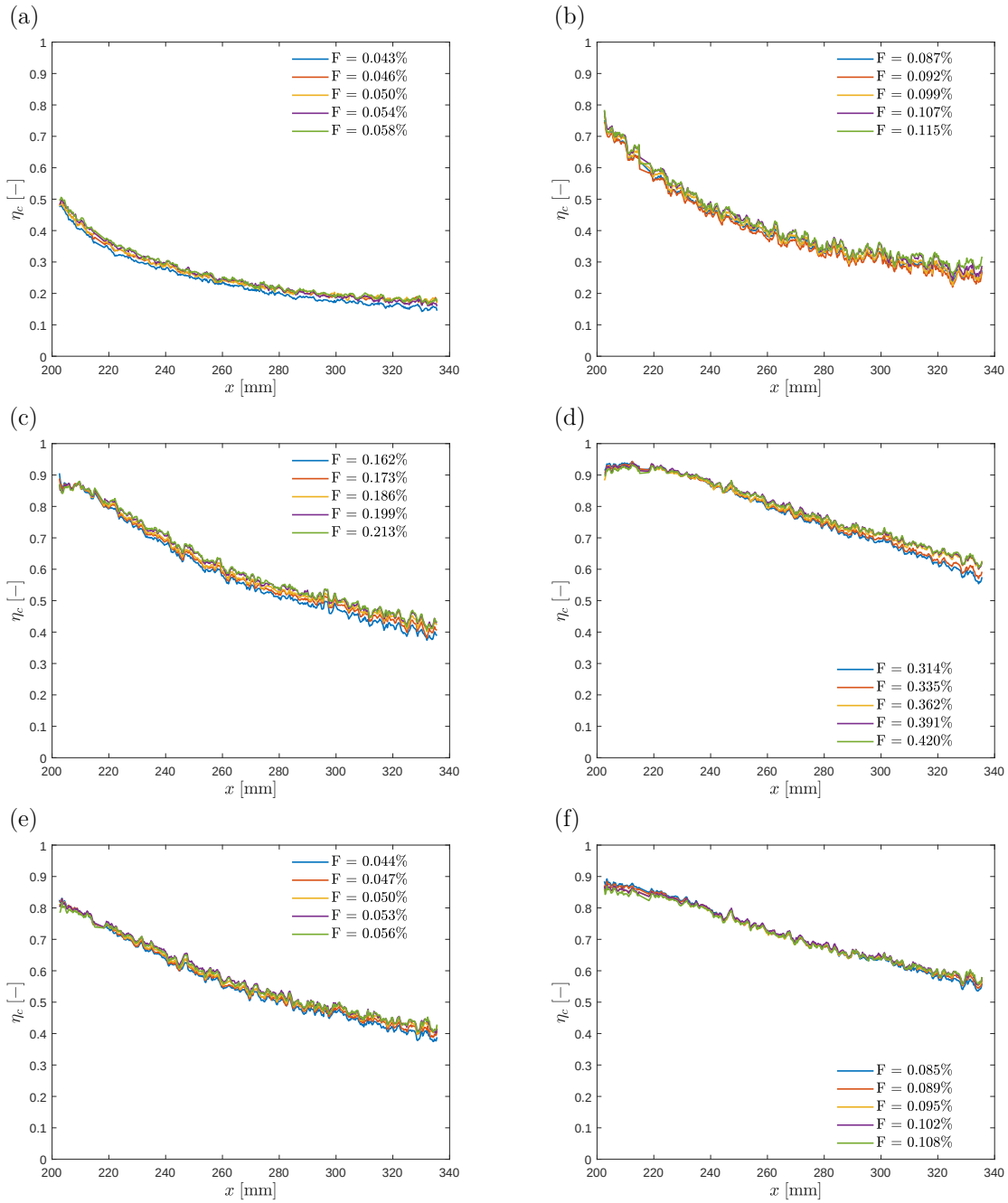

Figure C.8: Span-wise averaged concentration-based effectiveness versus stream-wise direction for Conditions 1 to 5 : (a) Case 1, (b) Case 2, (c) Case 3, (d) Case 4, (e) Case 5, and (f) Case 6.

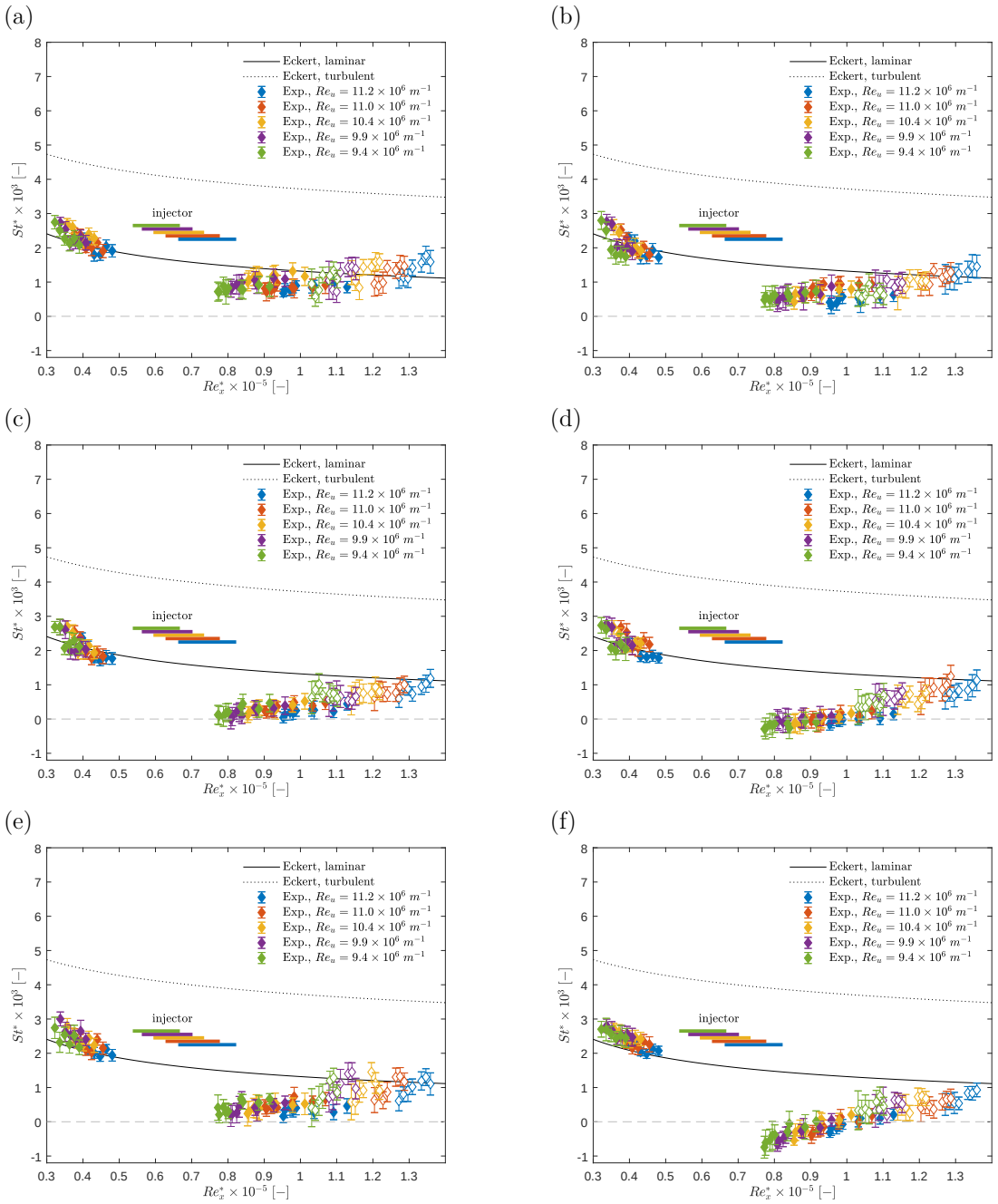

Figure C.9: Reference Stanton number versus reference Reynolds number based on the stream-wise direction for (a) Case 1, (b) Case 2, (c) Case 3, (d) Case 4, (e) Case 5, and (f) Case 6. Note: data points from gauges located downstream of $x = 300$ mm are face-marked with the colour white.

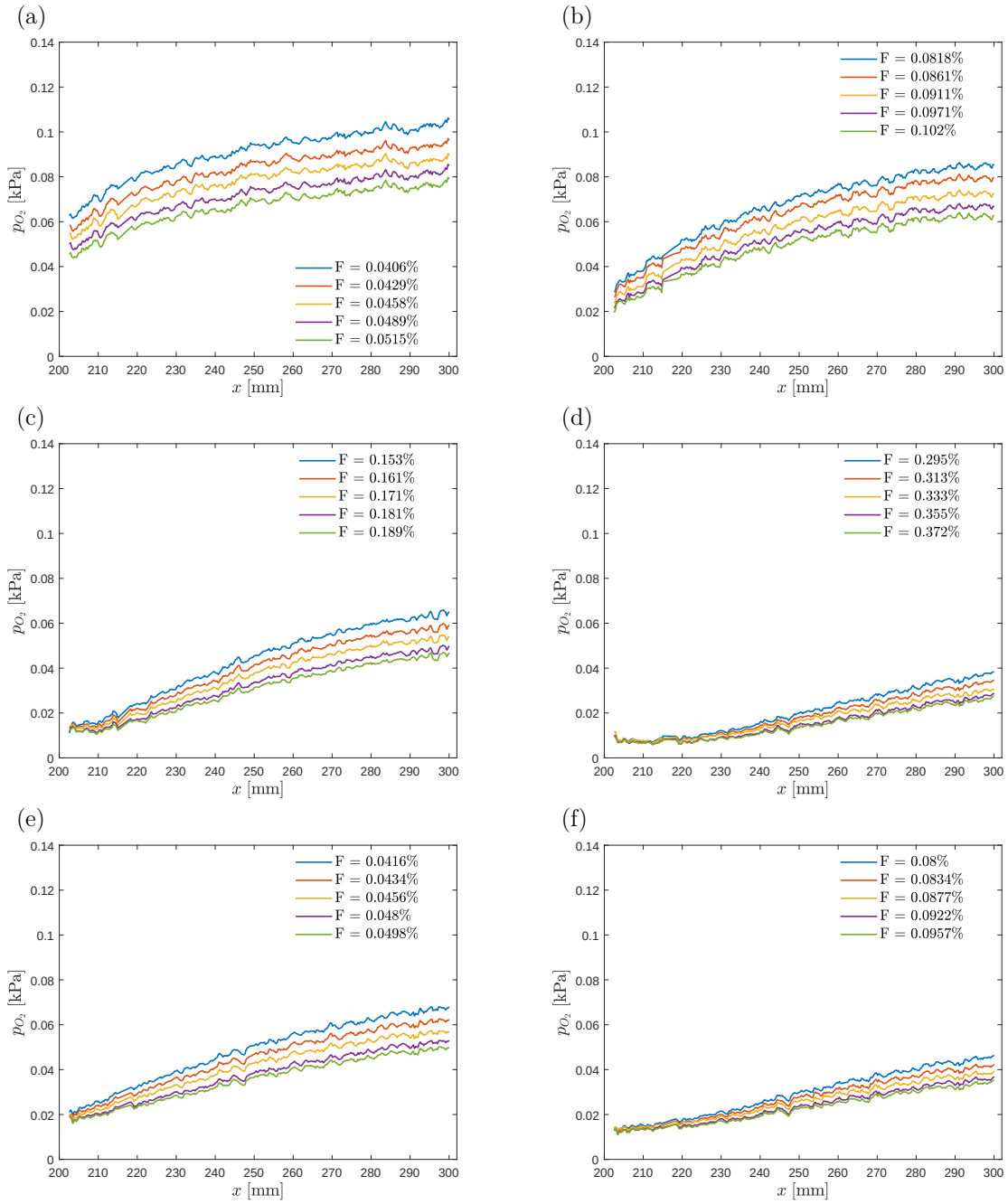

Figure C.10: Span-wise averaged plots : (a) Case 1, (b) Case 2, (c) Case 3, (d) Case 4, (e) Case 5, and (f) Case 6.

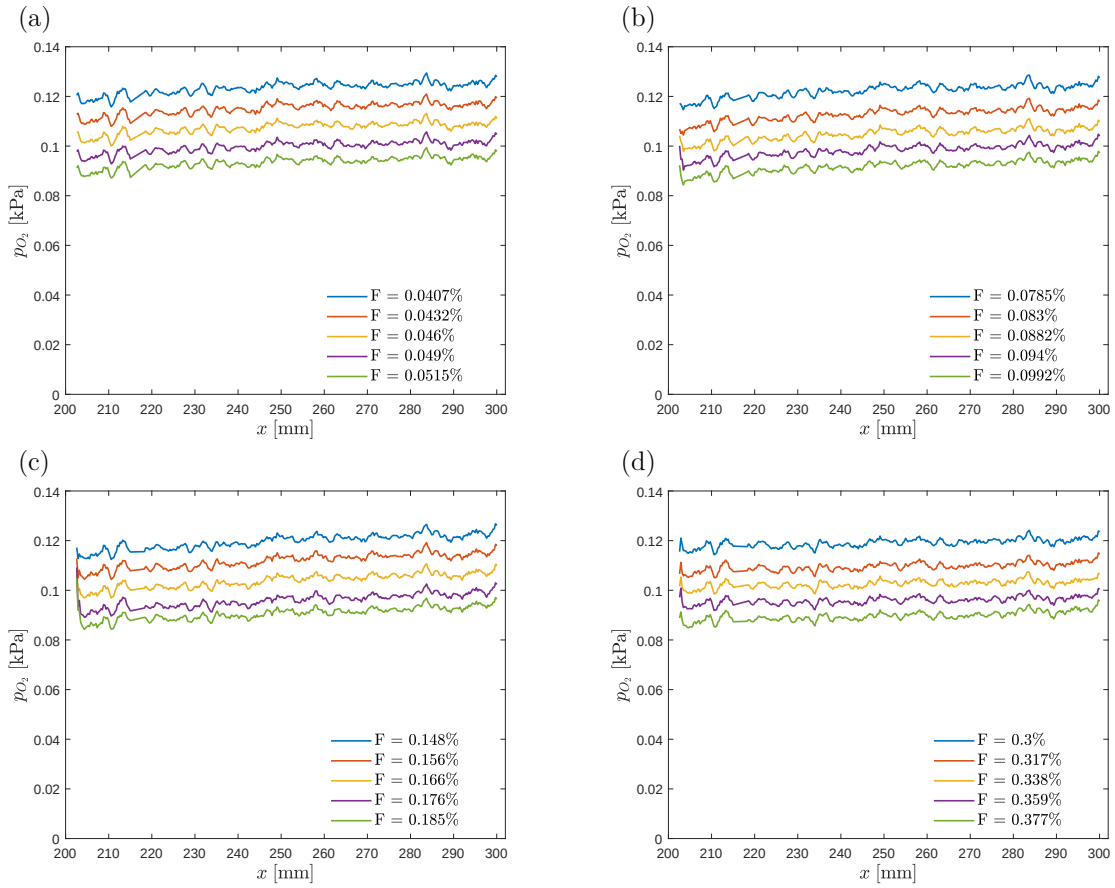

Figure C.11: Span-wise averaged plots (air): (a) Case 1, (b) Case 2, (c) Case 3, and (d) Case 4.

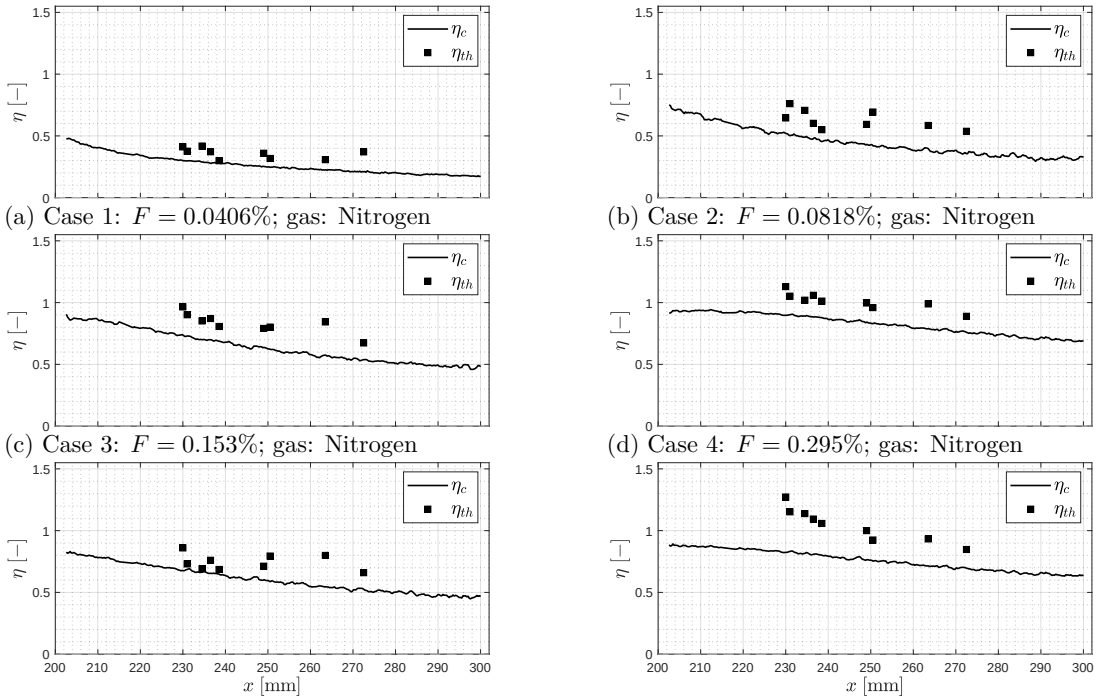

(a) Case 1: $F = 0.0406\%$; gas: Nitrogen
(b) Case 2: $F = 0.0818\%$; gas: Nitrogen
(c) Case 3: $F = 0.153\%$; gas: Nitrogen
(d) Case 4: $F = 0.295\%$; gas: Nitrogen
(e) Case 5: $F = 0.0416\%$; gas: Helium
(f) Case 6: $F = 0.08\%$; gas: Helium

Figure C.12: Concentration effectiveness, η_c, and thermal effectiveness, η_{th}, versus stream-wise direction, x, at $Re_u = 12.9 \times 10^6$ m^{-1} for (a) Case 1, (b) Case 2, (c) Case 3, (d) Case 4, (e) Case 5, and (f) Case 6.

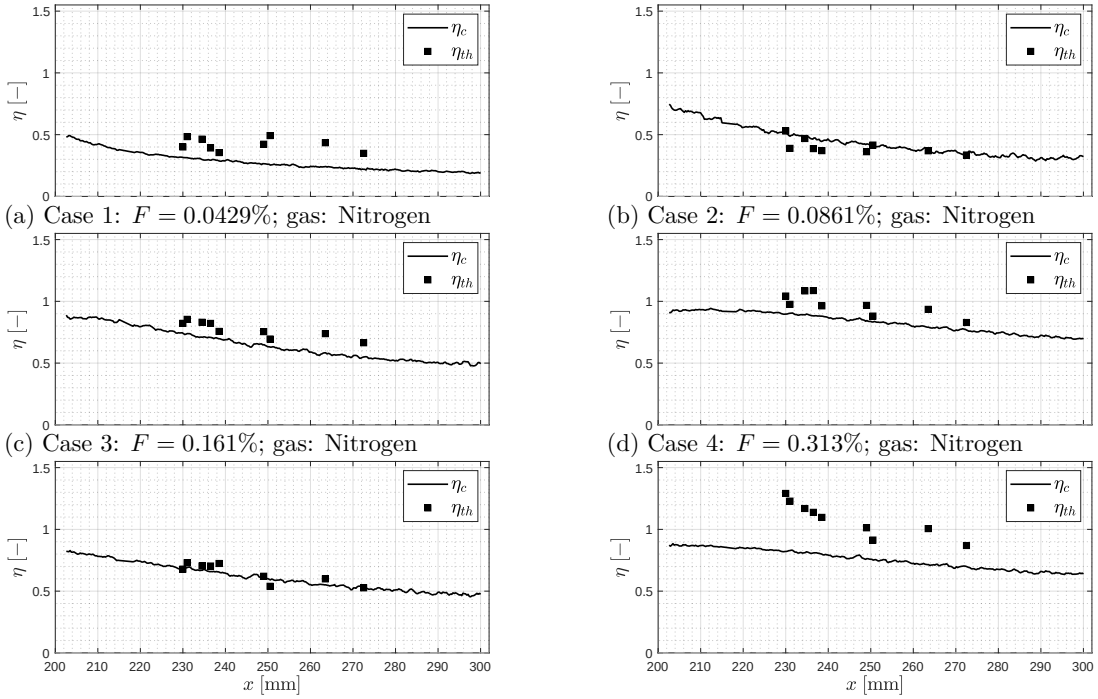

(a) Case 1: $F = 0.0429\%$; gas: Nitrogen
(b) Case 2: $F = 0.0861\%$; gas: Nitrogen
(c) Case 3: $F = 0.161\%$; gas: Nitrogen
(d) Case 4: $F = 0.313\%$; gas: Nitrogen
(e) Case 5: $F = 0.0434\%$; gas: Helium
(f) Case 6: $F = 0.0834\%$; gas: Helium

Figure C.13: Concentration-based effectiveness, η_c, and thermal effectiveness, η_{th}, versus stream-wise direction, x, at $Re_u = 12.8 \times 10^6$ m^{-1} for (a) Case 1, (b) Case 2, (c) Case 3, (d) Case 4, (e) Case 5, and (f) Case 6.

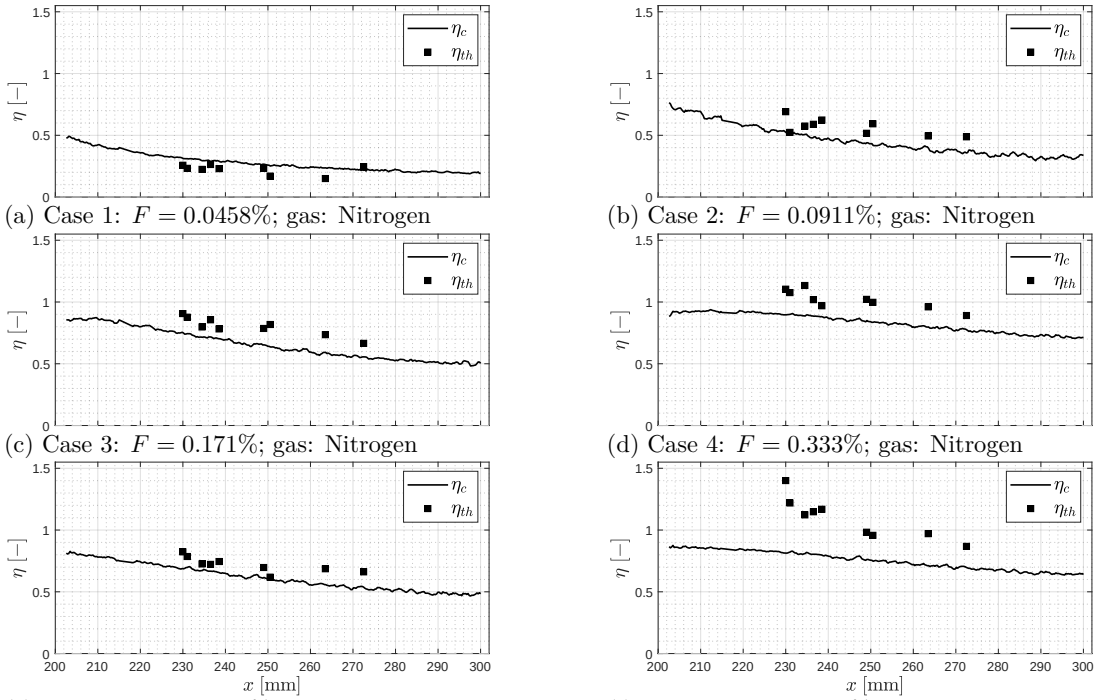

(a) Case 1: $F = 0.0458\%$; gas: Nitrogen
(b) Case 2: $F = 0.0911\%$; gas: Nitrogen
(c) Case 3: $F = 0.171\%$; gas: Nitrogen
(d) Case 4: $F = 0.333\%$; gas: Nitrogen
(e) Case 5: $F = 0.0456\%$; gas: Helium
(f) Case 6: $F = 0.0877\%$; gas: Helium

Figure C.14: Concentration-based effectiveness, η_c, and thermal effectiveness, η_{th}, versus stream-wise direction, x, at $Re_u = 12.3 \times 10^6$ m^{-1} for (a) Case 1, (b) Case 2, (c) Case 3, (d) Case 4, (e) Case 5, and (f) Case 6.

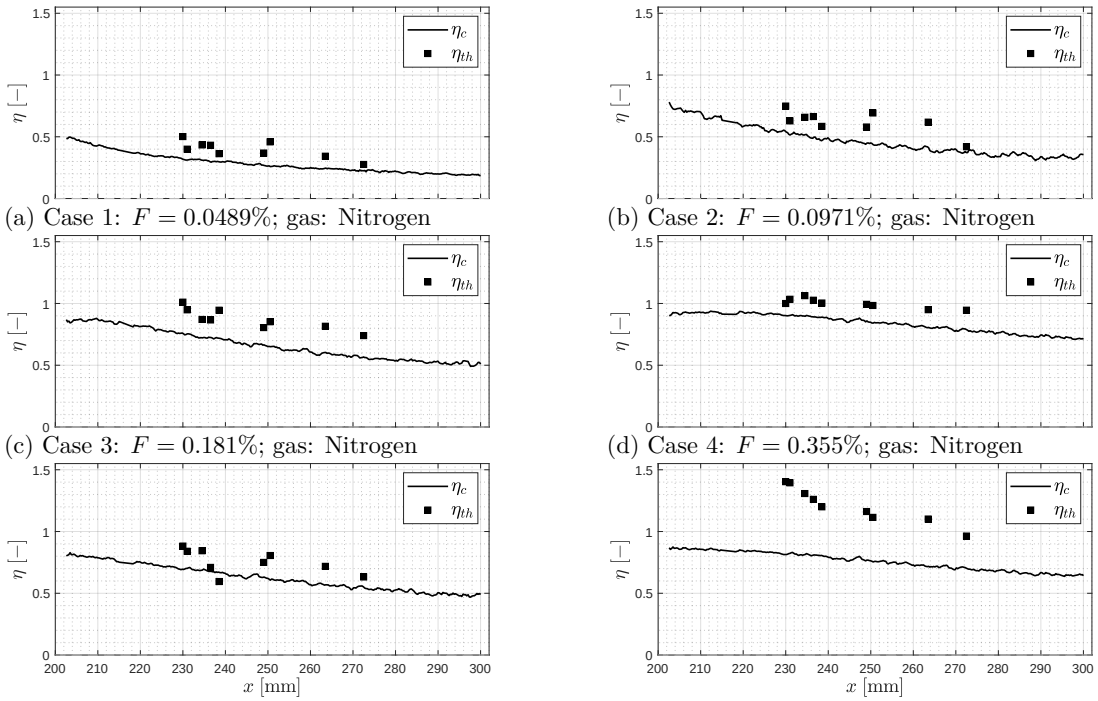

(a) Case 1: $F = 0.0489\%$; gas: Nitrogen
(b) Case 2: $F = 0.0971\%$; gas: Nitrogen
(c) Case 3: $F = 0.181\%$; gas: Nitrogen
(d) Case 4: $F = 0.355\%$; gas: Nitrogen
(e) Case 5: $F = 0.048\%$; gas: Helium
(f) Case 6: $F = 0.0922\%$; gas: Helium

Figure C.15: Concentration-based effectiveness, η_c, and thermal effectiveness, η_{th}, versus stream-wise direction, x, at $Re_u = 11.8 \times 10^6$ m^{-1} for (a) Case 1, (b) Case 2, (c) Case 3, (d) Case 4, (e) Case 5, and (f) Case 6.

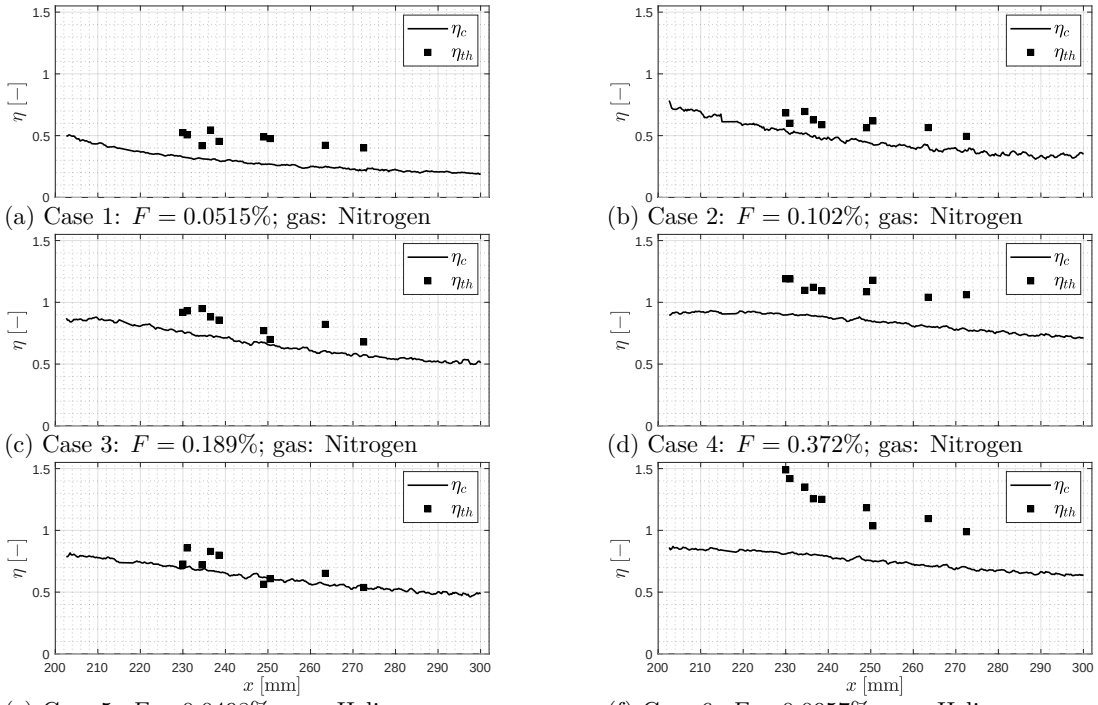

(a) Case 1: $F = 0.0515\%$; gas: Nitrogen

(b) Case 2: $F = 0.102\%$; gas: Nitrogen

(c) Case 3: $F = 0.189\%$; gas: Nitrogen

(d) Case 4: $F = 0.372\%$; gas: Nitrogen

(e) Case 5: $F = 0.0498\%$; gas: Helium

(f) Case 6: $F = 0.0957\%$; gas: Helium

Figure C.16: Concentration-based effectiveness, η_c, and thermal effectiveness, η_{th}, versus stream-wise direction, x, at $Re_u = 11.6 \times 10^6$ m^{-1} for (a) Case 1, (b) Case 2, (c) Case 3, (d) Case 4, (e) Case 5, and (f) Case 6.

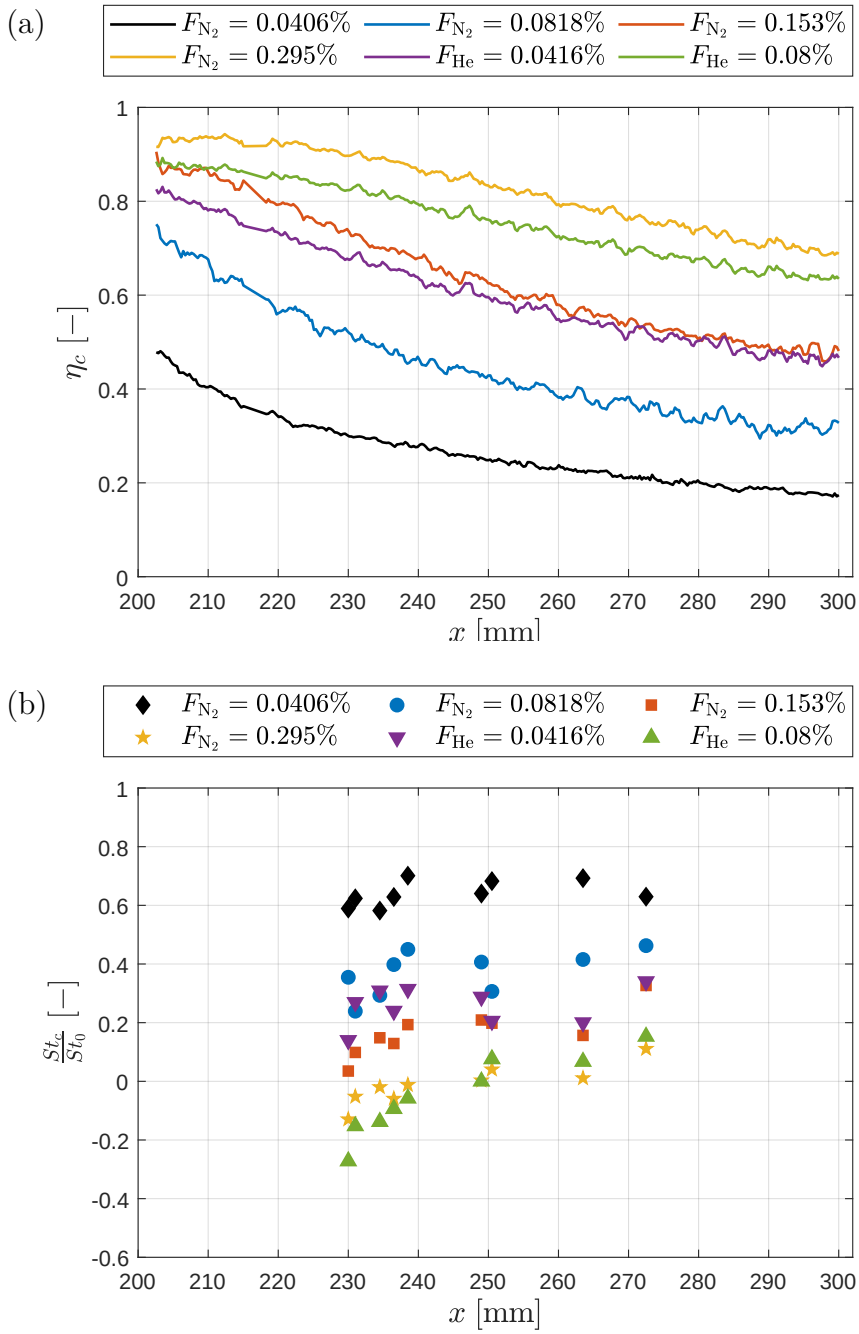

Figure C.17: (a) Span-wise averaged concentration effectiveness, η_c, versus stream-wise direction and (b) Stanton number reduction versus stream-wise direction. $Re_u = 12.9 \times 10^6$ m^{-1}.

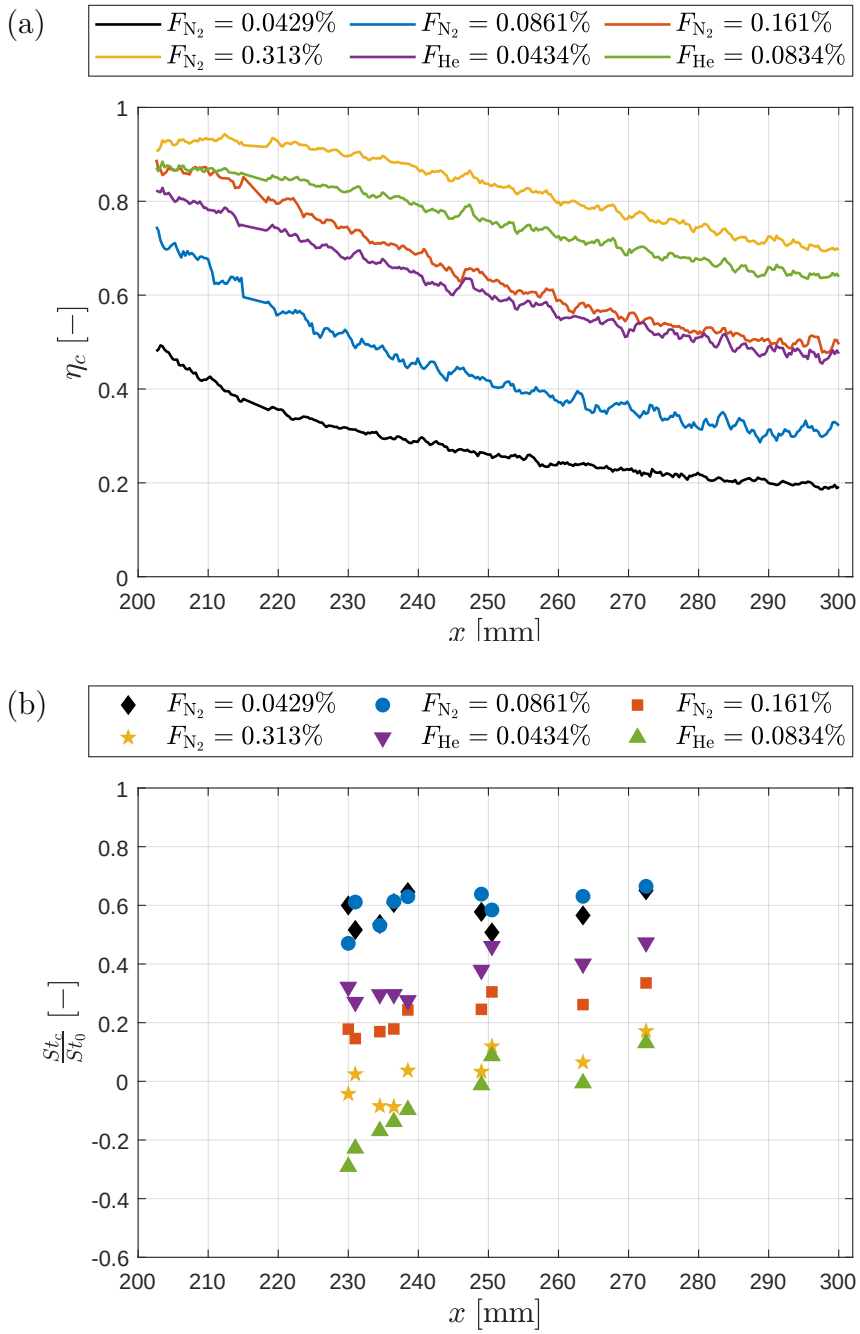

Figure C.18: (a) Span-wise averaged concentration effectiveness, η_c, versus stream-wise direction and (b) Stanton number reduction versus stream-wise direction. $Re_u = 12.8 \times 10^6$ m^{-1}.

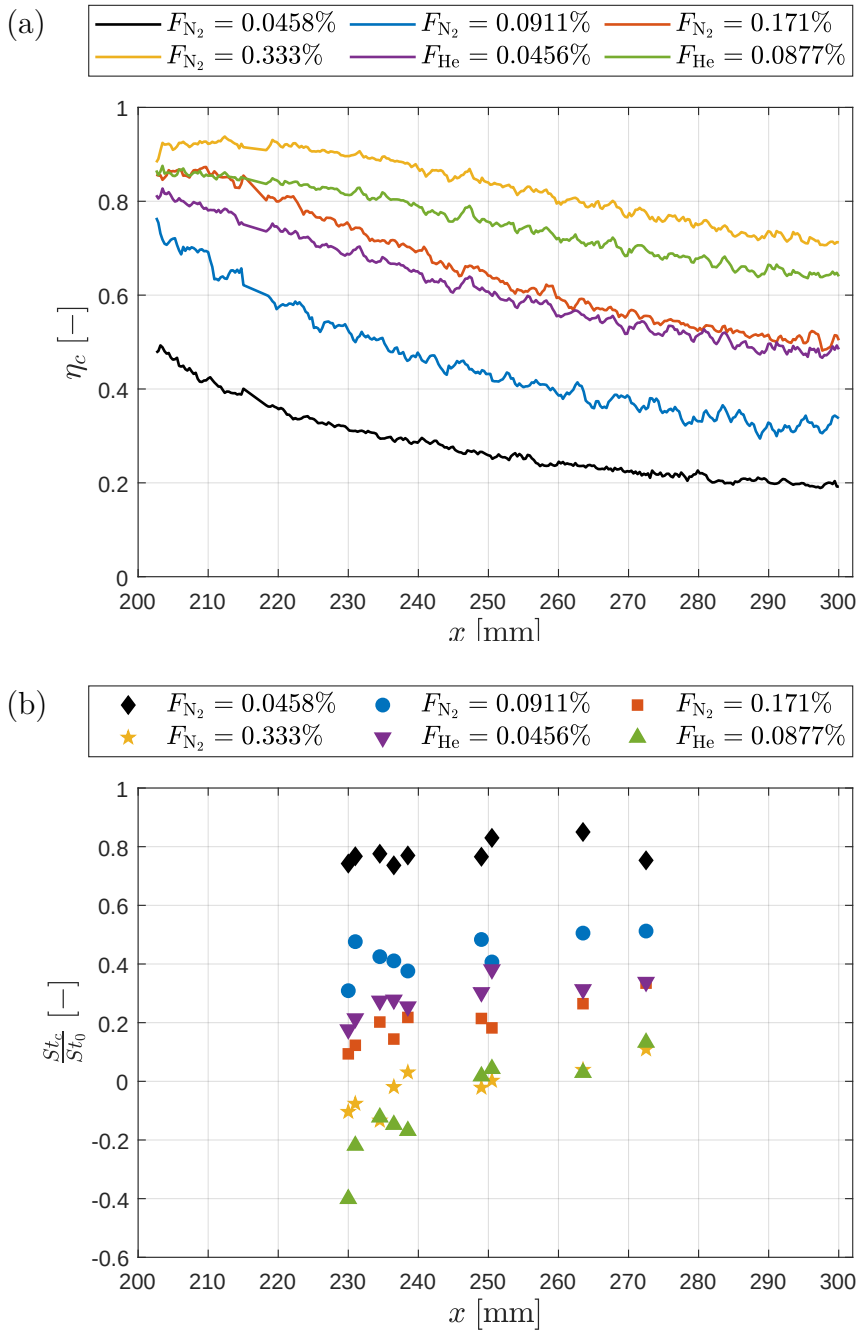

Figure C.19: (a) Span-wise averaged concentration effectiveness, η_c, versus stream-wise direction and (b) Stanton number reduction versus stream-wise direction. $Re_u = 12.3 \times 10^6$ m^{-1}.

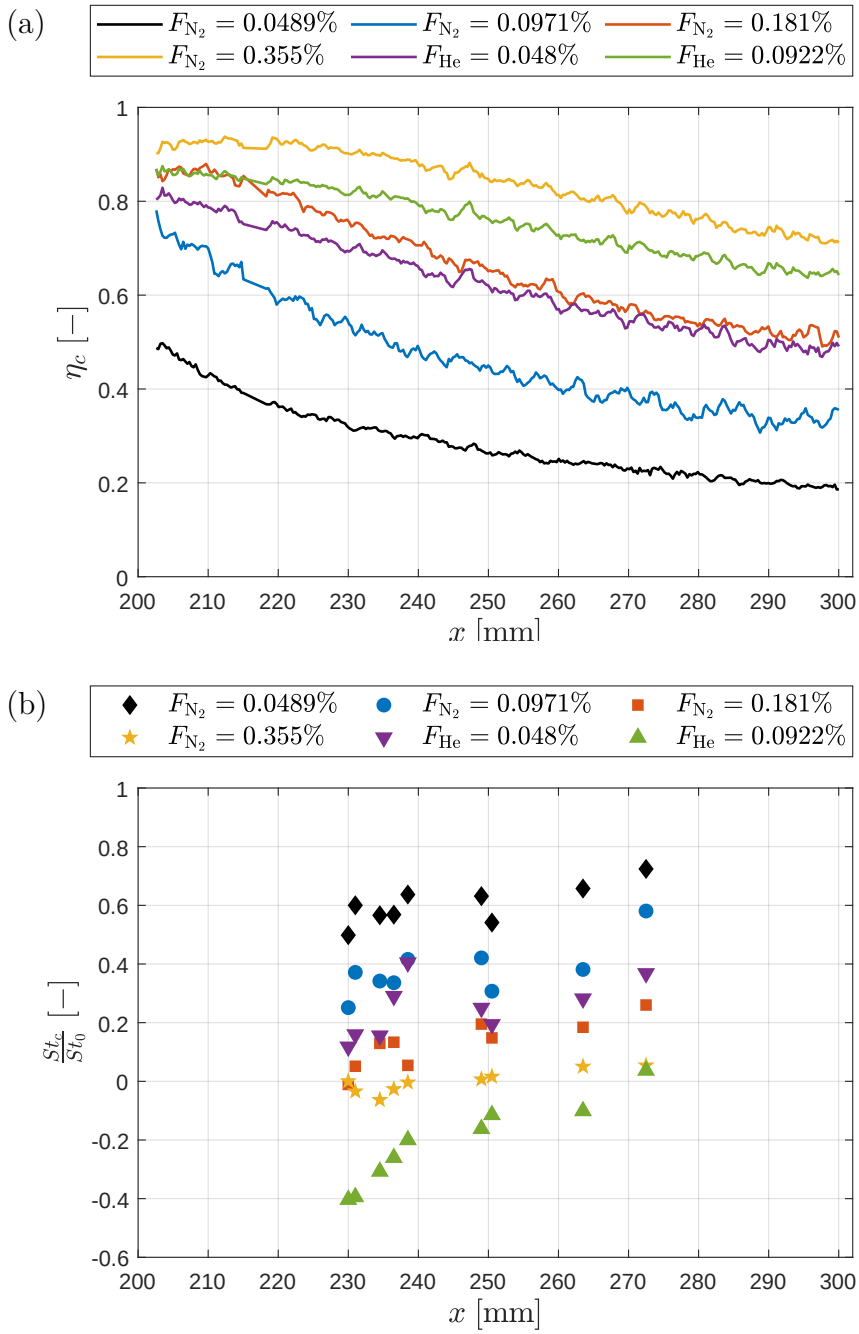

Figure C.20: (a) Span-wise averaged concentration effectiveness, η_c, versus stream-wise direction and (b) Stanton number reduction versus stream-wise direction. $Re_u = 11.8 \times 10^6$ m^{-1}.

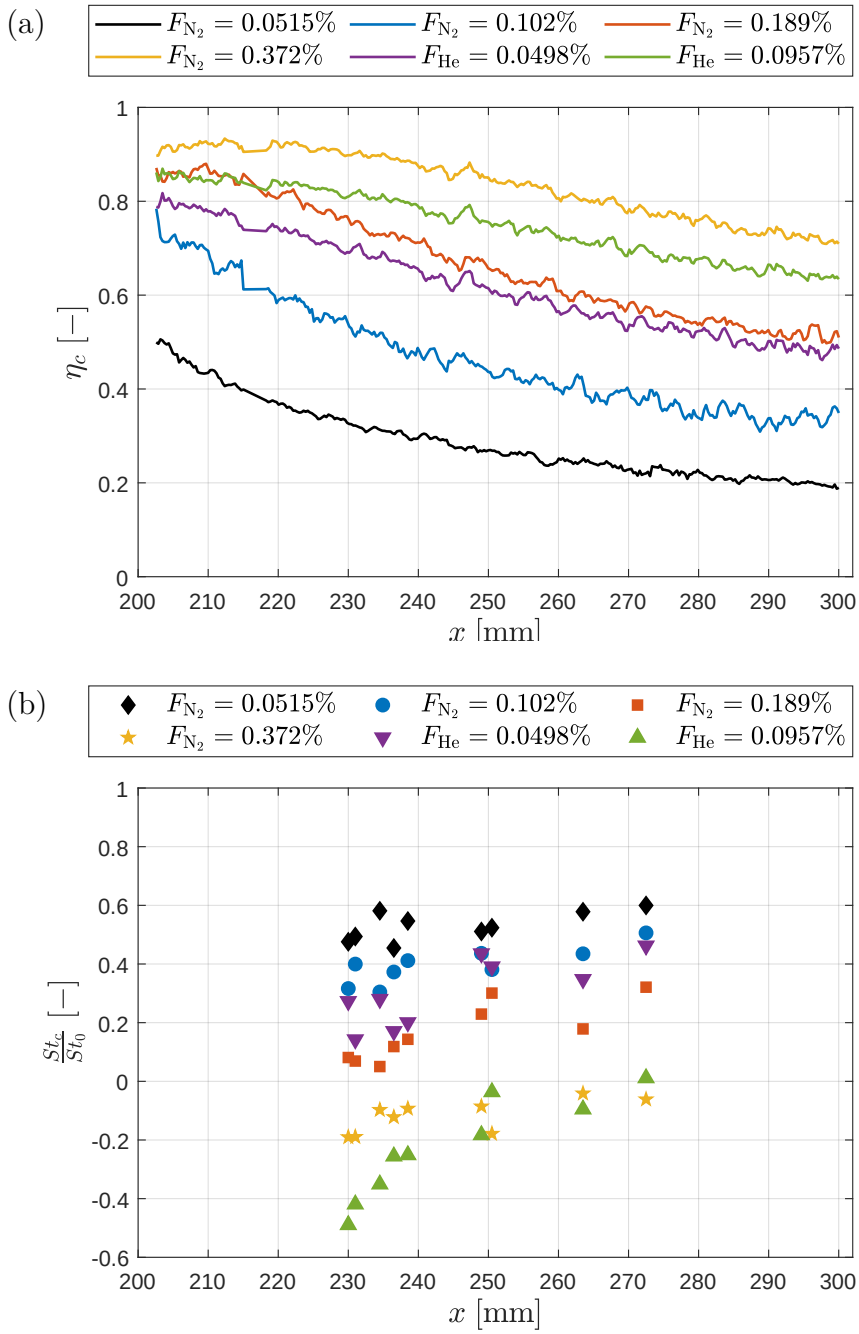

Figure C.21: (a) Span-wise averaged concentration effectiveness, η_c, versus stream-wise direction and (b) Stanton number reduction versus stream-wise direction. $Re_u = 11.6 \times 10^6$ m^{-1}.

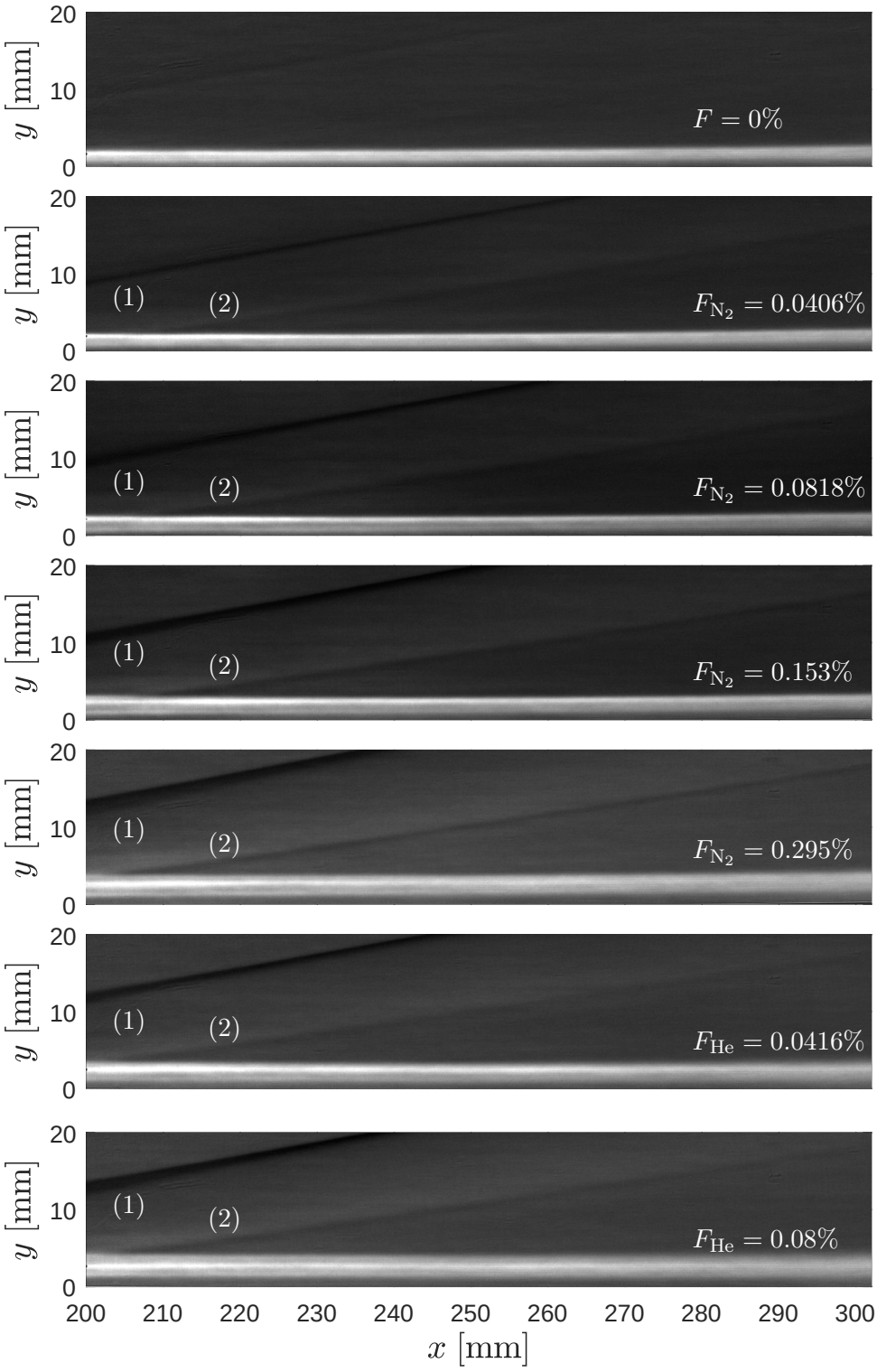

Figure C.22: Schlieren (experiment): all cases at $Re_u = 12.9 \times 10^6$ m^{-1}. View field starts immediately downstream of the injector. Shocks emanating from the start and end of the injector are respectively denoted with 1 and 2.

D
Uncertainty Analysis

The Kulites were calibrated against a reference pressure gauge (Infcon CDG025D) within the range of operation for the test campaign. The systematic uncertainties from installation effects for the Kulites and the reference gauge are estimated to be ±1% and ±0.5%, respectively. The reference gauges has a reading error of ±0.2%. The final systematic uncertainty for the calibrated Kulites are $\sqrt{1^2 + 0.5^2 + 0.2^2} = 1.14\%$, which represents the uncertainties in the measured static pressure, p_e, and the plenum pressure, p_{inj}. The uncertainty in the total temperature, T_0, and hence the edge temperature, T_e, is estimated to be ±3 K assuming steady state (Hermann *et al.*, 2019*a*). Error propagation according to Moffat (1988) yields uncertainties of ±3.34% and ±9.95% for the edge velocity, u_e, and edge density ρ_e, respectively. An uncertainty of ±11.0% in F is obtained by an error propagation in Eq.(B.7) with the uncertainties in p_e, p_{inj}, T_e, u_e, ρ_e, K_D and K_F (see Chapter 3) as input sources.

With an estimated uncertainty of ±9.5% in the wall heat flux, $\dot{q}_w$ (Hermann *et al.*, 2019*a*), a further error propagation yields uncertainties of ±25.6% for the Stanton number, St, and ±29.5% for the blowing parameter, B_h.

As reported in Ewenz Rocher *et al.* (2022), the overall uncertainty in the PSP intensity ratio, I_{ref}/I, is $\leq$ 2%. Since it is calibrated with pressure data obtained from the Kulites, the final error in the pressure measurements from PSP is $\leq \sqrt{2^2 + 1.14^2} = \pm 2.3\%$. According to Eq.(4.4), this results in an uncertainty of $\leq \pm 5\%$ in η_c.

The flat-plate model was mounted on a custom-made table in the test section, which has been used in several campaigns before Hermann *et al.* (2018); Ewenz Rocher *et al.* (2022) for an angle of attack of AoA = 0°. Its relative

positioning with respect to the tunnel is consistent with the automated traverse employed in Wylie (2020). The incoming flow can be misaligned with respect to the model by up to $-0.4°$ (Wylie, 2020, Chapter 5). A conservative estimate of $\pm 0.4°$ of uncertainty in the angle of attack results in uncertainties of up to 7.1% and 2.0% in the edge pressure, p_e, and the edge temperature, T_e, respectively.

E

Mach Angle Analysis and Technical Drawings

Results of a Mach angle analysis for the flat-plate model at Mach 7 is shown in Fig. E.1. The Mach cones emanating from the two corners meet at a distance of $x = 433$ mm from the leading edge. The green zone between the two cones is free of disturbance stemming from the corners, and therefore a 2D flow can be assumed here.

In addition, relevant technical drawings of the flat-plate model are enclosed herein. The internal pipework of the coolant injection system and locations of the slots for sensors are presented in the drawings.

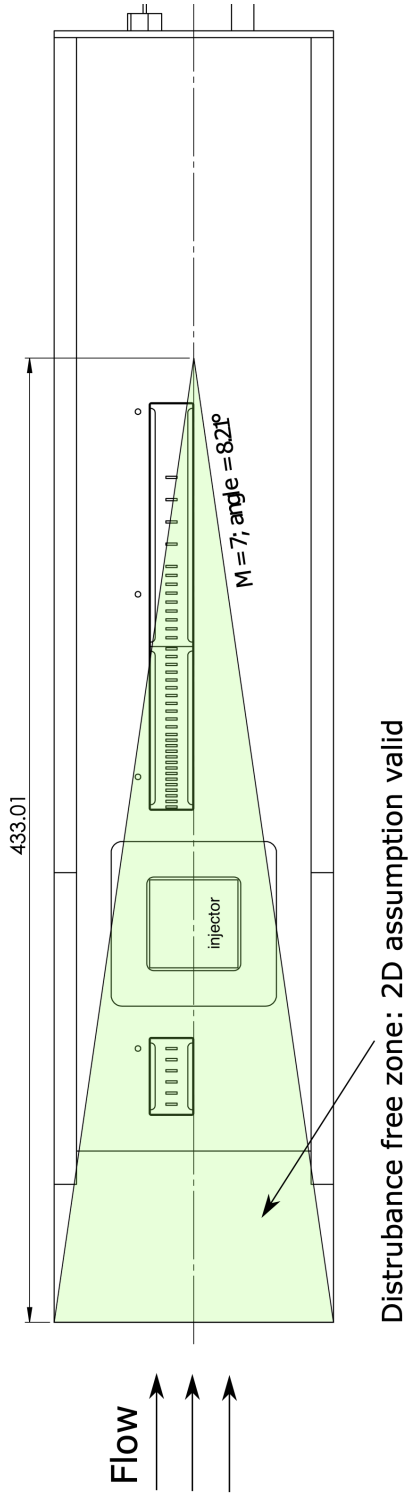

Figure E.1: Schematic of the flat-plate model with Mach cones emanating from the corners. The green zone denotes the area where a 2D assumption is valid.

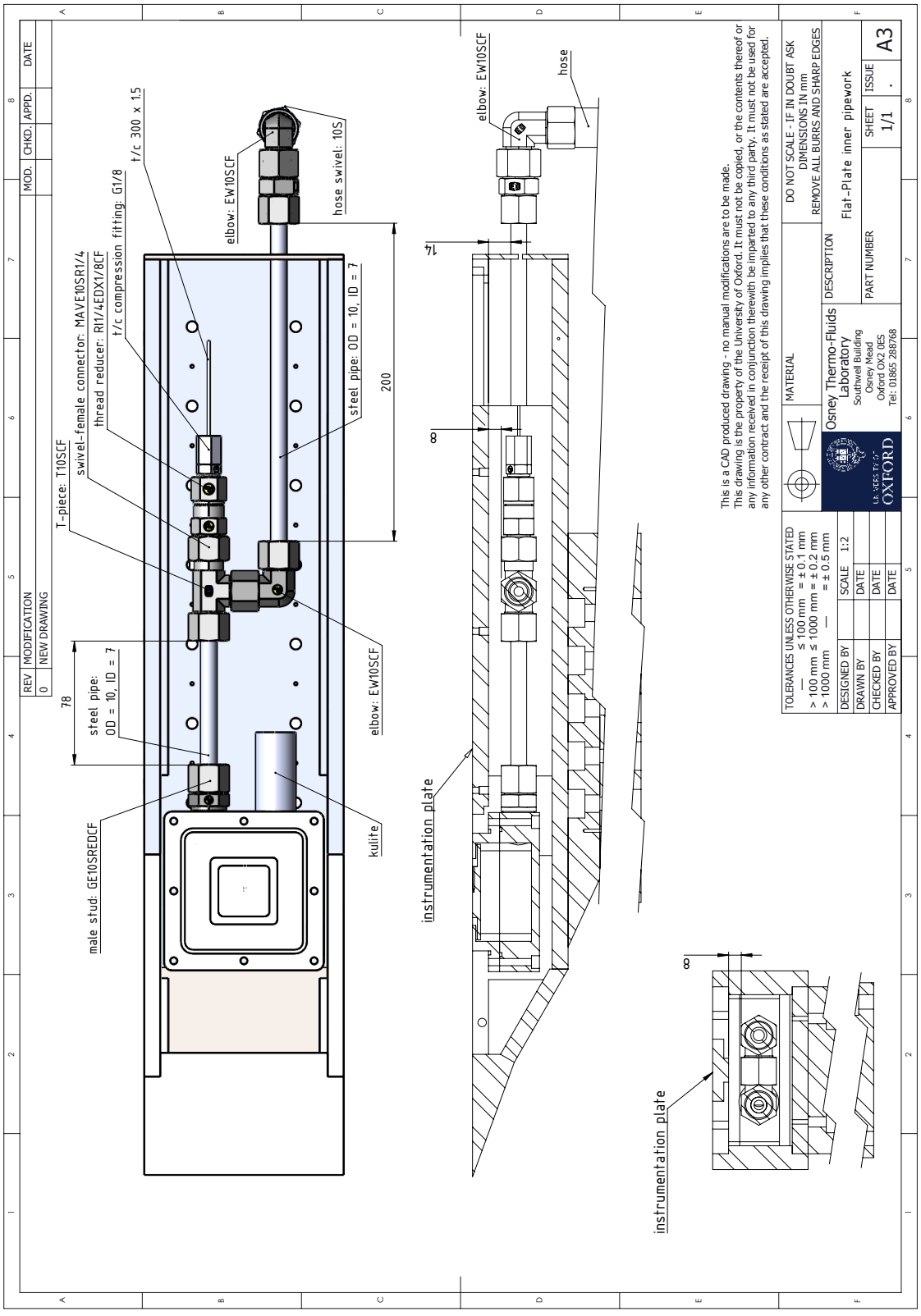
REV
MODIFICATION
DATE
MOD.
CHKD.
APPD.
0
NEW DRAWING
T-piece: T10SCF
swivel-female connector: MAVE10SR1/4
thread reducer: R11/4EDX1/8CF
t/c compression fitting: G1/8
t/c 300 x 1.5
elbow: EW10SCF
hose swivel: 10S
steel pipe: OD = 10, ID = 7
200
78
steel pipe:
OD = 10, ID = 7
elbow: EW10SCF
male stud: GE10SREDCF
kulite
instrumentation plate
elbow: EW10SCF
hose
12
8
instrumentation plate
8
This is a CAD produced drawing - no manual modifications are to be made.
This drawing is the property of the University of Oxford. It must not be copied, or the contents thereof or any information received in conjunction therewith be imparted to any third party. It must not be used for any other contract and the receipt of this drawing implies that these conditions as stated are accepted.
MATERIAL
DO NOT SCALE - IF IN DOUBT ASK
DIMENSIONS IN mm
REMOVE ALL BURRS AND SHARP EDGES
DESCRIPTION
Flat-Plate inner pipework
PART NUMBER
SHEET
1/1
ISSUE
.
A3
TOLERANCES UNLESS OTHERWISE STATED
— ≤ 100 mm = ± 0.1 mm
> 100 mm ≤ 1000 mm = ± 0.2 mm
> 1000 mm — = ± 0.5 mm
DESIGNED BY
SCALE 1:2
DRAWN BY
DATE
CHECKED BY
DATE
APPROVED BY
DATE
Osney Thermo-Fluids Laboratory
Southwell Building
Osney Mead
Oxford OX2 0ES
Tel: 01865 288768
UNIVERSITY OF OXFORD

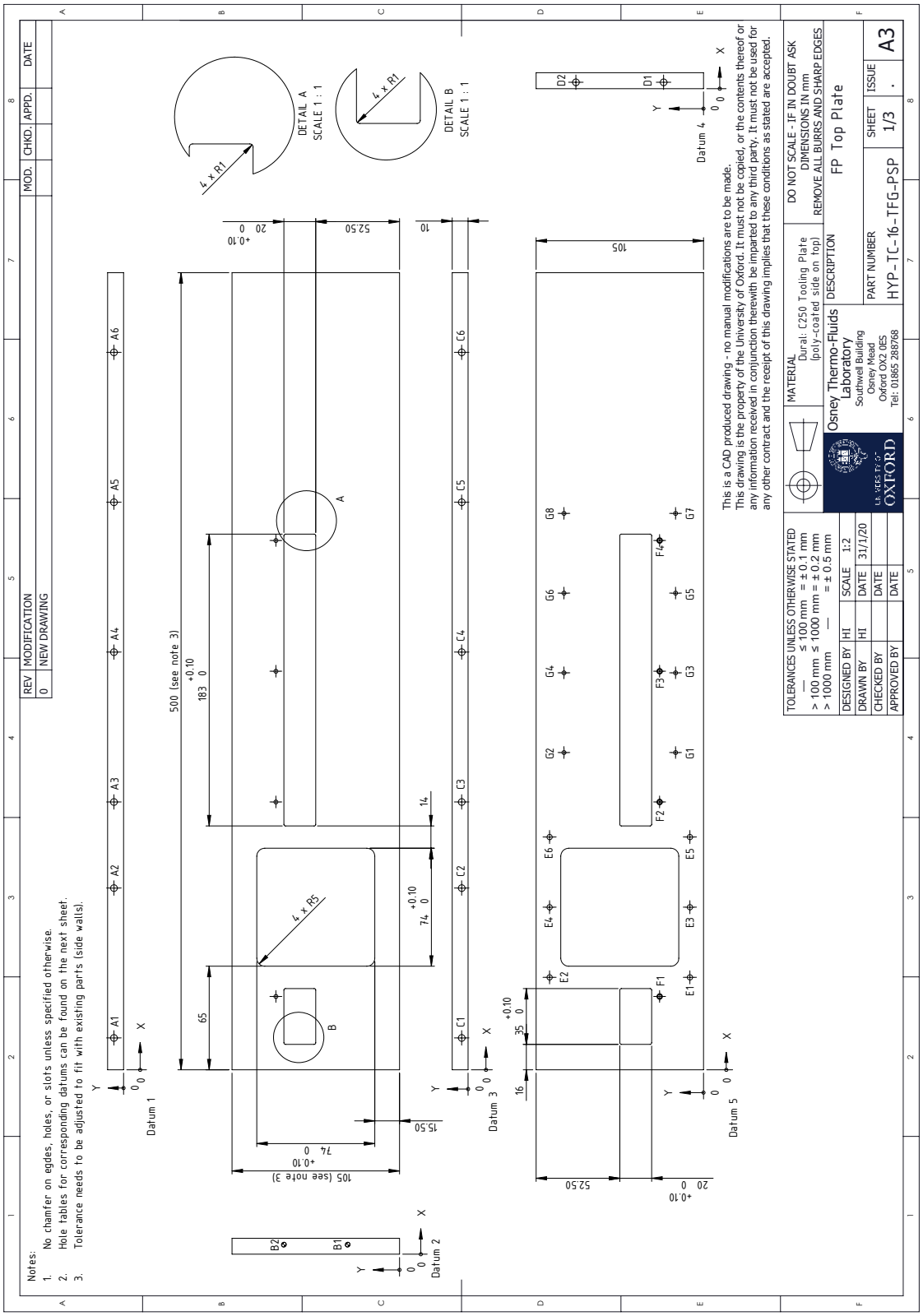
Notes:
1. No chamfer on egdes, holes, or slots unless specified otherwise.
2. Hole tables for corresponding datums can be found on the next sheet.
3. Tolerance needs to be adjusted to fit with existing parts (side walls).
REV MODIFICATION DATE
0 NEW DRAWING
MOD. CHKD. APPD.
DETAIL A SCALE 1 : 1
DETAIL B SCALE 1 : 1
4 x R1
4 x R5
500 (see note 3)
105 (see note 3)
52.50
15.50
65
183 +0.10 0
74 +0.10 0
20 +0.10 0
35 +0.10 0
Datum 1
Datum 2
Datum 3
Datum 4
Datum 5
TOLERANCES UNLESS OTHERWISE STATED
— ≤ 100 mm = ± 0.1 mm
> 100 mm ≤ 1000 mm = ± 0.2 mm
> 1000 mm — = ± 0.5 mm
DESIGNED BY HI SCALE 1:2
DRAWN BY HI DATE 31/1/20
CHECKED BY DATE
APPROVED BY DATE
MATERIAL
Dural: C250 Tooling Plate
(poly-coated side on top)
DESCRIPTION
FP Top Plate
DO NOT SCALE - IF IN DOUBT ASK
DIMENSIONS IN mm
REMOVE ALL BURRS AND SHARP EDGES
Osney Thermo-Fluids Laboratory
Southwell Building
Osney Mead
Oxford OX2 0ES
Tel: 01865 288768
PART NUMBER
HYP-TC-16-TFG-PSP
SHEET 1/3
ISSUE .
A3
This is a CAD produced drawing - no manual modifications are to be made.
This drawing is the property of the University of Oxford. It must not be copied, or the contents thereof or any information received in conjunction therewith be imparted to any third party. It must not be used for any other contract and the receipt of this drawing implies that these conditions as stated are accepted.

REV	MODIFICATION	MOD.	CHKD.	APPD.	DATE
0	NEW DRAWING				

Notes:

1. Corresponding datums for the hole tables can be found on the previous sheet.
2. It is essential to adjust the positions with existing parts for a flush fitment.
3. The existing part (tip) has dowel pins inserted. The pin size and location must be measured and new holes should be drilled according to this measurement for a flush fitment.

Datum 1 (see note 2)

TAG	X LOC	Y LOC	SIZE
A1	20	6	⌀ 4.20 ↧ 10 M5 - 6H ↧ 9.20
A2	114	6	
A3	168	6	
A4	262	6	
A5	356	6	
A6	450	6	

Datum 2 (see notes 2 and 3)

TAG	X LOC	Y LOC	SIZE
B1	6	32.50	⌀ 3 H7/h6 ↧ 11
B2	6	72.50	

Datum 3 (see note 2)

TAG	X LOC	Y LOC	SIZE
C1	20	4	⌀ 4.20 ↧ 10 M5 - 6H ↧ 9.20
C2	114	4	
C3	168	4	
C4	262	4	
C5	356	4	
C6	450	4	

Datum 4

TAG	X LOC	Y LOC	SIZE
D1	4	25	⌀ 4.20 ↧ 10 M5 - 6H ↧ 9.20
D2	4	80	

Datum 5

TAG	X LOC	Y LOC	SIZE
E1	58	8.50	⌀ 3.30 ↧ 7 M4 - 6H ↧ 6.30
E2	58	96.50	
E3	102	8.50	
E4	102	96.50	
E5	146	8.50	
E6	146	96.50	

TAG	X LOC	Y LOC	SIZE
F1	46	27.50	⌀ 2.50 THRU ALL ⌵ ⌀ 3.50 X 90°
F2	168	27.50	
F3	250	27.50	
F4	332	27.50	

TAG	X LOC	Y LOC	SIZE
G1	199	17.50	⌀ 2.50 ↧ 6 M3 - 6H ↧ 5.50
G2	199	87.50	
G3	249	17.50	
G4	249	87.50	
G5	299	17.50	
G6	299	87.50	
G7	349	17.50	
G8	349	87.50	

TOLERANCES UNLESS OTHERWISE STATED
— ≤ 100 mm = ± 0.1 mm
> 100 mm ≤ 1000 mm = ± 0.2 mm
> 1000 mm — = ± 0.5 mm

DESIGNED BY	HI	SCALE	1:2
DRAWN BY	HI	DATE	31/1/20
CHECKED BY		DATE	
APPROVED BY		DATE	

MATERIAL
Dural: C250 Tooling Plate
(poly-coated side on top)

DO NOT SCALE - IF IN DOUBT ASK
DIMENSIONS IN mm
REMOVE ALL BURRS AND SHARP EDGES

UNIVERSITY OF OXFORD
Osney Thermo-Fluids Laboratory
Southwell Building
Osney Mead
Oxford OX2 0ES
Tel: 01865 288768

DESCRIPTION: FP Top Plate

PART NUMBER	SHEET	ISSUE	
HYP-TC-16-TFG-PSP	2/3	.	A3

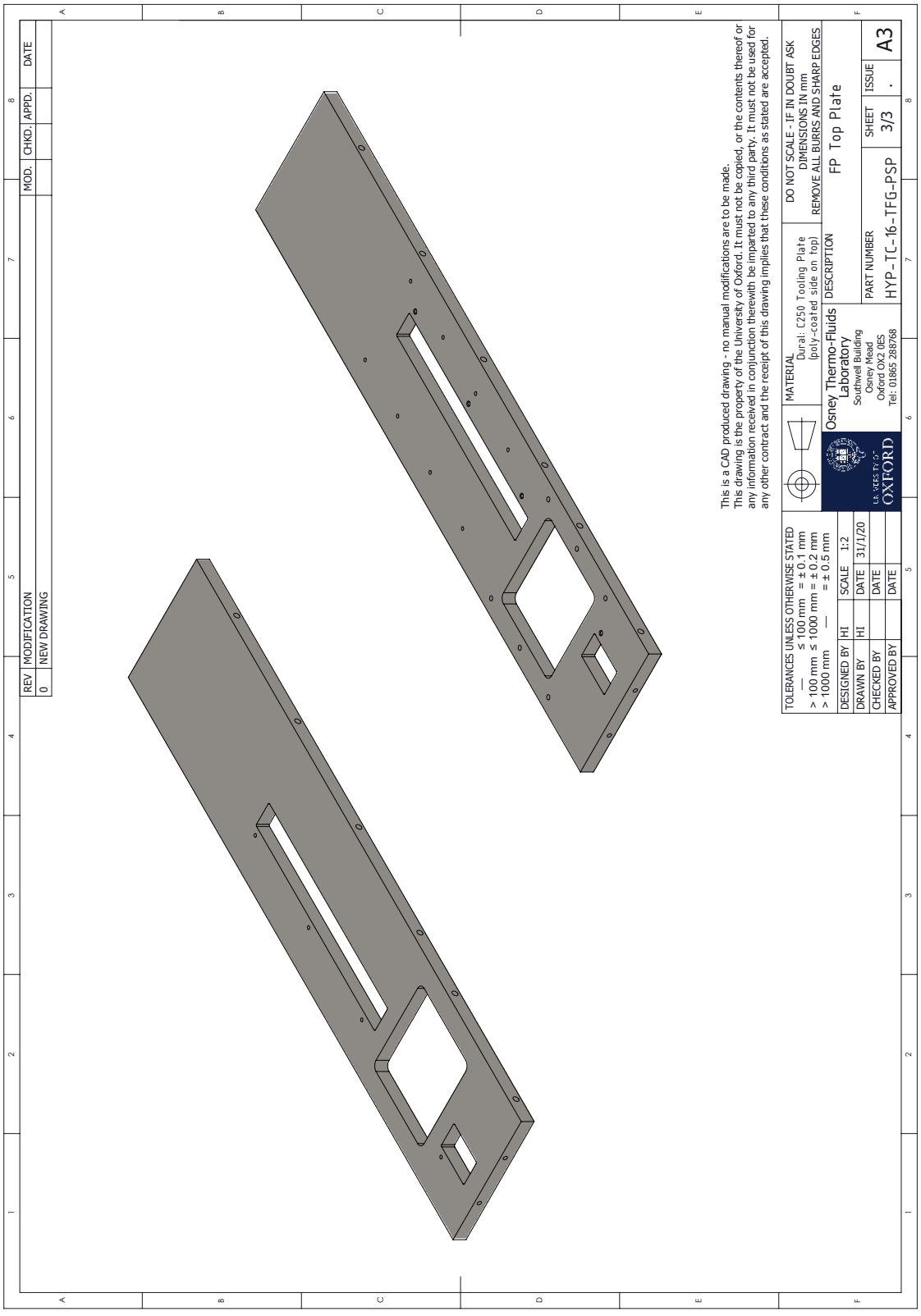
REV
MODIFICATION
DATE
MOD.
CHKD.
APPD.
0
NEW DRAWING
This is a CAD produced drawing - no manual modifications are to be made.
This drawing is the property of the University of Oxford. It must not be copied, or the contents thereof or any information received in conjunction therewith be imparted to any third party. It must not be used for any other contract and the receipt of this drawing implies that these conditions as stated are accepted.
TOLERANCES UNLESS OTHERWISE STATED
— ≤ 100 mm = ± 0.1 mm
> 100 mm ≤ 1000 mm = ± 0.2 mm
> 1000 mm — = ± 0.5 mm
DESIGNED BY HI SCALE 1:2
DRAWN BY HI DATE 31/1/20
CHECKED BY DATE
APPROVED BY DATE
MATERIAL
Dural: C250 Tooling Plate
(poly-coated side on top)
DO NOT SCALE - IF IN DOUBT ASK
DIMENSIONS IN mm
REMOVE ALL BURRS AND SHARP EDGES
DESCRIPTION
FP Top Plate
Osney Thermo-Fluids Laboratory
Southwell Building
Osney Mead
Oxford OX2 0ES
Tel: 01865 288768
PART NUMBER
HYP-TC-16-TFG-PSP
SHEET
3/3
ISSUE
.
A3

Bibliography

1976 U.S. Standard Atmosphere. U.S. Government Printing Office.

2003 Filter-Elements: High porosity sintered parts SIKA-B. GKN Sinter Metals Filters GmbH.

2006 BS EN ISO 4022:2006: Permeable sintered metal materials. Determination of fluid permeability.

Anderson, Jr John D 2006 *Hypersonic and High-Temperature Gas Dynamics, Second Edition*. Reston ,VA: American Institute of Aeronautics and Astronautics. doi: 10.2514/4.861956.

Aydin, M & Leutheusser, H J 1980 Very low velocity calibration and application of hot-wire probes. DISA Information, National Research Council of Canada.

Bacos, M P 1993 Carbon-carbon composites : oxidation behavior and coatings protection. *Le Journal de Physique IV* **03** (C7), C7–1895–C7–1903. doi: 10.1051/jp4:19937303.

Bashir, Muhammad Hassan, Shiau, Chao-Cheng & Han, Je-Chin 2017 Film cooling effectiveness for three-row compound angle hole design on flat plate using PSP technique. *International Journal of Heat and Mass Transfer* **115**, 918–929. doi: 10.1016/j.ijheatmasstransfer.2017.08.077.

Basore, K D, Selzer, M, Wheatley, V, Boyce, R R, Mee, D J, Capra, B R, Kuhn, M & Brieschenk, S 2016 Performance Comparison of Distributed Injection Methods for Hypersonic Film-Cooling. In *Twentieth Australasian Fluid Mechanics Conference*. Perth, Australia.

Bhatia, J C, Durst, F & Jovanovic, J 2006 Corrections of hot-wire anemometer measurements near walls. *Journal of Fluid Mechanics* **122** (-1), 411–431. doi: 10.1017/S0022112082002286.

Bird, R Byron, Stewart, Warren E & Lightfoot, Edwin N 2007 *Transport Phenomena*, 2nd edn. New York: John Wiley & Sons.

Blasius, H 1908 Grenzschichten in Flüssigkeiten mit kleiner Reibung. *Zeitschrift für angewandte Mathematik und Physik* **56**, 1–37.

Blottner, F G, Johnson, M & Ellis, M 1971 Chemically Reacting Viscous Flow Program for Multi-Component Gas Mixtures. *Tech. Rep.* SC-RR-70-754. doi: 10.2172/4658539.

Böhrk, Hannah 2014 Transpiration Cooling at Hypersonic Flight - AKTiV on SHEFEX II. In *11th AIAA/ASME Joint Thermophysics and Heat Transfer Conference*, p. 175. Reston, Virginia: American Institute of Aeronautics and Astronautics. doi: 10.2514/6.2014-2676.

Böhrk, H & Beyermann, U 2010 Secure tightening of a CMC fastener for the heat shield of re-entry vehicles. *Composite Structures* **92** (1), 107–112. doi: 10.1016/j.compstruct.2009.07.002.

Brune, A, Hosder, S, Gulli, S & Maddalena, L 2014 Variable Transpiration Cooling Effectiveness in Laminar and Turbulent Flows for Hypersonic Vehicles. *AIAA Journal* doi: 10.2514/1.J053053.

Bruun, H H 2002 *Hot-Wire Anemometry : Principles and Signal Analysis*. Oxford University Press.

Button, Keith 2018 Hypersonic Weapons Race, https://aerospaceamerica.aiaa.org/features/hypersonic-weapons-race, accessed: 17 December 2021 .

Charbonnier, D, Ott, P, Jonsson, M, Cottier, F & Köbke, Th 2009 Experimental and Numerical Study of the Thermal Performance of a Film Cooled Turbine Platform. In *ASME Turbo Expo Power for Land, Sea, and Air*, pp. 1027–1038. doi: 10.1115/GT2009-60306.

Coleman, Hugh W & Steele Jr., W Glenn 2009 *Experimentation, Validation, and Uncertainty Analysis for Engineers*. Hoboken, NJ, USA: John Wiley & Sons, Inc. doi: 10.1002/9780470485682.

Crank, John 1979 *The Mathematics of Diffusion*, 2nd edn. Oxford University Press.

Dittert, Christian, Selzer, Markus & Böhrk, Hannah 2017 Flowfield and Pressure Decay Analysis of Porous Cones. *AIAA Journal* **55** (3), 874–882. doi: 10.2514/1.J055298.

van Driest, E R 1952 Investigation of Laminar Boundary Layer in Compressible Fluids Using the Crocco Method .

van Driest, E R 1956 The Problem of Aerodynamic Heating. *Aeronautical Engineering Review* **15** (10), 26–41.

Eckert, E R G 1956 Engineering Relations for Heat Transfer and Friction in High-Velocity Laminar and Turbulent Boundary-Layer Flow over Surfaces with Constant Pressure and Temperature. *Transactions of the American Society of Mechanical Engineers* **78** (6), 1273.

Eckert, E R G, Schneider, P J, Hayday, A A & Larson, R M 1958 Mass-Transfer Cooling of a Laminar Boundary Layer by Injection of a Light-Weight Foreign Gas. *Journal of Jet Propulsion* doi: 10.2514/8.7218.

Erdim, Esra, Akgiray, Oemer & Demir, Ibrahim 2015 A revisit of pressure drop-flow rate correlations for packed beds of spheres. *Powder Technology* **283**, 488–504. doi: 10.1016/j.powtec.2015.06.017.

Ergun, Sabri 1952 Fluid flow through packed columns. *Chemical Engineering Progress* **48**, 89–94.

Esser, Burkard, Barcena, Jorge, Kuhn, Markus, Okan, Altug, Haynes, Lauren, Gianella, Sandro, Ortona, Alberto, Liedtke, Volker, Francesconi, Daniele & Tanno, Hideyuki 2016 Innovative Thermal Management Concepts and Material Solutions for Future Space Vehicles. *Journal of Spacecraft and Rockets* **53** (6), 1051–1060. doi: 10.2514/1.A33501.

Esser, B & Gülhan, A 2008 Qualification of Active Cooling Concepts in Ground Facilities. In *RESPACE – Key Technologies for Reusable Space Systems*, pp. 104–131. Springer, Berlin, Heidelberg. doi: 10.1007/978-3-540-77819-6_7.

Eucken, A 1913 Über das Wärmeleitvermögen,die spezifische Wärme und die innere Reibung der Gase. *Zeitschrift für Physik* **14**, 324–332.

Ewenz Rocher, Marc, Hermann, Tobias, McGilvray, Matthew, Ifti, Hassan Saad, Vieira, Joao, Hambidge, Chris, Quinn, Mark Kenneth, Grossman, Madeleine & Vandeperre, Luc 2022 Pressure-sensitive paint diagnostic to measure species concentration on transpiration-cooled walls. *Experiments in Fluids* **63** (1), 1–11. doi: 10.1007/s00348-021-03355-9.

Ewenz Rocher, Marc, McGilvray, Matthew, Hermann, Tobias A, Ifti, Hassan S, Hufgard, Fabian, Eberhart, Martin F, Meindl, Arne, Loehle, Stefan, Giovannini, Tommaso & Vandeperre, Luc J 2019 Testing a Transpiration Cooled Zirconium-Di-Boride sample in the Plasma Tunnel at IRS. In *AIAA Scitech 2019 Forum*, p. 01. Reston, Virginia: American Institute of Aeronautics and Astronautics. doi: 10.2514/6.2019-1552.

Fitt, A D, Ockendon, J R & Jones, T V 1985 Aerodynamics of Slot-Film Cooling: Theory and Experiment. *Journal of Fluid Mechanics* **160**, 15–27. doi: 10.1017/S0022112085003366.

Florio, Jr John, Henderson, Jack B, Test, Frederick L & Hariharan, Ramamurthy 2016 Characterization of Forced Convection Heat Transfer in Decomposing, Glass-Filled Polymer Composites:. *Journal of Composite Materials* doi: 10.1177/002199839102501108.

Fujiwara, K, Sriram, R, Kontis, K & Ideta, T 2017 Review on Film Cooling in High-Speed Flows. In *31st International Symposium on Shock Waves 2*, pp. 939–946. Springer, Cham. doi: 10.1007/978-3-319-91017-8_118.

Gascoin, N 2011 High temperature and pressure reactive flows through porous media. *International Journal of Multiphase Flow* **37** (1), 24–35. doi: 10.1016/j.ijmultiphaseflow.2010.09.001.

Gascoin, Nicolas, Fau, Guillaume, Gillard, Phillipe, Kuhn, Markus, Bouchez, Marc & Steelant, Johan 2012 Comparison of Two Permeation Test Benches and of Two Determination Methods for Darcy's and Forchheimer's Permeabilities. *Journal of Porous Media* **15** (2012), 705–720. doi: 10.1615/JPorMedia.v15.i8.10.

Giles, Daniel N 1988 Integral cooling system for high-temperature missile structures.

Gill, Bates 2021 AUKUS is a Big Deal, but Needs to be Put in Perspective, https://rusi.org/explore-our-research/publications/commentary/aukus-big-deal-needs-be-put-perspective, accessed: 17 December 2021.

Goldstein, Richard J 1971 Film Cooling. *Advances in Heat Transfer* **7**, 321–379. doi: 10.1016/S0065-2717(08)70020-0.

Goldstein, Richard J, Eckert, E R G & Wilson, D J 1968 Film Cooling With Normal Injection Into a Supersonic Flow. *ASME Journal of Engineering for Industry* **90** (4), 584–588. doi: 10.1115/1.3604692.

Goldstein, R J & Jabbari, M Y 1970 Film cooling effectiveness with helium and refrigerant 12 injection into a supersonic flow. *AIAA Journal* doi: 10.2514/3.6100.

Goldstein, R J & Jin, P 2000 Film Cooling Downstream of a Row of Discrete Holes With Compound Angle. *Journal of Turbomachinery* **123** (2), 222–230. doi: 10.1115/1.1344905.

Gülhan, A & Braun, S 2010 An experimental study on the efficiency of transpiration cooling in laminar and turbulent hypersonic flows. *Experiments in Fluids* **50** (3), 509–525. doi: 10.1007/s00348-010-0945-6.

Harrison, Ruth 2021 Hypersonix and Boeing Join Forces to Develop a Hypersonic Launch Vehicle, http://spaceaustralia.com/news/hypersonix-and-boeing-join-forces-develop-hypersonic-launch-vehicle, accessed: 17 December 2021.

Haven, B A & Kurosaka, M 1997 Kidney and anti-kidney vortices in crossflow jets. *Journal of Fluid Mechanics* **352**, 27–64. doi: 10.1017/S0022112097007271.

Hermann, T, Ifti, H S, McGilvray, M, Doherty, L & Geraets, R P 2018 Mixing characteristics in a hypersonic flow around a transpiration cooled flat plate model. In *International Conference on High-Speed Vehicle Science and Technology (HiSST)*. Moscow, Russia.

Hermann, Tobias, McGilvray, Matthew, Hambidge, Chris, Doherty, Luke & Buttsworth, David 2019*a* Total Temperature Measurements in the Oxford High Density Tunnel. In *International Conference on Flight vehicles, Aerothermodynamics and Re-entry Missions and Engineering, FAR*. Monopoli, Italy.

Hermann, Tobias, McGilvray, Matthew & Naved, Imran 2019*b* Performance of Transpiration-Cooled Heat Shields for Reentry Vehicles. *AIAA Journal* doi: 10.2514/1.J058515.

Heufer, K A & Olivier, H 2008*a* Experimental and Numerical Study of Cooling Gas Injection in Laminar Supersonic Flow. *AIAA Journal* doi: 10.2514/1.34218.

Heufer, K A & Olivier, H 2008*b* Experimental Study of Active Cooling in 8 Laminar Hypersonic Flows. In *RESPACE – Key Technologies for Reusable Space Systems*, pp. 132–150. Springer, Berlin, Heidelberg. doi: 10.1007/978-3-540-77819-6_8.

Hombsch, M & Olivier, H 2013 Film Cooling in Laminar and Turbulent Supersonic Flows. *Journal of Spacecraft and Rockets* doi: 10.2514/1.A32346.

Ifti, Hassan Saad, Hermann, Tobias, Ewenz Rocher, Marc, Doherty, Luke, Hambidge, Christopher, McGilvray, Matthew & Vandeperre, Luc 2022*a* Laminar transpiration cooling experiments in hypersonic flow. *Experiments in Fluids* **63** (6), 1–14. doi: 10.1007/s00348-022-03446-1.

Ifti, Hassan Saad, Hermann, Tobias & McGilvray, Matthew 2019 Transpiration Cooling At Mach 5 Employing Porous UHTC. In *Conference on Flight vehicles, Aerothermodynamics and Re-entry Missions and Engineering (FAR)*. Monopoli, Itlay: European Space Agency.

Ifti, Hassan Saad, Hermann, Tobias & McGilvray, Matthew 2022*b* Analytical Model of Transpired-Coolant Concentration at Downstream Wall in High-Speed Laminar Flow. *AIAA Journal* .

Ifti, Hassan Saad, Hermann, Tobias, McGilvray, Matthew, Larrimbe, Laura, Hedgecock, Rowan & Vandeperre, Luc 2022*c* Flow Characterization of Porous Ultra-High-Temperature Ceramics for Transpiration Cooling. *AIAA Journal* **60** (5). doi: 10.2514/1.J061009.

Ifti, Hassan Saad, Hermann, Tobias, McGilvray, Matthew & Merrifield, James 2022*d* Numerical Simulation of Transpiration Cooling in a Laminar Hypersonic Boundary Layer. *Journal of Spacecraft and Rockets* doi: 10.2514/1.A35325.

Jørgensen, Finn E 2005 *How to Measure Turbulence with Hot-Wire Anemometers*.

von Kármán, Theodore 1954 *Aerodynamics: Selected Topics in the Light of Their Historical Development*. Ithaca, New York: Cornell University Press.

Kays, W M, Crawford, M E & Weigand, Bernhard 2005 *Convective Heat and Mass Transfer*, 4th edn. McGraw-Hill Higher Education.

Keller, Michael A, Kloker, Markus J & Olivier, Herbert 2015 Influence of Cooling-Gas Properties on Film-Cooling Effectiveness in Supersonic Flow. *Journal of Spacecraft and Rockets* doi: 10.2514/1.A33203.

Kelly, H Neale & Blosser, Max L 1994 Active Cooling From the Sixties to Nasp .

Keyes, Frederick G 1952 The Heat Conductivity, Viscosity, Specific Heat and Prandtl Numbers for Thirteen Gases. .

Keyser, M J, Conradie, M, Coertzen, M & Van Dyk, J C 2006 Effect of coal particle size distribution on packed bed pressure drop and gas flow distribution. *Fuel* **85** (10-11), 1439–1445. doi: 10.1016/j.fuel.2005.12.012.

Koekemoer, Andrei & Luckos, Adam 2015 Effect of material type and particle size distribution on pressure drop in packed beds of large particles: Extending the Ergun equation. *Fuel* **158**, 232–238. doi: 10.1016/j.fuel.2015.05.036.

König, V, Rom, M, Müller, S, Selzer, M, Schweikert, S & von Wolfersdorf, J 2019 Numerical and Experimental Investigation of Transpiration Cooling with Carbon/Carbon Characteristic Outflow Distributions. *Journal of Thermophysics and Heat Transfer* doi: 10.2514/1.T5457.

Kuhn, M & Hald, H 2008 Application of Transpiration Cooling for Hot Structures. In *RESPACE – Key Technologies for Reusable Space Systems*, pp. 82–103. Springer, Berlin, Heidelberg. doi: 10.1007/978-3-540-77819-6_6.

Langener, Tobias, Wolfersdorf, Jens Von & Steelant, Johan 2011 Experimental Investigations on Transpiration Cooling for Scramjet Applications Using Different Coolants. *AIAA Journal* **49** (7), 1409–1419. doi: 10.2514/1.J050698.

Launius, Roger D & Jenkins, Dennis R 2012 *Coming Home: Reentry and Recovery from Space*.

Lee, Jong-Hun 1984 Basic Governing Equations for the Flight Regimes of Aeroassisted Orbital Transfer Vehicles. In *19th Thermophysics Conference*. Snowmass, CO, USA. doi: 10.2514/6.1984-1729.

Lee, William E, Giorgi, Edoardo, Harrison, Robert, Maître, Alexandre & Rapaud, Olivier 2014 Nuclear Applications for Ultra-High Temperature Ceramics and MAX Phases. In *Ultra-High Temperature Ceramics*, pp. 391–415. Hoboken, NJ: John Wiley & Sons, Inc. doi: 10.1002/9781118700853.ch15.

Leyva, Ivett A 2017 The Relentless Pursuit of Hypersonic Flight. *Physics Today* **70** (11), 30. doi: 10.1063/PT.3.3762.

Ligrani, P M, Wigle, J M & Jackson, S W 1994 Film-Cooling From Holes With Compound Angle Orientations: Part 2—Results Downstream of a Single Row of Holes With 6d Spanwise Spacing. *Journal of Heat Transfer* **116** (2), 353–362. doi: 10.1115/1.2911407.

Löhle, Stefan, Schweikert, Sven & von Wolfersdorf, Jens 2016 Method for Heat Flux Determination of a Transpiration-Cooled Wall from Pressure Data. *Journal of Thermophysics and Heat Transfer* **30** (3), 567–572. doi: 10.2514/1.T4815.

Macdonald, I F, El-Sayed, M S, Mow, K & Dullien, F A L 1979 Flow through Porous Media-the Ergun Equation Revisited. *Industrial Engineering Chemistry Fundamentals* **18**, 199–208. doi: 10.1021/i160071a001.

McGilvray, Matthew, Doherty, Luke J, Neely, Andrew J, Pearce, Robert & Ireland, Peter 2015 The Oxford High Density Tunnel. In *20th AIAA International Space Planes and Hypersonic Systems and Technologies Conference*, p. 17. Reston, Virginia: American Institute of Aeronautics and Astronautics. doi: 10.2514/6.2015-3548.

Meinert, Jens, J-ograve, Huhn, R G, Serbest, Erhan & Haidn, Oskar J 2001 Turbulent Boundary Layers with Foreign Gas Transpiration. *Journal of Spacecraft and Rockets* **38** (2), 191–198. doi: 10.2514/2.3693.

Moffat, Robert J 1988 Describing the uncertainties in experimental results. *Experimental Thermal and Fluid Science* **1** (1), 3–17. doi: 10.1016/0894-1777(88)90043-X.

Murray, A V, Ireland, Peter, Wong, T H, Tang, S W & Rawlinson, A J 2017 High Resolution Experimental and Computational Methods for Modelling Multiple Row Effusion Cooling Performance . In *Proceedings of th European Conference on Turbomachinery Fluid dynamics Thermodynamics ETC, April -, ; Stockholm, Sweden.*

Najmi, H, El-Tabach, E, Chetehouna, K, Gascoin, N & Falempin, F 2016 Effect of flow configuration on Darcian and Forchheimer permeabilities determination in a porous composite tube. *International Journal of Hydrogen Energy* **41** (1), 316–323. doi: 10.1016/j.ijhydene.2015.10.054.

Narzary, Diganta P, Liu, Kuo-Chun, Rallabandi, Akhilesh P & Han, Je-Chin 2012 Influence of Coolant Density on Turbine Blade Film-Cooling Using Pressure Sensitive Paint Technique. *Journal of Turbomachinery* **134** (3), 031006 (10 pages). doi: 10.1115/1.4003025.

Nelder, J A & Mead, R 1965 A Simplex Method for Function Minimization. *The Computer Journal* **7** (4), 308–313. doi: 10.1093/comjnl/7.4.308.

Netterfield, M P 1991 Hypersonic Aerothermodynamic Computations Using a Point - Implicit TVD Method. *First European Symposium on Aerothermodynamics for Space Vehicles, ESTEC* .

Netterfield, M P 1992 Validation of a Navier Stokes Code for Thermochemical Non Equilibrium Flows. In *AIAA Twenty-Seventh Thermophysics Conference.*

Nield, Donald A & Bejan, Adrian 2013 *Convection in Porous Media*, 4th edn. Springer, New York, NY. doi: 10.1007/978-1-4614-5541-7.

Oldfield, M L G 2008 Impulse Response Processing of Transient Heat Transfer Gauge Signals. *Journal of Turbomachinery* **130** (2), 709. doi: 10.1115/1.2752188.

Quinn, Mark Kenneth, Yang, Leichao & Kontis, Konstantinos 2011 Pressure-Sensitive Paint: Effect of Substrate. *Sensors* **11** (12), 11649–11663. doi: 10.3390/s111211649.

Rallabandi, Akhilesh P, Grizzle, Joshua & Han, Je-Chin 2011 Effect of Upstream Step on Flat Plate Film-Cooling Effectiveness Using PSP. *Journal of Turbomachinery* doi: 10.1115/1.4002422.

Ramshaw, J D 1990 Self-Consistent Effective Binary Diffusion in Multicomponent Gas Mixtures. *Journal of Non-Equilibrium Thermodynamics* **15**, 295–300. doi: 10.1515/jnet.1990.15.3.295.

Reimer, Thomas, Kuhn, Markus, Gülhan, Ali, Esser, Burkhard, Sippel, Martin & van Foreest, Arnold 2012 Transpiration Cooling Tests of Porous CMC in Hypersonic Flow. In *17th AIAA International Space Planes and Hypersonic Systems and Technologies Conference*, p. N978. Reston, Virigina: American Institute of Aeronautics and Astronautics. doi: 10.2514/6.2011-2251.

Richards, B E & Stollery, J L 1979 Laminar Film Cooling Experiments in Hypersonic Flow. *Journal of Aircraft* doi: 10.2514/3.58502.

Sauter, Josef 1926 *Die Grössenbestimmung der im Gemischnebel von Verbrennungskraftmaschinen vorhandenen Brennstoffteilchen*. VDI-Verlag.

Schneider, Steven P 2012 Hypersonic Boundary-Layer Transition with Ablation and Blowing. *Journal of Spacecraft and Rockets* **47** (2), 225–237. doi: 10.2514/1.43926.

Schultz, D L & Jones, T V 1973 Heat-Transfer Measurements in Short-Duration Hypersonic Facilities. *Tech. Rep.* AD-758 590. Advisory Group For Aerospace Research and Development, North Atlantic Treaty Organization.

Schweikert, Sven, von Wolfersdorf, Jens, Selzer, Markus & Hald, Hermann 2013*a* Characterization of Actively Cooled Porous C/C Wall Segments According to Pressure Loss and Internal Temperature Distribution. In *Proceedings of the Seventh European Workshop on Thermal Protection Systems Hot Structures, April , ESAESTEC, Noordwijk, the Netherlands*.

Schweikert, Sven, von Wolfersdorf, Jens, Selzer, Markus & Hald, H 2013*b* Experimental Investigation on Velocity and Temperature Distributions of Turbulent Cross Flows over Transpiration Cooled C/C-Wall Segments. In *Fifth European Conference For Aeronautics And Space Sciences Eucass*.

Sellers, Marvin, Nelson, Michael & Crafton, Jim W 2016 Dynamic Pressure-Sensitive Paint Demonstration in AEDC Propulsion Wind Tunnel 16T. In *54th AIAA Aerospace Sciences Meeting*. San Diego, California, USA. doi: 10.2514/6.2016-1146.

Stein, Liz 2021 Influx of Private Capital Marks Another Potential Hypersonic Inflection Point, https://aerospaceamerica.aiaa.org/year-in-review/influx-of-private-capital-marks-another-potential-hypersonic-inflection-point, accessed: 17 December 2021. .

Strauss, Friedolin, Wössner, Manuel, Weisswange, Matthias, Manfletti, Chiara & Schlechtriem, Stefan 2017 Experiments on Flow Interaction in a Transpiration Cooled Model Scramjet. In *7th European Conference For Aeronautics And Space Sciences Eucass*. doi: 10.13009/EUCASS2017-235.

Sutherland, William 1853 LII. The viscosity of gases and molecular force. *The London, Edinburgh, and Dublin Philosophical Magazine and Journal of Science* **36** (223), 507–531. doi: 10.1080/14786449308620508.

Tanno, H, Komuro, T, Itoh, K, Kuhn, Markus, Petkov, Ivaylo & Esser, B 2016 Transpiration cooling experiments in free-piston shock tunnel HIEST. In *Eighth European Workshop on Thermal Protection Systems and Hot Structures*. Noordwijk, Netherlands.

Tropf, William J, Thomas, Michael E, Harris, Terry J & Lutz, Steven A 1987 Performance of Optical Sensors in Hypersonic Flight. *Johns Hopkins APL Technical Digest* **8** (4).

Tsanis, Ioannis K 1987 Calibration of hot-wire anemometers at very low velocities. Dantec Information.

Uyanna, Obinna & Najafi, Hamidreza 2020 Thermal protection systems for space vehicles: A review on technology development, current challenges and future prospects. *Acta Astronautica* **176**, 341–356. doi: 10.1016/j.actaastro.2020.06.047.

Varvill, R & Bond, A 2008 The Skylon Space Plane: Progress to Realisation. *British Interplanetary Science* **61**, 412–418.

Wang, Jianye & Vandeperre, Luc J 2014 Deformation and Hardness of UHTCs as a Function of Temperature. In *Ultra-High Temperature Ceramics: Materials for Extreme Environment Applications* (ed. William G Fahrenholtz, Eric J Wuchina, William E Lee & Yanchun Zhou). Hoboken, NJ: John Wiley & Sons, Inc.

Wasserbly, Daniel 2021 Pentagon Budget 2022: Hypersonic Weapons Would Get USD3.8 Billion Boost, https://www.janes.com/defence-news/news-detail/pentagon-budget-2022-hypersonic-weapons-would-get-usd38-billion-boost, accessed 17 December 2021.

Wilke, C R 2004 A Viscosity Equation for Gas Mixtures. *The Journal of Chemical Physics* **18** (4), 517. doi: 10.1063/1.1747673.

Wylie, Sebastien 2020 Hypersonic Boundary Layer Instability Measurements at Low and High Angles of Attack. PhD thesis, University of Oxford.

Wylie, Sebastien & McGilvray, Matthew 2019 HIFiRE-1 Post-Flight Experiments in the University of Oxford's High Density Tunnel. In *AIAA Scitech 2019 Forum*. San Diego, California. doi: 10.2514/6.2019-1940.

Yavuzkurt, S, Moffat, R J & Kays, W M 1980*a* Full-Coverage Film Cooling. Part 1. Three-Dimensional Measurements of Turbulence Structure. *Journal of Fluid Mechanics* **101** (1), 129–158. doi: 10.1017/S0022112080001577.

Yavuzkurt, S, Moffat, R J & Kays, W M 1980*b* Full-Coverage Film Cooling. Part 2. Prediction of the Recovery-Region Hydrodynamics. *Journal of Fluid Mechanics* **101** (1), 159–178. doi: 10.1017/S0022112080001589.

Zhang, Luzeng J & Jaiswal, Ruchira Sharma 2001 Turbine Nozzle Endwall Film Cooling Study Using Pressure-Sensitive Paint. *Journal of Turbomachinery* **123** (4), 730–738. doi: 10.1115/1.1400113.

"One day, in retrospect, the years of struggle will strike you as the most beautiful."

— *Sigmund Freud*

Alles hat ein Ende, nur die Wurst hat zwei.

And thus, this thesis has an end too.